

The physics of collective cyclotron emission from fusion-born ions in deuterium-tritium and deuterium-helium-3 fusion plasmas

Submitted to the University of Warwick

by

Tobias Wiesław Slade-Harajda

for the degree of

Doctor of Philosophy

Department of Physics

March 14, 2025

“One never notices what has been done; one can only see what remains to be done.”

- Marie Curie

DRAFT

Contents

List of Figures	viii
List of Tables	ix
Acknowledgements	x
Declaration	xi
1 Introduction to fusion & plasma physics	1
1.1 Fusion	1
1.1.1 Aneutronic fusion	3
1.2 Plasma physics	5
1.2.1 Definition and quasi-neutrality	5
1.2.2 Plasma production	6
1.2.3 Single particle dynamics	7
1.2.4 Fundamental time and length scales	8
1.2.5 Kinetic theory	11
1.2.6 Waves in a plasma	12
1.3 Tokamaks	20
1.3.1 Plasma confinement	20
1.3.2 Trapped and passing orbits	23
1.3.3 Measuring plasma density	23
1.4 The magnetoacoustic cyclotron instability (MCI) and ion cyclotron emission (ICE)	25
1.4.1 Magnetoacoustic cyclotron instability (MCI)	25
1.4.2 Velocity space distributions	26
1.4.3 Ion cyclotron emission (ICE)	30
1.4.4 Re-energisation of minority particles	32

2 Computational methods	34
2.1 Particle-in-cell codes	34
2.1.1 Updating fields and pushing particles	35
2.1.2 Shape functions	37
2.1.3 Resolution scales	39
2.2 Benchmarking simulations	41
2.2.1 Two-stream instability	41
2.2.2 Cold plasma	46
2.3 Analytically solving the linearised Maxwell-Vlasov equation	48
2.4 Methods of analysis	52
2.4.1 Power spectra	52
2.4.2 Methods of comparing power spectra	53
2.4.3 Bicoherence and bispectral analysis	56
2.5 Summary	59
3 Parameter scan	60
3.1 Total length	60
3.2 Cell length	62
3.2.1 Resolved electron Larmor radii	64
3.2.2 Resolved deuteron Larmor radii	64
3.2.3 Resolved alpha particle Larmor radii	64
3.3 Summary	64
4 Multiple ions in PIC simulations	66
4.1 Considerations	67
4.1.1 Number of macroparticles per cell	67
4.1.2 Number density weighting (NDW)	68
4.1.3 Fast Alfvén wave dispersion and validity of low frequency regime for non-zero tritium concentrations	71
4.1.4 Minority concentration	73
4.2 Consequences	75
4.2.1 Particles per cell per species (PPCPS)	75
4.2.2 Gyro-resonance	79
4.2.3 Buchsbaum resonant frequency	80
4.3 Summary	85
5 PIC simulations of multicomponent DT fusion plasmas	86
5.1 Computational approach	86
5.1.1 Structure of simulations	87

5.1.2	Velocity space distributions	89
5.2	Time evolution of field and particle energies	90
5.2.1	First principles PIC simulation of MCI with zero tritium concentration	90
5.2.2	Field energy densities and dependence on tritium concentration	92
5.2.3	Particle energy and dependence on tritium concentration	93
5.3	Influence of tritium concentration on the spatiotemporal distribution of excited field energy	95
5.3.1	Group and phase speed of the MCI	96
5.4	Variation of simulated ICE frequency spectra with tritium concentration	97
5.5	Comparison of growth rates between simulation and MCI theory	100
5.6	Impact of tritium concentration on the distribution of field energy in wavenumber space	101
5.7	Influence of tritium concentration on nonlinear coupling of fields across wavenumber space	103
5.7.1	Frequency shifting	104
5.8	Quantitative comparisons of spectral dependence on tritium concentration	106
5.9	Summary and conclusions	107
6	Tritium ion influence on a Linear Maxwell-Vlasov solver extracting growth rates of the MCI	109
6.1	Computational method	109
6.2	Dependence of growth rates in $(k_{\perp}, k_{\parallel})$ space on tritium concentration	110
6.2.1	Linear growth rates as a function of tritium concentration	112
6.3	LMV output as a representation of MCI linear theory	117
6.4	Treatment of linear trends in peak growth rates	118
6.5	Peak frequency and growth rate dependence on tritium concentration	118
6.6	Equivalent Alfvén speed in D and DT plasmas	122
6.7	Summary and conclusions	125
7	PIC simulations of aneutronic D–3He fusion plasmas and the generation of ICE	126
7.1	Cylindrical approach and approximating the location of perpendicular birth velocity resonance with the FAW	126

7.2	Simulating Aneutronic Experiments	129
7.3	Particle-in-cell approach	132
7.3.1	Plasma density as a function of ${}^3\text{He}$ concentration	133
7.3.2	Number of particles per cell	135
7.3.3	Spatial resolution considerations	135
7.4	Results	136
7.4.1	Time evolution of field and particle energy densities	136
7.4.2	Energy partitioning via gyro-resonance	136
7.4.3	Doppler shifted ICE spectra and the spatiotemporal distribution of excited field energy	140
7.4.4	Simulated ICE power spectra	141
7.4.5	Exploring energy of minority species	145
7.5	Summary and conclusions	147
8	Summary & Conclusions	149
8.1	ICE from simulated DT plasmas	150
8.2	Analytically sourcing growth rates of the MCI	151
8.3	ICE from simulated D– ${}^3\text{He}$ plasmas	152
8.3.1	Future work	153
A	The shared area between curves	154
A.1	Shared area method	154
A.2	Alternative uses and multidimensionality	157
B	A two-dimensional maximal likelihood statistic	160
C	Gradient detection in (\mathbf{k}, ω) space using kernels	163
D	Isoangle data extraction in (\mathbf{k}, ω) and $(k_{\perp}, k_{\parallel})$ space	168
D.1	Constructing Doppler shifted power spectra in (\mathbf{k}, ω) space	168
D.2	Extracting growth rates for arbitrary magnetic field angles in $(k_{\perp}, k_{\parallel})$ space	169
Bibliography		171

List of Figures

1.1	Cross-section fusion probabilities for D–D, D–T, D– ${}^3\text{He}$ and p– ${}^{11}\text{B}$ reactions	5
1.2	Cold plasma dispersion relation for ions and electrons	18
1.3	Dispersion plots for IBW waves in high and low density plasma limits	19
1.4	Schematic of the magnetic field configuration in a tokamak cross-section	22
1.5	Schematic of a magnetic mirror	22
1.6	Diagram showing a trapped (banana) and passing orbit of fast particles in a cross-sectional view of a tokamak	24
1.7	Comparison between 3.5MeV α particle ring-beam distributions .	28
1.8	Ring-beam comparisons	29
1.9	Reproduction of the JET plasma 26148 ICE power spectra	30
1.10	ICE intensity as a function of fusion reactivity	32
2.1	Illustration of the Yee staggered grid	36
2.2	Shape functions	38
2.3	Two-stream phase space multi-plot through time	43
2.4	Two-stream energy histogram evolution	44
2.5	Evolution of the mean of the absolute electric field for a two-stream instability	45
2.6	Fourier transformations in space and time of the two-stream instability	46
2.7	Cold plasma spatiotemporal Fourier transform for a purely perpendicular magnetic field	47
2.8	Cold plasma spatiotemporal Fourier transform for a purely parallel magnetic field	48
2.9	Schematic of the bifurcation of iterative Nelder-Mead simplexes .	50
2.10	Example output of the Linear Maxwell-Vlasov code of growth rate solutions in $(k_{\perp}, k_{\parallel})$ space.	51

2.11	Phase correlation example between two Gaussians	54
2.12	Shared area example between two Gaussians	56
2.13	Bicoherence example of trace tritium JET 26148 simulation	58
3.1	Spatiotemporal Fourier transforms comparing spatial resolution in terms of Larmor radii	61
3.2	Resolution in wavenumber space comparisons	62
3.3	Three PIC simulations investigating the cause of numerical heating resulting from grid cell resolution.	65
4.1	Comparisons between two and three thermal ions for PIC simulations where NDW is held equal and unequal	70
4.2	Diagram of the process for comparing integer cyclotron harmonics with respect to secondary bulk ion concentration	72
4.3	Alfvén wavenumber as a function of tritium concentration	74
4.4	Collation of power spectral densities for increasing minority particle PPCPS	76
4.5	Mean peak signal-to-noise ratio of power spectra for increasing minority macroparticle number.	76
4.6	Collation of log velocity distributions per species for varying macroparticles per cell	77
4.7	Evolution of the squared ensemble Larmor radius through time for multiple ^3He concentrations.	81
4.8	Invariant gyro-resonant ratio for deuterons and ^3He ions	82
4.9	Buchsbaum resonance criteria and the maximal resonant amplitude as a function of secondary (tritium) concentration.	83
4.10	Maximum amplitude of the Buchsbaum multiple ion resonance as a concentration of mass ratio	84
5.1	Time evolution of the change in particle and field energy densities for a pure deuterium plasma	91
5.2	The fast alpha-particle velocity probability distribution function at the initial and end times of the simulation	92
5.3	Time evolution of the natural logarithm of the change in field energy densities, for a range of tritium concentrations	92
5.4	Time evolution of the change in mean kinetic energy per particle for multiple tritium concentrations	93
5.5	Gyro-resonance of DT energy densities through time	95

5.6	Spatiotemporal Fourier transforms and associated power spectral densities for multiple tritium concentrations	96
5.7	Phase and group velocity of the most excited MCI region	98
5.8	Power spectral density (PSD) comparison for multiple tritium concentrations	99
5.10	Spatial Fourier transform of the oscillatory B_z component through time	102
5.11	Bicoherence spectra of the oscillatory B_z field component for multiple tritium concentrations	103
5.12	Frequency offsets of simulated power spectra from JET DT 26148 plasmas with respect to pure deuterium trace	105
6.1	Growth rates in two dimensional wavenumber $(k_{\perp}, k_{\parallel})$ space	111
6.2	Growth rates in two dimensional wavenumber $(k_{\perp}, k_{\parallel})$ space focusing on the development of growth rates at high wavenumbers	112
6.3	Growth rates across $(k_{\perp}, k_{\parallel})$ space for zero and 95% tritium concentration for all k_{\parallel} and the $\theta = 89^\circ$ magnetic field orientation.	113
6.4	Linear MCI growth rates plotted as a function of frequency for isoangle magnetic field lines	114
6.5	Peak linear MCI growth rates as a function of frequency compared against the scaled JET 26148 power spectrum.	115
6.6	Linear MCI growth rates at multiple magnetic field orientations as calculated by the LMV code compared to linear theory.	116
6.7	Linear MCI growth rates as a function of frequency for tritium concentrations between zero and 90%.	119
6.8	Peak linear MCI growth rates as a function of frequency with the doublet splitting feature highlighted in red.	120
6.9	Peak growth rates as a function of frequency and tritium concentration	121
6.10	Zoom in plot of peak growth rates through concentration space highlighting the emergent trends labelled A and B.	122
6.11	Subtraction of growth rates between DT and D plasmas	124
7.1	Cylindrical approximation of tokamak	127
7.2	Density, magnetic field and Alfvén velocity profile in a tokamak cross-section	130
7.3	Change in field and particle energy densities through time for increasing ${}^3\text{He}$ concentration.	137

7.4	Ratio between the electrostatic and electromagnetic change in field energy densities	138
7.5	Ratio between change in kinetic energy per ion for multiple times and multiple ${}^3\text{He}$ concentrations	139
7.6	Spatiotemporal Fourier transform of the oscillatory magnetic field ΔB_z^2 for multiple ${}^3\text{He}$ concentration PIC simulations	140
7.7	Logarithmic power spectral densities of the ICE spectra from each helium-3 concentration simulation in horizontal scans of the wavenumber space	142
7.8	Logarithmic power spectral densities of the ICE spectra from each helium-3 concentration simulation in Doppler shifted scans of the wavenumber space	144
7.9	Spatiotemporal Fourier transforms of a D– ${}^3\text{He}$ plasma with drifting ring-beam protons of increasing energy	146
A.1	Shared area on noisy signals using a Monte Carlo method	155
A.2	Comparison between time taken to compute the shared area and cross-correlation algorithms	157
A.3	Shared area between 2d signals	158
B.1	Tau-squared example with noisy sinusoid curve	162
C.1	Diagram of the kernel gradient estimation method	164
C.2	Example gradient maps using the Sobel and Scharr kernels	166
D.1	Example of four power spectra reproduced using Doppler shifted isofrequency lines.	169
D.2	Growth rate extraction in (k_\perp, k_\parallel) space along lines angled positive clockwise from the k_\parallel line.	170

List of Tables

1.1	Characteristic frequency modes present in a plasma	10
1.2	Table of fusion devices and references, if applicable, to their ICE measurements	21
4.1	Spatial and temporal resolutions of the seven simulations carried out to study the effect of PPCPS on three ion DT- α JET fusion plasmas	78
5.1	Initial plasma parameters of PIC simulations of the JET plasma 26148	87
5.2	Concentration of ions, length scales and birth velocities of the minority energetic alpha-particles, for all tritium concentrations .	89
5.3	Tau-squared parameter between power spectra of the JET plasma 26148 and each tritium concentration	106
6.1	Plasma parameters of the JET plasma 26148 used in our LMV runs including tritium ions	110
7.1	Cylindrical parameters for a model D- 3 He plasma	129
7.2	Invariable plasma parameters of the D- 3 He simulations	133
7.3	Typical length scales normalised by the maximal Larmor radii of each ion species in the D- 3 He plasma	133
7.4	Aneutronic simulation parameters of varying fuel ratio D- 3 He fusion plasmas	134
7.5	ICE Doppler shift from large non-zero parallel drift velocity components in terms of its velocity gradient and angle in 2D FFT space from theory and the empirical kernel method	145

Acknowledgements

Firstly, I would like to thank Prof. Richard Dendy and Prof. Sandra Chapman for their continued mentorship and advice. Their experience both in plasma physics and as supervisors has been invaluable, and I have been extremely lucky to have stood on the shoulders of such academic giants.

I am also grateful to the learned Dr. James Cook (UKAEA). I am honoured to have contributed towards the development of your LMV code, and to have had the pleasure of collaborating.

A special thank you to Omstavan Samant for being the friendly face that helped me throughout my Ph.D. Our countless discussions during our shared time at Warwick and your willingness to share your experiences was more appreciated than I ever had the chance to admit. In this regard, an extended thanks to: Alina, Alun, Andrew, Freya, Jacob, Sam M., Shahbaz and Will.

Lastly, I would like to thank all of my family for all of their continued love and support, especially my fiancée, Lauren Gobey. For her extensive patience, love and optimism, particularly during my more stressful periods.

Declaration

I declare that the work presented in this thesis is my own original work, unless otherwise indicated, and has not been submitted, partially or entirely, for the attainment of a degree in this or other academic institution. All the work presented here was carried out during the period from October 2021 to April 2025 under the supervision of Prof. Richard O. Dendy and Prof. Sandra C. Chapman. Some parts of this work have been published or await to be published as indicated below:

Chapter 5

T. W. Slade-Harajda, R. O. Dendy and S. C. Chapman, “The consequences of tritium mix for simulated ion cyclotron emission spectra from deuterium-tritium plasmas” *Nucl. Fusion*, **64**, 126051, Oct. 2024

Chapter 6

T. W. Slade-Harajda, J. W. S. Cook, R. O. Dendy and S. C. Chapman, “Effects of deuterium-tritium mix on linear growth rates of the magnetoacoustic cyclotron instability in fusion plasmas” *In preparation for submission to Physics of Plasmas*, 2025

Chapter 7

T. W. Slade-Harajda, R. O. Dendy and S. C. Chapman, “Simulations of ion cyclotron emission from highly energetic fusion-born protons in aneutronic deuterium-helium-3 plasmas” *In preparation for submission to Nuclear Fusion*, 2025

Abstract

This thesis presents particle-in-cell (PIC) code simulations using EPOCH and computationally extracted solutions to the linearised Maxwell-Vlasov (LMV) system of equations for fusion plasmas. These plasmas feature highly energetic minority fusion-born populations with strongly non-Maxwellian distributions in velocity space. Positive gradients in their velocity distribution lead to the magnetoacoustic cyclotron instability (MCI), where resonance between the energetic population and the fast Alfvén wave (FAW) at integer, narrowly peaked, evenly spaced cyclotron harmonics of the minority ion leads to ion cyclotron emission (ICE). Measurement of ICE is both passive and multi-angled, and its intensity has been observed to scale linearly against fusion reactivity in the JET and TFTR devices for deuterium–tritium (DT) and deuterium–deuterium (D–D) plasmas respectively.

We begin our study on JET plasma 26148 in two distinct ways, both featuring the 3.5 MeV alpha-particle species. Firstly, running PIC simulations which evolve particle and field dynamics according to the Maxwell-Lorentz system of equations. And secondly, using the LMV numerical solver to extract growth rates in two-dimensional wavenumber space of the linear unsaturated phase of the MCI, covering all arbitrary magnetic field orientations. In both studies, tritium is introduced at significant concentrations (ξ_T) with respect to electron number density which had previously not been studied. New particle-particle gyro-resonant behaviour was revealed, dictating energy exchange via Larmor radii matching, and growth rate and power spectral dependencies on plasma density. These results indicate the reliance of ICE frequency spacing and intensity on the admixture of multicomponent plasma constituents.

Whilst DT fusion presents the highest reactivity cross-section at currently attainable tokamak plasma core temperatures, it also produces neutrons which poison the plasma, lowering its efficiency. Aneutronic reactions (those absent of neutrons) are an ideal alternative, with ICE, therefore, presenting itself as a plausible diagnostic to measure fusion reactivity. We use EPOCH to simulate the aneutronic thermal deuterium–helium-3 (D– ^3He) plasma and its highly energetic 14.68 MeV minority proton species for increasing ^3He concentrations (ξ_{He3}). These future aneutronic fusion plasmas confirm the presence of ICE, and further analysis reveals ICE scaling criteria dependent on fuel admixture and at-birth parameters of the minority species, vital in reconstructing their velocity distributions.

Chapter 1

Introduction to fusion & plasma physics

The UK's dependency on coal as a means of energy production since 2012 has fallen sharply, accounting for about 38% of total energy produced in the UK, to below 2% just 10 years later. Over the same time range, the production of energy from wind rose from over 5% to 24%, with other forms of renewable energy growing to make up 40% of the UK's total energy supply. The recent Russian invasion of Ukraine has highlighted the UK and EU's dependency on gas and oil which, as of 2022, still made up over 40% of the UK's total energy production [1]. Coupling this with the declining production of nuclear energy, despite the governments committal to reverse the declining trend of nuclear power capacity to aid in a 2050 Net Zero [2], the question of "what other renewable sources can reliably produce energy at scale?" is raised. One such answer is fusion energy. It remains to be asked, is the current level of fusion research funding sufficient? And, as wind has done to coal over the last 20 years, could it outstrip gas as the dominant energy supply in the UK? It stands that in order to make fusion energy viable and help in ousting fossil fuels as the primary source of energy production, one needs to better study the tools with which fusion energy production is diagnosed and made more efficient.

1.1 Fusion

Fusion is a method of producing clean, renewable energy through the utilisation of the exchangeable description of mass and energy. Before the 1950s, fusion was only theorised in stars under a process called stellar nucleosynthesis [3, 4]. This

involves the fusing together of light materials into heavier ones, from protons up to iron, and accounts for the majority of elements in the universe. Heavier elements than these are produced through the explosive supernovae, but these are not covered here. Harnessing fusion, which is the release of energy from the mass difference between parent and child nuclei, would grant a long-term clean source of energy whose fuel is more readily available and by a means which is more fuel efficient than the burning of fossil fuels or by fission.

In the last few decades there has been substantial improvements in the fusion energy gain factor, \mathbf{Q} , which is the ratio between energy output and input and defines the “break-even” point, for $\mathbf{Q} = 1$. Above this break-even point ($\mathbf{Q} \gtrsim 5$ [5]), fusion can be considered an economic means of energy production at large scales. In December of 2022, the first recorded energy break-even was observed at the National Ignition Facility (NIF) [6], where 3.15 MJ of energy was produced. A milestone achievement in the field of fusion energy research. Approximately one year later, a groundbreaking 69 MJ of energy was achieved in JET in its last run of DT experiments in plasma pulse 104522 [7]. Both of these were record-breaking in their respective devices, and in NIF, proved for the first time, that we can achieve break-even of a singular shot in ICF devices.

Research surrounding fusion energy considers: the methods used to contain them, including magnetic confinement fusion (MCF) and inertial confinement or inertial electrostatic confinement fusion (ICF & IECEF); methods of making the energy transfer more efficient; the types of fuels used; and methods of improving and expanding data collection and analysis. This thesis will look at MCF plasmas, primarily focusing on the large toroidal devices called tokamaks, including JET, DIII-D and the upcoming ITER. Results will still be applicable to the more modern stellarators, such as LHD and Wendelstein 7-X (W7-X). Later, developments into the existing and the construction of novel methods to analyse fast time-scale nonlinear instabilities, will also be discussed.

Operational MCF reactors use large super-conducting magnets to generate toroidal and poloidal magnetic fields. In the case of tokamaks, the poloidal field is generated implicitly through the application of a plasma current sent through the centre of the device, which in turn generates a magnetic field perpendicular to it. In stellarators, the field components are generated by a series of twisting magnets which result in a field topology sufficient to confine the fusion plasma throughout the device. Refer to §1.3 for a discussion on both tokamaks and stellarators.

Thus far the focus of fusion reaction experiments has been on the fusing of deuterium with deuterium (DD), or deuterium with tritium (DT), i.e. isotopes

of hydrogen, as it benefits from the largest fusion reactivity cross-section, σ , (a measure of fusion probability) at the lowest temperature [8], see Fig. 1.1. Deuterium is stable and readily available across the globe, being found in relative abundance in sea water [9]. Tritium is produced in the atmosphere through the interaction of cosmic rays, where it is found in its most abundant state as tritiated gas and water [10]. Tritium is less stable than deuterium as it has a half-life of around 12 years, and significantly less abundant. Fusion products of the fusion between DT fuels include an energetic alpha-particle and neutron,



The 14 MeV neutron carries over 80% of the total energy released in the DT reaction, and is absorbed by the tokamak walls and used to generate steam, producing energy. Being of neutral charge, it is not controlled by the tokamak's magnetic fields, and as a result, collides with the first tokamak wall, its sensitive equipment, superconducting coils and various other measuring equipment. This irradiates the material and leads to nuclear fallout. Tight laws on the proper handling and disposal of nuclear waste in the UK [11] indirectly increase the running cost of using DT fuels. With the arrival of ITER, however, the UK may stand to reduce this cost if they were to adopt the improvements to the techniques used in cleaning and disposing of its irradiated material.

ITER aims to install, as a contingency, a lithium blanket on the tokamak wall to capture these high energy neutrons, protecting the tokamak wall and breed tritium. For this to be effective in the long-term, fusion-reactivity rates need to be sufficiently high so as to produce neutrons for energy extraction, run diagnostics requiring neutron measurement, and to provide sufficiently high tritium breeding rates to sustain the fusion reaction. If the lithium blankets are successful in breeding tritium, it would also reduce the dependency on already scarce tritium sources on Earth and improve the longevity of the device and its equipment. The wider market dependency on lithium [12, 13] however, may prove problematic for DT fusion in the long-term, but in the short-term, recent oversupplies of lithium in 2024/5 highlights the benefits of lithium's dependencies on commercial markets over tritium's reliance on nuclear and defence sectors.

1.1.1 Aneutronic fusion

Reactions which do not produce neutrons, aptly named aneutronic, have been considered to replace their neutronic counterparts for the long-term sustainable generation of fusion energy [14–19]. There are experimental cases regarding aneutronic fuel sources, including in JET [20, 21], but in general they are, as of

yet, unexplored to the extent of DT and DD experiments. The future of clean fusion energy production could, therefore, be one which, in its primary reaction, does not produce neutrons and whose surplus energy is extracted through a form of direct energy conversion (such as direct electricity recapture proposed by the private company Helion [22]) rather than neutron capture. One example of an aneutronic reaction is that between deuterium and helium-3, ($D + ^3He$) [15]



which produces a 3.67 MeV energetic alpha-particle and a higher energy 14.68 MeV proton. These can be utilised in the same way as the products from neutronic reactions can, to heat the parent isotope plasma, sustain the thermonuclear burn, and for fusion plasma diagnosis. Another aneutronic reaction is the fusion of a singular proton to a boron-11 isotope, $p + ^{11}B$ [19, 23],



Here, the energetic product is just three 5.5 MeV helium-4 particles. This reaction is more attractive for a few reasons. Firstly, both fuel sources are more readily available on Earth, whereas sources of both tritium and helium-3 (the latter of which is abundant on the Moon [17] but not Earth) are more scarce. Secondly, subsequent reactions that produce neutrons in the $D - ^3He$ reaction chain occur less frequently in the $p - ^{11}B$ reaction chain, around 0.1% [14], and as such there is a lower chance of irradiation of the tokamak walls. There is, however, other secondary reactions [14] such as $p + ^{11}B \rightarrow n + ^{11}C$, which produces low energy neutrons (around the ion temperature) as well as a radioactive carbon isotope; but this quickly decays to boron-11.

Fusion reactivities are presented in Fig. 1.1, where aneutronic reactions are displayed as dashed-lines, and are comparable to the DT and DD cross-sections at temperatures well above the highest recorded core electron temperature ($\lesssim 14\text{keV}$) in an MCF device [25]. For aneutronic reactions to become viable, temperatures within the plasma core need to exceed hundreds of keV, which has not yet been achieved in any MCF device. Methods for increasing the cross-sectional area for aneutronic fusion is, therefore, a major proponent of aneutronic fusion research, and has been the topic of many discussions of private ventures, such as Helion [22] and HB11 [26].

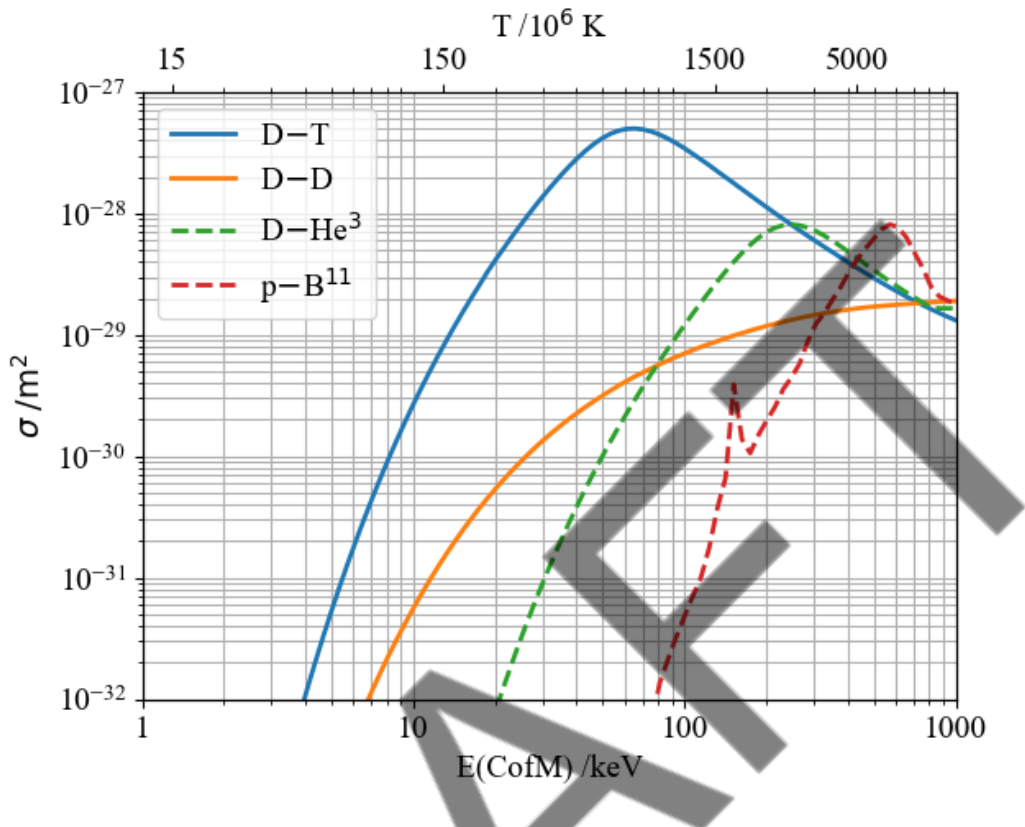


Figure 1.1: Cross-sections (probabilities) for the neutronic (solid lines) fusion reactions of D–D, D–T and the aneutronic reactions (dashed lines) D– ^3He and p– ^{11}B . Data provided by the International Atomic Energy Agency’s (IAEA) Evaluated Nuclear Data File (ENDF) [24]

1.2 Plasma physics

This section will discuss: what a plasma is, including it’s quasi-neutral definition; the ways in which modern plasmas are produced; fundamental time and length scales, including natural frequencies summarised in Table 1.1; and examples of waves supported by a plasma, including the fast Alfvén wave (FAW) supported by the bulk ions under the influence of a background magnetic field, and the Ion Bernstein wave (IBW). Solutions to these wave equations are then presented in spatiotemporal (2D) Fourier transforms (FFT) in Figs. 1.2 and 1.3.

1.2.1 Definition and quasi-neutrality

Plasma is the fourth state of matter, hotter than gas, and is comprised of ions and unbound energetic electrons. One key assumption we make of a plasma, and that which defines it as originally posed by Langmuir in 1928, is that, on macroscopic

scales, and hence ignoring smaller net currents, the plasma is neutrally charged. This is also referred to as quasi-neutrality and is a vital assumption in our simulations.

Quasi-neutrality is maintained when the summation of the charge number weighted ion number densities equals that of the electrons,

$$n_e = \sum_{\sigma} Z_{\sigma} n_{\sigma}, \quad (1.1)$$

where σ defines the species, Z_{σ} the charge number and n_{σ} the number density, with n_e representing the background number density of electrons. Physically, quasi-neutrality describes a plasma's ability to shield external charge and electric potentials. This is also referred to as Debye shielding, which we will discuss in §1.2.4

To define a quasi-neutral three ion component plasma (e.g. DT- α), we introduce four ratios which define each component's number density indexed 1–3, with respect to the electron number density, and a bulk plasma component ratio (between components 1 and 2)

$$\begin{aligned} \xi_1 &= n_1/n_e, \quad \xi_3 = n_3/n_e, \\ \xi_2 &= n_2/n_e, \quad (\xi_2/\xi_1) = n_2/n_1. \end{aligned} \quad (1.2)$$

In simulations, these ratios can be used to define computational limits, equal particle number weightings and correspond to commonly prescribed parameters in experiment; such as the fuel ratio, (ξ_2/ξ_1) , or the minority concentration, ξ_3 , which will henceforth be written as ξ_{min} to avoid confusion from bulk ions.

For any N number of ion component plasmas, $N - 1$ concentration ratios must be known to run simulations. Typically, the secondary fuel concentration, ξ_2 , and minority concentration, ξ_{min} , are either known or wish to be found in experiments of fusion plasmas, so for our simulations we will follow suit, calculating the remaining concentration ratio ξ_1 accordingly. Rearranging for these parameters yields the solution to ξ_1 as

$$\xi_1 = \frac{1}{Z_1} (1 - Z_2 \xi_2 - Z_{min} \xi_{min}). \quad (1.3)$$

1.2.2 Plasma production

Plasmas are most commonly found in stars and other astrophysical sources such as interstellar nebulae or solar wind; but there are a few natural examples on Earth, including lightning, auroras and the ionosphere. Plasmas can now be

readily produced on Earth, from fluorescent lighting to plasma televisions. Methods of producing plasma are varied and the type of plasma produced has various applications depending on its temperature, density, stability and, therefore, its longevity [27, 28].

Plasmas in ICF devices are produced by firing high powered lasers at frozen fuel pellets (typically made of DT ice) to ablate their surfaces and force the pellet to implode, creating a plasma which undergoes fusion under great temperature and pressure. Cyclotron resonance heating is most commonly used in MCF plasmas [29], where tokamak plasmas are generated with alternating electric fields within its vacuum chamber.

Cyclotron resonant heating involves the application of an alternating electric current to drive cyclotron resonant frequencies of the ions (or electrons) within gases, heating them up and breaking them down into a plasma. The frequency of the alternating current dictates whether it directly drives the electrons or ions. Frequencies in the electron range ($\gtrsim 100\text{GHz}$, assuming the magnetic field strength is on the order of a few Tesla) hence refer to electron cyclotron resonance heating (ECRH) and those in the ion range ($\gtrsim 10\text{MHz}$) refer to ion cyclotron resonance heating (ICRH).

Plasma temperatures are maintained through further cyclotron resonance heating, or through neutral beam injection (NBI). NBI involves externally heating low pressure gases to a plasma state, accelerating its ions to fusion temperatures, adding electrons back to the positive ions to re-neutralise the NBI ions and finally, injecting it into the plasma. This method also maintains a constant fuel input to sustain further reactions.

1.2.3 Single particle dynamics

A single charged particle, q , travelling at a velocity, \mathbf{v} , through an electromagnetic field is under the influence of the Lorentz force,

$$\mathbf{F} = \frac{q}{m} (\mathbf{E} + \mathbf{v} \times \mathbf{B}) . \quad (1.4)$$

where \mathbf{E} and \mathbf{B} are the electric and magnetic fields, respectively, and the particle has some charge q , mass m and velocity \mathbf{v} . One notices, for a homogeneous magnetic field, the cross-product between velocity and magnetic field yield no force on the particle in its direction parallel to the magnetic field. However, there exists a force which acts to oscillate the particle perpendicular to the magnetic field, in a circle around its guiding centre, which is directed by the orientation of magnetic field lines. Therefore, under an external magnetic field and no electric

field, charged particles follow their guiding centre path (which is directed parallel to the magnetic field lines) and perpendicular circular motion, i.e. a helical orbit.

The charged particle's circular orbit around its guiding centre is done so with a radius known as the Larmor radius

$$r_{L\sigma} = \frac{m_\sigma v_\perp}{q_\sigma B} \quad (1.5)$$

$$\approx \frac{\sqrt{2E_\sigma m_\sigma}}{q_\sigma B}, \quad (1.6)$$

and at a frequency known as the cyclotron frequency (or gyro-frequency)

$$\Omega_\sigma = \frac{v_\perp}{r_{L\sigma}} = \frac{q_\sigma B}{m_\sigma}. \quad (1.7)$$

Summating the Lorentz forces of all particles within a volume (including positive and negative charges), can predict macroscopic responses to external currents and electromagnetic fields, defined by Maxwell's equations,

$$\nabla \cdot \mathbf{E} = \frac{\rho}{\epsilon_0}, \quad (1.8a)$$

$$\nabla \cdot \mathbf{B} = 0, \quad (1.8b)$$

$$\nabla \times \mathbf{E} = -\frac{\partial \mathbf{B}}{\partial t}, \quad (1.8c)$$

$$\nabla \times \mathbf{B} = \mu_0 \mathbf{J} + \mu_0 \epsilon_0 \frac{\partial \mathbf{E}}{\partial t}, \quad (1.8d)$$

where the constants μ_0 and ϵ_0 have their usual meaning; \mathbf{E} and \mathbf{B} are the electric and magnetic fields, respectively; ρ is the charge density encapsulated by the Gaussian surface; and \mathbf{J} is the current density.

In this sense, plasmas (and their waves) can be described as a collection of coupled oscillators. The study of which forms a proponent of plasma instability theory [30].

1.2.4 Fundamental time and length scales

Natural lengths

Quasi-neutrality characterises a degree of charge and electrical potential shielding by the plasma from external sources. The degree of charge shielding is dependent on the temperature and density of its ions and electrons. Assuming: an infinite mass limit scenario $M_i/m_e \rightarrow \infty$ such that the ions form a solid

background such that the electrons are free to move (not inconsistent considering electron time scales); ions are distributed homogeneously; both electrons and ions are defined by some mean number density $n_e \equiv n_0$; and electrical potentials are much less than thermal fluctuations; then the mean distance of shielding is defined by the Debye length λ_{De} ,

$$\lambda_{De} = \sqrt{\frac{\epsilon_0 k_B T_e}{n_e e^2}}. \quad (1.9)$$

Beyond this Debye radius sphere of influence, all charged particles are considered shielded and do not interact nor influence one another.

Natural frequencies

Here we provide brief discussions of natural frequencies that appear in plasmas with and without a magnetic field, including the electron plasma frequency, lower and upper hybrid frequencies, and a resonant frequency of multiple ions. Table 1.1 gives equations for the fundamental frequencies we derive within plasmas, including the full unsimplified form of the lower hybrid frequency.

1) Electron plasma frequency

A slab of electrons whose thermal motions are negligible, extent is infinite and which lack a background magnetic field, when displaced from its equilibrium by some distance x , is restored to equilibrium by the restoring force of an electric field using Gauss' law, Eq. (1.8a). This results in simple harmonic motions (SHM), with a characteristic frequency known as the electron plasma frequency. This can be written as

$$\omega_{pe} = \sqrt{\frac{n_e q_e^2}{m_e \epsilon_0}}. \quad (1.10)$$

For the full derivation (a process involving linearisation) see Section 4.3 of Ref. [31].

2) Lower and upper hybrid frequencies

In a magnetised plasma, electrostatic waves propagate perpendicular to the magnetic field direction, and ions and electrons oscillate with a frequency known as the lower hybrid frequency,

$$\omega_{LH}^2 \approx \left(\omega_{pi}^{-2} + (\Omega_i \Omega_e)^{-1} \right)^{-1}, \quad (1.11)$$

where it is assumed that $\omega_{pi} \gg \Omega_i$, where ω_{pi} is the ion plasma frequency and Ω_σ is the cyclotron frequency for both the ions (i) and electrons (e). This derivation involves the Poisson equation, and in the high plasma density limit can be approximated as $\omega_{LH}^2 \approx (\Omega_i \Omega_e)$.

Lower hybrid oscillations occur for magnetic fields orientated close to perpendicular ($\pi/2$) with respect to the direction of motion, but not exactly, otherwise the electrons would be able to shield the displaced ions. This is the low frequency extension of the upper hybrid frequency [31, 32], given by

$$\omega_{UH}^2 = \Omega_e^2 + \omega_{pe}^2 , \quad (1.12)$$

which is the frequency of oscillation of electrons perpendicular to a background magnetic field.

3) Multiple ion resonance

Plasmas consisting of multiple bulk ion species leads to, as a result of cyclotron resonance, the driving of degenerate harmonics between both ion populations. This is known as Buchsbaum resonance of multiple ion species, and was originally derived in Ref. [33]. We discuss this further in §4.2.3 as it arises only as a result of multiple positively charged ions at non insubstantial concentrations. Likewise, we reproduce figures 2 to 4 as presented in Ref. [33], to compare findings. In the large plasma density limit there exists three resonances, two involving both electrons and ions, and an additional involving only the two bulk ion species, labelled “1” and “2”,

$$\omega_{BB}^2 = \Omega_1 \Omega_2 \frac{\xi_1 m_1 + \xi_2 m_2}{\xi_1 m_2 + \xi_2 m_1} . \quad (1.13)$$

Name	Equation
Cyclotron/gyro-frequency	$\Omega_\sigma = q_\sigma B_0 / m_\sigma$
Plasma frequency	$\omega_{p\sigma}^2 = n_\sigma q_\sigma^2 / m_\sigma \epsilon_0$
Upper-hybrid (UH)	$\omega_{UH}^2 = \omega_{pe}^2 + \Omega_e^2$
Lower-hybrid (LH)	$\omega_{LH}^2 = (\omega_{pi}^2 + \Omega_i^2) / (1 + \omega_{pe}^2 / \Omega_e^2)$
Buchsbaum resonance [33]	$\omega_{BB}^2 \approx \Omega_1 \Omega_2 [(\xi_1 m_1 + \xi_2 m_2) / (\xi_1 m_2 + \xi_2 m_1)]$

Table 1.1: Summary of characteristic frequencies present within a cold magnetised plasma. Numbered indices represent species forming multiple ion bulk plasmas (e.g. deuterons and tritons).

1.2.5 Kinetic theory

In §1.3 plasma behaviour within the specific geometries and magnetic field topologies of a tokamak device are discussed. In this section however, the behaviour of plasma particles is developed through the kinetic theory, which involves the contribution of single charged particle dynamics with the statistical description of a fluid.

The macroscopic fluid description of a plasma is referred to as magnetohydrodynamics (MHD) whereby a statistical approach utilising the distribution function, $f(\mathbf{r}, t)$, of the particles allows for the combination of the Navier-Stokes fluid equations with the Maxwell-Lorentz equations for charged particles, Eqs. (1.4) and (1.8). One such equation used in MHD is the conservation of mass,

$$\frac{\partial \rho}{\partial t} + \nabla \cdot (\rho \mathbf{v}) = 0 . \quad (1.14)$$

where symbols are as previously defined.

Kinetic theory of a plasma uses both the microscopic single particle dynamics and the macroscopic fluid description to predict plasma responses using the variables of time, t , position, \mathbf{r} , and velocity, \mathbf{v} , of the particles. This is where previous theories differ, as the introduction of single particle dynamics to the fluid dynamic approach directly leads to the inclusion of a particle's velocity as an independent variable. Now a plasma can be defined by six (seven including time) coordinates via its distribution function $f(\mathbf{r}, \mathbf{v}, t)$. Due to the analogy between it and mass density, along with its dependency on velocity, one can rewrite Eq. (1.14) as

$$\frac{\partial f}{\partial t} + \nabla_r \cdot (f \mathbf{v}) + \nabla_v \cdot (f \mathbf{a}) = \left(\frac{\partial f}{\partial t} \right)_c , \quad (1.15)$$

which may also be referred to as the Boltzmann equation, with \mathbf{a} being the acceleration of charged particles (see the Lorentz force, Eq. (1.4)) ∇_r and ∇_v the derivative functions with respect to the positional vector ($\nabla_r = \partial/\partial\mathbf{r}$) and velocity ($\nabla_v = \partial/\partial\mathbf{v}$), and $(\partial f/\partial t)_c$ the rate of change of the distribution function due to collisions.

Neglecting collisional terms under the assumption that the plasma is sufficiently hot so that $(\partial f/\partial t)_c = 0$, Eq. (1.15) is developed into the collisionless Maxwell-Vlasov equation, which is written [32]

$$\frac{\partial f}{\partial t} + \mathbf{v} \cdot \nabla_r f + \frac{q}{m} (\mathbf{E} + \mathbf{v} \times \mathbf{B}) \cdot \nabla_v f = 0 . \quad (1.16)$$

Taking moments; i.e. integrals of the Vlasov equation with respect to position and velocity, returns macroscopic variables of the system, such as the

continuity equation (zeroth moment), fluid velocity (first moment), heat flow (second moment) and conductivity (third moment). In practice, a closing statement is introduced so the sequence of moments is terminated. Commonly the third moment, thermal conductivity, is set to zero [34].

Extracting plasma properties and wave dispersion relations from the Vlasov equation is done using perturbation theory, assuming some small change from an initial unperturbed state, then through linearising, see §2.3 for details on an analytical approach. The distribution function, electric and magnetic fields, are presumed to be perturbed from their equilibrium state, such that

$$f(\mathbf{r}, \mathbf{v}, t) = f_0(\mathbf{r}, \mathbf{v}, t) + \varepsilon f_1(\mathbf{r}, \mathbf{v}, t), \quad (1.17a)$$

$$\mathbf{E}(\mathbf{r}, \mathbf{v}) = \mathbf{E}_0(\mathbf{r}, \mathbf{v}) + \varepsilon \mathbf{E}_1(\mathbf{r}, \mathbf{v}), \quad (1.17b)$$

$$\mathbf{B}(\mathbf{r}, \mathbf{v}) = \mathbf{B}_0(\mathbf{r}, \mathbf{v}) + \varepsilon \mathbf{B}_1(\mathbf{r}, \mathbf{v}), \quad (1.17c)$$

where the parameter ε is presumed to be very small.

Assuming only first order perturbations (i.e. $\forall n \in \mathbb{Z}^+, n > 2 : \varepsilon^n = 0$) and that the unperturbed distribution f_0 is both homogeneous ($\nabla_r f_0 = 0$) and static ($\partial f_0 / \partial t = 0$), we can find the first order perturbed linearised Vlasov equation by substituting Eqs. (1.17a–1.17c) into Eq. (1.16) and subtracting the equilibrium unperturbed state, giving

$$\begin{aligned} \frac{\partial f_1}{\partial t} + \mathbf{v} \cdot \nabla_r f_1 + \frac{q}{m} (\mathbf{E}_0 + \mathbf{v} \times \mathbf{B}_0) \cdot \nabla_v f_1 = \\ - \frac{q}{m} (\mathbf{E}_1 + \mathbf{v} \times \mathbf{B}_1) \cdot \nabla_v f_0. \end{aligned} \quad (1.18)$$

We can then solve the linearised Maxwell-Vlasov equation to investigate properties of plasmas for time intervals $< \tau_{b.c.}$, where $\tau_{b.c.}$ is the mean collisional time between two particles (binary collision) [35, 36]. Assumptions about the electric and magnetic fields can yield solutions to Eq. (1.18) that are specific to different types of waves. Further discussion on the linearisation process of the Maxwell-Vlasov equation and computational methods employed to extract solutions for a general distribution function is found in §2.3.

1.2.6 Waves in a plasma

A plasma can support a large number of oscillations as it is, in essence, made up of a finite collection of coupled oscillators [30]. From starting with single-particle dynamics and summing over all particles through the use of Ohm's law, we can

arrive at a matrix description of the normal modes within a magnetized plasma depending on the angle of propagation. The dispersion relation, the relationship between a waves frequency, ω , and wavenumber, k , is shown to be contained within the plasma's dielectric tensor, $\underline{\epsilon}$. A full discussion on this process using linearised forms of the Maxwell-Vlasov set of equations is detailed in §1.2.5. Here, we derive the dielectric tensor from the Ohm and Ampère law, written respectively as

$$\mathbf{J} = \underline{\sigma} \cdot \mathbf{E} , \quad (1.19a)$$

$$\nabla \times \mathbf{B} = \mu_0 \mathbf{J} + \mu_0 \epsilon_0 \frac{\partial \mathbf{E}}{\partial t} , \quad (1.19b)$$

where $\underline{\sigma}$ is the conductivity tensor. Provided the electric and magnetic fields oscillate in time and space as $\exp(\mathbf{k} \cdot \mathbf{r} - i\omega t)$, we can substitute Eq. (1.19a) into Eq. (1.19b) and take the Fourier transform, giving

$$i\mathbf{k} \times \mathbf{B} = -\frac{i\omega}{c^2} \underline{\epsilon} \cdot \mathbf{E} , \quad (1.20)$$

where the dielectric tensor, $\underline{\epsilon}$, is defined as

$$\underline{\epsilon} = \left(\underline{\mathbb{I}} + \frac{i}{\omega \epsilon_0} \underline{\sigma} \right) , \quad (1.21)$$

where $\underline{\mathbb{I}}$ is the identity matrix.

Taking the Fourier transform of the cross product of the Maxwell-Faraday equation, Eq. (1.8c), crossing with wavenumber \mathbf{k} and substituting Eq. (1.20) gives

$$\mathbf{k}\mathbf{k} \cdot \mathbf{E} - k^2 \mathbf{E} = -\frac{\omega^2}{c^2} \underline{\epsilon} \cdot \mathbf{E} . \quad (1.22)$$

This can be rewritten as

$$\underline{\underline{\mathbf{M}}} \cdot \mathbf{E} = 0 , \quad (1.23)$$

with the matrix $\underline{\underline{\mathbf{M}}}$ defined as,

$$\underline{\underline{\mathbf{M}}} = \left(\frac{\omega^2}{c^2} \underline{\epsilon} + \mathbf{k}\mathbf{k} - k^2 \underline{\mathbb{I}} \right) , \quad (1.24)$$

where $\mathbf{k}\mathbf{k}$ represents the Kronecker product (\otimes) between the vector wavenumbers, and $\underline{\mathbb{I}}$ and $\underline{\epsilon}$ retain their definitions from above.

Solutions to Eq. (1.23) give the normal modes within the plasma and are found in the roots of $\det(\underline{\underline{\mathbf{M}}}) = 0$. A more detailed explanation of a root finding

algorithm is given in Ref. [37] and repeated in §2.3. For waves that propagate at some angle to the magnetic field, given by $\mathbf{B} = B_0\hat{z}$, such that the wavevector is $\mathbf{k} = (k_x, 0, k_z)$, solutions in terms of the dielectric tensor are given as

$$\left(\epsilon_{xx} - \frac{k_z^2 c^2}{\omega^2}\right) \left(\epsilon_{yy} - \frac{k_z^2 c^2}{\omega^2}\right) + \epsilon_{xy}^2 = 0 , \quad (1.25)$$

where c is the speed of light, ω is the wave frequency, and where we have also used the fact that $\epsilon_{xy} = -\epsilon_{yx}$ [38]. One can derive, using specific distribution functions, the linear growth rates of the MCI as a function of frequency [38, 39] for obliquely propagating fast Alfvén waves. As of yet, this linear MCI growth rate theory has not been developed to include multiple ions, but recent computational work [37] is able to solve Eq. (1.24) for an arbitrary number of bulk thermal ions and one energetic ion species, extracting growth rates in (k_\perp, k_\parallel) space (see discussion in §2.3).

Now that we are armed with the statistical tools of kinetic theory and the dielectric tensor to define a plasma's response to an initial perturbation, we consider a simple case, where electric field perturbations are solely caused by the perturbation in charge density, i.e. $\mathbf{B} = \mathbf{E}_0 = 0$. This is an electrostatic wave, and is longitudinal in the direction of the perturbing electric field. First, recall that the current density \mathbf{J} in Ohm's law Eq. (1.19a) can be defined as both the response of the electric field multiplied by the conductivity tensor $\underline{\sigma}$, and the integral over velocity of the distribution as

$$\mathbf{J} = nq \int \mathbf{v} f(\mathbf{v}) d^3\mathbf{v} . \quad (1.26)$$

If the wave is purely a result of the perturbation of the electric field \mathbf{E}_1 , then the perturbed current density will be a result of the perturbed distribution function. Taking the Fourier transform of the linearised Vlasov equation, Eq. (1.18), and rearranging for f_1 gives

$$f_1(\mathbf{v}) = -i \frac{q}{m} \frac{\mathbf{E}_1 \cdot \nabla_v f_0}{(\omega - \mathbf{k} \cdot \mathbf{v})} . \quad (1.27)$$

Substituting Eq. (1.27) into Eq. (1.26) gives

$$\mathbf{J}_1 = -i \frac{nq^2}{m} \mathbf{E}_1 \int \mathbf{v} \frac{\partial f_0(\mathbf{v}) / \partial \mathbf{v}}{\omega - \mathbf{k} \cdot \mathbf{v}} d^3\mathbf{v} . \quad (1.28)$$

Using the relation between the dielectric and conductivity tensors from Eq. (1.21) and Eq. (1.19a), then substituting into Eq. (1.28) gives

$$(\underline{\epsilon} - \underline{\underline{\epsilon}}) \frac{\omega \epsilon_0}{i} \cdot \mathbf{E}_1 = -i \frac{nq^2}{m} \mathbf{E}_1 \int \mathbf{v} \frac{\partial f_0 / \partial v}{\omega - \mathbf{k} \cdot \mathbf{v}} d^3\mathbf{v} . \quad (1.29)$$

Taking only longitudinal solutions for this electrostatic wave, we find the longitudinal component of the dielectric tensor as

$$\epsilon_{zz}(k, \omega) = 1 + \frac{\omega_p^2}{\omega} \int v \frac{\partial f_0 / \partial v}{\omega - kv} d^3v, \quad (1.30)$$

where we used the definition of the plasma frequency ω_p^2 as in Eq. (1.10).

The description of our ϵ_{zz} dielectric tensor component is additive over all species, electrons and ions, and depends upon their initial velocity space distributions, the frequency, and the wavenumber. The full dielectric tensor $\underline{\epsilon}(\mathbf{k}, \omega)$, which describes the plasma's response to an arbitrary electric and magnetic field, can be generally written as a summation over species σ (not to be confused with conductivity) of the plasma susceptibilities χ_σ as

$$\underline{\epsilon}(\mathbf{k}, \omega) = 1 + \sum_{\sigma} \underline{\chi}_{\sigma}(\mathbf{k}, \omega), \quad (1.31)$$

In the context of plasma waves, $\underline{\epsilon}(\mathbf{k}, \omega) = 0$ represents a “transparent” plasma. Mathematically, this implies a plasma that is strongly coupled to, and in resonance with, an EM wave with frequency ω . For the most general velocity distribution function $f(v_{\parallel}, v_{\perp})$, making no assumptions about EM fields, magnetic field orientation or wave polarisation, the dielectric tensor is written in its non-relativistic limit as

$$\underline{\epsilon}(\mathbf{k}, \omega) = \underline{\mathbb{I}} + \sum_{\sigma} \frac{\omega_{p\sigma}^2}{\omega} \sum_{n=-\infty}^{\infty} \int_0^{\infty} \int_{-\infty}^{\infty} \frac{\underline{\mathbf{S}}_{\sigma,n} 2\pi v_{\perp} dv_{\perp} dv_{\parallel}}{\omega - k_{\parallel} v_{\parallel} - n\Omega_{\sigma}}, \quad (1.32)$$

where $\underline{\mathbb{I}}$ is the unit dyadic and $\omega_{p\sigma}$ and Ω_{σ} are the plasma and cyclotron frequency, respectively. The $\underline{\mathbf{S}}_{\sigma,n}$ tensor is comprised of integrals over partial derivatives of distribution functions in velocity space, combined with Bessel functions of the first kind J_n with index n and argument $(k_{\perp} v_{\perp} / \Omega_{\sigma})$ [32, 37], given as

$$\underline{\mathbf{S}}_{\sigma,n} = \begin{bmatrix} \frac{n^2 J_n^2}{z_{\sigma}^2} p_{\perp} U_{\sigma} & \frac{i n J_n J'_n}{z_{\sigma}} p_{\perp} U_{\sigma} & \frac{n J_n^2}{z_{\sigma}} p_{\perp} W_{\sigma,n} \\ -\frac{i n J_n J'_n}{z_{\sigma}} p_{\perp} U_{\sigma} & (J'_n)^2 p_{\perp} U_{\sigma} & -i J_n J'_n p_{\perp} W_{\sigma,n} \\ \frac{n J_n^2}{z_{\sigma}} p_{\parallel} U_{\sigma} & i J_n J'_n p_{\parallel} U_{\sigma} & J_n^2 p_{\parallel} W_{\sigma,n} \end{bmatrix}, \quad (1.33)$$

where

$$U_{\sigma} = \frac{\partial f_{\sigma}}{\partial p_{\perp}} + \frac{k_{\parallel}}{\omega} \left(v_{\perp} \frac{\partial f_{\sigma}}{\partial p_{\parallel}} - v_{\parallel} \frac{\partial f_{\sigma}}{\partial p_{\perp}} \right), \quad (1.34a)$$

$$W_{\sigma,n} = \left(1 - \frac{n\Omega_{\sigma}}{\omega} \right) \frac{\partial f_{\sigma}}{\partial p_{\parallel}} + \frac{n\Omega_{\sigma} p_{\parallel}}{\omega p_{\perp}} \frac{\partial f_{\sigma}}{\partial p_{\perp}}. \quad (1.34b)$$

Analytically solving Eq. (1.33) for $\underline{\epsilon}(\mathbf{k}, \omega) = 0$ is extremely difficult, and has only been done using implicit assumptions about the distribution function, EM field orientations and Bessel function solutions. It was shown in Ref. [37], that numerical solutions to the linearised Maxwell-Vlasov equations can be found using the LMV Julia code [40]. This calculates the integrals of Eq. (1.32) spanning $(k_{\perp}, k_{\parallel})$ space for complex frequency solutions $z_{\omega} = \omega + i\gamma$, where γ is the growth rate of the wave and or instability, and which satisfies $\underline{\epsilon}(\mathbf{k}, \omega) = 0$.

With the introduction of the dielectric tensor description, we are able to describe a plasma's response to arbitrary distribution functions, including growth rates and frequencies of waves and instabilities. Using this concept, we show in the following section the derivation of the FAW in a cold (background) plasma.

Cold plasma

For a plasma featuring no energetic minority and subject to a background magnetic field at some angle with respect to wave propagation such that $\mathbf{B} \angle \mathbf{k} \equiv \theta = \arccos(\mathbf{B} \cdot \mathbf{k} / (|\mathbf{B}| |\mathbf{k}|))$, assuming that it makes no angle to the y-axis (as in the above section) the dielectric tensor can be written as a matrix of solutions, given in Refs. [41] and [42], as

$$\underline{\epsilon} = \begin{bmatrix} \epsilon_{xx} & \epsilon_{xy} & \epsilon_{xz} \\ \epsilon_{yx} & \epsilon_{yy} & \epsilon_{yz} \\ \epsilon_{zx} & \epsilon_{zy} & \epsilon_{zz} \end{bmatrix} = \begin{bmatrix} S - n^2 \cos^2 \theta & -iD & n^2 \cos \theta \sin \theta \\ iD & S - n^2 & 0 \\ n^2 \cos \theta \sin \theta & 0 & P - n^2 \sin^2 \theta \end{bmatrix}, \quad (1.35)$$

where we write $\mathbf{n} = \mathbf{k}c/\omega$ as the refractive index of the plasma. The components of the dielectric tensor are

$$\begin{aligned} R &= 1 - \sum_{\sigma=i,e} \frac{\omega_{p\sigma}^2}{\omega(\omega + \Omega_{\sigma})}, & P &= 1 - \sum_{\sigma=i,e} \frac{\omega_{p\sigma}^2}{\omega^2}, & S &= \frac{1}{2}(R + L), \\ L &= 1 - \sum_{\sigma=i,e} \frac{\omega_{p\sigma}^2}{\omega(\omega - \Omega_{\sigma})}, & & & D &= \frac{1}{2}(R - L), \end{aligned} \quad (1.36)$$

with R , L , P , S and D standing for: right, left, polarisation, sum and difference respectively. Solutions to this tensor are written in the form

$$n^2 = \frac{B \pm F}{2A}, \quad (1.37)$$

which is an equivalent of the Appleton-Hartree dispersion relation [32], and where the remaining parameters are defined

$$\begin{aligned}
B &= RL \sin^2 \theta + PS(1 + \cos^2 \theta) , \\
F^2 &= (RL - PS)^2 \sin^4 \theta + 4P^2 D^2 \cos^2 \theta , \\
A &= S \sin^2 \theta + P \cos^2 \theta .
\end{aligned} \tag{1.38}$$

In the limits for waves perpendicular ($\theta = \pi/2$) and parallel ($\theta = 0$) to the magnetic field, we find two sets of solutions

$$\begin{aligned}
\text{Perpendicular : } n^2 &= \frac{RL}{S}, \quad n^2 = P , \\
\text{Parallel : } P &= 0, \quad n^2 = R, \quad n^2 = L .
\end{aligned}$$

Plots of the dispersion relations for a purely perpendicular magnetic field are given in Fig. 1.2 for frequencies on the order of the ion (left panel) and electron (right panel) cyclotron frequencies. For parallel propagation, see Fig. 2.8. We refer to Eq. (1.37) as the FAW dispersion relation as it covers both low and high frequency regimes encapsulating the descriptions of the ordinary (O) mode and extraordinary (X) waves within a plasma - see Ref. [32].

We note that the terminology for “cold” plasma may also be confused with regions of plasma stability. These are defined by the ratio between thermal and magnetic pressure

$$\beta = \frac{p}{P_B} = \frac{2\mu_0 n_e (T_e + T_i)}{B^2} , \tag{1.39}$$

also known as the plasma beta parameter, characterised by the magnetic field strength, B , temperatures of ions and electrons, $T_{i,e}$, and the core electron number density, n_e . A “cold” plasma in this case is one in which $\beta \ll 1$. Simulations presented throughout this thesis will henceforth be referred to as “cold” when no energetic minority species is present. These may also be referred to as “background” or “benchmark” plasmas, as they are used to compare between fusion plasmas with and without velocity space instabilities.

Monetarily, a high plasma beta is always more advantageous in fusion plasmas as this optimises fusion plasma reactivity which is related to plasma temperature and pressure [27], for the lowest possible magnetic field.

Ion Bernstein waves (IBW)

Bernstein waves for electrons (EBW) and ions (IBW) propagate purely perpendicular to the background magnetic field ($k_{\parallel} \rightarrow 0$) [43]. They were experimentally measured in laboratories through the 1960s to late 1970s and have often been observed from spacecraft which, mapping to the dispersion relation, allow

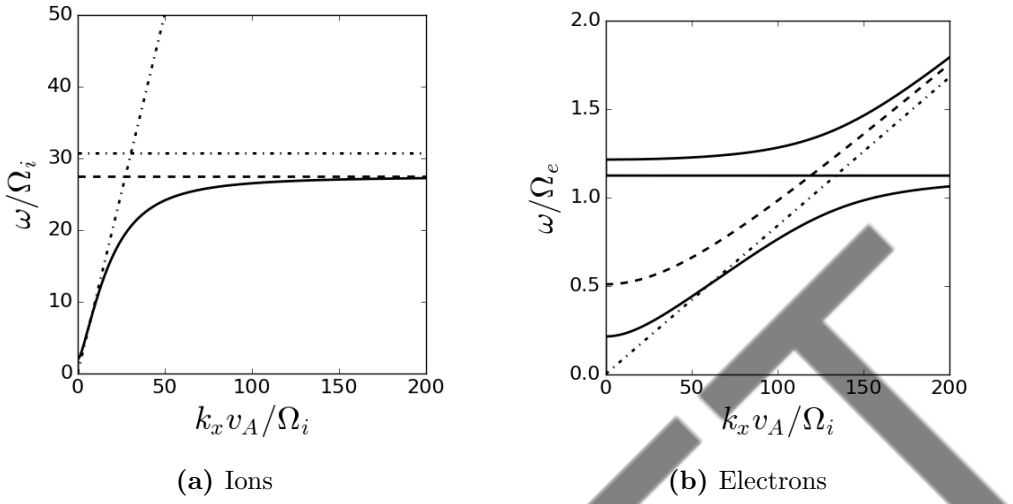


Figure 1.2: Cold plasma dispersion, Eq. (1.37), for the (a) ions and (b) electrons, both given in solid black. *Left-hand* figure: dashed horizontal is the lower-hybrid frequency, dot-dashed horizontal is the ion plasma frequency and the dot-dashed straight line going through the origin is the compressional Alfvén wave. *Right-hand* figure: curved dashed line is the O-mode, straight horizontal line is the upper-hybrid frequency and the dot-dashed line is the photon, $\omega = kc$, dispersion.

for the measurement of electron temperatures in solar wind as well as in the plasma torus layer of Jupiter's moon Io [44, 45]. IBWs are used in tokamaks to heat the core of the ion plasma and increase the efficiency of energy transfer from the fusion-born 3.5 MeV alpha-particles to the DT ions. Ultimately, IBWs have been used in tokamak devices to greatly improve their efficiency through an increase in fusion reactivity [46].

One can work through the derivation of the IBW dispersion function using the full dielectric tensor in Eq. (1.32), simplifying the description for various choices of field orientations or wave propagation domains where appropriate. Showing the full derivation here would be superfluous, but we encourage the reader to explore Ref. [43] for the original derivation, which includes arbitrary propagation angles not strictly perpendicular, and also Ref. [47], for an extension of the IBW for ions distributed as a ring-beam. The latter serves as particularly interesting reading material for this thesis, considering that the MCI was, originally, considered to be the result of coupling between the IBW and FAW as a result of a ring-beam distribution of fast ions [38].

The dispersion relation for IBWs is given as [43, 44],

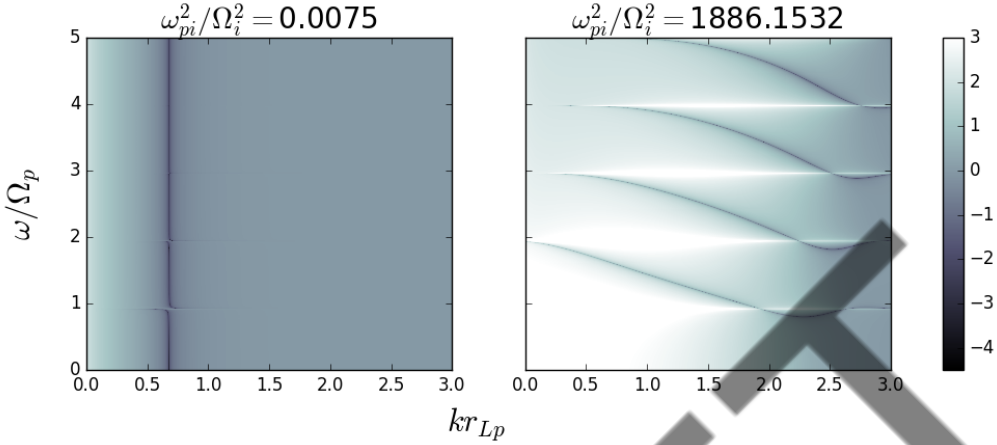


Figure 1.3: Dispersion plots for IBW waves in low (left) and high (right) density plasma limits with a colour scale indicating the logarithmic base-10 absolute value of Eq. (1.40) summated between Bessel function indices of $1 < n < 10$.

$$1 = \sum_{\sigma} \frac{e^{-\zeta_{\sigma}}}{\zeta_{\sigma}} \sum_{n=1} \frac{2n^2 \omega_{p\sigma}^2}{\omega^2 - n^2 \Omega_{\sigma}^2} I_n(\zeta_{\sigma}), \quad (1.40)$$

where $r_{L\sigma}$ is the Larmor radius of each species (σ), I_n is the modified Bessel function of the first kind with argument ζ_{σ} , where we have adopted an alternate notation for $\zeta_{\sigma} = k^2 r_{L\sigma}^2$ to avoid confusion with the Debye length, as per the original notation. All remaining terms are as previously defined. The dispersion relation solutions presented in Fig. 1.3 are summed over modified Bessel function indices n between zero and 10, as this was found to sufficiently encapsulate the dispersion relation solutions.

A figure of the IBW dispersion relation for a simple proton-electron plasma with low and high density limits is shown in Fig. 1.3. The frequencies are normalised by the proton cyclotron frequency and the wavenumber k is as given by ζ above. The low and high density limits are given in panels left to right, as indicated by their plasma to cyclotron frequency ratios in the title. Our high density plasma (right hand panel) had a magnetic field strength of 1.0T and an electron plasma density of 10^{19}m^{-3} . In this panel we see clear solutions (within $10^{-4.5}\Omega_p$) of Eq. (1.40) at integer cyclotron frequency harmonics of the protons that fall in frequency through normalised wavenumber space. The low density plasma limit (left hand panel) had a magnetic field strength of 5.0T and an electron plasma density of 10^{15}m^{-3} . Here, solutions are less defined at integer harmonics of the proton cyclotron frequency, but originate at a consistent wavenumber $kr_{Lp} \simeq 0.6$, splitting at integer harmonics to low and high wavenumbers.

1.3 Tokamaks

We've spoken briefly on the production of plasmas, have identified some of the natural lengths and frequencies present, and have given dispersion relations for the most common types of waves within plasmas. The approaches of deriving natural frequencies and wave dispersion relations mostly assume an infinite geometry, under which there are no physical bounds on the plasma and it is free to evolve within space and time. Now, we consider bounded plasmas, specifically those within a device called a tokamak; a doughnut shaped device named after the acronym of the full Russian name (phonetic equivalent) "toroidal'naya kamera s magnitnymi katushkami", which directly translates to "toroidal chamber with magnetic coils". We direct the reader's attention to Fig. 1.4, which illustrates the tokamak's cross-sectional area, with appropriately labelled coils, currents and magnetic fields. Under this new geometry, we introduce hard bounds and symmetries, which ultimately influence how the plasma behaves.

There are many MCF devices around the world, including stellarators, tokamaks and spherical tokamaks. Some of the most well known devices are given in Table 1.2, where we have given the references relating to the study and measurement of ion cyclotron emission power spectral features relevant to this thesis (see 1.4.3). For those devices where results are not present, we have listed this as "N/A".

1.3.1 Plasma confinement

Early work on MCF devices focused on the principle of a magnetic mirror. Devices relying on the magnetic mirror depend upon the invariance of a particle's magnetic moment μ , given by

$$\mu_\sigma = \frac{m_\sigma v_{\perp\sigma}^2}{2B}, \quad (1.41)$$

where m_σ and $v_{\perp\sigma}$ are the mass and velocity perpendicular to the magnetic field B of the charged particle. In a magnetic mirror, an increase in the local magnetic field strength leads to an increase in the velocity perpendicular to the magnetic field direction, and hence, since energy is conserved, a decrease in the particle's parallel velocity component v_{\parallel} . At the boundary where the magnetic field strength increases such that $v_{\parallel} \rightarrow 0$, the particle is reflected back and is considered confined. This process is visualised in Fig. 1.5. This concept forms the basis of tokamak particle confinement, but by itself is unable to provide the

Name	Location	Year opened	Type	ICE Refs.
TFR	Fontenay-aux-Roses, France	1973	Tokamak	[48]
PDX	PPPL, New Jersey, USA	1978	Tokamak	[49]
DIII-D	San Diego, California, USA	1978(86)	Tokamak	[50–55]
TFTR	PPPL, New Jersey, USA	1980	Tokamak	[56]
JET	Culham, Oxford, UK	1983	Tokamak	[57–62]
W7-AS	Garching, Germany	1988	Stellarator	[63, 64]
TUMAN-3M	Saint Petersburg, Russia	1990	Tokamak	[65]
ASDEX-U	Garching, Germany	1991	Tokamak	[66–69]
JT-60U	Naka, Japan	1991	Tokamak	[70–74]
LHD	Toki, Gifu, Japan	1998	Stellarator	[75–79]
MAST	Culham, Oxford, UK	1999	Spherical T.	[80, 81]
NSTX-U	PPPL, New Jersey, USA	1999	Tokamak	[82, 83]
HL-2A	Chengdu, China	2002	Tokamak	[84]
EAST	Hefei, China	2006	Tokamak	[85–87]
KSTAR	Daejeon, South Korea	2007	Tokamak	[88, 89]
W7-X	Greifswald, Germany	2015	Stellarator	[90]
EXL-50U	Langfang, China	2023	Spherical T.	N/A

Table 1.2: Table of fusion devices, the date of their first operation and references, if applicable, to experiments related to ICE measurements.

magnetic field topology suitable for fusion as particle confinement times are too short [27].

As a result of particle drifts, a purely toroidal magnetic field introduces $\nabla\mathbf{B}$ gradients directed towards the central axis of tokamak symmetry. This leads to drift forces on particles directed tangential to B_ϕ and $\nabla\mathbf{B}$. If the magnetic field is orientated into the page and $\nabla\mathbf{B}$ is directed upwards, then positively charged ions drift upwards, and electrons drift downwards. The charge separation between both species generates an electric field (directed upwards) which generates an $\mathbf{E} \times \mathbf{B}$ drift velocity, pushing both ions and electrons to the wall of the tokamak. To avoid a loss of confinement in a tokamak and to confine particles in gyro-orbits, an additional poloidal field component is required. This is induced through the primary current (in the primary coil) linked to the plasma, leading to a plasma current, typically on the order of a few megaamps to 20MA. The initial poloidal magnetic field induces a secondary toroidal plasma current which feedbacks again into the poloidal field. Further plasma stability in the vertical direction is achieved with additional external control coils. The combined mag-

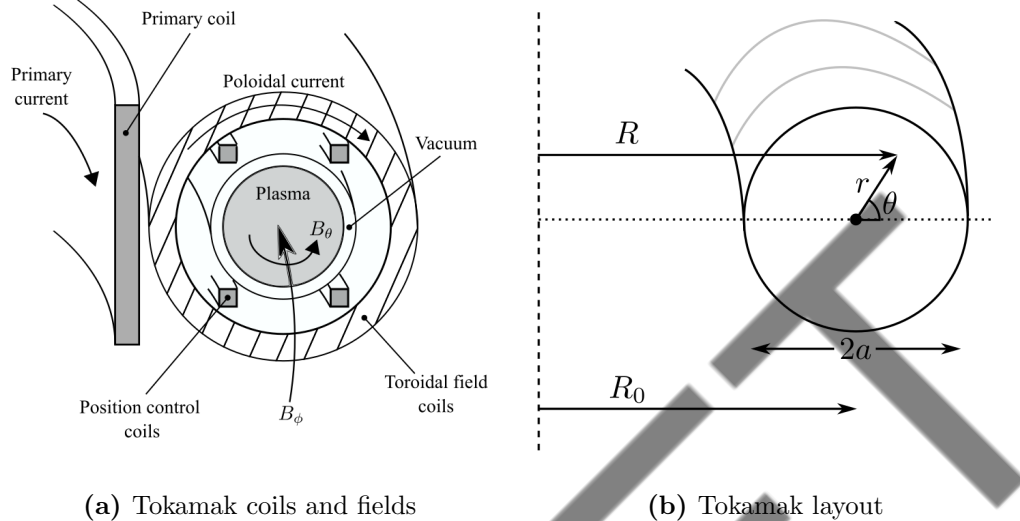


Figure 1.4: Schematic of (a) the electric coils and their magnetic field configurations in a tokamak cross-section, remade from Ref. [27], and (b) the tokamak cross-section with major, R_0 , and minor, a , radius as labelled, remade from Ref. [35]. Here, the total radius (R) is the horizontal distance between the centre of the tokamak and local location in the tokamak chamber, r , and can therefore be written as $R = R_0 + r \cos \theta$.

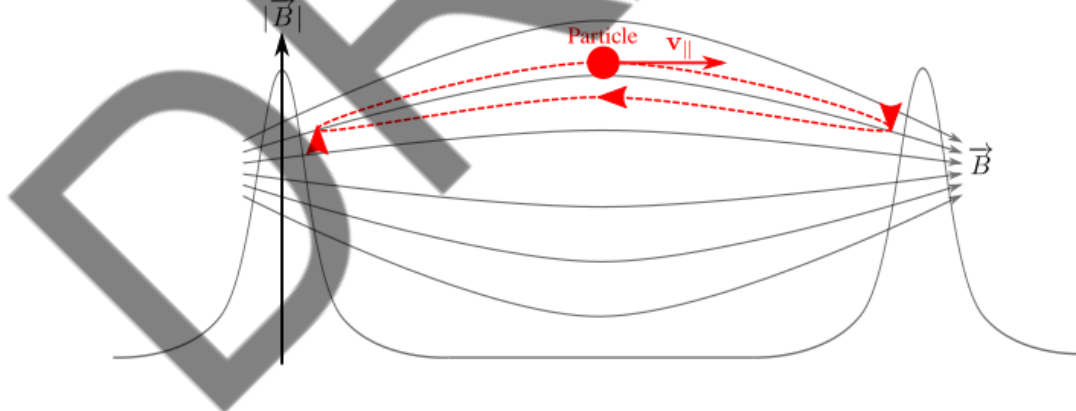


Figure 1.5: Schematic of the magnetic mirror, adapted from Ref. [36]. Magnetic field strength is plotted as two bumps along the x-axis, and is visualised by the in-plane compacted field lines. Charged particles are reflected back at the boundary of high magnetic fields due to the conservation of the particle's magnetic moment, Eq. (1.41).

netic field topology forms helical lines around the tokamak confining charged particles along curved orbits.

1.3.2 Trapped and passing orbits

As discussed and shown in panels (a) and (b) of Fig. 1.4, plasmas are controlled within a tokamak using toroidal and poloidal magnetic fields. Generally, in cylindrical coordinates (r, θ, ϕ) , the total magnetic field within a tokamak is given by [35],

$$\mathbf{B} = (0, B_\theta(r), B_0) \cdot \left(1 - \frac{r}{R_0} \cos \theta\right), \quad (1.42)$$

so surfaces of constant magnetic field lie on circular loops around the tokamak at constant radius r . The total number of times these lines of constant magnetic field loop around the tokamak is given by the winding number $q(r)$ (also called the safety factor), which takes the form

$$q(r) = \frac{d\phi}{d\theta} = \frac{rB_0}{R_0 B_\theta(r)}, \quad (1.43)$$

which under safe operation, for most large MCF devices, falls in the range $0.7 < q(r) < 4$ [35].

Particles which are reflected along some point of their helical orbit as a result of the magnetic mirroring effect are considered trapped. Constraining their magnetic moment one finds the range $E_k/B_0(1+r/R_0) < \mu < E_k/B_0(1-r/R_0)$ of kinetic energies, E_k , and positions r which allow for such trapping. Particles which traverse a full winding helical orbit are referred to as passing. A diagram of two such orbits is reproduced in Fig. 1.6, where the left-hand panel shows a trapped particle, following a banana orbit [27, 35], and the right-hand panel shows the orbit of a passing particle, whose parallel velocity is influenced by variations in the local magnetic field, but which does not change sign.

1.3.3 Measuring plasma density

Density fluctuations within tokamaks can lead to the growth of waves or instabilities which can destabilise the plasma and damage the inner wall. Being able to measure changes in electron and ion density is, therefore, a critical measure in maintaining the confinement of the plasma and ensuring its stability.

The two primary methods of electron density measurement are through Doppler reflectometry and interferometry, the latter of which is most commonly used in tokamaks [27]. Reflectometry uses the concept that as an electromagnetic wave passes through a plasma it's phase shifts in accordance to the local density

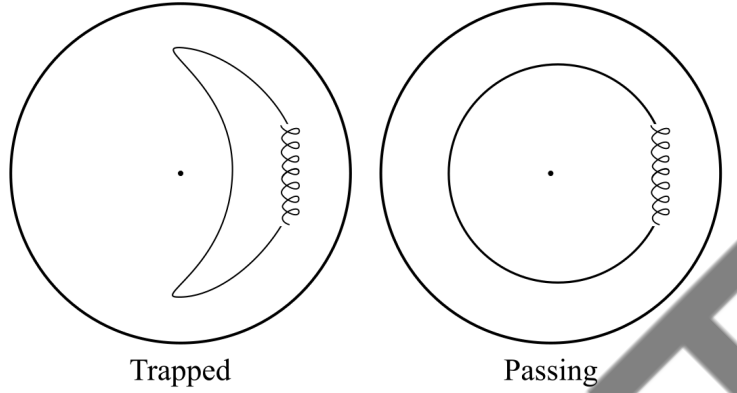


Figure 1.6: Diagram showing (*left*) a trapped (banana) orbit and (*right*) a passing orbit of a fast particle species through the view of a tokamak. Local Larmor oscillations around its guiding centre are illustrated as helical screws along the guiding-centre averaged path.

(hence its refractive index) and the magnetic field. In one-dimension, this involves the propagation of a wave into the plasma with some cut-off frequency ω_c . This wave is reflected at the cut-off layer - a density corresponding to a refractive index of zero - and the phase shift between the known wave frequency and measured frequency can be calculated. Mapping between frequency and density is trivial, as it will depend on the perpendicular propagation of the ordinary (O) and extraordinary (X) modes, of which the critical frequency chosen will depend on density. Launching multiple waves from various locations helps to map the density of the plasma at any given time [91].

Interferometry, the more widely used diagnostic, involves the radiation of a coherent beam with respectively high wavelengths (sub-millimetre or infrared) towards the plasma. The phase shifted wave is then measured on the other side of the tokamak and treated as the line integral of the density over the tokamak cross-section over which the wave traversed,

$$\Delta\phi \propto \int_0^L n_e dl . \quad (1.44)$$

As with reflectometry, interferometry benefits from multiple measurements along varying poloidal angles and line of sights to rebuild the total electron density profile within the tokamak - hence it's wide use and application in present day devices and, in the future, in ITER [92].

1.4 The magnetoacoustic cyclotron instability (MCI) and ion cyclotron emission (ICE)

1.4.1 Magnetoacoustic cyclotron instability (MCI)

The magnetoacoustic cyclotron instability (MCI) was first theorised in 1976 by Belikov and Kolesnichenko [93] and observed in TFR in 1978 [48]. Originally, the MCI was believed to be a result of the near frequency resonance between magnetoacoustic cyclotron waves (MCW) and the integer cyclotron frequencies of the fusion-reaction products, namely 3.5 MeV energetic alpha-particles in a DT fusion plasma. Later, in 1992 [38], the MCI was considered to be the result of resonances between the FAW and IBW [38], see §1.2.6. Now, the MCI is characterised by the near frequency resonance between the FAW, supported by the bulk plasma, and the integer cyclotron frequencies of the fusion-born energetic minority propagating quasi-perpendicular to the magnetic field, resulting in a transverse wave polarised in the poloidal direction. Through the MCI, energy is transmitted to the electromagnetic fields and to the bulk ions via resonant excitation of waves at, or near, integer ion cyclotron harmonics, which results from the collective relaxation of a strongly non-Maxwellian population of energetic ions [38, 39, 94–102].

The necessary velocity distribution $f(v_{\parallel}, v_{\perp})$, for strong MCI drive requires an inversion in velocity space such that $\partial f / \partial v_{\perp} > 0$ for values of $v_{\perp} \simeq v_A$, where v_A denotes the Alfvén speed. This can arise for fusion-born minority energetic ion species, NBI ions, and species heated by ICRF waves. Therefore, the ratio between the fusion-born ions perpendicular birth velocity and the local Alfvén wave speed, v_{\perp}/v_A is a key parameter. For a ratio near unity the growth rate of the MCI is maximised as a result of phase matching [42, 100, 101, 103–106]. This holds for frequencies on the order of and below $10\Omega_{\alpha}$, where Ω_{α} is the cyclotron frequency of the minority ion species (classically, alpha-particles).

The choice of minority distribution is, therefore, an important factor in calculating growth rates of the MCI. More “realistic” distributions using the TRANSP/NUBEAM code have been used to fit observations of ASDEX-Upgrade proton NBI-heated helium plasmas [103], as well as in EAST [107]. These have been used as the basis of analytical linear MCI calculations, yielding strong correlation between the resulting growth rates and the time-evolving ICE intensity, as shown in Fig. 10 of Ref. [103].

1.4.2 Velocity space distributions

The velocity space distributions of the minority ions, which transfer free energy back to the thermal ions, are of great interest to fusion plasma researchers as they lead to a multitude of unstable behaviours. The linear growth rate theory of a two-energy ion component plasma are considered in Ref. [108] and simulated in Ref. [109]. These distributions consist of a ring-beam structure in velocity space for a secondary monoenergetic ion species. These are similar to those required for the development of the MCI. Many such examples exist for the development of the MCI, the most common being Dirac-delta functions centred on the perpendicular velocity, as originally used in [93], whose work on the MCI formed the basis for a lot of subsequent developments. Velocity distribution functions are important in this sense, as they effect the tensor elements of the dielectric permittivity ϵ_{ij} and hence the growth rate criteria of magnetoacoustic waves [93]. Therefore, there is motivation for work to investigate more realistic velocity distributions and their effect on the linear MCI growth rates. This would improve, also, the tractability from observed growth rate frequency spectra to initial velocity distributions.

The simple Dirac-delta distribution for particles with no parallel or perpendicular velocity spread and no parallel drift, is written as

$$f_\alpha(v_\parallel, v_\perp) \propto \delta(v_\parallel)\delta(v_\perp - u_0), \quad (1.45)$$

where u_0 is the birth velocity of the minority energetic ion fusion product, given by $u_0 = \sqrt{2E_\sigma/m_\sigma}$, with σ representing the minority energetic species, such as alphas (α) or protons (p). Through including some non-zero parallel drift birth velocity, one writes

$$f_\alpha(v_\parallel, v_\perp) \propto \delta(v_\parallel - u_{\parallel 0})\delta(v_\perp - u_{\perp 0}), \quad (1.46)$$

where the components of the birth velocity parallel and perpendicular are written as $u_{\parallel 0}$ and $u_{\perp 0}$, respectively, with $u_0^2 = u_{\perp 0}^2 + u_{\parallel 0}^2$ and whose ratio is defined by the particle's pitch-angle ϕ , accordingly, $\tan \phi = u_{\perp 0}/u_{\parallel 0}$.

More realistic depictions of the velocity distributions for the purpose of MCI theory development, both for a formalism of its linear stage growth rate as well as the investigation of the plasma instability within PIC simulations, introduces some non-zero spread in its velocity components. Firstly, spread in the parallel component

$$f_\alpha(v_\parallel, v_\perp) \propto \exp\left(-\frac{(v_\parallel - u_{\parallel 0})^2}{u_{\parallel r}^2}\right) \delta(v_\perp - u_{\perp 0}), \quad (1.47)$$

with the intensity of parallel velocity spread determined by $u_{\parallel r}$. This approach has been utilised in previous drifting ring-beam kinetic simulations from other plasmas, notably those in JET [62, 100, 101, 105, 110], ASDEX-Upgrade [103, 111], KSTAR [112–114] and LHD [79, 104, 115, 116]. The ring-beam and shell distributions have also been used throughout linear MCI theory [38, 39, 96, 97, 117].

Presently, PIC simulations initialise the fast particle by including spreads in both parallel and perpendicular directions. The distribution function in velocity space is known as a drifting ring-beam, and is defined in Ref. [37, 118] as,

$$f_\alpha(v_\parallel, v_\perp) \propto \exp\left(-\frac{(v_\parallel - u_{\parallel 0})^2}{u_{\parallel r}^2}\right) \exp\left(-\frac{(v_\perp - u_{\perp 0})^2}{u_{\perp r}^2}\right). \quad (1.48)$$

This model forms the basis of several analytical studies of the linear MCI [37–39, 59, 62, 94, 96, 97, 103, 117, 119–122], and was used to initialise the energetic ion distributions in previous computational kinetic PIC studies [39, 42, 56, 59, 62, 100, 101, 104–106, 111–114, 116, 120, 123]. The crossover, in this context, between finite thickness drifting ring-beam and spherical shell distribution functions is examined in Ref. [106], and the relation of Eq. (1.48) to other representations of energetic ion distributions is examined in Ref. [124]. Equation (1.48) approximately captures the wedge structure in velocity space shown in Fig. 16 of Ref. [58], peaking at $(u_{\parallel 0}, u_{\perp 0})$ and with spread parameterised by $(u_{\parallel r}, u_{\perp r})$.

This description of the energetic ions velocity distribution is used frequently throughout this thesis, with some of the simplified forms, Eqns. (1.45)–(1.47), scattered throughout in examples and baseline tests. In literature, the energetic minority bump-on-tail is oft-described with one of the simpler distribution functions as the physics associated with the development of the MCI can still be generated by a single velocity minority species with velocity spread only in the parallel direction.

Ring-beam structures are useful to visualise, both for the reader and in analysis. Simple examples of the ring and beam component are represented in Fig. 1.7. This velocity space representation shows four cases for a minority particle with one purely beam and one purely ring component, then for two ring-beam distributions with two magnetic field angles with respect to the simulation domain at 90° and 25° .

Multiple beam and ring spreads are visualised in Fig. 1.8, where we have used Eq. (1.48) with varying ring and beam thermal spread parameters and pitch-angles. These parameters are given, respectively, in the title of each sub-figure separated by colons - see caption. Pitch-angles of $-\pi/2$ and $-\pi/3$ are

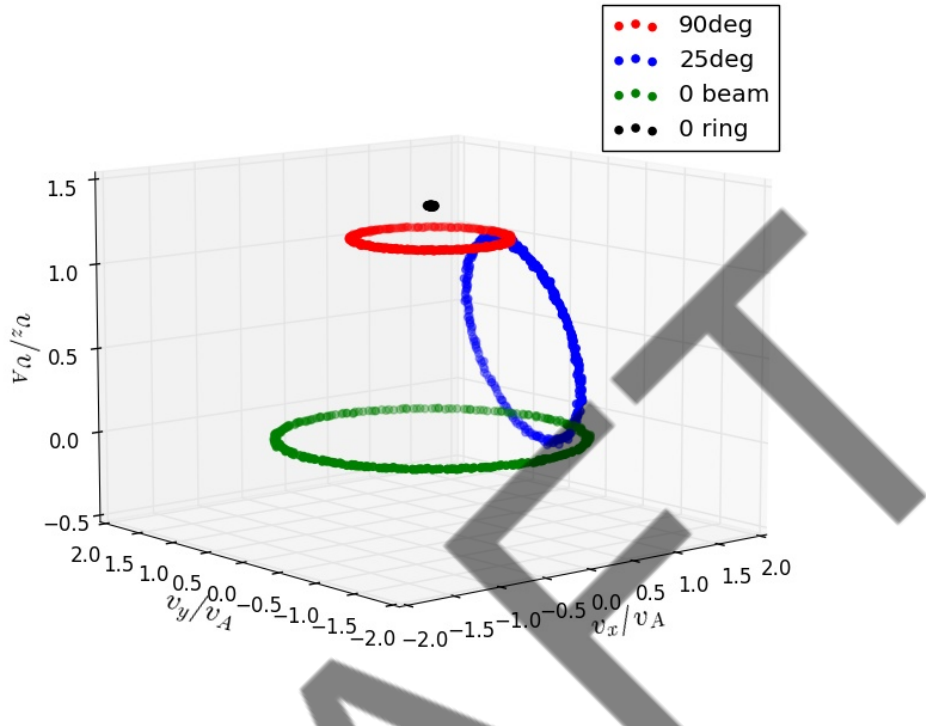


Figure 1.7: Multiple distributions of the 3.5 MeV alpha-particle. Angles given in the legend are between the \hat{x} and \hat{z} axes.

coloured red and blue respectively. The top row of Fig. 1.8 represents a constant perpendicular spread of $v_{\perp r} = v_0/1000$, and the bottom row a perpendicular spread of $v_{\perp r} = v_0/100$. Notice that for a given column in this figure, the influence of the perpendicular spread is greater over the total distribution than that of the parallel spread. In simulations, it is common to use a greater parallel spread than perpendicular, as particles are born or injected quasi-perpendicular with respect to the magnetic field angle. This also aligns well with previously simulated distributions, where perpendicular spread was minimal, or ignored entirely using a Dirac-delta.

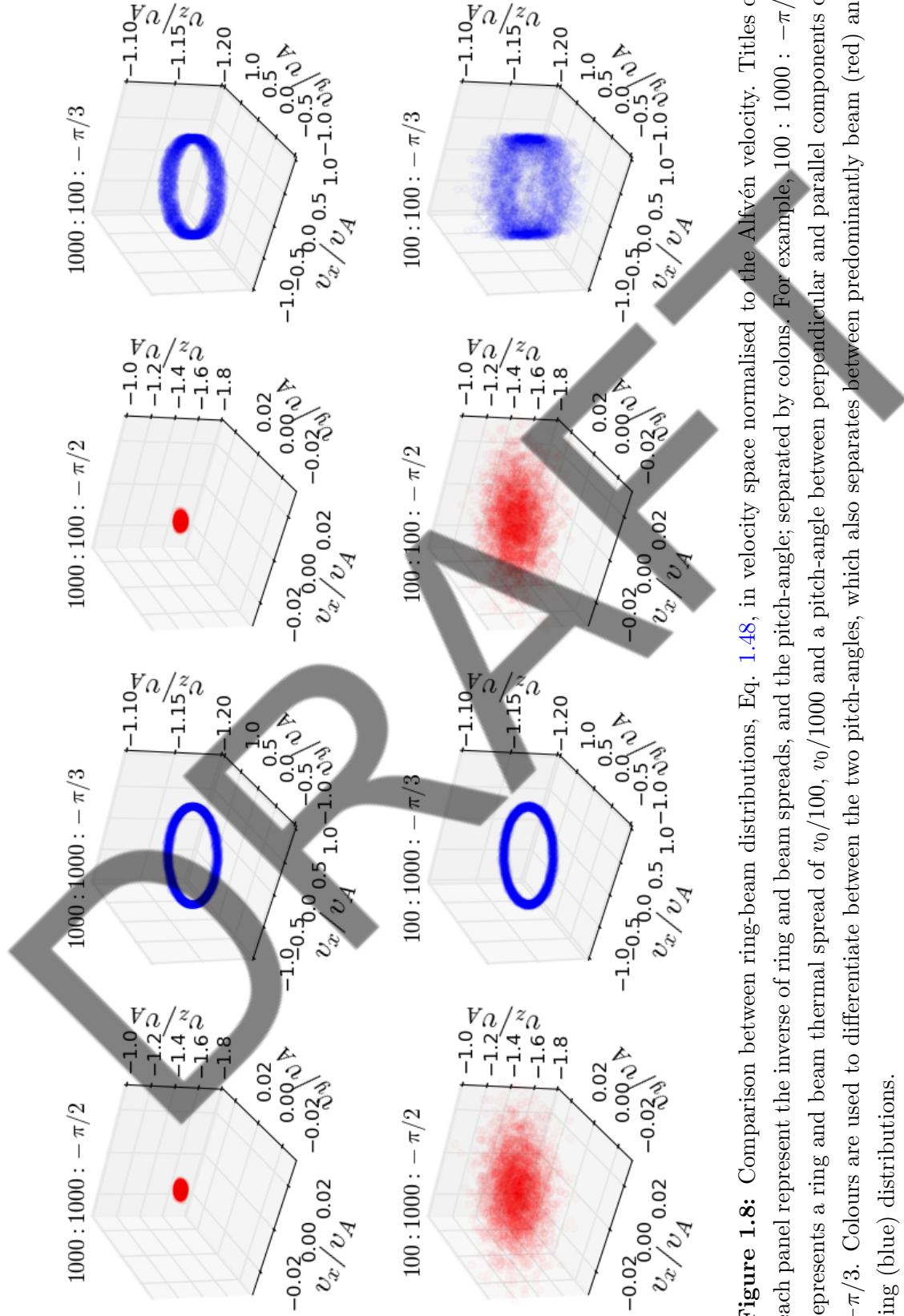


Figure 1.8: Comparison between ring-beam distributions, Eq. 1.48, in velocity space normalised to the Alfvén velocity. Titles of each panel represent the inverse of ring and beam spreads, and the pitch-angle; separated by colons. For example, 100 : 1000 : $-\pi/3$ represents a ring and beam thermal spread of $v_0/100$, $v_0/1000$ and a pitch-angle between perpendicular and parallel components of $-\pi/3$. Colours are used to differentiate between the two pitch-angles, which also separates between predominantly beam (red) and ring (blue) distributions.

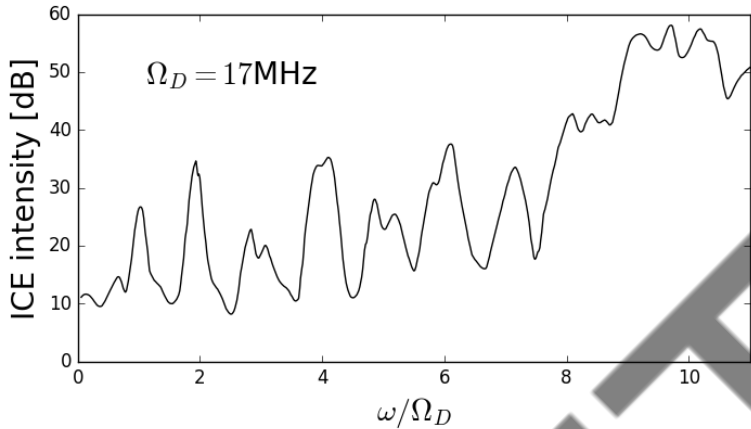


Figure 1.9: Reproduction of the JET plasma 26148 ICE power spectra [58], where a spacing between peaks of $\Omega_D = 17\text{MHz}$ was identified and is annotated.

1.4.3 Ion cyclotron emission (ICE)

The MCI is of great practical interest for MCF plasmas because it underlies the widespread phenomenon of ion cyclotron emission (ICE) [53–55, 57–59, 65, 68, 71, 73, 75–77, 79, 82, 87, 88, 103, 104, 107, 111–114, 116, 120, 121, 125–133] from energetic ion populations. ICE is characterised by multiple narrow and strongly suprathermal spectral peaks, whose separation is defined primarily by the cyclotron resonant frequency of the minority energetic ion at a radial position corresponding to the inferred magnetic field strength. ICE has been observed from most large MCF plasmas. Early results were obtained from TFR [48], and from JET [57–59], before and during the first deuterium-tritium experiments. The original JET plasma 26148 power spectra, which identified ICE, is reproduced in Fig. 1.9. Subsequently, ICE was observed from tokamaks including ASDEX-Upgrade [66–69], DIII-D [50–55], EAST [85–87], HL-2A [84], JET [60–62], JT-60U [70–74, 134], KSTAR [88, 89], NSTX-U [82, 83], PDX [49], TFTR [56, 120, 121] and TUMAN-3M [65] as well as the stellarators, LHD [75–79, 104, 116], W7-AS [63, 64] and W7-X [90]. Exploitation of ICE for studying burning plasmas has been suggested for future ITER experiments [42, 135].

Observations of ICE using external magnetic loops and ICRH antennas set to receive have allowed for a high quality description of its toroidal structure. As a result, the radial and poloidal components are less understood as these are unable to measure directly the RF field components, and those diagnostic components that do measure the poloidal structure of instabilities do not measure in a suitable frequency range. Work has been done using Phase Contrast Imaging (PCI) [136], which converts phase shifts of probing waves to amplitude variations along the

probing wave's plane. This work extended the frequency range of poloidal and radial measurements to better map the radial structure of the electron density fluctuations to ICE signals.

The primary diagnostic applications of ICE relate to the measurement of fusion reactivity and in determining the velocity space distribution of energetic ions. Correlations between the measured intensity of ICE and the fusion neutron rate for various plasmas in JET, from Ref. [58], are reproduced in Fig. 1.10, and in DT supershot plasmas in TFTR is shown in Fig. 6 of Ref. [56]. More recently, ICE observations have enabled the identification of unanticipated fusion-born proton populations in deuterium plasmas in the KSTAR tokamak [112, 113] and the LHD heliotron-stellarator [79]. The observed power spectrum of ICE from a given plasma can be related to the velocity-space distribution of the minority energetic ion population that drives it. This rests on a physical understanding of the excitation process, namely the MCI in its linear phase, accessible to analytical theory [39], and in its nonlinear and saturated phases, accessible to first principles computational studies using kinetic PIC codes [79, 100, 101, 104, 110, 113, 137]. Recent advances include the use of deep neural networks to reconstruct the velocity-space distribution of the minority energetic species [134, 138].

Studies of future aneutronic fusion plasmas, such as those comprising D– ^3He or p– ^{11}B , will not be able to exploit neutron-based diagnostics, and so ICE is positioned as an ideal candidate in these aneutronic plasmas for the measurement of fusion reactivity. A potential alternative diagnostic is the measurement of gamma rays from the low-likelihood fusion path of DT to the unstable ^5He isotope. The production of a ^5He isotope includes the release of a 16 MeV gamma ray whose energy is unique and narrowly peaked [139, 140]. Similarly, for the aneutronic D– ^3He reactions, one may measure the emission of the 5.5 MeV gamma ray [141]. The ability to measure these energies and determine the rate of decay to these unstable isotopes to a high level of accuracy remains pivotal in these methods.

One expects that fusion born ions should dominate power spectral features. However, linear MCI theory reveals a linear scaling between the growth rate of ICE power and the concentration of resonant fast ions [39, 93], later confirmed with hybrid-PIC simulations [105]. Since NBI ions are in a higher abundance in the fusion plasma than the fusion born products, we should predict a quicker driving of the MCI, and that its ICE signals should dominate power spectral features. ICE was originally used to determine the location of emitting ions in Ref. [58] and recent work suggests it can also be used to reconstruct velocity space distributions [142], but, while sources of ICE have been observed from

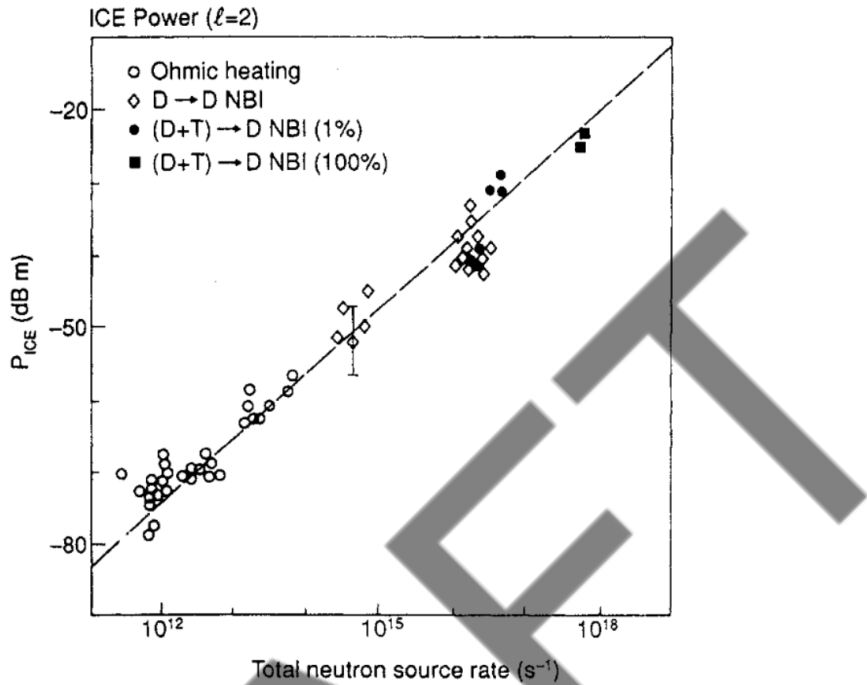


Figure 1.10: Measured correlation between the fusion reactivity (here labelled total neutron source rate) and the intensity of the ICE signal from the $l = 2$ harmonic. Reproduced from Fig. 5 of Ref. [58].

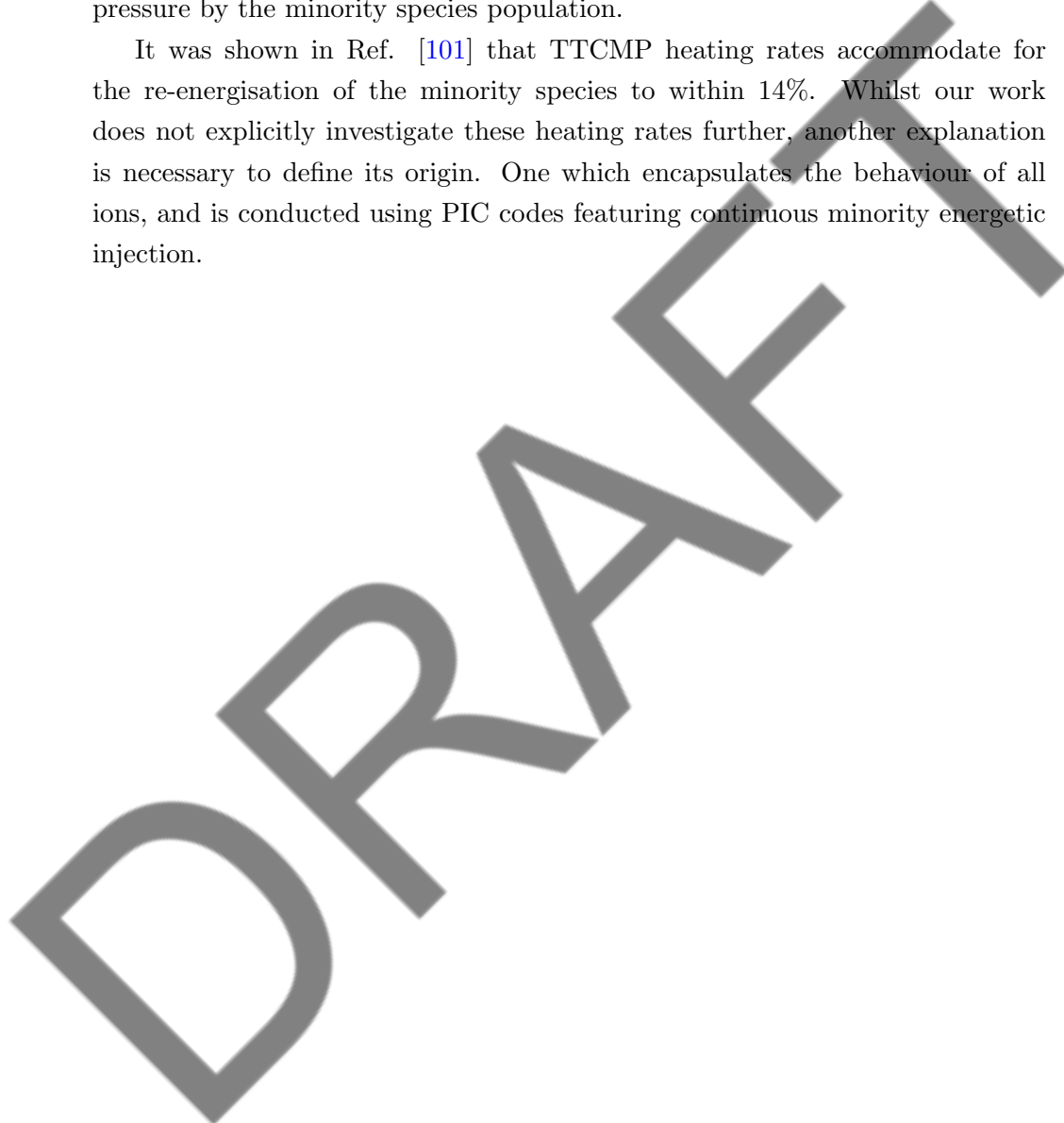
both fusion born and NBI ions, its use as a plasma diagnostic is, as yet, unable to differentiate between resonant ion sources [132]. Work presented later in this thesis, may, with adequate post-processing, shed light on this discussion. Likewise, a current challenge lies in distinguishing the spatial location of ICE spectral peak origin from different energetic ion species, including the plasma core and edge [53, 67, 68, 129] and intermediate locations [79, 132]. Recent results using the Chinese You Only Look Once (YOLO) neural network [133] has provided a model which can differentiate between the edge and core emission locations of ICE emitting ions with an accuracy of over 80%. With intelligent assumptions and further modelling, one may be able to extract yet more valuable information from the ICE spectrum.

1.4.4 Re-energisation of minority particles

The re-energisation of the minority species that occurs in the saturated nonlinear regime of the MCI, see Refs. [79, 101, 104, 106, 114, 116] and Chapters 5 & 7, is not handled or discussed further in this thesis other than this sub-section. Physically, the re-energisation of the energetic minority species, after the period of

de-energisation synonymous with linear MCI growth, was initially considered to be an artefact from the initialisation of PIC simulations. In Ref. [101] the transit time compressional magnetic pumping (TTCMP) mechanism was explored as an explanation for re-energisation, implying that it is fully physical and related to the phase delay between the oscillations of the magnetic field and perpendicular pressure by the minority species population.

It was shown in Ref. [101] that TTCMP heating rates accommodate for the re-energisation of the minority species to within 14%. Whilst our work does not explicitly investigate these heating rates further, another explanation is necessary to define its origin. One which encapsulates the behaviour of all ions, and is conducted using PIC codes featuring continuous minority energetic injection.



Chapter 2

Computational methods

In the following chapter we will: provide a general overview of how a particle-in-cell (PIC) code works, including shape functions and the particle push and field update processes; present benchmarking simulations in EPOCH of a two-stream instability and cold plasma; provide a brief discussion on extracting growth rate solutions of the MCI in two-dimensional wavenumber space (expanded in Chapter 6); and detail a few of the analytical methods employed in correlating ICE power spectra, and measuring the strength of MCI wave resonance coupling.

2.1 Particle-in-cell codes

Particle-in-cell (PIC) codes have been used extensively in plasma research from the early 1970s with various improvements over time allowing for the modelling of collisions, ionisation, ablation, QED and relativistic effects. Early texts by Ref. [41] summarise well the methodology behind PIC codes, their stability, methods of self-heating due to grid forces, and provide for their reader various examples throughout. For a brief summary of the history of PIC codes and their development from the 1950s, we refer to Ref. [143] and the references therein.

A PIC code discretises physical space into grid cells of finite width, distributing a number of mass and charge scaled pseudo/macroparticles within each cell, self-consistently solving the gyro-orbit-resolved Lorentz dynamics for the tens of millions of interacting plasma particles in combination with their electric and magnetic fields, all evolving under the Maxwell-Lorentz system of equations, Eqns. (1.8). Macroparticles have the same charge-to-mass ratio as the collection of real particles that they represent, and hence the same Larmor radii and gyro-frequency. This collection of particles make up a finite volume which is fixed over particle motion. Typically, the number of real particles that one macroparticle represents, also known as the species “weighting”, is on the order of 10^8

for most simulations of a fusion plasma, reducing the strain on computational memory by a substantial order of magnitude. Using the macroparticles charge and current, which will be on the order of the particle weighting greater than that of a real particle, one can then evolve the fields at the grid points, see §2.1.1, through an interpolation between macroparticle position and grid values via a shape function. Similar techniques are also used to simulate galactic clusters, as in Ref. [144].

EPOCH [145] is a highly parallelised, second order accurate PIC code developed at the University of Warwick and used around the globe. It utilises a finite difference time domain (FTDT) method for collectively solving Maxwell-Lorentz's system of equations, is fully relativistic, and is capable of modelling QED, lasers and collisions. Simulating a fusion plasma using EPOCH starts with defining the distribution function of particles, $f(\mathbf{x}, \mathbf{v})$, which positions the particles in phase space (\mathbf{x}, \mathbf{v}) . The work showed herein uses a 1D3V approach, or what is also referred to as “slab” geometry, and is consistent with MCI linear growth rate theory. Throughout this thesis, the remaining spatial dimensions will be ignored. Whilst this does miss out on the toroidal geometry and its associated instabilities, such as compressional Alfvén eigenmodes (CAEs) [80, 146, 147], the one-dimensional structure of PIC codes is sufficient in capturing the majority of the observed MCI physics at play. Despite coming at a greater computational cost, the two-dimensional structure of ICE has been explored in hybrid-PIC codes [148].

2.1.1 Updating fields and pushing particles

Within a PIC code the electromagnetic fields are defined on a Yee staggered grid [149] shown in Fig. 2.1, and the particle phase space positions are updated following the Boris scheme [150] by the particle charges and currents inferred from their position within space to the grid points through a shape function, see §2.1.2. Particle positions are then updated according to their Lorentz forces from the half-stepped field values at the grid position. These allow for a second order accurate calculation of a field update as well as an initialisation (and conservation) of Gauss' law for magnetism, Eq. (1.8b).

A detailed look at the operations of updating the fields and pushing the particles through integer time steps, indexed n , are detailed below,

1. Update electric field by half time step,

$$\mathbf{E}^{n+1/2} - \mathbf{E}^n = \frac{\Delta t}{2} \left(c^2 \nabla \times \mathbf{B}^n - \frac{\mathbf{J}^n}{\epsilon_0} \right) . \quad (2.1)$$

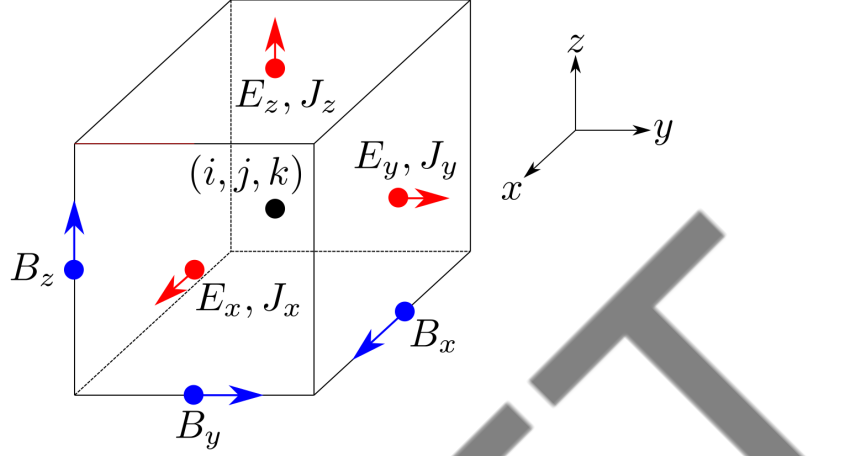


Figure 2.1: Illustration of the staggered Yee grid in 3D space, adapted from Refs. [145] and [151], for a cell centred coordinate (i, j, k) .

2. Using half-step electric field, update magnetic field by a half time step,

$$\mathbf{B}^{n+1/2} - \mathbf{B}^n = -\frac{\Delta t}{2} (\nabla \times \mathbf{E}^{n+1/2}) . \quad (2.2)$$

3. *Particle push:*

- 3.1. Update particle position by half time step,

$$\mathbf{x}^{n+1/2} = \mathbf{x}^n + \frac{\Delta t}{2} \mathbf{v}^n .$$

- 3.2. Update relativistic Lorentz force on particles of species σ using the values at a half time step and the average velocity which represents the velocity at the half-step,

$$\frac{\mathbf{u}^{n+1} - \mathbf{u}^n}{\Delta t} = \frac{q_\sigma}{m_\sigma} \left(\mathbf{E}^{n+1/2} + \frac{\mathbf{u}^{n+1} + \mathbf{u}^n}{2c\gamma^{n+1/2}} \times \mathbf{B}^{n+1/2} \right) . \quad (2.3)$$

- 3.3. Given that we write this relativistic velocity as $\mathbf{u} = \gamma \mathbf{v}$ with $\gamma^2 = 1 + \frac{u^2}{c^2}$ for a particle with rest mass m , the updated velocity, \mathbf{u}^{n+1} , is thus entangled in the calculation of the Lorentz force. EPOCH utilises the Boris scheme, introducing a rotation in velocity space of the velocity vectors,

$$\mathbf{u}^n = \mathbf{u}^- - \frac{q_\sigma \Delta t}{2m_\sigma} \mathbf{E}^{n+1/2} , \quad (2.4a)$$

$$\mathbf{u}^{n+1} = \mathbf{u}^+ + \frac{q_\sigma \Delta t}{2m_\sigma} \mathbf{E}^{n+1/2} . \quad (2.4b)$$

3.4. Substituting into Eq. (2.3) allows EPOCH to update the velocity by another half time step.

3.5. Finally, update the position by a further half step,

$$\mathbf{x}^{n+1} = \mathbf{x}^{n+1/2} + \frac{\Delta t}{2\gamma^{n+1/2}} \mathbf{u}^{n+1} . \quad (2.5)$$

4. Update magnetic field by another half time step,

$$\mathbf{B}^{n+1} - \mathbf{B}^n = -\frac{\Delta t}{2} (\nabla \times \mathbf{E}^{n+1/2}) . \quad (2.6)$$

5. Finally, update the electric field by another half time step, using the updated magnetic field and current:

5.1. Using the $n + 1/2$ and $n + 3/2$ time steps, update the change in charge density on the grid using the particle position [151], using charge conservation update the current J^n to J^{n+1} ,

$$\frac{\partial \rho}{\partial t} = \nabla \cdot \mathbf{J} . \quad (2.7)$$

5.2. Update the electric field by another half-time step

$$\mathbf{E}^{n+1} - \mathbf{E}^{n+1/2} = \frac{\Delta t}{2} \left(c^2 \nabla \times \mathbf{B}^{n+1} - \frac{\mathbf{J}^{n+1}}{\epsilon_0} \right) . \quad (2.8)$$

Now, using the particle's $n + 3/2$ time stepped velocity and position, the process repeats for updating the field, currents and particle quantities. This is the method by which EPOCH is made second order accurate in time. A more detailed explanation is given in Refs. [41] and [151], which also describe these processes in higher dimensions.

2.1.2 Shape functions

Since the grid is discretised, interpolations must be made between particle quantities; position and velocity, and grid quantities; fields and densities. As an example, in its simplest form a particle's charge contribution can be interpreted from its spatial position to its nearest grid point through a top-hat, giving all of it's charge to the cell in which it is positioned. In this scheme, on passing between grid cell boundaries the top-hat interpolation leads to large jumps in the current contribution per cell, leading to large jumps in the update of the electric field, conversely effecting the particle's velocity, *et cetera*. The granularity of interpolation of the macroparticle quantities to grid positions is therefore greatly

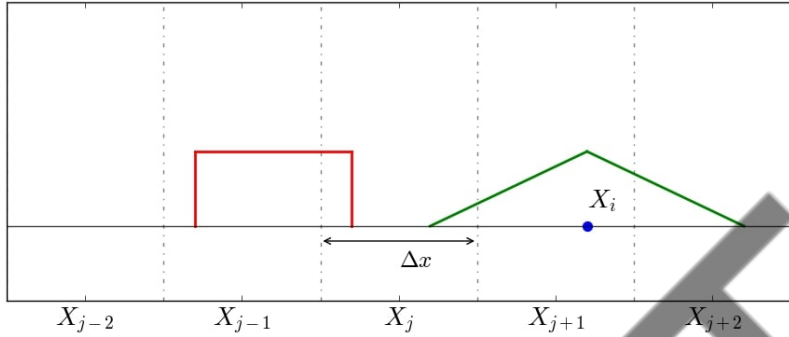


Figure 2.2: Schematic of the first (red) and second (green) order shape functions for a domain with grid centroids X_j , distance by a cell width of Δx . A particle (blue) is located at X_i . Grid cell boundaries are drawn as *dashed-black* vertical lines. Forces on the particle will be an interpolation of the X_j , X_{j+1} and X_{j+2} grid values to the particle's position. Figure adapted from Ref. [41].

improved for a more realistic particle contribution, one that tapers off with distance and influences multiple grid cells. As a result of the particle push and field update, this improvement compounds through the Lorentz force calculation used to push the particle's position and velocity, reducing the PIC numerical noise.

Each shape function defines the particle's charge contribution to the grid points and is appointed an order parameter starting from one. The most basic shape function is a square top-hat (order one) whose width is the same as one grid cell's length, Δx . The next order up is a triangle, whose width is twice that of a grid cell. A schematic of the first (red) and second order (green) shape functions are given in Fig. 2.2. The grid is defined along the x -axis with cells positioned at increments, indexed j , labelled X_j , and a particle, indexed i , positioned at X_i . In general, the shape function is written as $S_m(x)$ where m is a positive integer which defines the shape's order. Using a higher order shape function increases the accuracy of the field updates through the Lorentz force as charge contributions are spread over a larger collection of grid points, but results in a more computationally expensive simulation. The force on the i^{th} particle in Fig. 2.2 is written as a summation of the forces at the grid points, multiplied by the shape function,

$$F_i = \frac{1}{\Delta x} \sum_j F_j \int_{X_j - m\Delta x/2}^{X_j + m\Delta x/2} S_m(X_i - x) dx . \quad (2.9)$$

For a second order shape function ($m = 2$), the particle's contributions include the cell it is in, as well as its two neighbours. Only when the particle lies

perfectly on a cell boundary, $X_i = X_j + \Delta x/2$, is the force on the particle only influenced by two cells.

The default shape function in EPOCH is of second order, implemented for field and current density interpolations to the particles. This is because the trade-off between the quality of the solutions and computational speed are optimised, and whilst higher order shape functions, such as $m = 3$ (which is a Gaussian and takes the contribution of the five most adjacent cells) reduce noise, they are, computationally, significantly slower and often mask unwanted non-physical behaviour.

2.1.3 Resolution scales

Just as forces on particles and particle contributions to the grid are simplified via shape functions, we utilise characteristic length and time scales within plasmas to decrease computational strain without sacrificing on resolved plasma physics phenomenology.

One must be careful, therefore, in reducing the spatial and temporal resolutions of their PIC simulations so as to still resolve the plasma activity of interest. In frequency space, (k, ω) , the bounding box within which we can measure waves are given by the Nyquist limits (positive and negative) for wavenumber $k_{Nyq} = 2\pi/(2\Delta x)$ and (angular) frequency $\omega_{Nyq} = 2\pi/(2\Delta t)$. For example, if we wish to measure a wave with an angular frequency of $\omega = \omega_{pe}$, our temporal resolution needs to be $\Delta t < 2\pi/(2\omega_{pe})$, to encapsulate the wave's oscillations. If our resolutions in (k, ω) space do not extend well past the frequencies and wavelengths of interest, aliasing will result. Aliasing is the process by which waves at the edges of our frequency space bounding box reflect back into a region of lower frequency/wavenumber, and interact with real waves and modes within the plasma, leading to spurious non-physical behaviour in our simulations, and giving rise to significant power at unexpected (k, ω) coordinates. To mitigate aliasing, simulations can be run with more granular resolutions (increasing the limits of the frequency space bounding box) or through spatial and temporal averaging, the latter of which can be toggled through corresponding flags in EPOCH.

Spatial resolution

The natural length scale associated with charge shielding of plasma ions is the Debye length, §1.2.4. Charges within a sphere of radius λ_{De} are shielded from those outside. Because of this, if λ_{De} is not resolved in a simulation, $\Delta x > \lambda_{De}$,

then particles exponentially heat as a result of the restoring electric fields generated by large charge density fluctuations, increasing the average electron thermal energy $k_B T_e$ until $\Delta x \approx \lambda_{De}$. This condition is not standard in simulations of laser-plasmas [145], but for simulations studying the growth of instabilities (such as our work) with small comparable growth magnitudes, computational exponential heating of ions can dominate.

Recent work suggests that with proper implementation of high order shape functions, numerical self-heating will not occur even for $\Delta x \not\lesssim \lambda_{De}$ [152] (see also §3.1 for a discussion). It should be noted that the Larmor radii of each species including electrons should also be resolved, otherwise a similar linear numerical self-heating of the particle can occur [153] - see for example Ref. [137] for PIC simulations with fully-resolved ion and electron gyro-motion.

Temporal resolution

The Courant-Friedrich-Lewey (CFL) condition describes a minimal time-step necessary to allow for relativistic capabilities and resolution within a finite difference PIC scheme. In one-dimensional EPOCH, the minimal simulation time-step is defined as $\Delta t = \Delta t_{mult} \frac{\Delta x}{c}$ where the time-step multiplier defaults to 0.95, unless otherwise specified. Generally, in three dimensions, the CFL condition is given as,

$$\Delta t < \frac{(\Delta x^2 + \Delta y^2 + \Delta z^2)^{1/2}}{c}, \quad (2.10)$$

where the maximal time-step is given as the total displacement Δs , being the Pythagorean sum of each cell spacing in Cartesian coordinates, divided by the speed of light c .

For EPOCH simulations whose time-steps are larger than the CFL condition, especially those of the DT- α plasmas presented later in this thesis, EPOCH defaults to the CFL time-step with the default multiplier. However, time-steps at which data is dumped to file are held consistent, allowing for multiple hundreds of CFL compliant time-steps before one output file is produced. EPOCH continues to push particles and update fields within these default CFL time-steps allowing for accurate evolution of the particle velocities and fields, but with a reduced computational stored memory to account for computational limits. With this capability, one can average quantities across many CFL time-steps to reduce computational noise, for example, from large current jumps between steps, or to measure non-relativistic processes, with less computational storage, whilst maintaining all of the relevant physics. It is the responsibility of the user,

therefore, to make sure this condition is maintained in their simulations whilst also resolving other resonant behaviour.

2.2 Benchmarking simulations

To assess the quality of output from EPOCH, we run a series of 1D3V tests for plasmas whose phenomenology is well understood. We present results from two well studied scenarios, the two electron stream and a cold plasma, also typically referred to later as a “background” plasma when discussing simulations of the MCI.

2.2.1 Two-stream instability

A plasma consisting of two oppositely travelling beams of charged particles is considered to be a two-stream. Multiple streams can exist within real plasmas, and so the study of the transference of the free energy of the beam(s) becomes important. We do this through the calculation of the stability of the beam species, in a manner similar to that of finding wave solutions in the cold plasma dielectric tensor.

Theory of the two-stream instability

The growth rate of the two-stream instability is exponential. This is, empirically, a result of density perturbations brought on by one beam which are reinforced by the bunching of particles in the other, i.e. $\Delta n \propto n$. One can define a beams’ velocity distribution as a Dirac-delta function centred on its mean velocity, $f(\mathbf{v}_\sigma) = \delta(\mathbf{v} - \mathbf{u}_{\sigma 0})$ where $\mathbf{u}_{\sigma 0}$ is the birth velocity of a beam of species σ . For multiple N beams of equal magnitude, the kinetic description of the dielectric tensor is the summation over species of the integrals of the distribution functions over velocity space §1.2.5. Using the distribution of both beams and following Refs. [41] and [154], the dielectric tensor is written as

$$\epsilon(\mathbf{k}, \omega) = 1 - \sum_{\sigma} \frac{\omega_{p\sigma}^2}{(\omega - \mathbf{k} \cdot \mathbf{u}_{\sigma})^2}. \quad (2.11)$$

If the beams are the same species, equally populated, but travel in opposite directions, then $\omega_{p\sigma} \equiv \omega_{pe}$ and $\mathbf{u}_1 = -\mathbf{u}_2 = \mathbf{u}_0$. Solutions to the dielectric tensor are found when $\epsilon(\mathbf{k}, \omega) = 0$, therefore, we rearrange to find

$$\omega^4 + 2k^2 u_0^2 \omega^2 - 4k^2 u_0^2 \omega^2 + k^4 u_0^4 - 2\omega_p^2 [\omega^2 + k^2 u_0^2] = 0, \quad (2.12)$$

whose solutions are quartic in frequency ω ,

$$\omega = \pm \left(k^2 u_0^2 + \omega_p^2 \pm \omega_p [4k^2 u_0^2 + \omega_p^2]^{1/2} \right)^{1/2}. \quad (2.13)$$

There are four boundaries for imaginary solutions to Eq. (2.13) which will give the growth rate of a two-stream instability. However, the maximum growth rate of the instability is found when

$$\Im[\omega]_{max} \equiv \gamma_{max} = \omega_{pe}/2, \quad (2.14)$$

at a wavenumber of

$$\mathbf{k} \cdot \mathbf{u}_{0x}/\omega_{pe} = \frac{\sqrt{3}}{2}. \quad (2.15)$$

Simulating the two-stream instability

Here we present a simulation of the two-stream instability carried out in EPOCH for a plasma consisting of three species, two electron beam species with equal and opposite velocities with a magnitude $|u_{0x}|$, and a stationary proton species to maintain quasi-neutrality. Number densities of the electrons (e) and proton ions (i) are both $n_{i,e} = 10\text{m}^{-3}$ and the temperature is kept cold at $T_{i,e} = 273\text{K}$ to limit thermal noise. The simulation ran for six electron plasma periods, $6\tau_{pe} = 6 \cdot (2\pi/\omega_{pe})$, in order to resolve the frequencies of the instability and ignore ion cyclotron motion effects. The domain length was $L = 5 \times 10^5\text{m}$, with a grid spacing $\Delta x = 1250\text{m}$, equivalent to $\lesssim 3.5\lambda_{De}$, and is sufficient in resolving the strongest growing wavenumber, Eq. (2.15). In this scenario, the grid spacing is permitted to be larger than the Debye length as the two-stream instability grows quickly and thermal fluctuations are minimal.

Snapshots of the evolution of the phase space of both electron beams are presented in Fig. 2.3. Here, both beams are coloured according to their initial velocity distribution. After some time in the range $2 < t/\tau_{pe} < 4$, the instability grows and dominates over their initial drifting motion, resulting in a mixing of both beams and the swirling around well defined potential wells, i.e. the bunching and dispersion of electrons.

Figure 2.4 presents the energy distributions of both electron beams through time normalised to the electron plasma period. Here, birth velocities are $u_{0x} \simeq \pm 42v_{th}$ where v_{th} is the thermal velocity, given by $v_{th,e} = \sqrt{k_B T_e / m_e}$. In Fig. 2.4, at a given time, the distribution of energy is normalised such that $\int_0^{E_{max}} H_E(t)dE = 1$, where $H_E(t)$ is the histogram of energy distribution at a time t . These “flutes” of energy distribution evolve linearly for times less than

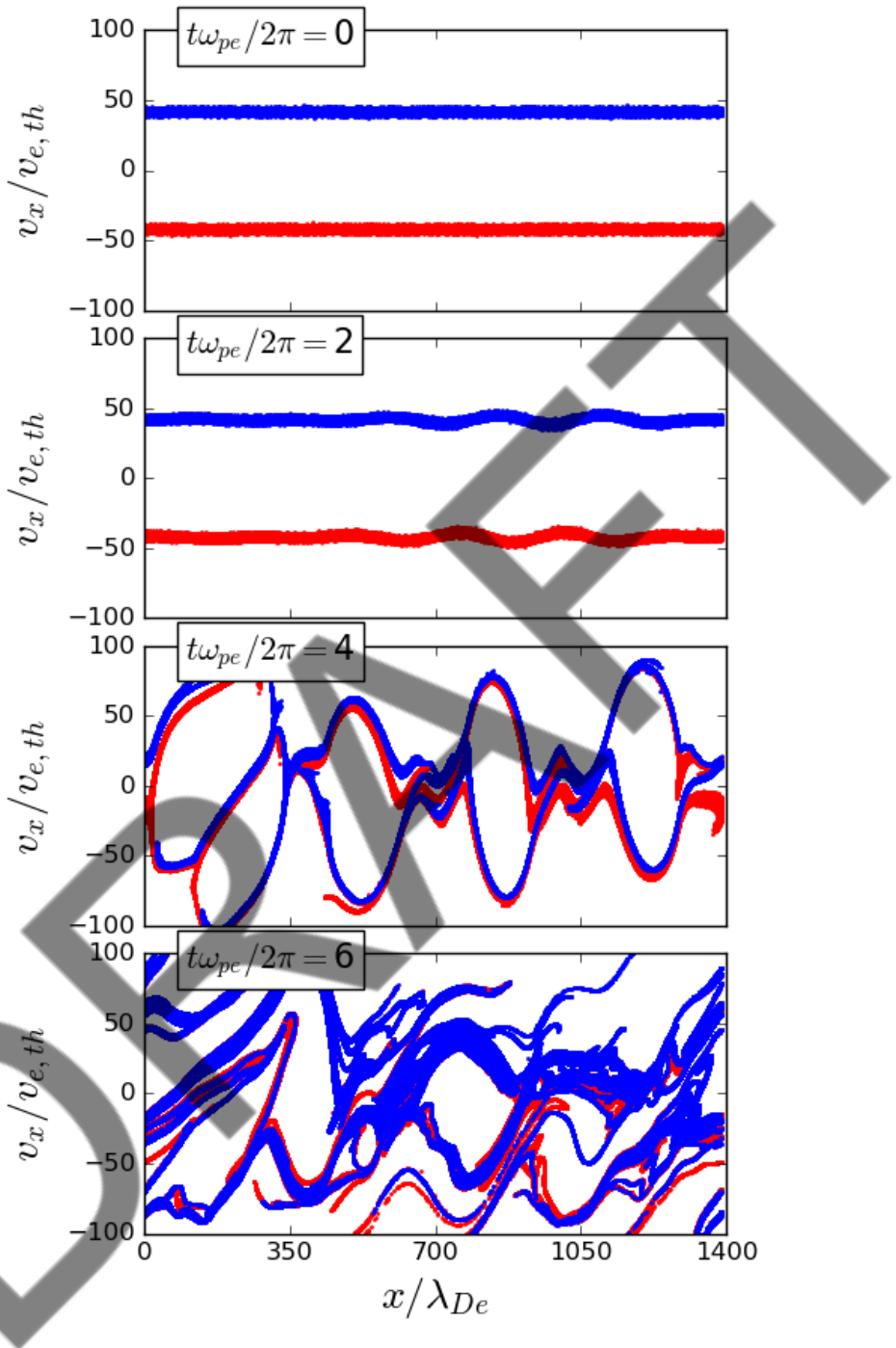


Figure 2.3: Phase space diagrams of the two-stream instability through time, with two species of equal and oppositely travelling electrons coloured in red and blue for their initial velocity. Here the initially stationary background population of protons are not shown. Potential wells develop between $2 < t\omega_{pe}/2\pi < 4$, where ω_{pe} is the electron plasma frequency.

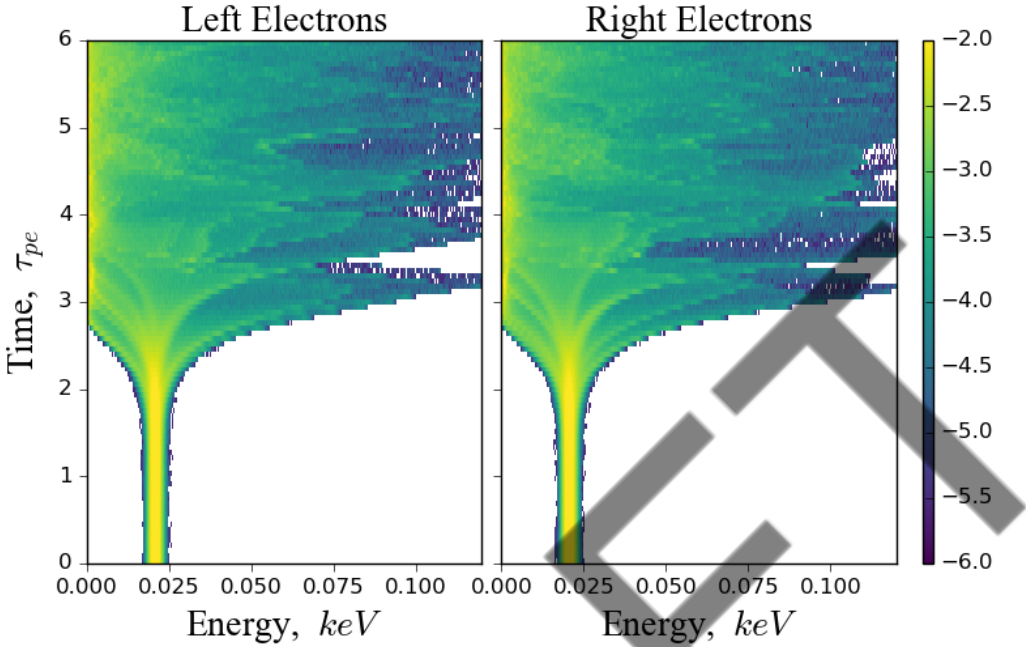


Figure 2.4: Histogram of energy for the left and right electrons through time, normalised to the electron plasma period τ_{pe} . The histogram is normalised such that at a given time trace the integral of the histogram over energy equals unity. Shading is the log base 10 of the histogram distribution of energy for each species.

$2\tau_{pe}$, during which time the two-stream instability develops, until the potential wells, as observed in Fig. 2.3, accelerate and decelerate electrons. This is seen in the blooming of their energy distributions, with a majority of the electrons decelerating to become almost stationary, and a small proportion accelerating to the maximum velocity of their potential wells. The swirling potential wells accelerate electrons periodically, over approximately an electron plasma period, and maintain the plasma's electrical potential wells for the remainder of the simulation duration.

Assuming the charge density perturbation, and hence dominant instability mechanism, is characterised by the electrostatic E_x field, then the two-stream growth rate can be measured through the change in the mean absolute electric field. This is plotted in Fig. 2.5, where the maximum growth rate γ_{max} , Eq. (2.14), is overlaid as a dashed red line, with an enlarged portion of the instability's growth at early times is inlaid. Figure 2.5 shows that the instability growth rate agrees with the theoretical descriptions of the plasma instability, and as such our EPOCH simulation accurately predicts the physical phenomenology of these two oppositely travelling electron beams.

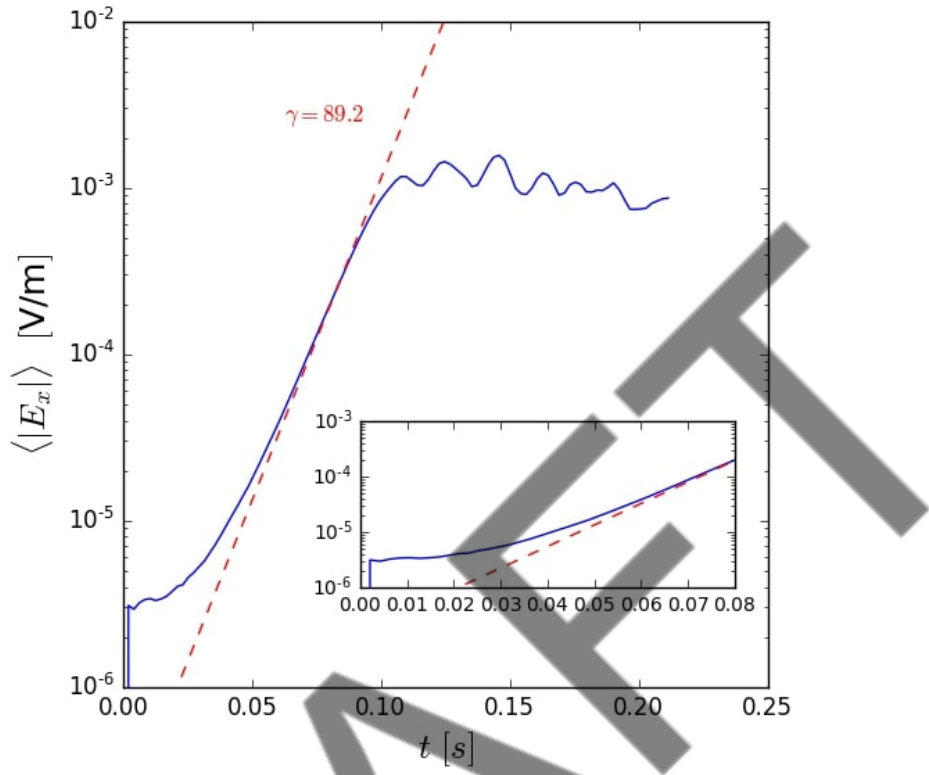


Figure 2.5: The evolution of the mean of the absolute of the E_x electric field component within a simulation of the two-stream instability for two equal and oppositely travelling electron species. Dashed red line indicates the strongest growth rate predicted from theory as per Eq. (2.14) and inset shows tendency of the growth of the field energy to the theoretical maxima at early times.

Fourier transforms of the spatial (1D) electric and spatiotemporal (2D) magnetic fields are presented in the left and right hand panels of Fig. 2.6. In the spatial Fourier transform (left) the strongest growing wavenumber, Eq. (2.15), is plotted as a vertical dashed line, showing strong agreement with the 1D FFT heatmap which grows quickly and whose stronger intensity is sustained throughout. In the spatiotemporal Fourier transform (right) the lower resolution in time leads to a leakage of power at a given frequency, however one can still determine that the strongest growing wave is one with a group velocity equal to that of the particle's initial velocity, $\pm u_{0x}$, in positive and negative wavenumbers as shown by diagonal dashed black lines.

This shows that EPOCH has captured the development of the two-stream instability in frequency and wavenumber space on electron time scales. It can also offer compelling insights through fully tractable phase space representa-

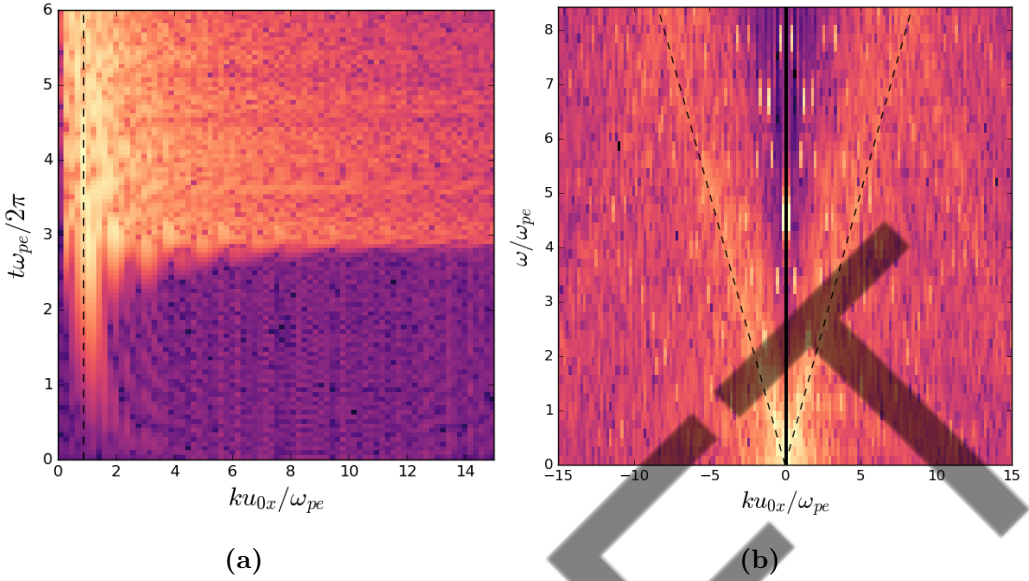


Figure 2.6: *Left:* spatial (1D) Fourier transformation of the E_x electric field component. *Right:* spatiotemporal (2D) Fourier transform of the B_z magnetic field component. In each panel: time, wavenumber and frequency are normalised by the electron plasma frequency ω_{pe} (see §1.2.4) and the mean velocity of the beams u_{0x} . Also, presented as a dashed black line are (left panel) the strongest growing wavenumber $ku_{0x}/\omega_{pe} = \sqrt{3}/2$ and (right panel) the beam's velocities $\omega = ku_{0x}$.

tions. Through EPOCH’s ability to individually track particles, this has further potential to deliver unique insights into individual particle behaviour.

2.2.2 Cold plasma

The theses of Refs. [155] and [118] presented benchmarking simulations for a two-stream instability and cold background plasma. As we have already demonstrated EPOCH’s capability in the former, we present here the latter, a simulation of a singular ion cold plasma (neutralised by an equally numerous electron species) for both a purely perpendicular and parallel magnetic field direction with respect to our spatial dimension.

These simulations were carried out using plasma parameters reminiscent of the edge region of JET. These include: a grid length $L = 2\text{m}$; magnetic field strength $B = 2\text{T}$; cell width $\Delta x = 0.7\lambda_{De}$ where λ_{De} is the Debye length of the electrons, Eq. (1.9); an electron density $n_e = 10^{19}\text{m}^{-3}$; and ion and electron temperatures $T_D = T_e = 1\text{ keV}$. Because of these high spatial resolutions, wavenumbers as small as $\Delta k \geq 0.32 [\Omega_D/v_A]$, and frequencies of $\Delta\omega \geq 0.5 [\Omega_D]$

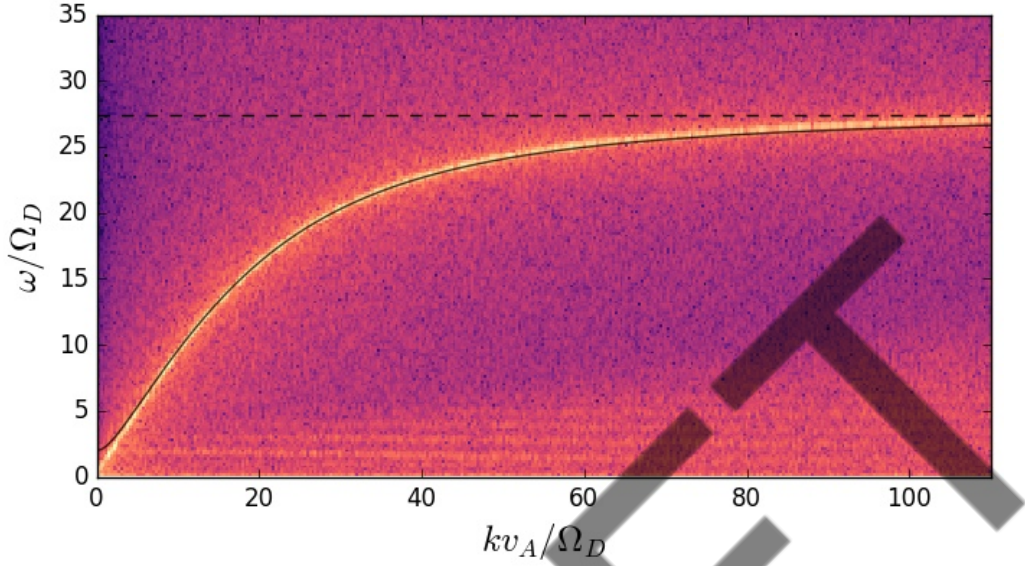


Figure 2.7: Spatiotemporal Fourier transforms of a $D - e$ cold plasma with a purely perpendicular background magnetic field. The FAW dispersion relation Eq. (1.37) and LH frequency Eq. (1.11) are shown as curved black and horizontal dashed-black lines respectively. Deuteron harmonics are seen at integer multiples for frequencies $< 10\Omega_D$ over a range of wavenumbers.

were resolved.

The spatiotemporal FFT of a purely perpendicular cold background plasma is shown in Fig. 2.7. Here we see the dispersion relation, Eq. (1.37), for $\theta = \pi/2$ plotted over-top in a solid black line, and the lower hybrid frequency, Eq. (1.11), as a horizontal dashed black line. Ion harmonics are observed at low frequencies $< 10\Omega_D$ for a large range of wavenumbers $0 < kv_A/\Omega_D < 100$. The spatiotemporal FFT for the same plasma with the same frequency-wavenumber resolution limits as in Fig. 2.7, but with a purely parallel background magnetic field ($\theta = 0$) is shown in Fig. 2.8. Once again, EPOCH is able to correctly predict the dominant modes, on this scale, of the parallel FAW as predicted by theory (solid black line).

Whilst Fig. 2.7 resolved integer multiples of the deuteron cyclotron frequency harmonics, we see in Fig. 2.8 the consequence of resolution limits at lower scales. If a wave were to exist below these resolution limits, our Δk and $\Delta\omega$ would effectively skip over it, resulting in a bleeding of power to its adjacent frequencies and wavenumbers.

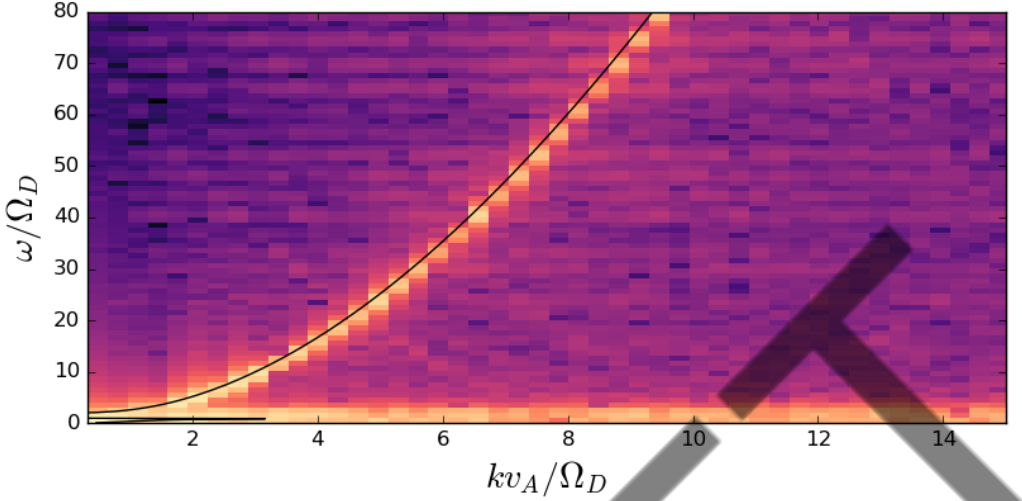


Figure 2.8: The same as Fig. 2.7, but for a purely parallel background magnetic field.

2.3 Analytically solving the linearised Maxwell-Vlasov equation

Following the work presented by Ref. [37], we find solutions to the linearised Maxwell-Vlasov equations using the similarly named Julia code [40] to perform the integrations over velocity space of Eq. (1.32) spanning various values of (k_\perp, k_\parallel) . One can summate the hot dielectric tensor over an arbitrary number of ions, easily capturing the additional contributions to the linear growth rate of the MCI. Energetic species are distributed as a drifting ring-beam, Eqs. (2.16) to (2.18), which is separable in its parallel $f_{\alpha,\parallel}(v_\parallel)$ and perpendicular $f_{\alpha,\perp}(v_\perp)$ velocity distribution components

$$f_\alpha(v_\parallel, v_\perp) = f_{\alpha,\parallel}(v_\parallel) f_{\alpha,\perp}(v_\perp), \quad (2.16)$$

where

$$f_{\alpha,\parallel}(v_\parallel) = \frac{\exp\left(-\frac{(v_\parallel - u_\parallel)^2}{v_{\parallel,th}^2}\right)}{v_{\parallel,th}\sqrt{\pi}}, \quad (2.17)$$

and

$$f_{\alpha,\perp}(v_\perp) = \frac{\frac{1}{2\pi} \exp\left(-\frac{(v_\perp - u_\perp)^2}{v_{\perp,th}^2}\right)}{\left(\frac{\sqrt{\pi}}{2} v_{\perp,th} u_\perp (1 - \text{erf}(-\frac{u_\perp}{v_{\perp,th}})) + \exp\left(-\frac{u_\perp^2}{v_{\perp,th}^2}\right) \frac{v_{\perp,th}^2}{2}\right)}. \quad (2.18)$$

The Bessel functions within Eq. (1.33) are summed over a sufficiently extensive complex wavenumber space for indices, n , which are incremented outwards from zero in both positive and negative directions until the change in the sum is less than a tolerance level of 10^{-8} . Roots are found using a combination of the Nelder-Mead optimisation [156] and the winding number method. At each node of the Nelder-Mead simplex (in this case, a triangle) the complex solution of $\underline{\epsilon}(\mathbf{k}, \omega) = 0$, written in the form $z_v = a + ib$, are calculated along with its corresponding complex frequency $z_\omega = \omega + i\gamma$, whose growth rates and real solution are deposited on the grid in (k_\perp, k_\parallel) space. Roots are centred on the complex frequency plane when the complex dielectric tensor values of a and b are both zero. If the simplex does not contain a root, then the simplex nodes are walked across the grid according to a Nelder-Mead search [156]. The solver determines if the simplex encapsulates a root when both the values of a and b change sign, equivalent to the winding number method. In this case, the simplex bifurcates and the winding numbers at each node are recalculated for each child simplex, halving each time until the real frequency extent of the simplex is less than $10^{-4}\Omega_i$, where Ω_i is the cyclotron frequency of the alpha (and deuteron) particles. The complex frequency solutions are then considered found and written to disk for our wavenumber coordinates.

A schematic of the bifurcation process is shown in Fig. 2.9, where the Nelder-Mead simplex has walked across the complex solution plane until encapsulating a solution, whereby it bifurcates. One can, in practice, draw any regular polygon to find the frequency roots, with increased computational cost. It would be possible to increase the root finding speed by dividing the parent simplex further. One could split the triangle into three, called trifurcation, or utilise a rectangle, called quadrification.

Solutions to the perpendicular velocity component integrals of the alpha-particles in Eq. (1.24), are calculated numerically using Gauss-Kronrod quadrature [157] and it's similarly named Julia library GaussGK.jl [158]. An absolute and relative tolerance of 0 and 10^{-8} , respectively, are used to confirm the convergence of integral values, as stated above. For all species, the integrals over parallel velocity components are calculated via the plasma dispersion function [32], and as discussed in the Appendix of Ref. [37].

Frequencies are initially calculated for a cold plasma at each (k_\perp, k_\parallel) position using the high frequency expression of the FAW dispersion relation, given by Eqs. (25) and (11) in Refs. [39] and [97] respectively,

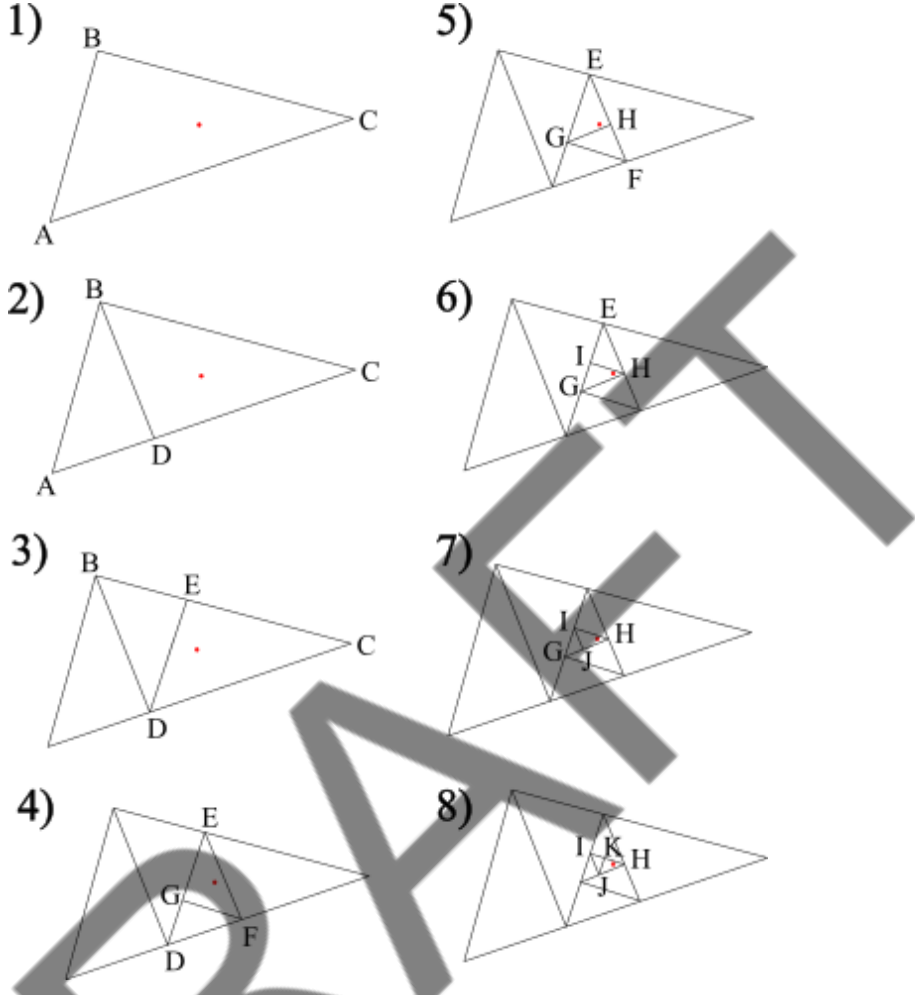


Figure 2.9: Schematic of the bifurcation process through iterative winding number calculation of a Nelder-Mead simplex. Here, the unknown solution (red dot) is known to exist within the simplex because both of the real and imaginary components of Eq. (1.24) cross over their axes and hence contain the origin. Iterative simplexes are constructed from the bifurcation of the previous simplex. In this example, the original $\angle ABC$ simplex (1) is bifurcated into (2) the $\angle ABD$ and $\angle DBC$ simplexes. The winding number is calculated again, revealing that the root lies within the $\angle DBC$ simplex. The bifurcation process is then repeated until finally the extent of the simplex contains the root to within $10^{-4}\Omega_i$. This process is considerably faster than just the traditional Nelder-Mead optimisation.

$$\omega^2 = \frac{v_A^2}{2} \left[k^2 + k_{\parallel}^2 + k^2 k_{\parallel}^2 \frac{v_A^2}{\Omega_i^2} + \sqrt{\left(k^2 + k_{\parallel}^2 + k^2 k_{\parallel}^2 \frac{v_A^2}{\Omega_i^2} \right)^2 - 4k^2 k_{\parallel}^2} \right]. \quad (2.19)$$

Here, Ω_i is the energetic minority particle cyclotron frequency, $\Omega_i \equiv \Omega_\alpha$, v_A is the local Alfvén speed and $k^2 = k_{\parallel}^2 + k_{\perp}^2$. These serve as initial guesses for the root finding algorithm, which then returns real and imaginary frequency components as discussed. The results of this are presented in Fig. 5 of Ref. [37], which shows a close agreement, at low wavenumbers, between the FAW dispersion, Eq. (2.19), and the real frequencies extracted by the LMV code. For $k_{\parallel} = 0$, this reduces to the perpendicular Alfvén dispersion relation $\omega = kv_A$. This frequency definition is an extension of the Appleton-Hartree definition at low frequencies [32], which calculates the refractive index of the plasma, kc/ω , as a function of frequency, as opposed to Eq. (2.19) which returns frequency as a function of wavenumber. For Maxwellian thermal plasmas under the influence of a background magnetic field, its solution is given as a quartic $\pm\sqrt{(B \pm F)/2A}$, as previously defined as Eq. (1.36) in §1.2.6.

An example of output from the LMV code is shown in Fig. 2.10. This presents growth rates of the linear MCI calculated by the LMV code across $(k_{\perp}, k_{\parallel})$ space for a pure 1 keV thermal deuterium plasma normalised by the alpha-particle cyclotron frequency $\Omega_i \equiv \Omega_\alpha$. This corresponds to Fig. 4 from Ref. [37], which was also obtained for a pure deuterium bulk plasma under

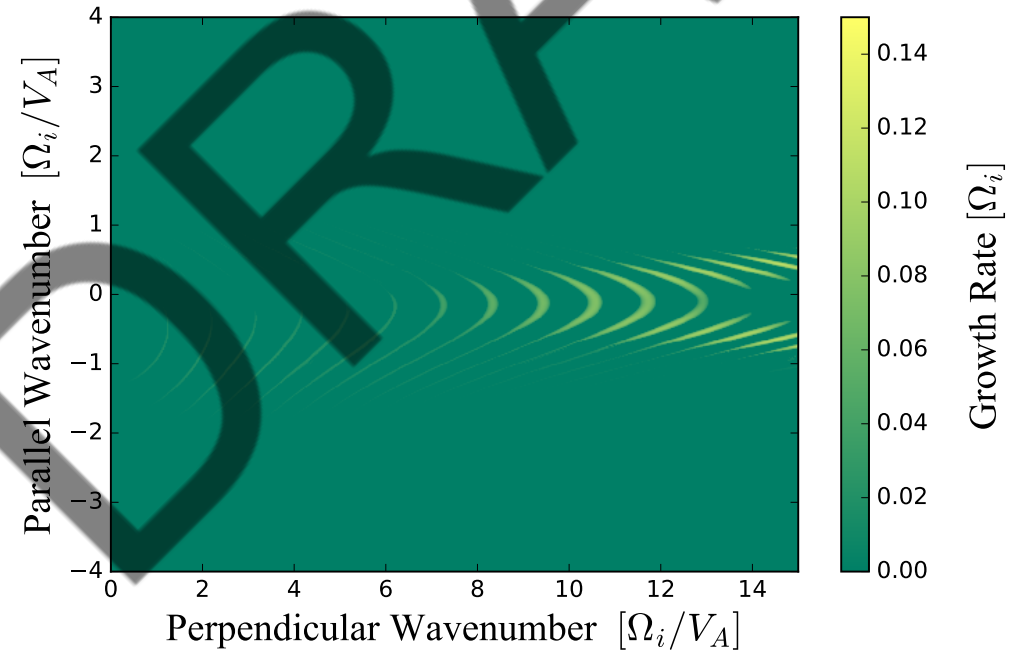


Figure 2.10: Linear MCI growth rates (colour scale right, normalised to Ω_i) for a pure deuterium plasma plotted across the full two-dimensional $(k_{\perp}, k_{\parallel})$ domain, normalised to Ω_i/V_A , calculated by the LMV code.

JET plasma 26148 conditions. Here, the magnetic field had a strength of 2.07 T, the electrons have a number density $n_e = 1.7 \times 10^{19} \text{ m}^{-3}$, and a minority 3.5 MeV alpha-particle population, at a concentration of $\xi_\alpha = 1.5 \times 10^{-4}$, is initialised as a drifting ring-beam with thermal velocity spreads of $u_{\parallel,th} = 0.01u$ and $u_{\perp,th} = 0.01u$. This figure shows that growth rates of the MCI, γ_{MCI} , can be numerically extracted for arbitrary magnetic field angles, θ , and demonstrates the capability of the LMV code in quickly capturing linear MCI theory and revealing additional behaviour.

The LMV code is optimised for the current generation of commodity computational hardware, and takes only a few minutes on a desktop, or laptop, to scan a 512×512 wavenumber grid (as in Fig. 2.10). It is parallelised and works well for plasma parameters similar to those of the JET plasma 26148, with varying degrees of tolerance on the initial electron density and magnetic field strength. Whilst it is able to extract growth rates for a relativistic minority species, the computational cost greatly increases. For further results of a DT plasma similar to that of the JET 26148 experiment see Chapter 6, where we introduce tritium at non-zero concentrations.

2.4 Methods of analysis

In this section, we'll address some of the principal data analysis methods employed in the field of fusion plasma research, most notably in EPOCH PIC simulations, for the generation of and comparison between power spectra. This will also include the measuring of normalised coherence between two wave-packets in frequency-wavenumber space.

2.4.1 Power spectra

The traditional measurement of power spectra involves the receiving of plasma oscillation signals from probes positioned at the tokamak's walls. Early measurements of ICE involved the use of probes initially designed for ICRH, set to receive. Measurements like this remain a diagnostic for tokamak devices around the world and, typically, result in what we will refer to here as “lab-frame” power spectra. That is, frequencies of emission of the plasma and its constituent ions with respect to the stationary probe attached to the tokamak wall. Later, in Chapter 6 and Appendix D, we consider other frames of reference for calculating power spectra.

In simulations, we produce spatiotemporal (2D) Fourier transforms of the

entire domain over time and space. Examples of these have been seen earlier in §2.2.2. Power spectra are then obtained by summing squared FFT magnitudes across horizontal frequency bands over wavenumber space. This forms a power spectra representation that resembles that of the stationary probe (antenna) of the plasma’s magnetic (electric) oscillations in 1D frequency space. Therefore, the power P as a function of frequency ω , is the summation over wavenumbers of the square of the power of the Fourier transformation of the field component \hat{F} ,

$$P(\omega) = \sum_{k=0} \hat{F}^2(k, \omega). \quad (2.20)$$

Normalisation is carried out by dividing each power $P(\omega)$ by the simulation’s frequency and wavenumber resolutions, $\Delta\omega$ and Δk , to return the average power per frequency step, also called the power spectral density (PSD). This is beneficial as it allows for the drawing of comparisons between spectra, simulated or observed, with differing resolutions.

2.4.2 Methods of comparing power spectra

We detail here two methods to compare power spectra which could represent two or more simulations, experimental results or a combination thereof. Another method, discussed in Appendix B, includes the two-dimensional minimisation method of τ^2 . This was employed in Ref. [110], and its results are presented in Chapter 5.

Phase correlation

Typically used in image correlation and correction [159–161], the phase correlation method has found wide application in medical image processing [160], financial time series [162], stereo disparity estimation [161, 163] and motion of optical flows [164, 165] alongside others (see Refs. [160] and [161]). Phase correlation has applications to the analysis of ICE power spectra from PIC simulations through the comparison to either (1) power spectra resulting from our plasma simulations or (2) power spectra sourced through experiments. Assuming that two 1D data sets are purely just translations of one another, we can write each as $f_1(t)$ and $f_2(t) = f_1(t - t_0)$. The Fourier transform of such functions gives

$$\hat{f}_2(\omega) = \hat{f}_1(\omega) \exp(-i\omega t_0), \quad (2.21)$$

which gives the normalised cross power spectrum as

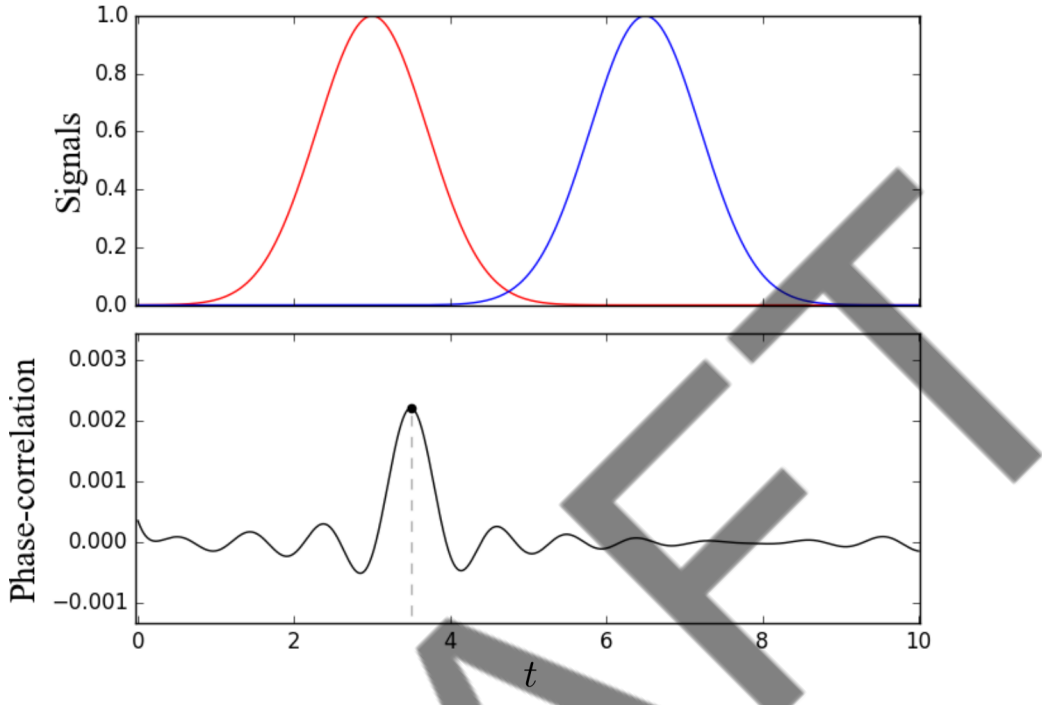


Figure 2.11: Simple example of the phase correlation method (*bottom*) extracting the shift between two Gaussians (*top*) centred on $t_1 = 3.0$ and $t_2 = 6.5$ for the red and blue curves respectively. The translation between signals, $|t_2 - t_1| = 3.5$, is calculated from the phase correlation maxima.

$$\frac{\hat{f}_2(\omega)\hat{f}_1(\omega)^*}{|\hat{f}_1(\omega)\hat{f}_1(\omega)^*|} = \exp(-i\omega t_0), \quad (2.22)$$

where $*$ represents the complex conjugate of the Fourier transformed function $f(\omega)$, and ω is the frequency domain of the variable t . Taking the inverse Fourier transform of Eq. (2.22) yields a Dirac delta centred on the separation between both signals; $\delta(t - t_0)$.

As an example, take two Gaussian pulses in space, $f_1(t) = \exp(-(t - t_1)^2)$; and $f_2(t) = \exp(-(t - t_2)^2)$ such as those in Fig. 2.11. The separation between the two signals, $|t_2 - t_1| = 3.5$, is easily found using phase correlation. Since the accuracy of the phase correlation method hinges on the initial assumption that both signals are simply a shift, or a rotation in 2D space, of one another, divergences from this assumption, e.g. by introducing a level of inconsistent noise between the two signals, results in a sharp decline in the accuracy of the phase correlation method. The introduction of random noise at a level of even

one-tenth the amplitude of the signal proves problematic, and it is therefore best used sparingly in this regard, as power spectral output from PIC simulations and experimental observations are, inherently, noisy (see Fig. A.3 for a comparison between the phase correlation method and shared area §2.4.2 for 2D signals following the introduction of noise).

In Chapter 5 we utilise the phase correlation method in 1D to compare multiple power spectra outputs from PIC simulations to experimental data. It's use is justified here as the shifts and scaling is minimal between power spectra since features are dominated by the most active MCI region.

Shared area

Novel to this thesis is an analytical method of deriving frequency offsets from power spectra called shared area. We briefly detail here its calculation and provide an example, but refer to Appendix A for more details, including comparisons to the cross-correlation algorithm and its use for data in higher dimensionalities. To calculate the shared area, one slides a signal over another and calculates the area of the lowest bounding curve across the whole domain, repeating for multiple signal offsets until one builds a picture of shared area through offset space. This is written as

$$SA(\tau) = \int_0^T [B_f(t, \tau)f(t) + B_g(t, \tau)g(t - \tau)] dt . \quad (2.23)$$

which is defined by two boolean arrays B_f and B_g , calculated by the logical comparison returning the lowest bounding curve. More explanation of the boolean arrays is given in Appendix A. As a 1D example, take two Gaussian signals $f(t)$ and $g(t)$, such as those shown in Fig. 2.11, centred on $t = 6$ and $t = 1$ respectively. Figure 2.12 presents (top row) four panels of both Gaussian signals at various sliding offsets τ of the (blue) signal $g(t - \tau)$, and the stationary (black) signal $f(t)$. The bottom panel is the resulting shared area calculated between both signals as a function of offset, maximised for $\tau = 5$, as per the original signals Gaussian centres.

A summary of findings from Appendix A is that the shared area method is excellent at resolving the offset between two noisy data sets, even for noise amplitudes well above the signal amplitude. Considering that applications of the shared area method throughout this thesis do not benefit from the large scale mean estimation of offset, and that the noise floor is an order of magnitude or greater below the ICE signals (as they are suprathermal), this method is more than suitable in determining the offset between power spectral curves,

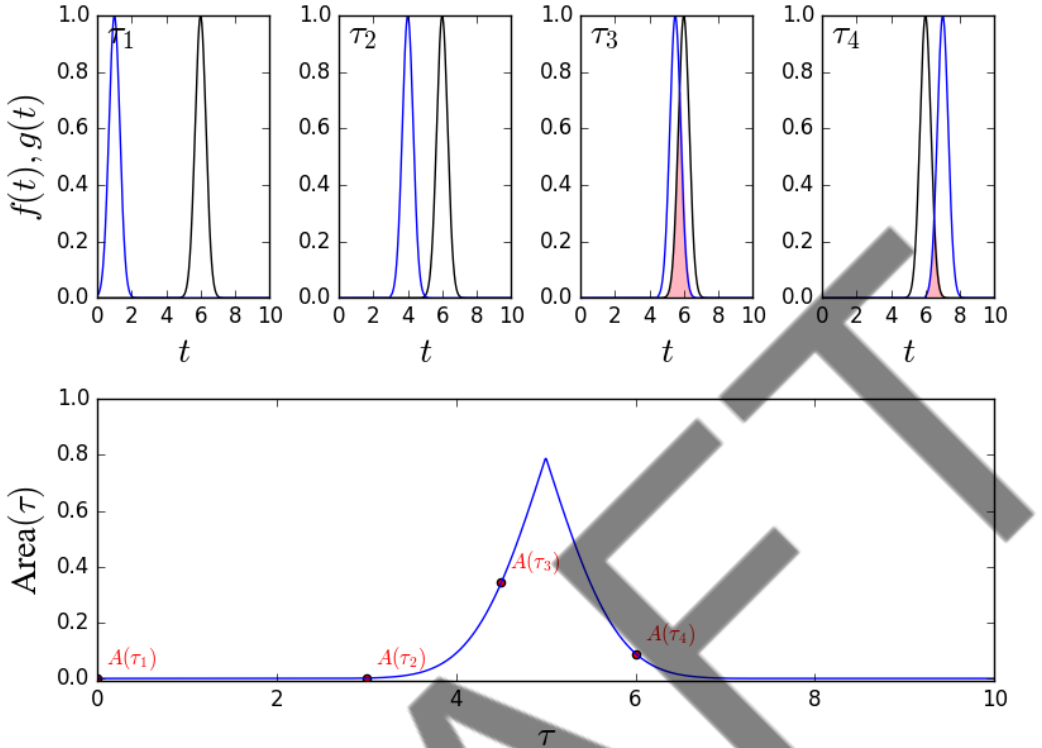


Figure 2.12: *Top row:* two Gaussians, $f(t)$ and $g(t)$, which are centred on $t = 6$ and $t = 1$ respectively. The sliding of $g(t)$ over $f(t)$ is periodic between $\pm T$, where $T = 10$ and is the x -axis limit. *Bottom row:* shared area (shown as top row pink area) as a function of x -axis offset of $g(t - \tau)$. Each area $A(\tau_i)$ of the top row offsets, τ_i , are shown as scatter points along the blue shared area curve.

and complements the phase correlation and cross-correlation methods. Future application of the shared area method in data analysis or signal processing for a variety of signals are likely to be numerous, as considered in Appendix A.

2.4.3 Bicoherence and bispectral analysis

To identify nonlinear phase coupling within plasmas, we utilise the bispectral analysis technique. First introduced in Ref. [166], it presented a novel high order diagnostic tool with which to measure the strength of coupling/interaction between waves. As ICE signals are understood to be a result of the coupling between the alpha-particle and FAW dispersion, the bispectral analysis technique is well suited to our study. It has been previously implemented, generally, in plasma scenarios [167–170] as well as specifically in ICE research [101, 113, 114, 137, 171] providing useful insights into characteristics of ICE at the saturated

and unsaturated regimes of the MCI.

The bispectrum describes the extent of phase coherence between two waves (labelled 1 and 2) that produce a third (3). The original bispectrum/bicoherence theory considers only one dimensional time-dependent signals. For nonlinear interaction in wavenumber-frequency space (k, ω) , this is satisfied for the matching conditions

$$\mathbf{k}_3 = \mathbf{k}_1 + \mathbf{k}_2 .$$

$$\omega_3 = \omega_1 + \omega_2 .$$

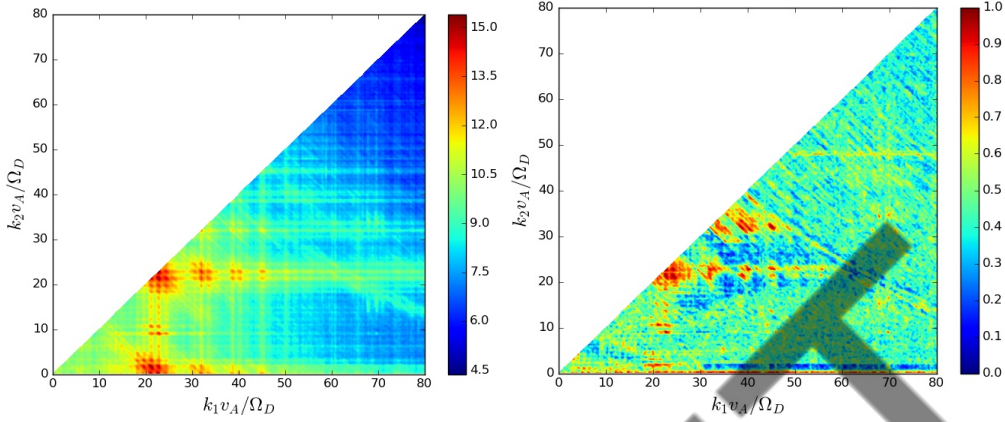
Considering that the resonance between our fast-particles and the FAW occurs for low frequencies where $\omega \simeq kv_A$, where frequency and wavenumber map to one another through the Appleton-Hartree dispersion relation for cold plasmas, Eq. (1.37), we can reduce our free parameters to just two wavenumber (frequency) components for one frequency (wavenumber) axis [171]. Assuming that the field quantity we are observing is real, stationary and has zero mean (e.g. change in magnetic field) the bispectrum can be written as

$$b_s^2(\omega_1, \omega_2) = \left\langle \hat{F}(\omega_1) \hat{F}(\omega_2) \hat{F}^*(\omega_1 + \omega_2) \right\rangle , \quad (2.24)$$

where brackets $\langle \cdot \rangle$ denote averaging over time and the Fourier transform of our field quantity is written as \hat{F} and its complex conjugate \hat{F}^* . The results of the bispectrum give a measure of the flow of energy exchange between wave packets of two different frequencies and wavenumbers. This, however, doesn't account for wave amplitudes which are small but demonstrate high levels of phase coherence and, as such, will have negligible influence on the observed spectra. Therefore, it is important to normalise our bispectrum. To do this, we introduce the bicoherence,

$$b_c^2(\omega_1, \omega_2) = \frac{b_s^2(\omega_1, \omega_2)}{\left\langle \left| \hat{F}(\omega_1 + \omega_2) \hat{F}(\omega_1) \hat{F}^*(\omega_2) \right|^2 \right\rangle} , \quad (2.25)$$

which is bounded between $0 \leq b_c^2 \leq 1$ [166]. The properly normalised bicoherence measures the extent of coupling between waves taking into account their amplitudes. Therefore, b_c^2 tends to unity for a frequency ω_3 which is strongly driven by the coupling of waves with frequencies $\omega_1 + \omega_2$. Conversely, $b_c^2 \rightarrow 0$ implies that the waves with ω_1 , ω_2 and $\omega_3 = \omega_1 + \omega_2$ are driven independently from one another. Considering the resolution of our simulations is finer in the spatial domain than time, we can easily exchange the frequency descriptions



(a) Bispectrum (b_s^2) on a logarithmic base 10 scale given as the colour bar.

(b) Bicoherence (b_c^2) between 0 and 1 as per the colour bar. Higher bicoherence corresponds to stronger nonlinear coupling between wavenumbers k_1 and k_2 .

Figure 2.13: Bispectrum (left) and bicoherence (right) of a simulation of the JET DT plasma 26148 featuring a concentration of tritons at 1% and a 3.5 MeV drifting ring-beam population of alpha-particles.

above and in Eqs. (2.24) & (2.25) with those for two wavenumbers k_1 and k_2 , as we will do from here on out.

Figure 2.13 presents (*left*) the bispectrum and (*right*) bicoherence for a DT plasma under JET plasma 26148 like conditions (see Chapter 5). In this well-studied plasma, a magnetic field of strength 2.1T was orientated 89° to the simulation domain and a minority 3.5 MeV energetic species of drifting ring-beam alpha-particles was evolved in a 1 keV thermal plasma of deuterons and tritons, at a tritium concentration ξ_T of 1% with respect to the electron number density; $n_e = 10^{19} \text{ m}^{-3}$. These panels reveal that there are three features of clearly defined energy transfer and nonlinear coupling. These are the: (*i*) vertical coupling for constant $k_1 \simeq 22[\Omega_D/v_A]$ between $0 < k_2 < 22[\Omega_D/v_A]$ with specific growth of integer multiples of wavenumbers $k_2 \leq 10[\Omega_D/v_A]$; (*ii*) horizontal coupling for two constant values of $k_2 \simeq 0$ and $22[\Omega_D/v_A]$ for $k_1 \geq 20[\Omega_D/v_A]$; and finally (*iii*) nonlinear secondary coupling branches correlating to the “ghost” features [113] along the FAW at twice the strongest regions at lower wavenumber, most noticeably the horizontal coupling for $k_1[\Omega_D/v_A]$ for a range of k_2 of $30 \leq kv_A/\Omega_D \leq 40$.

2.5 Summary

In this chapter we have discussed the workings of the PIC code EPOCH, including considerations of the particle solver and field updater, shape functions and numerical grid forces which have the potential to perturb results. The importance of resolution in frequency space was considered through calculation of the Nyquist frequency in ω and k . Dependencies of a PIC code on the cell size and time step were also discussed, including the requirement of the CFL condition.

Example simulations to demonstrate a proper working of EPOCH were conducted, starting with the two-stream instability along with its instability growth rate, then a cold plasma for purely perpendicular and parallel magnetic field orientations. The analysis of both cases agreed with theory, and further validate EPOCH's ability to accurately simulate our fusion plasmas.

Finally, we discussed methods of data analysis for correlation and coherence, with specific focus on power spectra and 2D FFTs. Here, we detailed how one calculates the power spectra from 1D PIC simulations, and listed two methods to compare them, with references therein to methods currently employed, including the phase-correlation algorithm. One of the novel methods developed was the calculation of shared area between signals, also discussed further in Appendix A. The final method of analysis presented was the calculation and use-case of the (normalised) bicoherence spectra, which has found application in multiple works investigating the nonlinear coupling of wavenumbers and frequencies associated with the MCI [101, 106, 111, 113, 137] and which will be invaluable in future investigations into its nonlinear regime.

Chapter 3

Parameter scan

This chapter investigates the effect of spatial resolutions on spatiotemporal Fourier transforms, power spectra and change in particle kinetic energies. We carry out multiple PIC simulations in EPOCH for domain lengths, L , of increasing size, and then for grid cell lengths, Δx , which resolve each population's ensemble mean Larmor radii.

3.1 Total length

Presented here are three simulation length scales L for a two ion plasma ($D-\alpha$) which are evolved, along with the EM fields, for a time of 10 deuteron gyro-periods $10\tau_{cD}$ with a time-step of $\tau_{cD}/200$. A background magnetic field of strength 2.1 T is orientated at an angle with respect to the simulation domain (\hat{x}) of 89°. The 3.5 MeV alpha-particles are distributed as Dirac deltas in parallel and perpendicular velocity space with zero thermal spread, see Eq. (1.46), centred on a perpendicular velocity equal to its birth velocity u , purely resulting from its kinetic energy, $u_0 = \sqrt{3.5\text{MeV}/(m_\alpha/2)}$, which in units of the Alfvén speed is $u_0 = 1.27v_A$. The length of each domain normalised by the alpha-particle Larmor radius $r_{L\alpha}$ was increased from five to 30. As the cell length was fixed, $\Delta x = 0.95\lambda_{De}$, the number of grid cells $N_x = L/\Delta x$ covering the simulation domain increased, giving a constant Nyquist wavenumber limit, but an increased wavenumber resolution.

Results of the parameter scan in spatiotemporal Fourier space are presented in Fig. 3.1. In each panel (left-to-right) the wavenumber resolutions, Δk , are 0.4988 [Ω_D/v_A], 0.1662 [Ω_D/v_A] and 0.0831 [Ω_D/v_A] respectively. These are normalised such that, for the FAW dispersion relation at low frequencies $\omega \approx kv_A$, a movement along the wavenumber axis leads to a $\Delta k \cdot v_A/\Omega_D$ movement along the frequency axis. Therefore, to accurately measure the driving of cyclotron

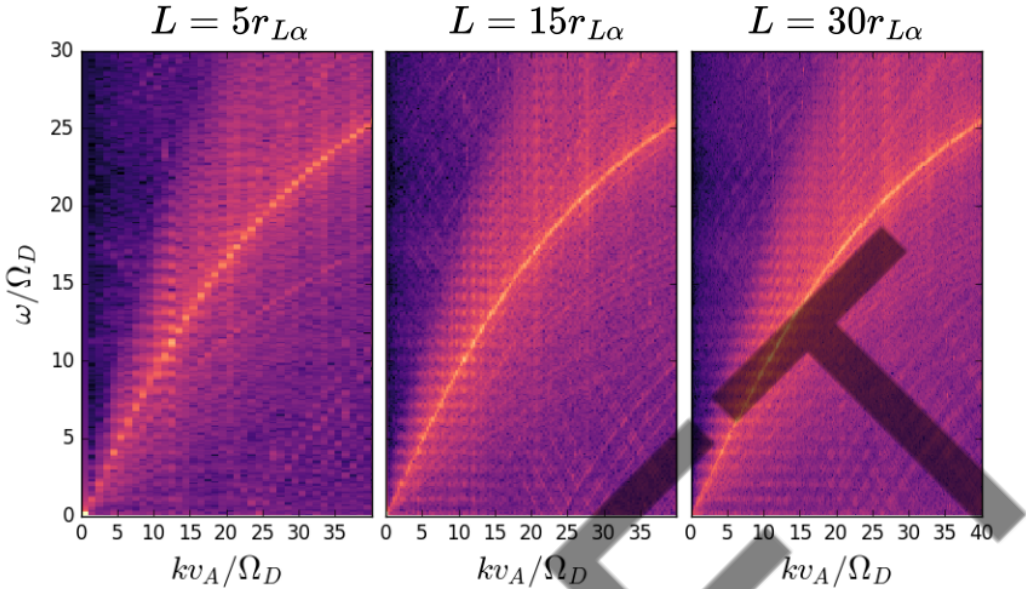


Figure 3.1: Spatiotemporal Fourier power of the oscillatory magnetic field δB_z . Each panel (left-to-right) represents an increase in the simulations total domain length as labelled $5r_{L\alpha}$, $15r_{L\alpha}$ and $30r_{L\alpha}$. Hence, these panels also correspond to an increase in the Δk resolution.

harmonics, the simulation needs to both have a small enough Alfvén speed (i.e. large mass density) and a small wavenumber resolution. If this is not achieved, then each pixel will “skip” over the harmonics and their power will bleed into surrounding wavenumbers. For these simulations $v_A/\Omega_D = 0.1018$, and so the values of Δk are sufficient to resolve ICE harmonics in each case. Visually however, one notices a significant improvement in the resolution as the total FFT becomes less pixelated in both frequency and wavenumber.

The power spectra of each simulation are shown in Fig. 3.2. These are calculated by summatting the squared spatiotemporal Fourier transform magnitude δB_z^2 between $0 < kv_A/\Omega_D < 40$, up to a normalised frequency of $\omega/\Omega_D = 30$. The decrease in the power for frequencies $> 25\Omega_D$ are a result of the dominant FAW dispersion becoming shallower, combined with wavenumber bounds used to calculate the power spectra which do not include the horizontal portion of the FAW dispersion. For each trace, it is revealed that a larger domain length increases the power in spectral features by multiple orders of magnitude. This is an important concept for later discussions, as changes in the spatial and temporal resolutions can lead to features which may be misconstrued as physical behaviour rather than numerical. For this reason, power spectra such as those shown in Fig. 3.2 are normalised by their resolution limits, giving the power

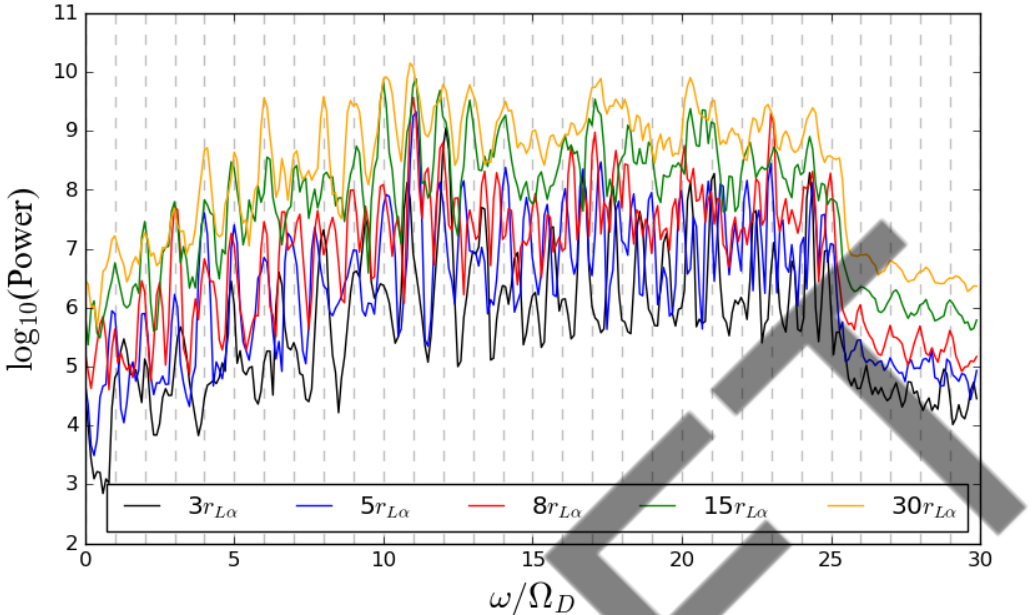


Figure 3.2: Power spectra of the data presented in Fig. 3.1 alongside additional domain lengths of $3r_{L\alpha}$ and $8r_{L\alpha}$. A larger grid size results in a more powerful and better defined spectra due to adequate sampling. Too small of a grid leads to under-sampling and bleeding of power between ICE harmonics.

spectra density (PSD) per frequency space box, i.e. the power that falls in a pixel box of sides Δk and $\Delta \omega$.

One may also draw conclusions from under resolved grids that are non-physical and are instead representative of the large discretisation of frequency-wavenumber space. For example, in Fig. 3.2, high frequency components $15 < \omega/\Omega_D < 25$, of the simulated power spectra for the simulations with the two shortest domain lengths ($3r_{L\alpha}$ and $5r_{L\alpha}$) are much sharper compared to their larger domain length counterparts. As a result of the high level of pixelation in the FFT for small domain lengths, the significance of peaks in the spectrum become dependent on our resolution limits, rather than real excitations or particle resonant phenomenology.

3.2 Cell length

In the PIC regime, cell widths which are greater than the electron Debye length λ_{De} result in exponential numerical self-heating until the Debye length is resolved ($\Delta x < \lambda_{De}$). The extent of this numerical heating can be reduced by using a higher order shape function [118, 152], which comes at an increased

computational cost, and is removed entirely with a sufficiently low grid-spacing along with the resolution of all gyro-orbits.

We discuss here additional conditions on cell length resolutions of each species' ensemble Larmor radii, Eq. (1.6), including the electrons. Since this numerical linear heating is also dependent on the resolution of the electron Larmor radii, it becomes imperative to either (1) mitigate this heating or (2) determine its magnitude, as resolution of the electron Larmor radius would increase already tight computational restraints.

The resolution of a given species Larmor radii can be approximated as some ratio between their maximal ensemble Larmor radii and the electron Debye length. As the electrons have the lowest mass, the lowest spatial resolution needed will be of the electron Larmor radii, $r_{Le} \simeq (2k_B T_e m)^{1/2} / eB_0$. Using Eq. (1.9), we find a ratio between the electron Larmor radii and Debye length as

$$\frac{r_{Le}}{\lambda_{De}} \approx \left(\frac{2m_e n_e}{\epsilon_0 B_0^2} \right)^{1/2}, \quad (3.1)$$

which, substituting the magnetic field strength B_0 and electron number density n_e , returns the maximum multiple of the electron Debye length needed in order for one cell length to resolve both the electron Larmor radii and Debye length. As an example, for a magnetic field of 2.1 T and an electron number density of 10^{19} m^{-3} , the maximum cell length that would completely remove heating from unresolved gyromotion would be $\Delta x = 0.683\lambda_{De}$.

With this concept in mind, we compare three distinct regimes for cell lengths in a simulation of entirely thermal populations of different mass and charge, whose cell lengths are increased, first resolving the electron Larmor radius, then a species of thermal deuterons, and finally a species of thermal alpha-particles. In each simulation, there is no free energy and hence no velocity space instabilities, therefore they draw comparison to those presented in §4.1.2 of similar compositions, including having a total grid length of $L = 30r_{L\alpha}$. Magnetic field strengths for each simulation were 2.1 T at an angle with respect to the simulation domain of 89°. Electron number density was $n_e = 10^{19} \text{ m}^{-3}$ and the temperature of all ions and electrons was initialised at 1 keV. The alpha-particles are a minority (0.1%), to diminish linear heating resulting from NDW conservation, decreasing the computational cost and time taken to run these parameter scans. These are not dissimilar to those presented in Chapter 3 of Ref. [118], which investigated the minimisation of linear heating through the use of higher (≥ 3) order shape functions. Each simulation was run for $10\tau_{cD}$ with a time step of $0.005\tau_{cD}$, well resolving the gyro-periods of the deuterons and alpha-particles, but not the electrons, as that would require 20 times as many time-steps, leading to a simulation

size on par with those which resolve the deuteron gyro-orbit and conserve the NDW, which was not the aim of this section. For this, see Chapter 5.

3.2.1 Resolved electron Larmor radii

For the parameters discussed with fixed domain size and cell lengths equal to Eq. (1.6), the maximal ensemble Larmor radii of the thermal electrons, $\Delta x = r_{Le}$, we present in the left most panel of Fig. 3.3 the change in kinetic energy densities of each species through time, normalised by the deuteron cyclotron period. The natural thermal fluctuations for each species are very small, confirming that all of the gyro-orbits and gyro-periods are well resolved by the 75806 grid cells.

3.2.2 Resolved deuteron Larmor radii

Increasing the cell length to the maximal ensemble Larmor radii of the thermal deuterons, $\Delta x = r_{LD}$, the middle panel of Fig. 3.3 presents the same change in kinetic energies. Notice now that the electron species heat substantially through multiple orders of magnitude. The heating of the electrons, through interaction between electromagnetic fields, leads to heating of both the deuterons and alphas, despite the deuteron (and hence alpha-particle) gyro-orbit being just resolved over a domain made up 1251 grid cells.

3.2.3 Resolved alpha particle Larmor radii

And finally, for a simulation whose cell width only resolves the simulated minority thermal alpha-particle species (and no other) see the right-most panel of Fig. 3.3. Despite expecting heating of the deuterons and electrons, we only see it in the latter. This is surprising for multiple reasons, but represents the sensitivity of these simulations to inadequate spatial resolutions, especially since this is now comprised of only 30 grid cells, which will ultimately have adverse effects on the stepping procedure responsible for updating the current and energy exchange.

3.3 Summary

In this chapter we briefly considered the effects of the spatial resolutions of our PIC simulations on the quality of Fourier transforms, power spectra and ensemble descriptions of the change in particle and field energy densities. We discussed the responsibility of the simulator in choosing adequate spatial and temporal resolutions to observe wave excitations of interest, which in our research, include

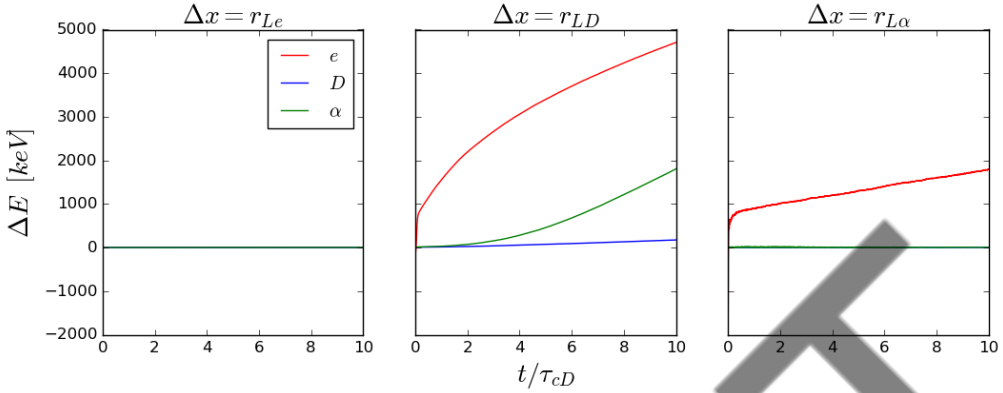


Figure 3.3: Three PIC simulations of entirely thermal plasmas consisting of electrons, deuterons and minority alpha-particles. Each panel (left-to-right) gives an increasing cell length, resolving the (*left*) electron, (*middle*) deuteron and (*right*) alpha-particle Larmor radii, Eq. (1.5), given by each panel’s title.

integer multiples of the cyclotron harmonics at wavenumbers associated with ICE.

Our resolution studies involved PIC simulations using conditions reminiscent of the outer mid-plane edge of the JET tokamak, and featured thermal populations of electrons and deuterons, excited by a drifting ring-beam minority 3.5 MeV energetic alpha-particle species. Following previous studies of similar scenarios, these simulations, too, did not conserve the NDW that is otherwise imperative for simulations with multiple majority bulk ions. As the concentration of alpha-particles was so small (0.1%) the non-physical linear heating artefact was negligible, hence, we were able to run multiple simulations at a much lower computational cost with only 100 macroparticles per cell of each species, as opposed to the thousands and tens-of-thousand that the NDW conserved simulations demand.

This chapter also confirmed the importance of resolving maximal ensemble Larmor radii of each species, including the electrons. We introduced here a parameter dependent on electron number density and magnetic field to determine the maximum cell length required to completely remove numerical linear heating resulting from inadequate resolution of the simulation domain. For simulations where the change in energy is dominated by the characteristic exponential growth phase of the MCI, numerical heating from unresolved Larmor radii result in an additive systematic error to the change in energy density. For sake of computational strain one can either resolve the electron Debye length or mitigate it through the use of high order shape functions and electric current averaging.

Chapter 4

Multiple ions in PIC simulations

Simulations of multiple ion fusion plasmas investigating the MCI and ICE in PIC simulations have not yet included both majority ion species, rather opting to alter the conditions of the energetic minority species, such as the energetic particle's mass, energy, concentration and pitch-angle. Future fusion energy production should aim to significantly reduce neutron tokamak wall damage and plasma poisoning. This will involve aneutronic fusion products, such as those noted in Ref. [21] and §1.1. The plasmas parameters of the aneutronic D– ^3He plasma are significantly different to that of the DT plasma, including their combined charge-to-mass ratio, secondary fuel concentrations and resonant behaviour, and therefore should be studied under the PIC regime first.

In order to apply the findings from ICE analysis on aneutronic fusion plasmas to the MCI, we develop here concepts relating to the physical processes under which multiple ions exchange energy, and resonate with the local FAW. In this chapter we discuss the considerations one must take when simulating multiple non-insignificant thermal ions in a PIC code. These arise primarily out of computational limitations, but their subsequent consequences on real measurable quantities such as the: energy exchange; MCI growth rate theory validity; emergent collective gyro-resonant behaviour; and the theoretical resonant Buchsbaum frequency (which would potentially allow for a more effective form of ion heating) are discussed. Findings from this chapter specifically relate to the results presented in Chapters 5 and 7.

4.1 Considerations

4.1.1 Number of macroparticles per cell

The ideal number of macroparticles per cell would be equal to the number of real particles which they represent. However, within most computational limits, this is not feasible. Instead, for each species, a number of macroparticles are chosen with scaled mass and charge of the number of real particles it represents (given by a weighting parameter in EPOCH). Inherent noise in the EM fields from simulating discrete particles scales as $C^{-1/2}$, where C is the number of (macro) particles per cell per species (PPCPS), as per §4.1.2. So, for a factor 2 increase in the number of particles, there is only a $2^{-1/2}$ factor decrease in the noise.

Previous work studying the effects of macroparticle numbers in a PIC code on noise can be found in Refs. [172] and [173]. In the former, four particles per species were used, and in the latter a comparison study varying particle number in two-dimensional EPOCH achieved a tolerable signal-to-noise ratio convergence for 500 to 1000 PPCPS. In simulations presented in Chapters 5 and 7, this PPCPS convergence is far lower than those of the electrons and deuterons, but considerably larger than the secondary bulk and minority ions.

We saw in §1.2.1 that the inclusion of an additional ion introduced the ratio ξ_2 into the quasi-neutrality condition. This forms a family of solutions in concentration space defined by the charge of each species. Choosing two ratios fixes the third, so that a quasi-neutral simulation can be run containing three (or any number of) positive ions. Simulations investigating the consequences of PPCPS number are shown in §4.2.1.

Typical ratio choices are ξ_{min} and (ξ_2/ξ_1) . These represent, respectively, the minority concentration (previously denoted $\xi = n_{min}/n_1$ in Refs. [100, 101, 106, 111, 114, 123]) and the concentration of our two fuel sources with respect to one another. In the DT scenario shown here, indices 1 and 2 correspond to the deuterium and tritium ions respectively. One may be curious, as the author was, to learn of the correlation between the minority concentration with respect to the electron number density, $\xi_{min} = n_{min}/n_e$, and to the primary bulk ion, $\xi = n_{min}/n_1$. The use of the latter in previous work questions whether ξ_{min} will provide comparative results. Rearranging the quasi-neutrality condition for two ions, one is able to find that if ξ_{min} is less than the inverse of the majority ions charge number Z_1 , the ratios ξ_{min} and ξ can be used interchangeably. For three quasi-neutral ions however, this relation, even at small concentrations, breaks down. Therefore, for simulations involving three ions, the concentration

of minority ions cannot be directly compared to its equivalent in a two ion simulation.

4.1.2 Number density weighting (NDW)

Quasi-neutrality within a plasma requires that the summation of charge weighted ion number densities is equal to the electron number density. Re-writing Eq. (1.1) in a normalised form,

$$1 = \sum_{\sigma} Z_{\sigma} \xi_{\sigma}, \quad (4.1)$$

where the concentration ratio for a given species σ is written $\xi_{\sigma} = n_{\sigma}/n_e$. It follows from Eq. (4.1) that only two concentration parameters are independent, which, in our simulations, is usually in terms of the secondary and minority ion's concentration.

Non-physical heating of particles within PIC codes can arise from sub-optimal discretisation of the grid leading to grid forces [41], or from inadequate volume weightings on simulated particles. It has been shown that if the per-particle weighting between each species is not equivalent, the exchange of energy between species does not represent the actual mass weighted equipartition between species, leading to a numerical plasma heating. See Refs. [172–176] for details on previous studies of weighting in multi-species fusion plasma PIC simulations, and for the handling of numerical weighting of particles in the particle-in-cell code Smilei, see Ref. [177]. PIC codes which conserve momentum and energy rely on this appropriate scaling of macroparticles to accurately represent the correct particle species. A breaking of this leads to a violation of the conservation of momentum and/or energy, manifesting within PIC simulations through the particles' inability to thermalise with one another through their numerical collisions and, hence, leading to linear heating.

It is important, therefore, to hold the per-particle number density weight equal across all species, including electrons [174], such that the computational weighted masses accurately scale to the real masses of the simulated particles. This is mathematically defined as

$$\frac{n_e}{C_e N_x} \simeq \frac{n_D}{C_D N_x} \simeq \dots \simeq \frac{n_{\sigma}}{C_{\sigma} N_x}, \quad (4.2)$$

which is henceforth referred to as the number density weighting (NDW) condition. Here, the total number of particles is written as the multiplication between the number of grid cells, N_x , across our domain (labelled x) with the average

number of PPCPS written as C_σ . It follows from Eq. (4.2) that, for a multi-component plasma, given an initially fixed number of electrons per cell C_e , the number of particles per cell per species can be, generally, written as $C_\sigma = \xi_\sigma C_e$. One also finds that the quasi-neutrality condition manifests here, such that

$$C_e = \sum_\sigma Z_\sigma C_\sigma . \quad (4.3)$$

Maintaining a constant NDW between species introduces a new computational limiting factor, which we write in terms of C_{min} . The computational limits of the ARCHER2 and Avon HPC used in this paper allowed for a tolerable convergence between computational speed and accuracy for a maximum C_{min} of five - see Table A.1 in Ref. [110]. As an example, if we require 100 minority particles per cell at a concentration of 0.1% ($\xi_{min} = 10^{-3}$) with a fuel ratio (ξ_2/ξ_1) of 1%; we require, per cell: 10^5 electrons, 98812 majority (1) species particles, and 988 majority (2) species particles, each. Since the cost of a simulation scales with its resolution, the computational expense of holding the NDW constant between species becomes exponential.

In simulations where a constant number of PPCPS were used [79, 100, 104, 111, 114, 116, 123, 131, 137], run-times were more than three times faster compared to those with a constant NDW, and required much less computational memory to track fewer macroparticles. With the advancements of computational power, for the first time, we are able to completely eradicate numerical linear heating resulting from inadequate NDW conservation, which up until now has either been ignored for sake of low concentrations, or mitigated through utilising higher order shape functions to smooth jumps in the electric current.

We are left, however, with the issue of larger charge contributions per particle leading to larger noise amplitudes in energy transfer and field-particle interactions, contributing to the updates of field values and particle velocities. These errors have been shown to have negligible effects on the noise floors in power spectral densities for $2 < C_{min} < 64$, see Figs. 4.6 and 4.5, and are overall negligible when considering collective behaviour through ensemble means, which we are justified in taking since MCI is a collective instability.

For a better representation of the significance of the conservation of the NDW on the eradication of numerical linear heating, four simulations each representing a thermal plasma made of two and three ions all with unequal masses (deuterons, protons and alpha-particles) were carried out. Their change in kinetic energy densities, along with the electrostatic E_x and oscillatory electromagnetic ΔB_z field energy densities, are presented in Fig. 4.1. Concentration of minority (α) and secondary bulk (p) ions were 1% and 20% of the background electron number

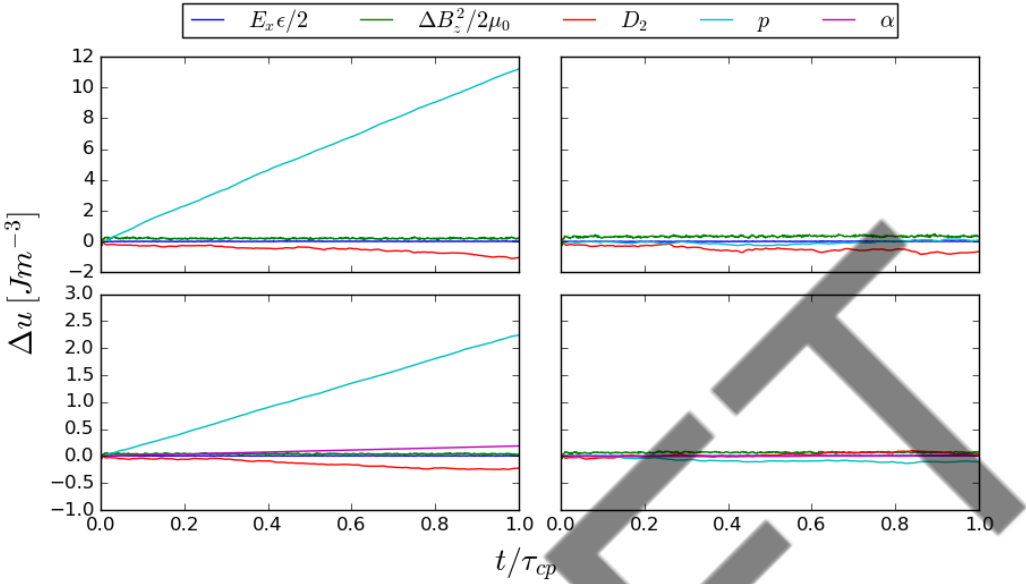


Figure 4.1: Change in energy densities of the field and particle components for (top row) two thermal ion species and (bottom row) three thermal ion species. Left (right) column represents unequal (equal) NDW across all ion species.

density, respectively. The background magnetic field strength was set to 2.1 T at an angle $\theta = 89^\circ$ to the simulation domain \hat{x} , giving a proton gyro-period of $\tau_{cp} = 31.2 \mu s$. Electron number density n_e was initialised at $10^{19} m^{-3}$ and the temperature of all particle populations were set to 1 keV. Simulations ran for only a single proton gyro-period, and particles were randomly distributed over a 1D grid of length $L = 0.125 m$, with a cell size of $\Delta x = 0.3\lambda_{De}$, where λ_{De} is the electron Debye length, so as to sufficiently resolve the electron gyro-radius - §3.2. All species were initially distributed as thermal Maxwellians, so as to avoid inciting any velocity space instabilities, and were pushed through time with a time-step of $\tau_{cp}/750$.

For both two and three ions, we find, purely as a result of conserving the NDW between all species via Eq. (4.2), numerical linear heating is removed entirely, leaving only transient fluctuations of energy within the plasma. Because our time step does not resolve a full electron cyclotron period, we have not plotted in Fig. 4.1 the change in electron energy density, as they present numerical linear heating that is not associated with the conservation of the NDW. Numerical linear heating of this kind does not present an issue for simulations throughout this thesis, as it is minimal with respect to the MCI, and has been a by-product of previous PIC simulations for years; see Fig. 2 of Ref. [111], Fig. 4 of Ref. [114] and Fig. 1 of Ref. [148]. For the simulations shown in Fig. 4.1, Eq. (3.1) gives

$r_{Le} = 0.683\lambda_{De}$. Therefore, for a simulation to just resolve the electron gyro-radius, we require $\Delta x \lesssim 0.683\lambda_{De}$. This has been shown to completely remove linear heating of this kind for grid spacings which just resolve r_{Le} (see Chapter 3 and Table 5.1, which used $\Delta x = 0.67\lambda_{De}$). However, for large scale three ion simulations the conservation of the NDW along with an even smaller grid length can at times prove too great of a computational cost. Another possible mitigation of electron numerical heating would be to increase the order of the shape function, alongside decreasing the cell width [118, 153].

Our work was the first of its kind on magnetized multi-ion 1D fusion plasmas which: included a tertiary ion, removed all numerical heating by resolving the electron Larmor radius (see Chapter 5), and maintained a constant NDW between species. Despite the large computational cost of holding all of these conditions true, it is seen that we can completely remove the numerical heating resulting from the discretization of a PIC grid due to unequal particle weightings and unresolved electron Larmor radii. For the sake of researchers who do not have access to large HPCs, it is recommended to introduce a higher-order shape function and intermediate current smoothing within EPOCH, made accessible by multiple flags in the input deck.

4.1.3 Fast Alfvén wave dispersion and validity of low frequency regime for non-zero tritium concentrations

Linear stage MCI growth rates are strongest for minority energetic particles whose perpendicular velocities are comparable to the Alfvén wave speed $v_\perp \sim v_A$ [39]. An equivalent expression is that, in frequency space, the strongest growth rates of the MCI are for wavenumbers which lie along the FAW dispersion curve, see §1.2.6, at frequencies where the slope of the FAW approximates $\omega \approx kv_A$, such that $l\Omega_\sigma - kv_A = \Delta$, where $\Delta = 0$ for integer multiples l of the cyclotron harmonic. This is typically true for low frequencies, $\leq 10\Omega_\alpha$. The inclusion of tritium as a secondary bulk species at concentrations that are not equal to the deuterium species, contradictory to the assumption in Ref. [93], introduces a perturbation to the growth rate calculation as a result of $\Delta \neq 0$. Therefore, for linear MCI theory to encompass multiple ion component fusion plasmas it would need to summate over the additional species in the dielectric tensor elements, account for the excitation of its cyclotron frequency, carrying it through to the calculation of Bessel functions which, ultimately, dictate the rate of growth of the MCI. A computational approach is discussed further in §2.3 and employed in Chapter 6.

Since both the FAW dispersion curve and the Alfvén speed are dependent on

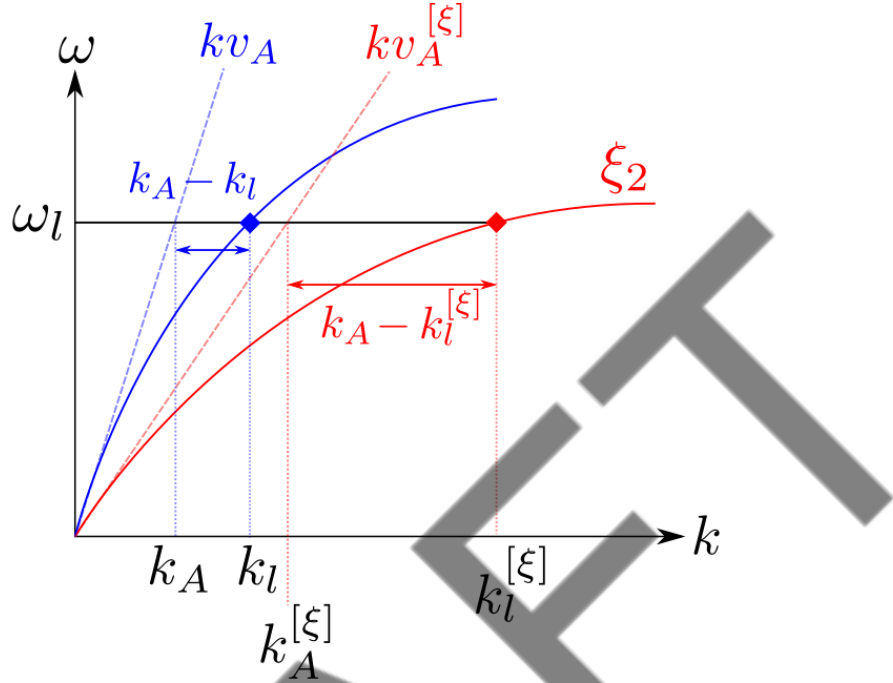


Figure 4.2: Diagram of the process for comparing integer cyclotron harmonics with respect to secondary bulk ion concentration ξ_2 , used to create Fig. 4.3.

the plasma's mass density, the concentration of the plasma's secondary bulk ion - see the summation over species given in Eq. (1.36) - is therefore important in determining if $\Delta = 0$ for all secondary ion concentrations, $\xi_2 > 0$. The question then arises: if a plasma consists of multiple ion species, are the FAW dispersion relation and Alfvén speed still approximately equal at low frequencies?

Shown in Fig. 4.2 is the process by which the FAW and Alfvén dispersion relations are compared, through frequency space, for multiple tritium concentration, ξ_T , DT- α plasmas, as those shown in Chapter 5. We calculate the FAW dispersion curve through wavenumber and tritium concentration space for a given integer ICE harmonic i.e. $\omega_l = l\Omega_\sigma$, along with its corresponding wavenumber $k_l(\xi) = k_x(\xi, \omega_l)$. A difference between the wavenumbers along the FAW and Alfvén dispersion, $k_A(\xi) = k_x v_A(\xi)$, is then calculated, $k_A(\xi) - k_l(\xi)$. The top panel of Fig. 4.2 gives the FAW wavenumber normalised by the Alfvén speed v_A and the deuteron cyclotron frequency Ω_D , and the bottom panel shows the difference between wavenumbers expressed as a ratio to the Alfvén wavenumber k_A as a function of tritium concentration. The l^{th} harmonic is annotated above each line.

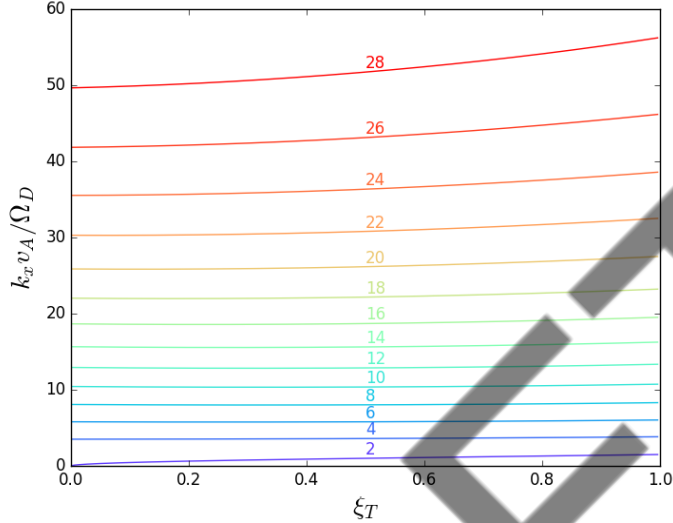
Repeating this for a range of wavenumbers spanning multiple harmonics l ,

and over the tritium concentration space ξ_T , we determine the trend in, and hence immutability between, the cold plasma (FAW) dispersion relation for a typical multicomponent JET-like plasma, and the Alfvén dispersion, across a range of frequencies. The results seen in Fig. 4.3 show that the curve of the FAW dispersion roughly equates to v_A for frequencies below $12\Omega_D$ (here $\Omega_D \equiv \Omega_\alpha$) with a slowly growing divergence for tritium concentrations above 50%. This difference is enhanced at greater frequencies, confirming that with the inclusion of tritium ions, for frequencies below $12\Omega_D$, the FAW dispersion can be approximated by the Alfvén dispersion. This was already valid at low frequencies for zero tritium concentration, and as such the introduction of a tritium species does not interfere greatly with the linear theory growth rate calculation of the MCI at low frequencies.

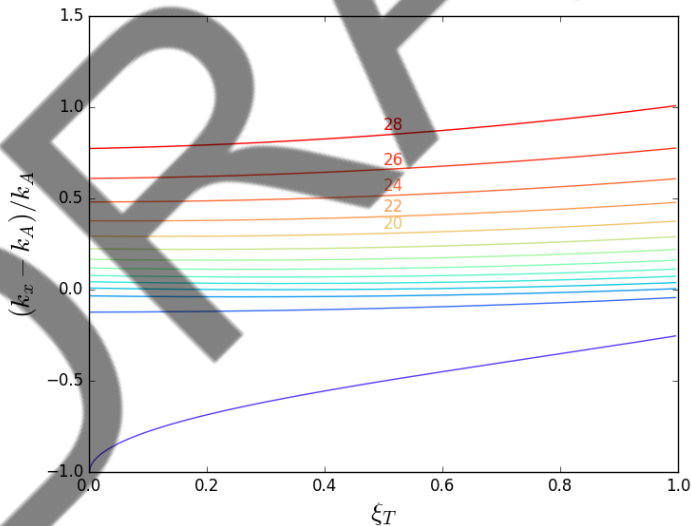
4.1.4 Minority concentration

An increase in the concentration of the minority energetic species (in this example alphas) is equivalent to artificially increasing the fusion reactivity. We refer to Ref. [105], which showed that the ICE intensity scaling is linear with n_α/n_e , to good approximation, and specifically call on Fig. 3 of Ref. [105] in relation to the growth rate of the MCI at early times. The total energy transferred from the alpha-particles to excited fields and particles also scales with density as the minority particle becomes more dominant within the plasma. For large concentrations, the quality of agreement between the analytical and numerical growth rates falls.

In the large charge weighted concentration limit, i.e. $n_\alpha/n_e \simeq 0.5$, a strongly exponential growth period of thermalisation of the bulk deuterium and tritium ions occurs. Since the FAW is supported by the bulk ions, in this limiting regime, the alpha-particles support it instead, and as such, the resonant physical phenomenology of ICE associated with the bulk ions is hence associated with the energetic minority. This theoretical concentration limit is significantly larger, by powers of 100 or more, than those used in the present manuscript or in previous literature, even when concentrations are scaled up for computational considerations (such as $\xi_\alpha = 2 \times 10^{-3}$), so this limit poses no issues to our ICE measurements.



(a) Wavenumber solutions to the cold plasma dispersion relation, Eq. (1.37), at even integer deuteron harmonics (as labelled) normalised to the Alfvén wave speed and deuteron cyclotron harmonic, through increasing tritium concentration.



(b) Difference between the cold plasma wavenumber solutions and the Alfvén wavenumbers, normalised to the Alfvén wavenumber at a given deuteron harmonic.

Figure 4.3: The process of calculation is seen in Fig. 4.2. The alpha-particle concentration used in the calculation of v_A was held constant at 2×10^{-3} .

4.2 Consequences

4.2.1 Particles per cell per species (PPCPS)

The PPCPS influences the current \mathbf{J} calculation for each time increment in EPOCH, and plays a pivotal role in PIC codes. If the number of charge carrying macroparticles is low, the contribution of the charge they each carry is large, leading to larger transfers of current between cells and hence a sharp jump in the calculation of the EM fields, leading to an increase in the particle's velocities, *et cetera*. To smooth the current transitions between cells one can increase the order of the shape function, which smooths the current transfer influence on the field values, as its influence is extended beyond the immediately adjacent cells. It was demonstrated in Ref. [145] that increasing the order of the shape-function dramatically reduces said numerical self-heating, but at the cost of a significant increase in the computation time. This work also showed that one can achieve comparable results if the number of particles per cell was increased four fold for an inadequate grid spacing. It is therefore more efficient to increase the number of macroparticles per cell for a shape function order > 1 , so that each particle contributes a relatively smaller portion of current between grid cells, whilst conserving charge, leading to a smoother transition in the update of the EM fields and particle velocities.

We run seven simulations of a DT- α plasma, whose alpha-particle macroparticle number increases from two to 64 in random increments, but are otherwise identical. These simulations featured an electron number density $n_e = 10^{19} \text{ m}^{-3}$ and a background magnetic field of strength 1.4 T orientated 90° to the simulation domain. Thermal Gaussian distributed DT ions were given a temperature of 1 keV and the concentration of tritium ions (ξ_T) was set artificially higher than experiment [58] to 25%, reducing computational strain. For similar reasoning, the 100 keV alpha-particles were distributed at a concentration of $\xi_\alpha = 2 \times 10^{-3}$, which were initially distributed in velocity-space with a drifting Dirac delta function, Eq. (1.46), therefore featuring zero thermal spread.

These are the first instalment of three ion (four species) simulations, which underpins the main results presented in Chapters 5 and 7. Each of the simulations durations presented here were $0.468 \mu\text{s}$ ($5\tau_{c\alpha}$), with time-steps of 0.468 ns ($0.005\tau_{c\alpha}$). The total grid size L was 0.325 m ($5r_{L\alpha}$) and each cell measured $70.6 \mu\text{m}$ ($0.95\lambda_{De}$) across. This meant that we well resolved the alpha-particle and thermal ions' gyro-period and orbits by over 200 time-steps and 80 grid cells. For all ion resolutions see Table 4.1.

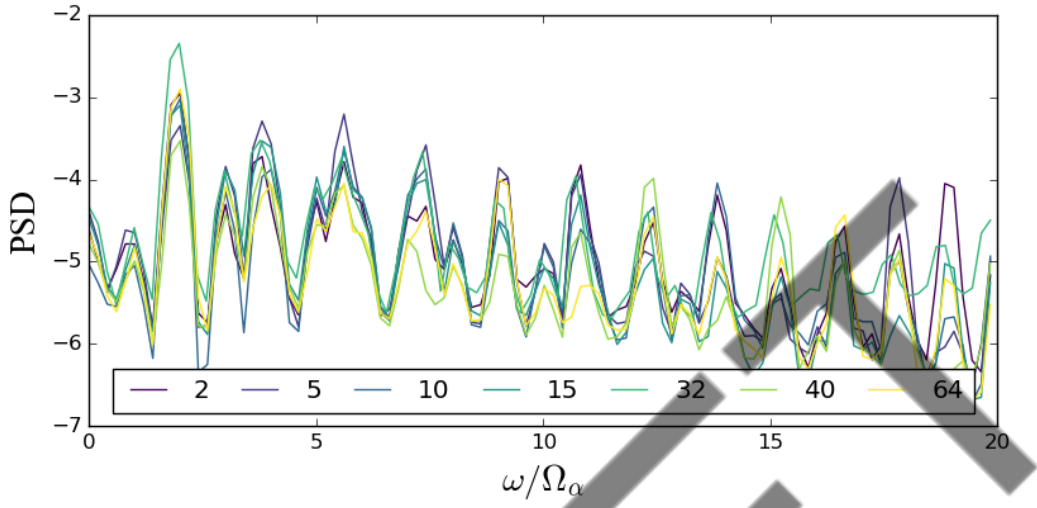


Figure 4.4: Logarithmic base 10 power spectral densities in simulations of a DT- α plasma modelled after the JET plasma 26148, for increasing PPCPS of the energetic minority alpha-particle population from two to 64 (as per legend), through frequency normalised to the alpha-particle cyclotron frequency Ω_α .

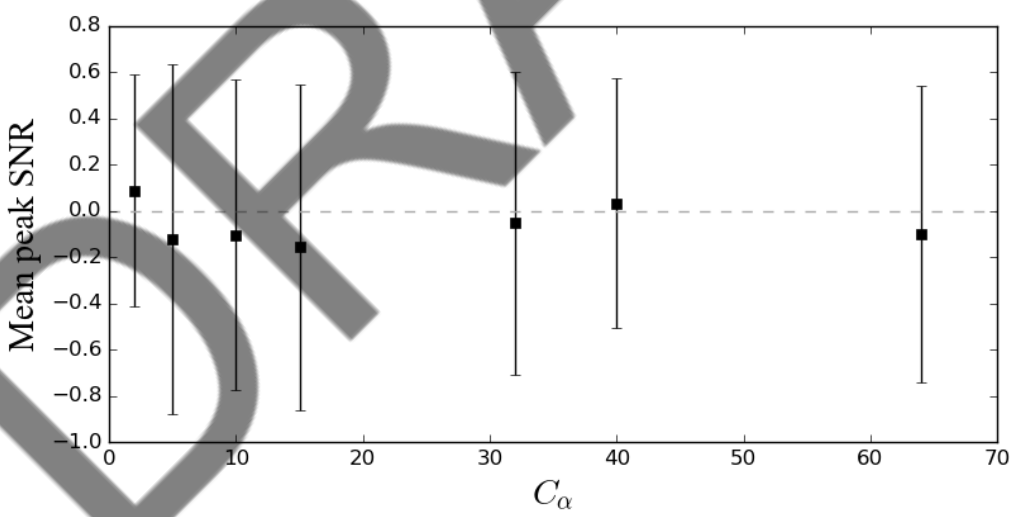


Figure 4.5: Mean peak signal-to-noise ratio (SNR) of the power spectra for simulations with an increasing number of macroparticles per cell, C_{min} , of the minority 3.5 MeV alpha-particle species. Error bars represent one standard deviation in the peak SNR per simulation. The zero line, above which a signal is considered significant, is plotted in dashed grey.

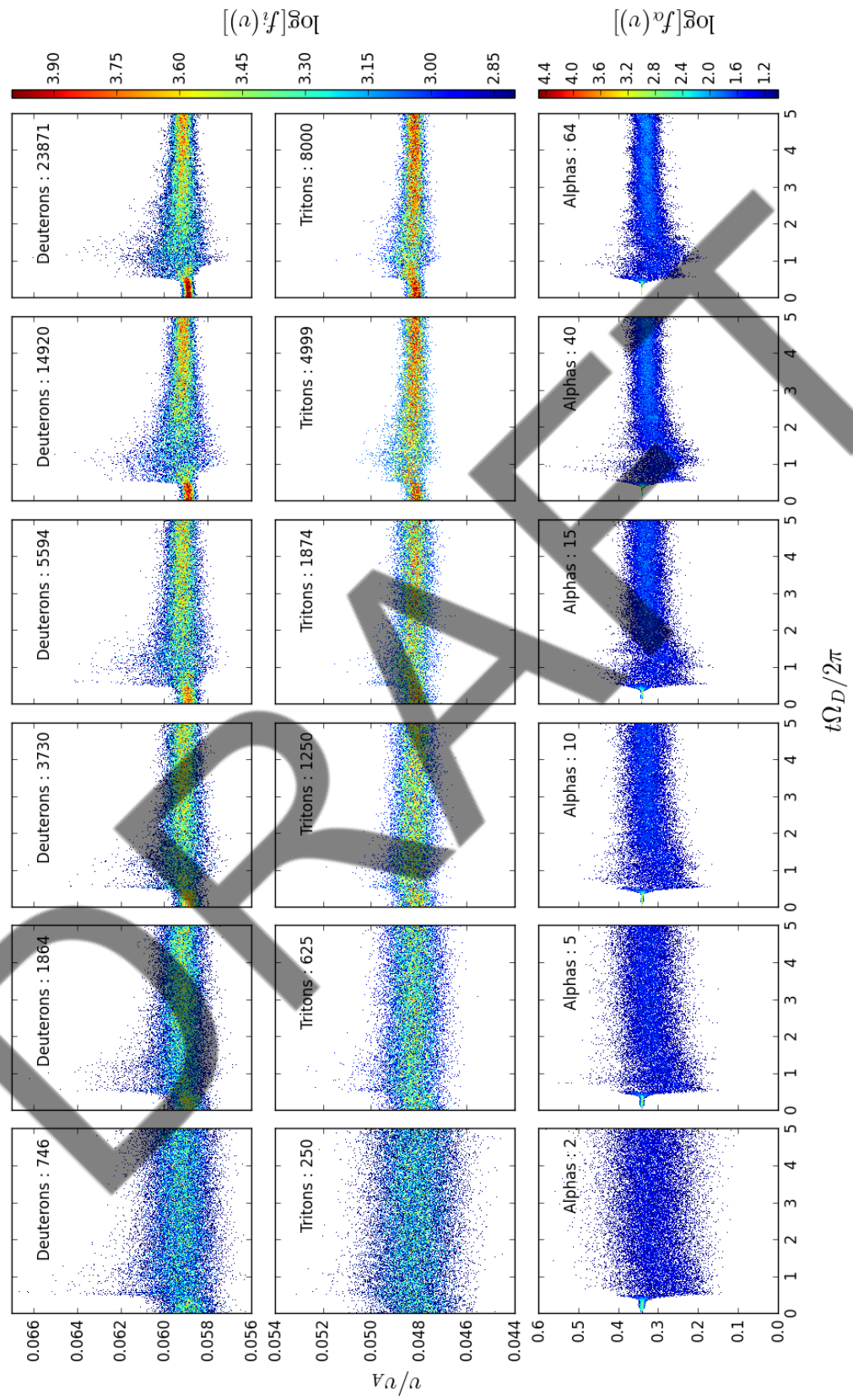


Figure 4.6: Logarithmic base 10 velocity distributions (as per shading) of the particles for each species, the PPCPS (panel annotation) for the species: deuterons (*top row*), tritons (*middle row*) and energetic alphas (*bottom row*) in a DT- α plasma modelled after the JET plasma 26148.

Quantity	Ion species		
	Deuterons	Tritons	Alphas
$r_L/\Delta x$	80	98	461
$\tau_c/\Delta t$	200	300	199

Table 4.1: Larmor radius and gyro-period normalised by the grid spacing Δx and simulation time-step Δt , respectively, for each ion in the seven simulations carried out to study the effect of PPCPS in three ion DT- α JET fusion plasmas.

Power spectral density features presented in Fig. 4.4 reveal that, following an increase in the number of macro alpha-particles, there is a decrease in the intensity of ICE peaks for frequencies $< 15\Omega_\alpha$. One notices that low alpha-particle numbers per cell (given in the legend) lead to powers that are marginally more intense than their high PPCPS counterparts at low frequencies, but less intense at higher frequencies. This difference is minimal, and is determined almost randomly through frequency space, but, in general, the intensity of power for a simulation characterised by 64 alpha-particles per cell, with the parameters given, appear in the lowest quartile of the intensities of all traces per ICE peak.

Since ICE analysis is largely dependent on the measurement of the power spectrum, it is vital therefore to determine whether its features arise as a result of the MCI or numerical aberrations, such as simulating with too few PPCPS, in our PIC simulations. We perform a cost-benefit analysis on these power spectra via measuring the signal to noise ratio (SNR) for the range of PPCPS presented. The SNR is calculated, in logarithmic space, as the signal minus noise, where the noise is, in its simplest sense, the mean plus one standard deviation. As thermal noise would be distributed evenly across frequency space, and there are no visible underlying trends, this choice is justified. Shown in Fig. 4.5, one finds that the mean (standard deviation) SNR of the ICE signals does not increase (decrease) greatly over a 32 fold increase in macroparticle number of the energetic minority alpha-particles, despite the sharp diffusion of current with low minority particle per cell numbers. The cost of simulating with a significantly higher number of minority particles per cell therefore outweighs its benefit, as the SNR of the power spectra does not increase at the same rate.

Figure 4.6 shows the evolution of the velocity (normalised to the Alfvén speed) probability density through time for six of the seven plasmas (excluding $C_\alpha = 32$). The species and their PPCPS is as given in the top right corner of each panel. The PPCPS increases for all species following an increase in the number of alpha-particles due to the quasi-neutrality relation, Eq. (4.3).

Following a 32 fold increase in the number of alpha-particles between two and 64, there is a substantial decrease in the spread of velocities of alpha-particles, all of which are subject to identical initial conditions save their PPCPS, signifying an improvement in the plasma's response to changes in the current between grid cells. The improvement in the current calculation is, however, at the expense of an unsubstantial decrease in the signal to noise ratio, Fig. 4.5.

4.2.2 Gyro-resonance

The ratio between the change in the energy densities of two bulk ion species, for now labelled 1 and 2, as a result of external physical heating (e.g. a minority energetic particle) can be written as

$$\frac{\Delta u_1}{\Delta u_2} = \frac{n_1[E_1(t) - E_1(0)]}{n_2[E_2(t) - E_2(0)]}, \quad (4.4)$$

where the change in energy density is $\Delta u_\sigma = n_\sigma \Delta E_\sigma$. If both bulk species are distributed as thermal Gaussians, then their velocity ensemble average relates to their energy and temperature as $E_\sigma(t) = \frac{3}{2}k_B T_\sigma(t) = \langle m_\sigma v_\sigma(t)^2 / 2 \rangle$ where velocities can be defined in their perpendicular and parallel components, with respect to the magnetic field, as $v_\sigma^2 = v_{\parallel\sigma}^2 + v_{\perp\sigma}^2$. Substituting this gives

$$\frac{\Delta u_1}{\Delta u_2} = \frac{n_1 m_1}{n_2 m_2} \left(\frac{[v_{\parallel 1}^2(t') - v_{\parallel 1}^2(0)] + [v_{\perp 1}^2(t') - v_{\perp 1}^2(0)]}{[v_{\parallel 2}^2(t') - v_{\parallel 2}^2(0)] + [v_{\perp 2}^2(t') - v_{\perp 2}^2(0)]} \right). \quad (4.5)$$

By definition $v_{\parallel}(t) - v_{\parallel}(0) \equiv \dot{v}_{\parallel} = 0$, therefore, these terms cancel. Similarly, perpendicular velocity can be defined by its Larmor radius Eq. (1.5) as a function of time. Substituting into Eq. (4.5) we find

$$\frac{\Delta u_1}{\Delta u_2} = \frac{n_1 m_2}{n_2 m_1} \left(\frac{q_1}{q_2} \right)^2 \frac{[r_{L1}^2(t') - r_{L1}^2(0)]}{[r_{L2}^2(t') - r_{L2}^2(0)]}, \quad (4.6)$$

where we have defined some time t' . As we make no assumption on the difference between each species change in squared Larmor radii, we are motivated to study this further.

Figures 4.7 and 4.8 show the change in the squared Larmor radii and Eq. (4.7) through time for two species of thermal D-³He ions at multiple ³He concentrations with respect to electron number density. These simulations were carried out under plasma parameters representative of those seen in Chapter 7, which include an electron plasma density of $n_e = 10^{19} \text{ m}^{-3}$, ion and electron temperatures of $T_{i,e} = 2 \text{ keV}$, a 14.68 MeV energetic minority proton species distributed as a drifting ring-beam and a magnetic field of strength 3.7 T at an orientation $\theta = 89^\circ$ to the simulation domain. Figure 4.7 presents the change in the squared

Larmor radii for each population using the ensemble perpendicular velocities of D– ^3He ions as calculated from their particle's full three dimensional velocities, $|v_{\perp}^2| = v_x^2 \sin^2 \theta + v_y^2 + v_z^2 \cos \theta$, assuming the magnetic field is perpendicular to \hat{y} . This shows that the mean change in the squared Larmor radius (i.e. kinetic energy) is equivalent between both bulk ion species at all times.

Similarly, Fig. 4.8 plots the rearrangement of Eq. (4.6) in terms of the ratio between changes in each species' squared Larmor radii. We normalise the energy densities by ξ_D and ξ_{He3} in each simulation to represent the ensemble kinetic energy per particle. Since each trace tends to unity at all times besides the turnover between saturated and unsaturated regimes of the MCI, $4.5 < t/\tau_{cp} < 5.5$, this figure also shows how the change in squared Larmor radii is equivalent for multiple concentrations of ^3He , i.e. $[r_{LD}^2(t) - r_{LD}^2(0)] / [r_{LHe3}^2(t) - r_{LHe3}^2(0)] = 1$. This implies that the magnetic flux enclosed by the particle's Larmor radii, $\Phi_B = \pi Br_{L\sigma}^2$, evolves at an equal rate between between both species, independent of the energy transfer mechanism. Whilst we don't derive here why this is the case, we do imply that it is likely a result of the principle of least action between two charges under the influence of work done in the form of kinetic energy, a perpendicular external magnetic field and Coulomb forces.

As we have shown that the change in squared Larmor radii is equivalent between species, we can generally write Eq. (4.6) as a change in the mean kinetic energy per-particle

$$\left\langle \frac{\Delta E_1}{\Delta E_2} \right\rangle = \frac{m_2 q_1^2}{m_1 q_2^2}. \quad (4.7)$$

If both thermal species are given non-zero initial drift velocities, we could quantify their change in squared Larmor radii through the charge and mass weighted change in kinetic energies. As we have made no assumption on the orientation of the background magnetic field, only noted that for all orientations $\dot{v}_{\parallel} = 0$, this gyro-resonant criteria should hold for arbitrary magnetic field angles, with the limiting case being one which is purely parallel. The scope of this theory outside of perpendicular magnetic fields, thermal Gaussian distributions and origins of energy transfer, is left as an exercise to the reader.

4.2.3 Buchsbaum resonant frequency

An additional resonant frequency resulting from the presence of multiple ions was first derived by Ref. [33] who found that hybrid resonances present for singular ion constituent plasmas exhibit wave absorption with the introduction of an additional ion species.

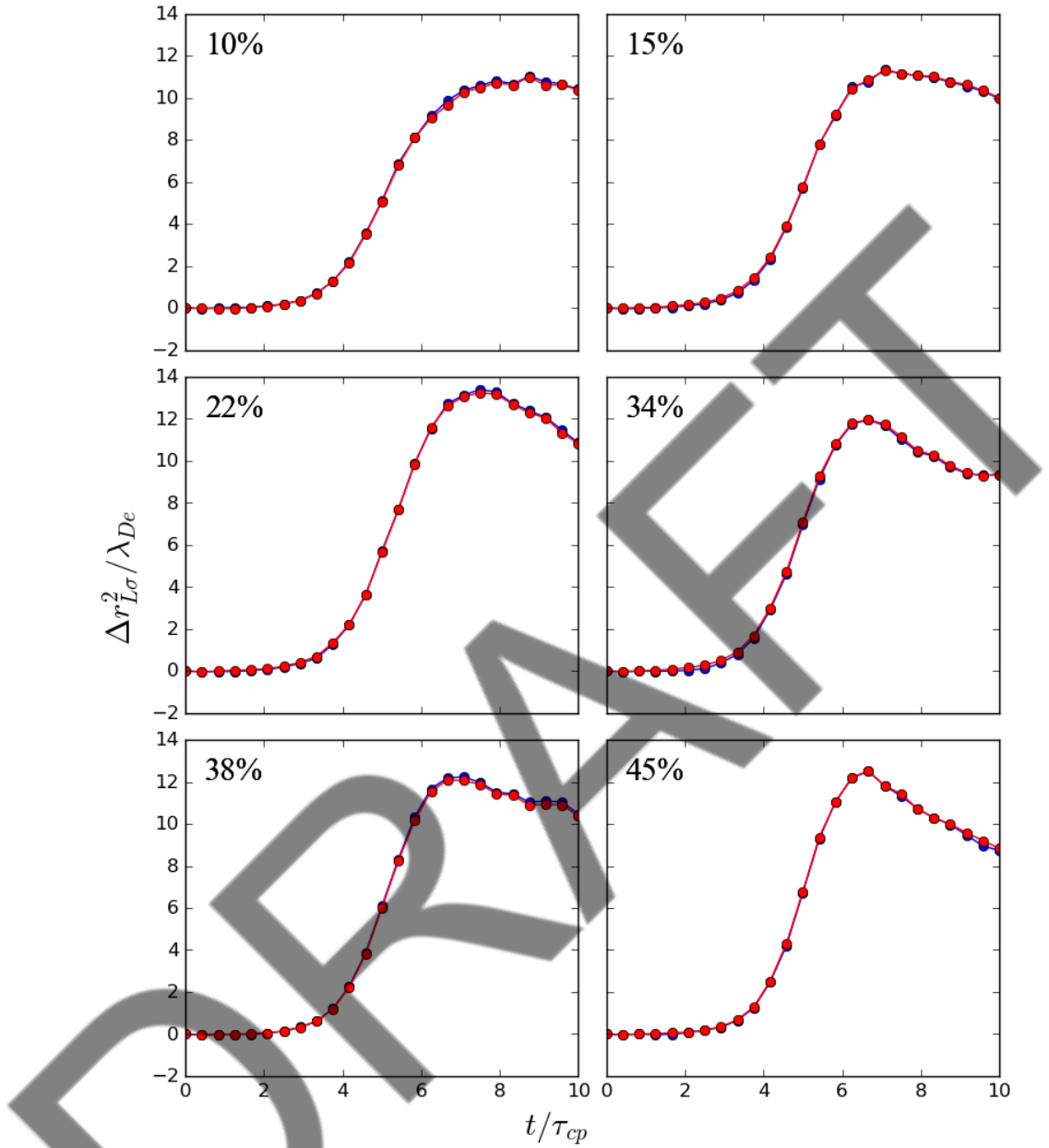


Figure 4.7: Evolution of the squared ensemble Larmor radius (representative of the enclosed magnetic flux) normalised by the invariant Debye length through time normalised to a proton cyclotron period τ_{cp} for deuterons (blue) and ^3He ions (red) for multiple ^3He concentrations, as given in the top left of each panel.

This driving resonant frequency leads to large absorption of energy by the plasma ions and as such can aid in plasma ion heating. For this reason, it is

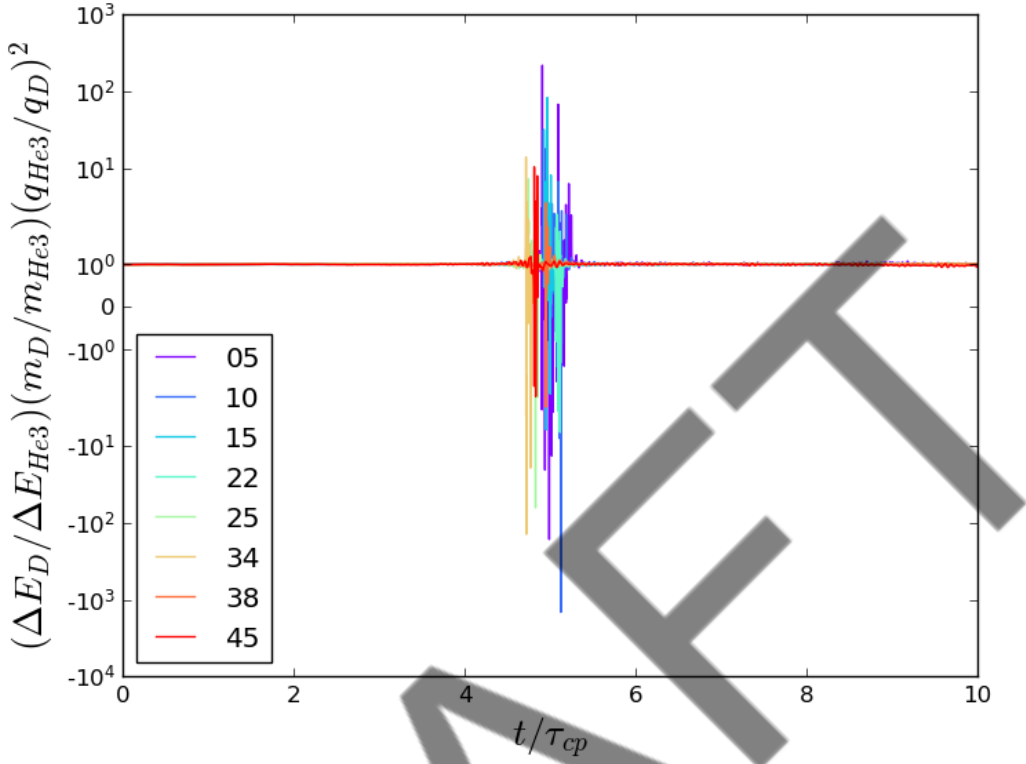


Figure 4.8: Gyro-resonant ratio Eq. (4.6) for deuterons and ${}^3\text{He}$ ions at multiple concentrations (see legend for $100\% \cdot \xi_{He3}$) through time normalised to the proton cyclotron period τ_{cp} . Confirmation of the equal change in enclosed magnetic flux as ratio tends to 1 for all times apart from turnover between saturated and unsaturated regimes of the MCI (see Fig. 7.3).

important to determine whether this driving frequency, observed between $1 < \omega/\Omega_2 < M_2/M_1$, is present in our simulations and can be observed. We have not reproduced Eq. (7) from Ref. [33] for sake of clarity, but have already stated one resonance condition in Table 1.1, and present the same findings through reproductions of their figures 2 to 4, for deuterium and tritium ions.

Figure 4.9 presents two reproductions of figures 2 and 3 in Ref. [33]. On the left, we show how the propagation constant wavenumber, $k_r = k_x/k_0$, as a function of frequency scales with increased relative ion concentration, given as $\xi_2/(\xi_1 + \xi_2)$ where indices 1 and 2 represent the deuterium and tritium populations respectively. Relative tritium concentration is increased left-to-right and, for each trace, its relative wavenumber diverges to infinity before reappearing negative, i.e. damped. The frequency at which each trace diverges to infinity is unique, and the difference between this and the frequency of the initial trace

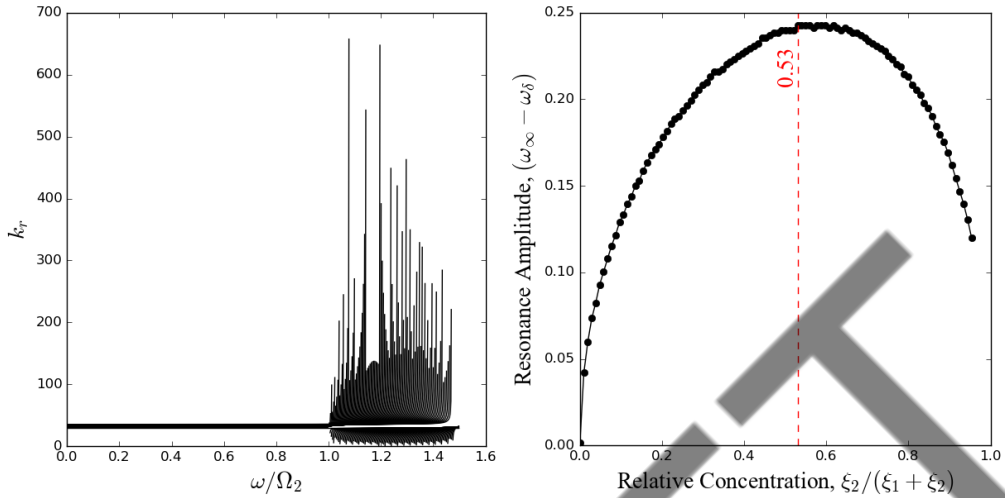


Figure 4.9: Deuterium (1) and tritium (2) multiple ion resonance and its maximal amplitude. *Left:* multiple ion resonant strength from Eq. 7 of Ref. [33], where $k_r = k_x/k_0$, plotted (black lines) for multiple relative concentrations of tritium ions ($\xi_2/(\xi_1 + \xi_2)$). *Right:* resonant amplitude as a function of relative tritium concentration defined by the difference between the (small percentage change from) initial and final frequencies, the latter of which is that which diverges to infinity ($\omega_\infty - \omega_\delta$). The red dashed vertical line highlights the relative concentration (as labelled) of the maximal resonant amplitude and is plotted as a function of mass ratio in Fig. 4.10.

(represented by some fractional change) represents the amplitude of resonance, shown by the right-hand panel of Fig. 4.9 and written as $\omega_\infty - \omega_\delta$, where ω_δ represents the frequency at which the propagation constant k_r increases by 1% with respect to its initial value at $\omega = 0$, as followed from Ref. [33].

The right-hand panel of Fig. 4.9 agrees well with figure 3 of Ref. [33] and suggests, for this real deuterium-tritium mass ratio plasma (as opposed to their 1:4 mass ratio) that optimum resonant driving of ion cyclotron heating via this behaviour is for a relative concentration of tritium of 53%, as given by the vertical dashed red line. This suggests that maximal driving of additional resonance between DT ions is achieved at an (almost) equal concentration of both ions (i.e. 50:50), agreeing both with concentrations used to describe linear MCI growth rate theory [93], as well as experimental results in TFTR [178, 179] and JET [179–182].

Figure 4.10 shows this process repeated for DT ions with mass ratios between one and eight. For constant charge numbers, it shows that, for increasing mass ratios, the optimum maximum concentration for driving multiple ion resonance

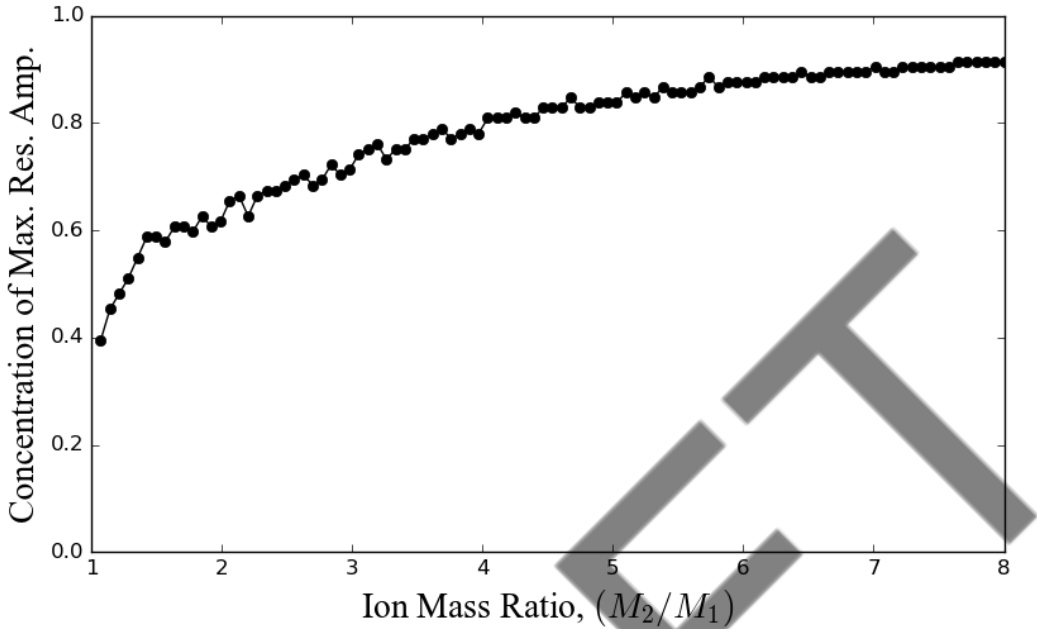


Figure 4.10: Maximal amplitude of the Buchsbaum multiple ion resonance as a function of mass ratio between each ion, as extracted from data, such as that presented in the right panel of Fig. 4.9, for ions with multiple mass ratios and equal charge.

tapers out at 90%. At our realistic mass ratio, as discussed, this is at an almost 50:50 split, but this is dependent on the frequency threshold ω_δ .

One potential issue of observing this low frequency driving, and distinguishing it against ICE power spectral features, is in the frequency resolution of our simulations. Typically, our frequency space granularity is so fine that we are able to resolve frequencies five or more times smaller than a cyclotron harmonic, Ω_i . However, combining our computational restraints (leading to lower frequency and wavenumber resolutions), thermal noise and ICE power at the primary harmonic, the driving of the Buchsbaum resonant frequency becomes difficult to detect with our current simulation setup. It is important to stress, however, that this does not mean the coupling is not present, rather that the growth rate and strength of the Buchsbaum resonance may not be significant against the growth rate of the MCI, and would therefore fail in dominating power spectra. We would suggest further study into the Buchsbaum resonance involving multiple ions including those of increasing charge number, such as our aneutronic fusion products, using PIC codes specifically focused on low frequency, $\omega < 5\Omega_i$, behaviour.

4.3 Summary

In this chapter we have considered key parameters necessary for PIC simulations of multicomponent plasmas and explored physical consequences from its supporting of additional resonances. Our considerations have included the number of PPCPS (a primary limiting factor); the NDW; and validity of the primary resonance condition for the MCI, $l\Omega_\sigma - kv_A = \Delta$. We showed that the PPCPS, whilst imperative for an accurate calculation and evolution of field energies through current evolution, did not improve the quality of power spectra or mean change in energies considerably over a 32 fold increase in number of macroparticles. The number of macroparticles per cell was dependent on a key parameter derived in this chapter for the simulation of multiple bulk ion simulations; the NDW. The NDW is manifested in the quasi-neutral condition of plasmas, and introduces a condition within PIC simulations of multicomponent fusion plasmas which must be maintained to avoid non-physical numerical linear heating of all species. Whilst our simulations may only include five minority macroparticles per cell, this results in multiple thousands of macroparticles for each of our majority species, and hence compensates for the jumps in current contribution of the minority species.

Also derived here was the gyro-resonance condition. This revealed that the change in the enclosed magnetic flux by one Larmor radius is equivalent between majority bulk ions, which was then confirmed with PIC simulations, and hence any gain in kinetic energy from the minority species does so in accordance to the ratio between both bulk species' mass and squared charge. Finally, we reproduced results from Ref. [33], which discussed multicomponent ion plasma resonances. These reproductions are helpful in understanding our multiple ion PIC studies, but are overall difficult to detect in our current PIC regime, which focuses on frequencies associated with ICE.

Chapter 5

PIC simulations of multicomponent DT fusion plasmas

In this chapter we discuss the output from seven individual PIC simulations of a DT fusion plasma, similar in plasma parameters to that of JET plasma 26148 [58], whilst varying the concentration of tritium ions with respect to electron number density. With recent results suggesting that the inclusion of tritium improves DT fusion plasma stability [183], we aim to find whether the inclusion of tritium, at varying concentrations, in PIC simulations leads to a more accurate representation of the JET plasma 26148 power spectra, and to build the foundations off of which further simulations involving multiple bulk ions and their analysis will grow from. Here we also introduce a number of novel analysis methods to the field of fusion plasma physics to compare power spectra.

5.1 Computational approach

As ICE is an ion cyclotron resonant phenomenon, it is essential that any simulation of ICE resolves the full gyro-orbits of the energetic and thermal ions and, for consistency, of the electrons. As described in Chapter 2.1, we employ the widely used PIC code EPOCH. We follow all three vector components of the velocity of each particle, and of the electric and magnetic fields. The simulation domain has one spatial co-ordinate axis, which is oriented arbitrarily with respect to the direction of the background magnetic field. Since the MCI is known to grow most strongly for quasi-perpendicular propagation [37, 39, 58, 121], the background magnetic field angle is chosen to be orientated at 89° with respect to the

Quantity	Value
n_e	$10^{19} m^{-3}$
B_0	$2.1 T$
L	$3.0 m$
T_D, T_e	$1.0 keV$
Δx	$0.67 \lambda_{De}$
λ_{De}	$74.3 \mu m$
L/r_{LD}	792
L/r_{LT}	796
$L/r_{L\alpha}$	23
L/r_{Le}	59037

Table 5.1: Overview of plasma parameters in relation to the spatial simulation domain. From top: the domain length, L ; electron Debye length, λ_{De} ; computational grid spacing, Δx ; equilibrium magnetic field strength, B_0 , and electron number density, n_e ; ion and electron temperatures, T_D, T_e ; and the domain length L normalised to the Larmor radius of each particle species (deuterons, tritons, alpha-particles and electrons) as respectively indexed.

spatial domain in the simulations presented here. This 1D3V configuration is sufficient to capture the collective relaxation of the energetic ion population, and the resulting excitation of electric and magnetic fields, in a regime corresponding to the slab geometry of analytical linear MCI theory [62, 100, 101, 105, 112].

Importantly, the PIC approach can carry the MCI into its nonlinear saturated regime which is beyond the reach of linear analytical theory. The saturated regime is likely to have the best correspondence with observed ICE signals, which nevertheless are often observed to carry a clear imprint of the linear MCI, see for example Fig. 1 of Ref. [101] and Figs. 2 and 3 of Ref. [105]. We emphasise that normal modes of the plasma, such as the fast Alfvén wave and cyclotron harmonic waves, are not imposed *ab initio* in the PIC approach; instead they arise naturally, as emergent consequences of the self-consistent Maxwell-Lorentz dynamics.

5.1.1 Structure of simulations

As summarised in Table 5.1, the spatial domain of these simulations has length $L = 3m$. The individual cell length $\Delta x = 0.67 \lambda_{De}$, where $\lambda_{De} = 74.3 \mu m$ is the electron Debye length for the plasma parameters specified in Table 5.1, thus there is a total of 60205 grid cells. This cell length is chosen to be smaller

than the electron Debye length, beyond which electrical charge is shielded in a plasma. In PIC codes, if λ_{De} and the gyro-motion of electrons are not resolved, the simulated plasma may undergo non-physical heating, see for example Ref. [153]. The spatial domain length, L , normalised to the Larmor radius, $r_{L\sigma}$, of each particle species is also given at the bottom of Table 5.1. These values show that the domain is sufficiently large to resolve the full spatial gyro-motion of each ion species in the simulation, including the energetic alpha-particles, which traverse over 2600 grid cells in a single gyro-orbit, and provide good energy conservation, within 1% over the duration of each simulation. Table 5.2 lists the key simulation parameters relating to the population of energetic alpha-particles and the concentrations of ion species, which are similar to those used in previous first-principles PIC studies of the collective relaxation of energetic populations under the MCI [79, 100, 101, 104, 113].

Implementation of charge neutrality with respect to the additional ion species (thermal tritons) is computationally demanding in comparison to previous PIC simulation studies. This is primarily due to the need to maintain a similar value for the number density weighting (NDW, see Eq. (4.2)), across all species, including electrons. We refer to §4.1.2 for details on how this constraint is accommodated in the present simulations. It places significant demands on computational resources and, partly in consequence, we use a simulation duration of seven deuteron gyro-periods, τ_{cD} . The computational time-step is $\tau_{cD}/1700$, or shorter. Hence the gyro-dynamics of all three ion species is highly resolved in time and space, such that cyclotron resonant phenomenology is captured from first principles.

Because of the increased computational cost resulting from the inclusion of a tritium population, it is necessary to drive the MCI sufficiently strongly that it enters its nonlinear phase within a few ion gyroperiods. This requires an increase, relative to the actual experimental value, of the concentration of minority fusion-born alpha-particles to $\xi_\alpha = 2 \times 10^{-3}$. This value is higher than in JET plasma 26148, for which ξ_α was of order 10^{-4} to 10^{-5} [38], but is on the order of previous first principles PIC simulations of the MCI [100, 101, 105, 114]. Physically, this strong linear drive of the MCI presents no particular issues, because the scaling properties of the MCI with respect to energetic ion concentration, and its effect on the power spectrum of simulated ICE, are already known. We refer to Ref. [105] for Figs. 1 and 2 in relation to the nonlinear saturated phase of the MCI, and Fig. 3 in relation to the growth of the MCI at early times.

5.1.2 Velocity space distributions

It is known that the ICE observed from the outer midplane edge of JET DT plasma 26148 was driven by a small subset of centrally born fusion alpha-particles which undergo large drift excursions from the core to the outer midplane edge [56–58, 120], and back again. These are shown, for example, in Fig. 3 of Ref. [58] in relation to JET magnetic field geometry and, for the counterpart phenomenon in TFTR, Fig. 1 of Ref. [120]. The location in velocity-space of this subset of the energetic ion population, originally predicted in Ref. [184], is narrowly defined: just on the trapped side of the trapped-passing boundary, with total velocity corresponding to the birth energy 3.5 MeV, see e.g. Fig. 16 of Ref. [58]. The source of free energy that drives the observed ICE is the resultant localised positive gradient in the perpendicular component of the velocity space distribution, $\partial f_\alpha / \partial v_\perp > 0$, for $v_\perp \sim v_A$. It has been found that this configuration is conducive to strong drive for the MCI [42, 100, 101, 103–106]. This population can be represented analytically by, Eq. (1.48), a drifting ring-beam distribution in velocity space [37, 118], which, as noted in the contemporary literature, provides a good analytical approximation to this distribution.

The parameter values for Eq. (1.48) that we use in these simulations are

Quantity	Tritium concentration [%]						
	0	1	5	11	18	30	50
ξ_T	0.0	0.01	0.05	0.11	0.18	0.30	0.50
ξ_D	0.996	0.986	0.946	0.886	0.816	0.696	0.496
ξ_α	0.002	0.002	0.002	0.002	0.002	0.002	0.002
(ξ_T/ξ_D)	0.0	0.010	0.053	0.124	0.221	0.431	1.008
λ_{DD} [μm]	74.5	74.9	76.4	79.0	82.3	89.1	105
$v_A/c [10^{-3}]$	34.2	34.1	33.8	33.3	32.7	31.9	30.6
$u_{\perp 0}/v_A$	0.977	0.980	0.989	1.00	1.02	1.05	1.09
$u_{\parallel 0}/v_A$	0.808	0.810	0.818	0.830	0.844	0.867	0.903

Table 5.2: Summary of particle species parameters in our simulations for different relative tritium concentrations, ξ_T , with respect to electron number density, see also §4.1.2. Concentration ratios for each ion species (σ) are denoted by ξ_σ , along with the fuel ion species ratio, ξ_T/ξ_D . Quantity λ_{DD} is the deuteron Debye length, which increases with tritium concentration. The perpendicular and parallel birth velocities of the alpha-particles remain fixed across all simulations. Their values normalised to Alfvén speed v_A therefore increase with tritium concentration, due to the resulting mass density effect.

inferred from the full orbit calculations for 3.5 MeV alpha-particles in JET already mentioned, as in previous analytical and PIC studies of ICE observations from JET plasma 26148 [39, 42, 56, 59, 101, 104–106, 120]. As an example, for a 1% tritium concentration, we have $u_{\perp 0} = 0.98v_A$, and the value of the parallel drift velocity $u_{\parallel 0}$ then follows from the total particle velocity $|u_0| = \sqrt{u_{\parallel 0}^2 + u_{\perp 0}^2} \approx [3.5\text{MeV}/(m_\alpha/2)]^{1/2}$, yielding $u_{\parallel 0} = 0.81v_A$. To further approximate the wedge distribution of ICE-generating alpha-particles that is believed to have arisen in the outer midplane edge of the JET plasma, we initialise with velocity spreads of the perpendicular and parallel components of the drifting ring-beam in Eq. (1.48) given by $u_{\perp r} = 0.001v_\alpha$ and $u_{\parallel r} = 0.01v_\alpha$ respectively.

Physically motivating the choice of initial velocity-space distribution for the minority energetic ion population driving ICE is central to both the PIC-based and analytical approaches to the interpretation and prediction of ICE spectra. This requires careful analysis of particle orbits, see also for example Fig. 2 of Ref. [112], Fig. 3 of Ref. [114], Table 1 of Ref. [79] and Refs. [127, 128]. The diagnostic goal of mapping back from observed ICE spectra, via MCI physics, to the most likely velocity-space distribution of emitting ions is under active investigation using a range of techniques, see for example Refs. [90, 138, 142, 185, 186], which include the application of deep neural networks.

5.2 Time evolution of field and particle energies

We first construct a physics baseline comprising three simulations, which have tritium concentrations representative of trace tritium (1%) and preliminary tritium experiment (11%) DT plasmas in JET [187], and of future high power conditions (50%) relevant to ITER [183, 188, 189]. Further simulations with tritium concentrations of 5%, 18% and 30% are also reported here. In order to establish the intrinsic noise level, we have run an EPOCH PIC computation with no energetic minority ions, 1% tritium and 99% deuterium, together with kinetic electrons. In order to benchmark with respect to earlier simulations of ICE from JET plasma 26148 that included the energetic alpha-particles with thermal majority deuterons [37, 100, 118], but omitted the thermal tritons, we have repeated this scenario, as described in the following sub-section.

5.2.1 First principles PIC simulation of MCI with zero tritium concentration

The time evolution of the energy densities of particles and fields for a plasma consisting of a thermal Maxwellian deuteron population and minority 3.5 MeV

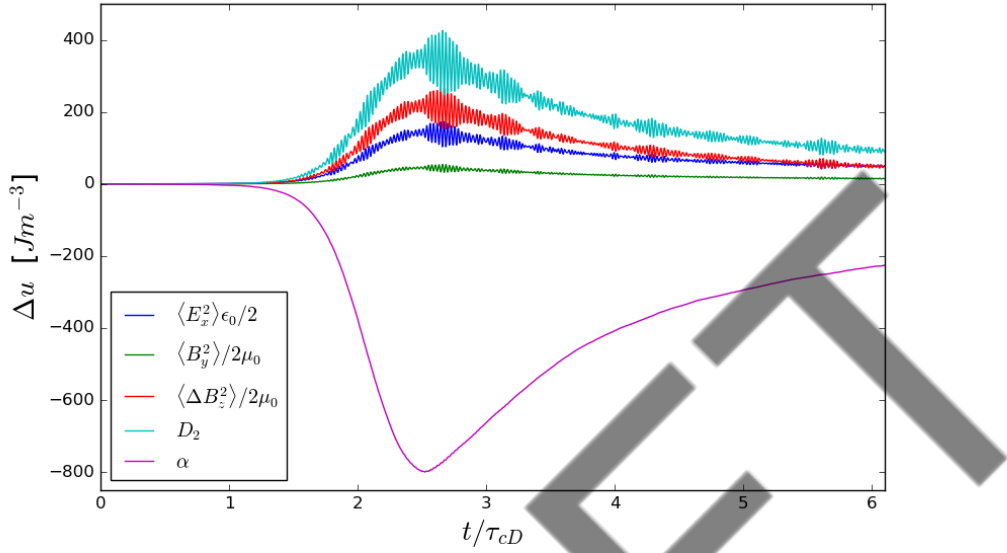


Figure 5.1: Time evolution, normalised to the deuteron cyclotron period, τ_{cD} , of the change in E_x , B_y and ΔB_z field energy densities, and deuteron and alpha-particle kinetic energy densities, as labelled, in units of $[Jm^{-3}]$. These traces are for a pure deuterium thermal plasma with a minority energetic 3.5 MeV alpha-particle population, initially distributed in velocity space as a drifting ring-beam, see Eq. (1.48). For parameters, see Table 5.1 and the first column of Table 5.2.

alpha-particles, initially distributed as in Eq. (1.48), is shown in Fig. 5.1. The free energy of the alpha-particles is transferred both to the excited electromagnetic (ΔB_z) and electrostatic (E_x) components of the fields, as well as to the thermal deuterons whose oscillation supports the excited fast Alfvén wave (FAW). These time traces are characteristic of the MCI, and correspond closely to equivalent plots in previous simulations, notably Fig 2 of Ref. [101]. Figure 5.1 thus provides an initial baseline for our simulations, presented below, which also include a thermal triton population.

Figure 5.2 shows the change in the probability distribution function of the alpha-particles with respect to the magnitude of their velocity normalised to the Alfvén speed $|\mathbf{v}|/v_A$. The difference between the initial (blue) and final (red) distributions reflects two main effects, as the collective relaxation of the alpha-particles transfers free energy to the bulk plasma and excited fields (see Fig. 5.1). These are spreading, combined with a corresponding decline in their mean velocity.

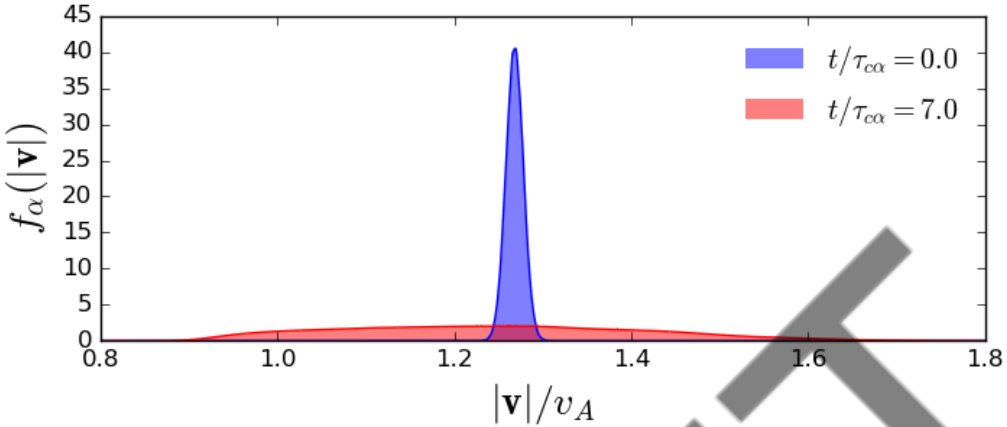


Figure 5.2: The probability distribution function of the fast alpha-particle's velocity throughout the simulation (as per legend), normalised to the Alfvén velocity, v_A .

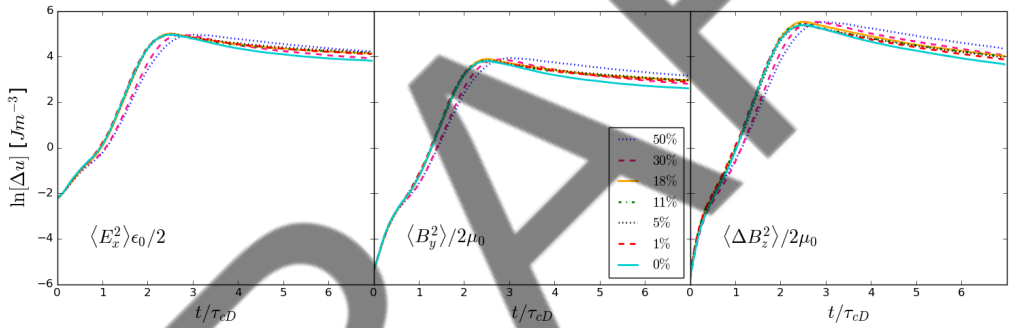


Figure 5.3: Time evolution of the natural logarithm of energy density [Jm^{-3}] of the three field components E_x^2 (left), B_y^2 (centre) and ΔB_z^2 (right), for different tritium concentrations colour-coded according to the legend in the central panel. Time is normalised to the deuteron cyclotron period τ_{cD} , and the interval plotted covers $0 < t/\tau_{cD} < 7$.

5.2.2 Field energy densities and dependence on tritium concentration

Figure 5.3 plots the time evolution of the change in energy density associated with field components E_x , B_y and the oscillatory part of B_z , for eight different tritium concentrations ranging from zero to 50%. A natural logarithmic vertical scale is used to assist visual identification of the initial exponential growth phase, corresponding to the linear MCI [38, 94, 96, 120], which ends by $t \simeq 2\tau_{cD}$. Thereafter, the instability saturates.

In Fig. 5.3 the structure of the time traces is similar across all three panels,

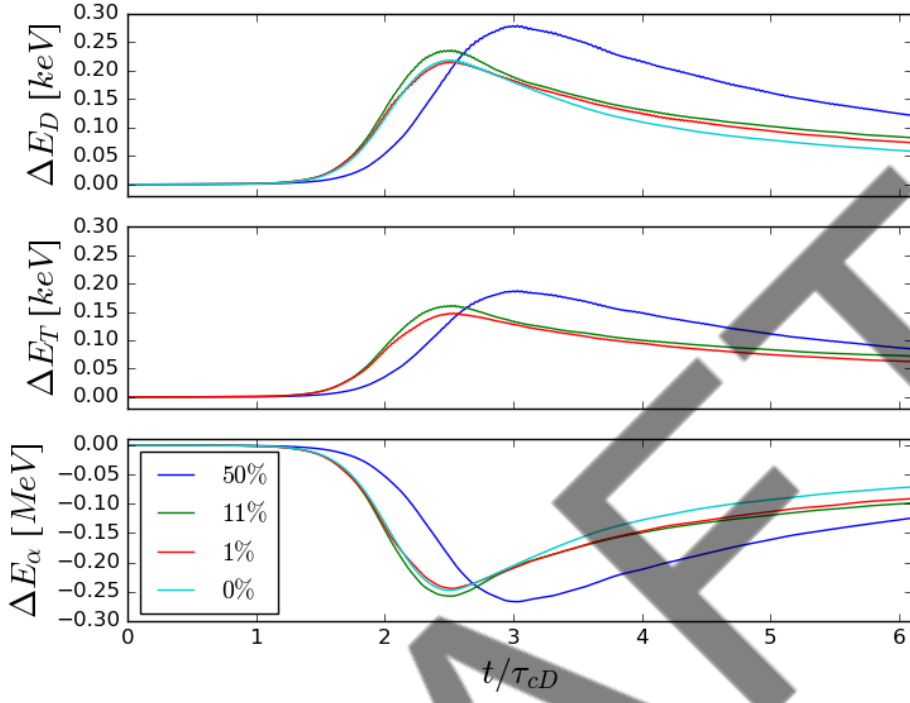


Figure 5.4: Time evolution of the change in mean kinetic energy per particle for: (*Top panel*) deuterons; (*Middle*) tritons; (*Bottom*) alpha-particles. Traces for four different tritium concentrations between zero and 50% (see legend) are shown in each panel. Units of energy are keV and MeV for the thermal and energetic ion species respectively. Time is normalised to deuteron cyclotron period, τ_{cD} .

and is essentially invariant against tritium concentration for each of the three field components. Increasing tritium concentration leads to slightly lower linear growth rates of the MCI for all three field components. By a small margin, the energy density associated with the oscillatory B_z component is larger than that for E_x , so that the electromagnetic component of the fields exceeds the electrostatic, in common with the zero tritium cases shown in Fig. 5.1 here, and in Figs. 2 of Refs. [111], [100] and [101].

5.2.3 Particle energy and dependence on tritium concentration

The variation of the time-evolving particle kinetic energy with respect to tritium concentration is shown in Fig. 5.4. This presents the time traces of the average change in kinetic energy per particle for all three ion species, in simulations with four different tritium concentrations in the range zero to 50%. In each

panel, it can be seen that the time traces are very similar for tritium concentrations of 11% and lower, but differ for the 50% tritium concentration. The traces are consistent with the expectation that, for a plasma with higher mass density and correspondingly lower Alfvén speed, the instability will take longer to evolve. The average energy transfer from alpha-particles to thermal ions increases slightly with tritium concentration in Fig. 5.4. We note from the bottom panel of Fig. 5.4 that each alpha-particle surrenders about 8% of its initial 3.5 MeV kinetic energy, as a consequence of its participation in the MCI.

Inclusion of the tritium ion species enables the comparison here, for the first time, between energy transfer to both thermal ion populations (deuterons and tritons) under the alpha-particle-driven MCI. The upper two panels of Fig. 5.4 show that the peak energy transfer to each deuteron and to each triton is approximately in the ratio 3:2, which is equal to the ratio of their masses, and that this ratio is invariant against tritium concentration. We now explore the conjecture that this partitioning of energy transfer between the two thermal ion species may arise from a Larmor radius matching condition in saturated gyro-resonance, similar to that recently identified in Ref. [190] for a different scenario also involving three ion species.

Let us follow the hypothesis that each ion species undergoing collection gyro-resonance evolves to a condition such that their Larmor radii match in the saturated nonlinear regime of the MCI. For the thermal deuterons and tritons, whose evolved Larmor radii scale with their perpendicular kinetic energy as augmented by the MCI, this would imply that the ratio of their change in kinetic energies is

$$\left\langle \frac{\Delta E_T}{\Delta E_D} \right\rangle = \frac{m_D q_T^2}{m_T q_D^2} \approx \frac{2}{3}. \quad (5.1)$$

Here q_σ is the charge of each species respectively and $\langle \cdot \rangle$ denotes the velocity-space ensemble average. The ratio 2/3 obtained in Eq. (5.1) corresponds to that inferred from Fig. 5.4, and this supports the conjecture.

Figure 5.5 plots the ratio of Eq. (5.1) for each tritium concentration as a function of time. Spurious features at the initialisation of the simulation quickly converge to the 2/3 constant value for all traces, and remain so for the remainder of the simulation duration, confirming the gyro-resonant behaviour of multicomponent plasma simulations.

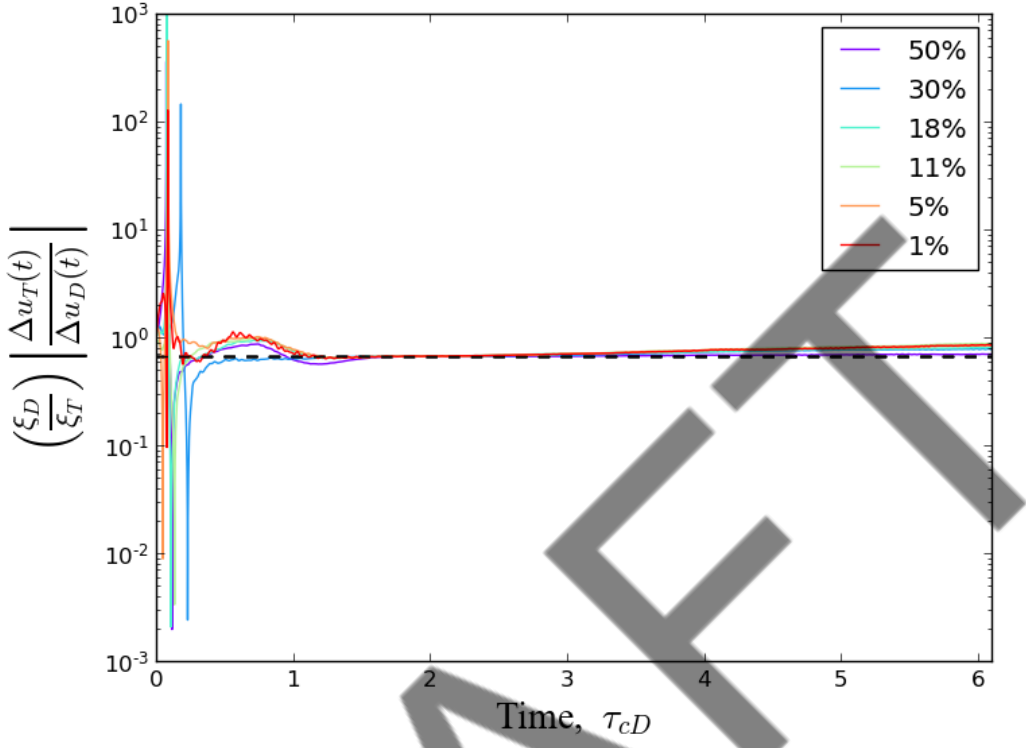


Figure 5.5: The gyro-resonance condition of the energy densities of the ion species deuterons (D) and tritons (T) through time, normalised to the deuteron cyclotron period τ_{cD} , for all of the varying triton concentrations from 1 to 50% (as labelled). The dashed horizontal line is the mass ratio between deuterons and tritons, as predicted by theory in Eq. (4.7) and Eq. (5.1).

5.3 Influence of tritium concentration on the spatiotemporal distribution of excited field energy

Spatiotemporal Fourier transforms of the energy density associated with the B_z component of the excited fields, for triton concentrations between zero and 50%, are presented in Fig. 5.6. Alongside each panel is shown the corresponding power spectral density (PSD) with respect to frequency, examined further in Fig. 5.8. All four panels of Fig. 5.6 show the same essential features, which are invariant against tritium concentration: the excited field energy is concentrated at the intersection of successive deuteron cyclotron harmonic waves at $\omega \sim n\Omega_D$ with the fast Alfvén wave (FAW) branch, with the strongest excitation at $(kv_A, \omega) \simeq (20, 18)\Omega_D$. The cyclotron harmonic waves are particularly well resolved in Fig. 5.6 for $\omega \leq 10\Omega_D$, as horizontal stripes.

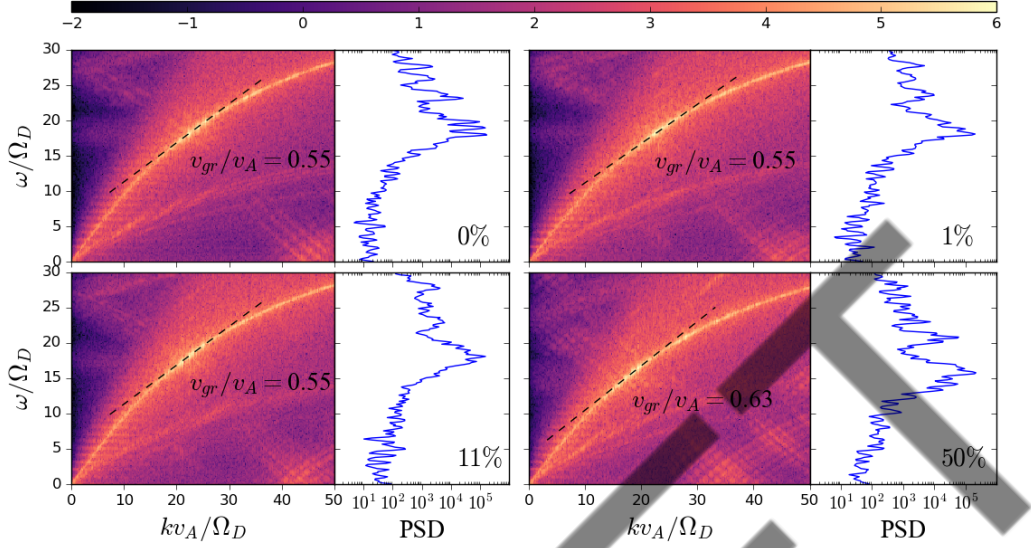


Figure 5.6: Distribution of energy in the oscillatory B_z magnetic field component in wavenumber-frequency space, for triton concentrations from zero to 50% as labelled. To the right of each spatiotemporal Fourier transform is the corresponding logarithmic (base 10) power spectral density (PSD) with respect to frequency. The colour scale (see legend) denotes the logarithm of the spectral field energy density. Frequency is normalised to the deuteron cyclotron frequency Ω_D and wavenumber is normalised using also the Alfvén speed, v_A . Group velocity at the peak power in the most excited region, characteristic of the MCI, drawn as a dashed black line and given per panel.

5.3.1 Group and phase speed of the MCI

One examination of the MCI through these tritium concentration simulations is to consider the position in frequency-wavenumber space of the most excited region and its corresponding group and phase speed. We note that, in previous simulations also, this region is present following the introduction of a minority energetic species, and hence we refer to this as the most excited MCI region. To calculate the phase and group velocity of this region, we find the corresponding (ω_{MCI}, k_{MCI}) co-ordinates of the maximum power along the FAW branch using the power spectra frequency at peak excitation in Fig. 5.8. Phase speed is calculated as ω_{MCI}/k_{MCI} , then, using the FAW dispersion relation Eq. (1.37), we extract the gradient along the curve, giving the group velocity $d\omega/dk|_{MCI}$. Shown in Fig. 5.7 are the phase and group speeds for each tritium concentration dependent FAW dispersion at (ω_{MCI}, k_{MCI}) .

With an increase in the mass density of the DT plasma through increased

tritium concentration, the FAW dispersion contracts in frequency space for a given wavenumber, leading to the most excited region of the MCI to appear at a lower frequency and wavenumber than for a plasma with a relatively lower plasma density (tending towards a pure deuterium). In this case, Fig. 5.7 reveals that the phase speed of the MCI decreases, as expected. However, it is interesting to find from this analysis that the group velocity of the most excited MCI region remains mostly unchanged between a rise in tritium concentration from zero to 50%. As the MCI is understood to grow most strongly for phase matching waves when $v_{\perp} \sim v_A$, it is of great importance for an investigation into the importance of plasma waves moving at a constant group velocity regardless of its density.

The origin of ω_{MCI} and k_{MCI} is as of yet unknown, but we propose here that it is the result of evanescent wave driving from the real and imaginary components to two solutions of the FAW dispersion, Eq. (1.37), accompanied with a Doppler shift, described in theory in §7.4.4. The FAW dispersion, repeated here, has solutions of $\mathbf{k}c/\omega = \pm\sqrt{(B \pm F)/2A}$, where we have found equivalent frequency-wavenumber pairs existing for the $\Re[\sqrt{(B - F)/2A}]$ and $\Im[\sqrt{(B + F)/2A}]$ solutions. These can be represented as a complex number, whose real and imaginary components are equated such that $\cos(\zeta) = \sin(\zeta)$ for some complex plane angle ζ . Whilst this could explain the origin of the most excited region, it would be necessary that this also be observed in cold plasmas, as FAW dispersions are not singularly dependent on the minority energetic particle population, but the summation over all ions and electrons.

5.4 Variation of simulated ICE frequency spectra with tritium concentration

Figure 5.8 presents power spectral densities (PSD) which are calculated by integrating the square of the spatiotemporal Fourier transforms, given in Fig. 5.6, over wavenumber at each frequency. The domain of integration is a $k > 0$ region which encompasses the FAW and the features which correspond to ICE. The intensity of the spectral peaks is suprathermal by two or more orders of magnitude, compared to the case of the thermal DT background plasma containing no energetic ions (black traces in Fig. 5.8). This reflects their origin in a collective instability, the MCI. For an 11% triton concentration, Fig. 5.8 shows that spectral peaks at deuteron cyclotron harmonics in the range $3 \leq \omega/\Omega_D \leq 15$ are much more intense than for the 1% and 0% triton concentrations, and are generally more sharply defined. Conversely, spectral peaks in the range $17 \leq \omega/\Omega_{\alpha} \leq 19$ are strongest for the lowest tritium concentrations. These trends can also be

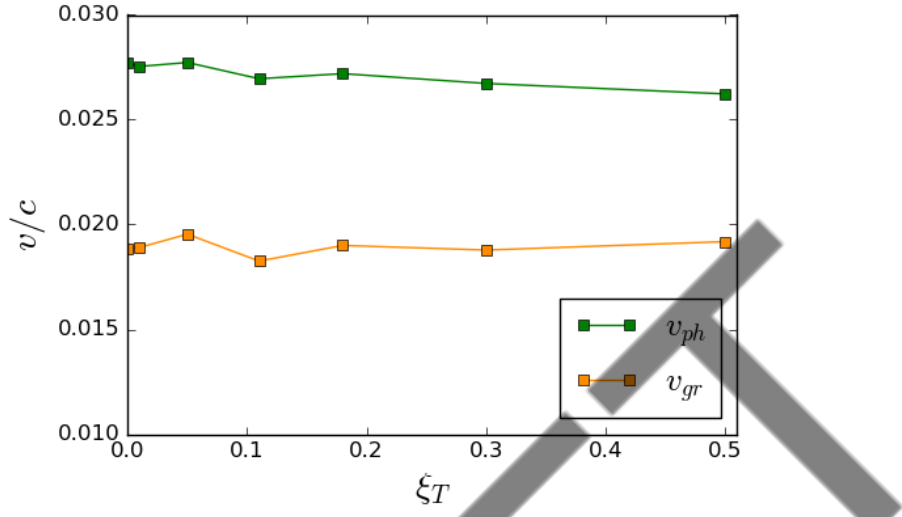


Figure 5.7: Phase and group velocity of the most excited MCI region in frequency-wavenumber space, normalised to the speed of light, which is invariable of tritium concentration. Extracted along the FAW following gradients of Eq. (1.37) in frequency-wavenumber space corresponding to the position of the strongest growing frequency as extracted from Fig. 5.8.

seen in Fig. 5.6. Doublet splitting [37] of some of the spectral peaks is observed for all tritium concentrations. This shows encouraging correspondence with the splitting of spectral peaks observed for the JET DT ICE data plotted in Fig. 2 of Ref. [58], particularly at the sixth deuteron cyclotron harmonic, which is also the ninth harmonic of the triton species. We note that doublet splitting appears to be a feature of the linear MCI, see for example Fig. 3 of Ref. [39] and Ref. [37], which is imprinted on the saturated nonlinear MCI, as here.

An unintended consequence of our computational limitations on ICE is that with a higher concentration of minority alpha-particles (such that NDW is conserved) the alpha-particles are no longer an energetic minority, $\xi_\alpha E_\alpha > \xi_D E_D$. This has the effect of driving stronger ICE and the potential of driving parallel wave modes, such as compressional Alfvén eigenmodes (CAEs) [146]. Since our simulations are in the 1D3V regime and the angle of the magnetic field is quasi-perpendicular, these parallel wave modes have little to no effect on the results presented. Work has also shown that ICE can still be driven for sub-Alfvénic minorities, such as those observed in LHD during NBI heating and subsequent PIC simulations [116].

Comparisons between the simulated ICE spectra shown in Fig. 5.8 thus reveal clear underlying trends with respect to increasing triton concentration,

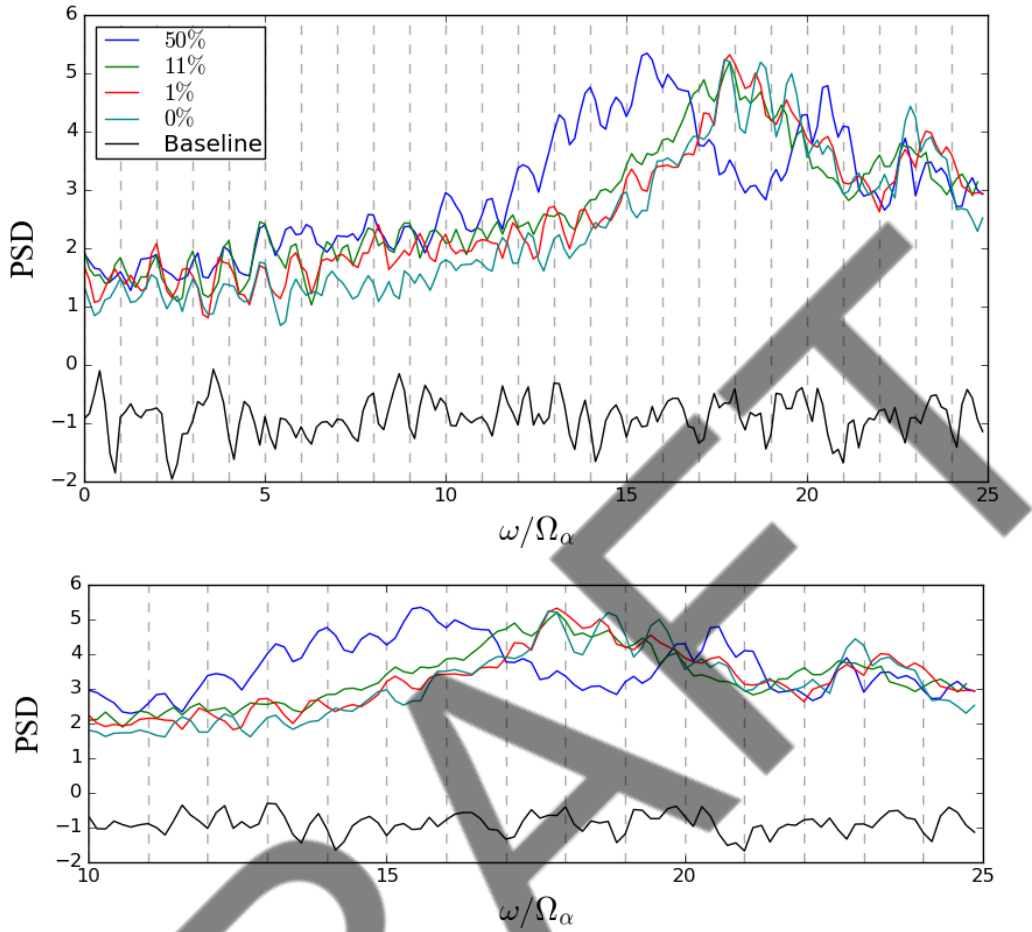


Figure 5.8: (*Upper*) Logarithmic (base 10) power spectral densities (PSD) of simulated ICE in the frequency range $0 < \omega < 25\Omega_\alpha$, for four tritium concentrations between zero and 50%, see legend. Vertical dashed lines indicate integer harmonics of the alpha-particle cyclotron frequency Ω_α . (*Lower*) Expanded version of the upper panel for the range $10\Omega_\alpha < \omega < 25\Omega_\alpha$, in which the variation between spectral structure is greatest. In both panels the black trace labelled “Baseline” is the noise level in a simulation for the thermal DT plasma in the absence of an additional energetic ion population.

whilst maintaining invariant the essential phenomenology of excitation at integer harmonics of the alpha-particle cyclotron frequency.

5.5 Comparison of growth rates between simulation and MCI theory

Previous first principles kinetic simulations using PIC codes have demonstrated good alignment with key aspects of the the analytical theory of the linear MCI. These include: the simultaneous excitation of fast Alfvén waves at multiple integer cyclotron harmonics of the energetic minority particles [58]; strong growth rates of waves propagating quasi-perpendicular to the magnetic field; scaling between field energy density growth rates and energetic minority particle concentration [100, 101]; and doublet splitting of the spectral peaks [37, 121].

Analytical growth rates of the MCI given by Eqns. (36), (19) and (29) from Refs. [38], [117] and [39] respectively, are shown in black in Fig. 5.9 for a thermal deuteron and energetic alpha-particle plasma, with peaks highlighted with crosses. Inferred growth rates of the excited B_z field component in our simulations, during the early time range corresponding to the phase of strongest

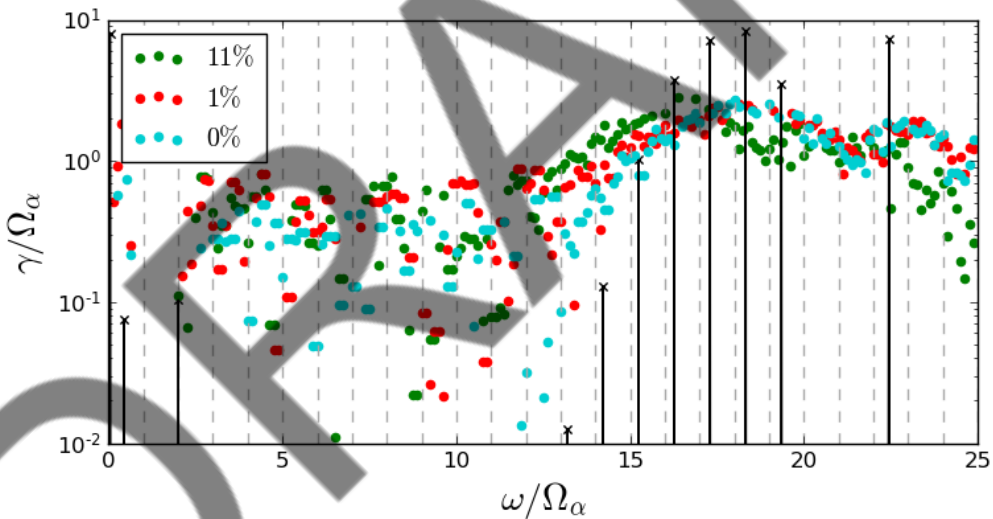


Figure 5.9: Analytical linear growth rates of the MCI (black vertical lines) calculated from Eq. (29) of Ref. [39], for a two-ion-species plasma comprising majority thermal deuterium with a small minority drifting ring-beam population of 3.5 MeV alpha-particles at a reduced concentration of 10^{-4} , and no tritium. Empirical growth rates (colour scheme according to previous figures) of the excited B_z field component in an 11% (green), 1% (red) and zero-percent (turquoise) simulation, inferred from the measured rise of its spatial Fourier transform, shown in Fig. 5.10, during the early time interval $0.5 < t/\tau_{cD} < 2$ which corresponds to the exponential growth phase inferred also from Fig. 5.4.

linear MCI growth, identified from Fig. 5.3, are given also in Fig. 5.9 as coloured scatter points. Growth rates are extracted empirically from our simulations by quantifying the time evolution of the spatial Fourier transform shown in Fig. 5.10. Normalisation of growth rates by the alpha-particle cyclotron frequency can be equivalently normalised by the deuteron cyclotron Ω_D , and can be seen in Fig. 5.6. We focus on solutions corresponding to frequencies that lie on the FAW dispersion relation identified in Fig. 5.6. These empirical growth rates are obtained from the mean values of the exponential fits to the simulation data, which are iteratively calculated following the same method as in Sec. 6 of Ref. [115].

Figure 5.9 shows that analytical linear MCI growth rates provide a good guide to the location, and relative strength, of field excitation in the frequency range of strongest initial growth in our simulations, $14 < \omega/\Omega_D < 19$. The analytical theory also captures the decline in growth rate seen in our simulations at $20\Omega_D$, and its recovery for the 22nd and 23rd deuteron harmonics. As tritium concentration increases, it can be seen that the empirical growth rates at the lowest cyclotron harmonics rise in comparison to the pure deuterium case (black). There is also an increase in the empirical growth rates for frequencies between $13\Omega_D$ and $17\Omega_D$, corresponding to the shift of the strongest MCI region noted in Fig. 5.10 (and, later, in Figs. 5.6 & 5.8). While all these trends are similar, the magnitudes of both calculated growth rates differ, in consequence of the value of ξ_α in the simulations, as discussed in §5.1.1.

5.6 Impact of tritium concentration on the distribution of field energy in wavenumber space

The time evolution of the spatial Fourier transform of the excited B_z field component is plotted with respect to normalised k -space in Fig. 5.10, for simulations with four different tritium concentrations, ranging from zero (top panel) to 50% (bottom panel). These plots encompass: the linear phase (from Fig. 5.3, $0.5 \leq t/\tau_{cD} \leq 2$), whose duration is briefest (because the MCI drive is strongest) for wavenumbers in the range $15 < kv_A/\Omega_D < 25$, which corresponds to frequencies in the range $13 < \omega/\Omega_D < 16$, as inferred from Fig. 5.6. It is evident from Fig. 5.10 that the region of strongest linear MCI drive shifts downwards in wavenumber space (and, consequently, in frequency) as the tritium concentration increases. We note that the value of the Alfvén velocity decreases from top to bottom of Fig. 5.10, since all simulations have the same value of electron number density n_e , whereas the mean ion mass increases.

The lower three panels of Fig. 5.10 show that, in contrast to the top panel with 0% tritium, the introduction of tritium leads to the growth, at early times $t \leq 2\tau_{cD}$, of localised concentrations of field energy in the region $kv_A/\Omega_D \leq 15$, which are separated by $kv_A/\Omega_D \sim 2.5$. These features are centred on wavenumbers which correspond to frequencies close to the joint cyclotron harmonics of the deuterons and tritons, such that $p\Omega_D = q\Omega_T$ where p and q are low integers. They evolve into the nonlinearly saturated regime of the MCI, after $2.5\tau_{cD}$. These features do not arise in the absence of tritium, but appear as soon as tritium is present at the 1% level. Their growth, localised to frequencies that correspond to cyclotron harmonic degeneracy between the deuterons and tritons, is a distinctive novel element of the simulations presented here. We conjecture that these features may play a role in establishing the Larmor radius matching that was previously identified in §5.2.3.

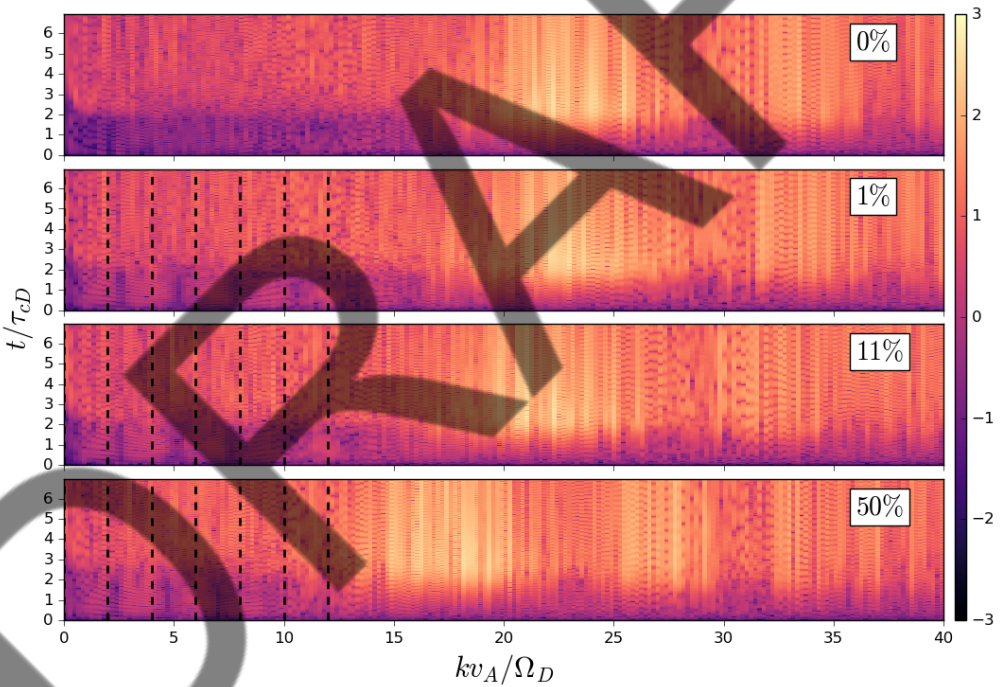


Figure 5.10: Time evolution of the spectral intensity of the spatial Fourier transform of the excited B_z field component, for tritium concentrations from zero (top panel) to 50% (bottom panel), as annotated. See Fig. 5.6 for the corresponding spatiotemporal Fourier transform. Wavenumber is normalised to Ω_D/v_A , and time to τ_{cD} . Features appearing for $\xi_T > 0$ at low wavenumber are highlighted by vertical dashed lines. The logarithmic colour scale is shown in the right-hand side colour-bar.

5.7 Influence of tritium concentration on nonlinear coupling of fields across wavenumber space

We are able to identify and quantify nonlinear wave coupling within our PIC simulations through normalised bispectral analysis [166, 191–194]. This technique is increasingly applied in plasma physics [167–170, 195], and was successfully used for this purpose on outputs from previous ICE simulations involving the MCI [101, 106, 111, 113, 171], as well as the observational ICE data from KSTAR [114]. The definition of normalised bicoherence in wavenumber space, $b_c^2(\mathbf{k}_1, \mathbf{k}_2)$, that we use is

$$b_c^2(\mathbf{k}_1, \mathbf{k}_2) = \frac{|\langle F(\mathbf{k}_1)F(\mathbf{k}_2)F^*(\mathbf{k}_1 + \mathbf{k}_2) \rangle|^2}{\langle |F(\mathbf{k}_1)F(\mathbf{k}_2)|^2 \rangle \langle |F^*(\mathbf{k}_1 + \mathbf{k}_2)|^2 \rangle}. \quad (5.2)$$

Here the value of b_c^2 , which is bounded between 0 and 1, represents the Fourier power of a signal due to quadratic nonlinear interactions between two waves driving a third wave with wavenumbers and frequencies that satisfy the matching conditions $\mathbf{k}_3 = \mathbf{k}_1 \pm \mathbf{k}_2$ and $f_3 = f_1 \pm f_2$ respectively. For the present applications of Eq. (2.25), F denotes the complex spatial Fourier transform of the magnetic field B_z , F^* is its complex conjugate and $\langle \cdot \rangle$ denotes averaging over timescales comparable to the simulation duration. We refer to Appendix B of Ref. [113] for a discussion of the counterpart to b_c^2 in frequency space. The strength of the

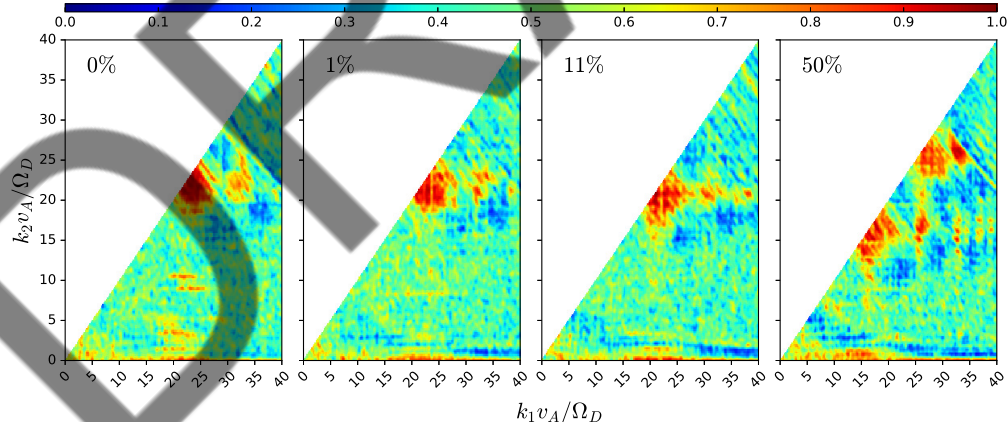


Figure 5.11: Normalised bicoherence of the Fourier power of the excited B_z component, for four simulations with increasing tritium concentration from zero and 50% (*left to right*), calculated using Eq. (2.25). The colour scale is linear and represents the strength of nonlinear coupling between wavenumbers k_1 and k_2 , both of which lie on the fast Alfvén wave dispersion relation seen in Fig. 5.6. On both axes the wavenumber variable kv_A/Ω_D is dimensionless.

nonlinear coupling is represented by the linear colour scale in Fig. 5.11, and is normalised across all four panels such that two waves which are not nonlinearly coupled have $b_c^2 = 0$ (dark blue), whereas those with the strongest nonlinear coupling have $b_c^2 = 1$ (deep red).

Turning first to the pure deuterium case whose bicoherence is plotted in the left panel of Fig. 5.11, we note two main regions of nonlinear wave coupling in wavenumber space. The most strongly driven modes, as identified from Fig. 5.6, occur for $20 < kv_A/\Omega_D < 25$; it is evident from Fig. 5.11 that these couple nonlinearly among themselves, and also to waves localised around $kv_A/\Omega_D \simeq 35$. A third, weaker, region of nonlinear coupling is also identifiable, between waves localised around $kv_A/\Omega_D \simeq 15$ and waves in the region $25 < kv_A/\Omega_D < 30$. We emphasise again that the bicoherence defined by Eq. (2.25) measures the strength of nonlinear coupling irrespective of wave amplitude, which may be small.

A new feature arrives in the bicoherence plots once tritium is introduced, even at the 1% level of concentration shown in the left centre panel of Fig. 5.11. This additional region of strong nonlinear coupling is between waves that have low integer values of kv_A/Ω_D and those in the region $15 \leq kv_A/\Omega_D \leq 20$.

5.7.1 Frequency shifting

Now we consider the extent of the shifting of frequencies observed in Fig. 5.8. This is dissimilar to the frequency shifts noted in Refs. [79] and [196], the former of which attributed a frequency shift to the parallel velocity of energetic protons and the subsequent parallel frequency resonance condition, but arises naturally out of the decreasing Alfvén wave speed, the inverse of which defines the strength of linear MCI growth. Multiple correlation methods were carried out to investigate said frequency shift between the zero and non-zero percent tritium concentrations simulations. These include: the cross-correlation and the phase-correlation; which has found application in financial markets [197] and two-dimensional image correction [159], respectively; the novel shared area method, see Appendix A; and measuring the change in frequency of the highest intensity peak. Extracting a frequency offset as a function of tritium concentration assumes that the underlying shape of power spectra dominates, as ICE remain mostly unaltered, and that the artefacts from treating the PSD data as periodic in the shared area method are insignificant with respect to the maximal overlap between spectra.

Figure 5.12 presents frequency offsets between power spectra presented in Fig. 5.8 with respect to the pure deuterium trace using the methods described.

All of the methods determined a linear relationship between the frequency offset in PSD features and tritium concentration. The ensemble averaged frequency offset was calculated as

$$\omega_{off}(\xi_T)/\Omega_D = (-4.74 \pm 0.34)\xi_T + (-0.01 \pm 0.16), \quad (5.3)$$

where errors are one standard deviation between fitting methods. As a general rule, it is found that for a $\sim 20\%$ increase in triton concentration, dominant power spectral features shift to lower frequencies by approximately a whole integer deuteron cyclotron harmonic.

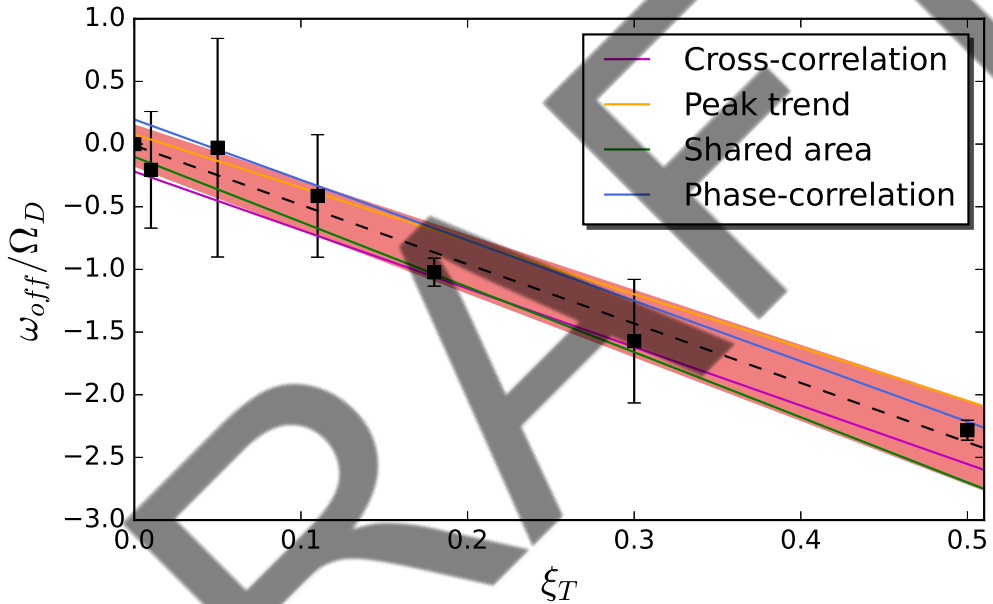


Figure 5.12: Frequency offset of the power spectra shown in Fig. 5.8 with respect to the pure deuterium simulation, normalised by the deuteron cyclotron frequency Ω_D , as a function of tritium concentration. Linear relationship derived from four methods, as named in the legend and presented as coloured lines. Scatter points are averaged frequency offsets calculated from each method, with one standard deviation error bars. Average overall relationship and its one standard deviation error are presented as a dashed black diagonal line and red area, respectively.

5.8 Quantitative comparisons of spectral dependence on tritium concentration

Let us now address the central question for this paper: does the inclusion of thermal tritons alongside the thermal deuterons lead to a more accurate simulated ICE spectrum driven by the fusion-born alpha-particles? To answer this – in the affirmative, as we now describe – it is necessary to quantify the difference between the simulated spectra shown in Fig. 5.8 (and other spectra, not shown here, at other tritium concentrations) and the observed alpha-particle-driven ICE spectrum from the JET plasma 26148 shown in Fig. 2 of Ref. [58]. For this, we adopt the peak-power-ratio (PPR) method, developed here, which is similar to the peak-to-average power ratio (PAPR) method [198–200]. To outline, the PPR method compares the relative power between peaks to determine both the location of peaks, but also the shape in the power spectra regardless of scale or units. The frequency-PPR plane which these points generate are drawn against the PPR of the JET 26148 spectra, the comparison of which produces a maximum likelihood (goodness-of-fit) statistic, denoted τ^2 [201–203] (see Appendix B for a detailed discussion on its calculation). The value of τ^2 , normalised to the number of spectral peaks over which it is calculated for each simulation (which varies, see again Fig. 5.8), is shown in Table 5.3 with respect to tritium concentration.

It follows from Table 5.3 that the PIC simulation with 11% tritium concentration has the lowest value of τ^2 and therefore gives rise to the spectrum which best matches the observed JET 26148 ICE power spectrum, outperforming the pure deuterium case and all others. Encouragingly, 11% was the actual tritium concentration in JET plasma 26148. This high degree of fidelity suggests that, in future, ICE spectra may acquire an additional diagnostic role by providing an independent indication of tritium concentration in DT plasmas.

$\xi_T [\%]$	0	1	5	11	18	30	50
τ^2/N_{peaks}	30.0	28.7	29.8	27.9	28.7	29.9	30.0

Table 5.3: Goodness-of-fit between simulated ICE spectra and the observed ICE spectra from JET plasma 26148. *Top row:* tritium concentration, ξ_T , in each simulation. *Bottom row:* maximum likelihood statistic τ^2 normalised to number of spectral peaks. This is minimised for an 11% tritium concentration simulation, which corresponds to the actual tritium concentration in JET plasma 26148.

5.9 Summary and conclusions

In summary, we have carried out a series of first principles kinetic simulations of the collective relaxation of a highly non-Maxwellian fusion-born alpha-particle population under JET edge plasma conditions. The character of the alpha-particle population remains invariant across this series. Its configuration in velocity-space is the wedge-type, drifting ring-beam, distribution of freshly born alpha-particles that was identified as the source of ion cyclotron emission in JET DT plasma 26148 and elsewhere. Our simulations are unique in that a gyro-resolved thermal triton population is present, in addition to the thermal deuterons that were the sole majority ion species in past simulations. Each of the simulations reported here has a different tritium concentration, ranging from zero to 50%. The presence of tritons increases the number of cyclotron resonant wave-particle interactions that are possible, together with the family of normal modes supported by the plasma. The associated change in mass density, at fixed electron number density, also changes the Alfvén speed in the plasma, and hence changes the ratio of alpha-particle velocity to the local Alfvén speed, which is an important parameter for the MCI which underlies ICE. A further novel question is the partitioning of energy between tritons and deuterons as the MCI proceeds. We emphasise that the fully gyro-resolved kinetic treatment enabled by the PIC computational approach of the EPOCH code addresses all these aspects from first principles without laying down modes for the plasma in advance, embodied in self-consistent solution of Maxwell's equations and the Lorentz force equation for very large numbers of particles. Importantly also, we can follow the system into its fully nonlinear regime, generating simulated ICE spectra for comparison with observation.

Our results show that the collective relaxation of the alpha-particle population leads to time-evolving flows of energy into the different excited field components (Fig. 5.3) that follow standard MCI phenomenology, and are largely invariant against tritium concentration. Greater differentiation with respect to tritium concentration occurs in the time-evolving flow of kinetic energy between ion species shown in Fig. 5.4. These changes are noticeable, but not major. Perhaps the most interesting novel aspect is that the change in ion kinetic energy is partitioned between deuterons and tritons in the ratio 3:2, and we have shown that this is consistent with a Larmor radius matching criterion for the MCI in its saturated state. The spatiotemporal distribution of excited field energy is captured in the Fourier transforms displayed in Fig. 5.6 for different tritium concentrations. Integration over wavenumber then gives rise to the simulated ICE spectra shown in the right panels of Fig. 5.6 and, in greater detail, in Fig.

[5.8](#). These show significant variation with respect to tritium concentration, such that it becomes meaningful to ask which simulated ICE spectrum best matches the observed ICE spectrum from JET plasma 26148. Remarkably, quantitative analysis of spectral peak heights and distribution shows (Table [5.3](#)) that our 11% tritium simulation best agrees; and 11% was the experimental value at peak performance. This provides motivation for further investigation of the underlying plasma physics.

Figure [5.9](#) shows good agreement between the system evolution at early times and the analytical theory of the linear MCI. In Fig. [5.10](#), plots of the time-evolving distribution of excited field energy in wavenumber space show noticeable differences between tritium concentrations of zero and just 1%. At the 1% level, features arise at wavenumbers corresponding to frequencies of the deuteron and triton cyclotron harmonics which are degenerate. The overall ICE spectrum is a product both of initial instability and of subsequent nonlinear coupling between the initially excited modes, which transfers energy across wavenumber space. In our simulations, we quantify the latter effect using bispectral analysis (Fig. [5.11](#)) to understand how the spectrum is built.

We conclude that the simulations presented here extend and reinforce the capabilities of ICE as a diagnostic of energetic ion populations in plasmas. We have shown that the introduction of thermal tritium in addition to thermal deuterium gives rise to detectable differences in the simulated ICE spectra generated by the fusion-born alpha-particles. There is major scope for exploiting the fidelity of these new simulations. As noted, of the different tritium concentrations used, the concentration 11% gives the best agreement with the observed ICE spectrum from the 11% tritium plasma in JET plasma 26148. It follows that, if all knowledge of the experimental tritium concentration had somehow become lost, it could be re-inferred from the measured ICE spectrum and the present simulations alone. Thus, ICE has become a potential diagnostic of thermal plasma ion species composition, as well as of energetic ion physics.

Chapter 6

Tritium ion influence on a Linear Maxwell-Vlasov solver extracting growth rates of the MCI

This chapter presents results from the newly developed linearised Maxwell-Vlasov code which numerically extracts linear MCI growth rate solutions across two dimensional wavenumber (k_\perp, k_\parallel) space of the generalised hot plasma dielectric tensor, given in Eq. (1.21). Departing from the LMV's origins in Ref. [37], this chapter reveals the consequences of the inclusion of tritium ions at various concentrations, most notably in forms of growth rate spectra and its doublet splitting. Doublet splitting is a unique spectral characteristic observed in the ICE spectrum of JET plasma 26148 [58] and in DIII-D [52]. In this chapter we show that its location in frequency and wavenumber space is a direct consequence of non-zero tritium concentrations. Comparisons between equivalent mass density DT and pure D plasmas are also considered. This suggests that the linear MCI growth rates dependency on the ratio between the minority energetic ion's perpendicular speed and the Alfvén speed, is instead implicitly dependent on the concentration of ions that constitute these multicomponent plasmas.

6.1 Computational method

We present here computationally enabled studies of the analytical linear MCI using the LMV Julia code (see §2.3)) of a minority fusion-born population of 3.5 MeV alpha-particles in a plasma comprising majority thermal deuterons and

Quantity	Value
n_e [10^{19}m^{-3}]	1.7
E_α [MeV]	3.5
B_0 [T]	2.07
ψ_0	55.2°
$u_{\parallel}/V_A(\xi_T = 0.0)$	−1.1
$T_{i,e}$ [keV]	1.0

Table 6.1: Initial quantities representative of the outer mid-plane edge of JET plasma 26148. Ion birth pitch angle ψ_0 is that expected at the location of observed ICE at a radial distance of $R_{ICE} = 4\text{m}$ (Fig. 3 of Ref. [58]).

tritons with concentrations between zero and 97.5%. This study complements recent PIC computational simulations, see Ref. [110] and Chapter 5, of the same scenario using a 1D spatial domain (hence 1D wave-vector). Those simulations thus focused on a relatively narrow range of wavenumbers for which MCI drive is strongest. In contrast, this chapter, while restricted to the linear regime, spans the whole of wavenumber space of (k_\perp, k_\parallel) . We use the same parameter sets to relate specifically to JET DT plasma 26148, see see Table 6.1, which was measured as having an 11% tritium concentration at maximum power. Earlier PIC simulations of ICE from this plasma [100, 113] used a single majority thermal deuterium ion bulk species and no tritium, owing to computational resource constraints.

The radial location of observed ICE within JET plasma 26148 was at $R_{ICE} \simeq 4\text{m}$. As the concentration of tritium ions in our LMV runs is increased, the mass density increases, reducing the Alfvén speed. Keeping the effective radial location R_{ICE} constant across multiple calculations, the pitch-angle ψ_0 of the minority energetic alpha-particles is also held constant, and from Ref. [37] $u_{\parallel} \approx -\cos(\arcsin(\sqrt{R_0 \sin(\psi_0) / R_{ICE}}))$, where $R_0 = 3.46\text{m}$ is JET’s major radius. As a consequence, the ratio between parallel birth velocity and Alfvén speed changes with tritium concentration ξ_T , for example $u_{\parallel} = -1.1V_A$ for $\xi_T = 0$, whereas $u_{\parallel} = -1.3V_A$ fo $\xi_T = 0.95$.

6.2 Dependence of growth rates in (k_\perp, k_\parallel) space on tritium concentration

Growth rates of the linear MCI calculated by the LMV code across (k_\perp, k_\parallel) space are presented in Fig. 6.1 for a pure deuterium plasma. This corresponds to Fig.

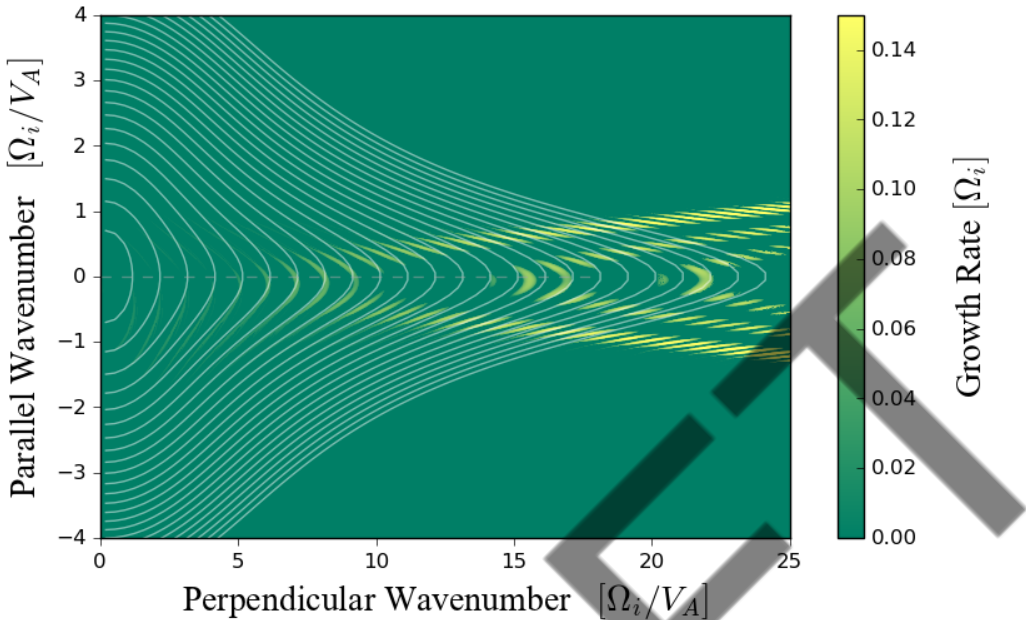


Figure 6.1: Linear MCI growth rates (colour scale right, normalised to Ω_i) for a pure deuterium plasma plotted across the two-dimensional (k_\perp, k_\parallel) domain [37] $0 \leq k_\perp V_A / \Omega_i \leq 25$, $-4 \leq k_\parallel V_A / \Omega_i \leq 4$, calculated by the LMV code. The white contours mark successive real frequencies $\omega = l\Omega_i$ corresponding to integer (l) ion cyclotron harmonics. This plot is obtained for a minority 3.5 MeV alpha-particles population, initialised as a drifting ring-beam with thermal velocity spreads of $v_{\parallel,th} = 0.01u$ and $v_{\perp,th} = 0.01u$, embedded in a majority thermal plasma specified in Table 6.1.

4 from Ref. [37], which was also obtained for a pure deuterium bulk plasma under JET plasma 26148 conditions. Figure 6.2 focuses upon the effects of the inclusion of tritium for concentrations $\xi_T \geq 0.45$, for mid-range perpendicular wavenumbers $11 \leq k_\perp V_A / \Omega_i \leq 15$, together with a zoom-in plot showing the birth and subsequent split of the 14th harmonic as ξ_T increases. In both Figs. 6.1 and 6.2, the isofrequency alpha-particle harmonics are plotted as curved white lines.

For a tritium dominant plasma (i.e. $\xi_T \gtrsim 0.5$), both rows of Fig. 6.2 show the development of islands of growth rates for integer perpendicular wavenumbers between $11 < k_\perp V_A / \Omega_i < 15$ focused along the $k_\parallel = 0$ line. Above 80% tritium, the $k_\perp \simeq 14\Omega_i/V_A$ (and higher) growth rate islands split asymmetrically above and below the $k_\parallel = 0$ line. This asymmetry between growth rates is a consequence of the non-zero parallel drift velocity $u_\parallel = -0.646u_0$, as seen in Figs. 3 and 4 of Ref. [37]. The splitting of the growth rate islands centred on

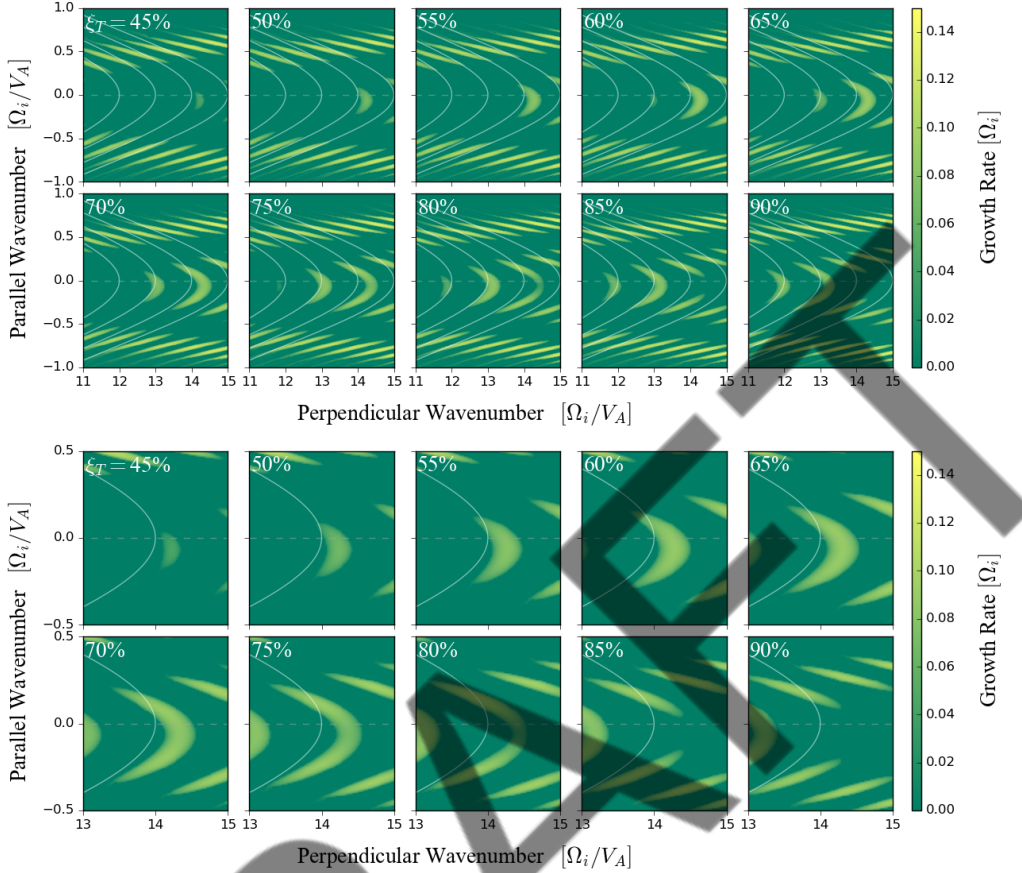


Figure 6.2: Linear MCI growth rates in $(k_{\perp}, k_{\parallel})$ space calculated for tritium concentrations $0.45 \leq \xi_T \leq 0.90$ as labelled top left, for the (top panels) quasi-perpendicular region $-1 \leq k_{\parallel}V_A/\Omega_i \leq 1$, $11 \leq k_{\perp}V_A/\Omega_i \leq 15$ in which the growth rate is greatest and the (lower panel) zoomed in portion $-0.5 \leq k_{\parallel}V_A/\Omega_i \leq 0.5$, $13 \leq k_{\perp}V_A/\Omega_i \leq 15$ of the growth of the 14th harmonic, with its corresponding harmonic isofrequency overlaid as a singular white contour line.

integer multiples of $k_{\perp}[\Omega_i/V_A] > 11$ highlights the beginnings of doublet splitting features, such as those present at the 10th and 11th alpha-particle cyclotron harmonics, see Figs. 6.7 and 6.8 below. This is a result of higher mass density, leading to a contraction of the frequency of the FAW dispersion relation for a given wavenumber.

6.2.1 Linear growth rates as a function of tritium concentration

The top two panels (a) and (b) of Fig. 6.3 show the growth rates for the propagation angle $\theta = 89^\circ$ of wavevectors \mathbf{k} with respect to the direction of the magnetic

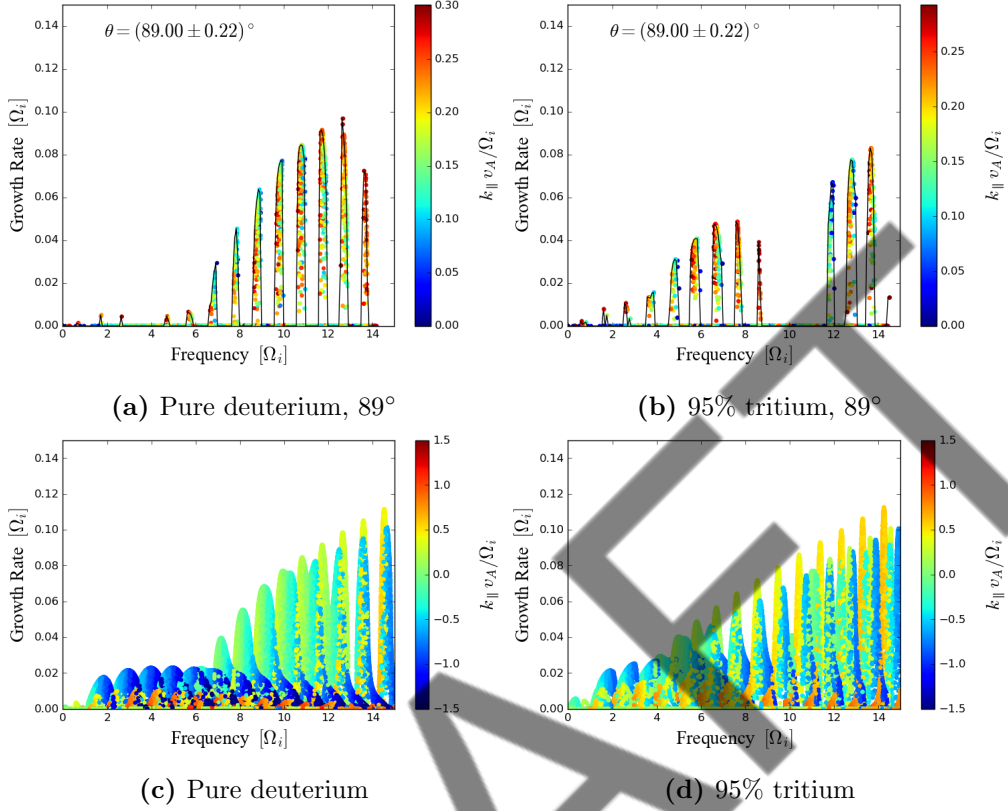


Figure 6.3: Panels (a) and (b) show the growth rates across $(k_{\perp}, k_{\parallel})$ space corresponding to an angle between the magnetic field and wave-vector ($\mathbf{B} \angle \mathbf{k}$) of $(89.00 \pm 0.22)^{\circ}$, as a function of frequency (see Eq. (2.19)) normalised to the alpha-particle cyclotron frequency for an (a) pure deuterium and (b) 95% tritium DT plasma. Panels (a) and (b) represent a subset of the data contained in panels (c) and (d), respectively, where the latter pair present growth rates across $(k_{\perp}, k_{\parallel})$ space for all propagation angles $\mathbf{B} \angle \mathbf{k}$. The linear shading scale indicates parallel wavenumber normalised by $[\Omega_i/V_A]$.

field \mathbf{B} . These are extracted across $(k_{\perp}, k_{\parallel})$ space for all combinations that satisfy $\theta \pm \Delta\theta = \arctan(k_{\perp}/k_{\parallel}) = (89 \pm 0.22)^{\circ}$. Panels (a) and (b) thus encompass power spectra for a range of parallel wavenumbers, whose values are indicated by the linear scale colour-bar, at some angle $\theta \pm \Delta\theta$ where $\Delta\theta$ is determined by the finite resolution of the $(k_{\perp}, k_{\parallel})$ domain. At this value of θ , there is a noticeable increase in the growth rate at low frequencies $< 7\Omega_i$ for $\leq 95\%$ tritium concentration compared to zero; whilst there is also a substantial decrease around $10\Omega_i$. Growth rates plotted with respect to the real frequency over the whole $(k_{\perp}, k_{\parallel})$ domain are shown for tritium concentrations of zero and 95% in the bottom two panels (c) and (d) of Fig. 6.3.

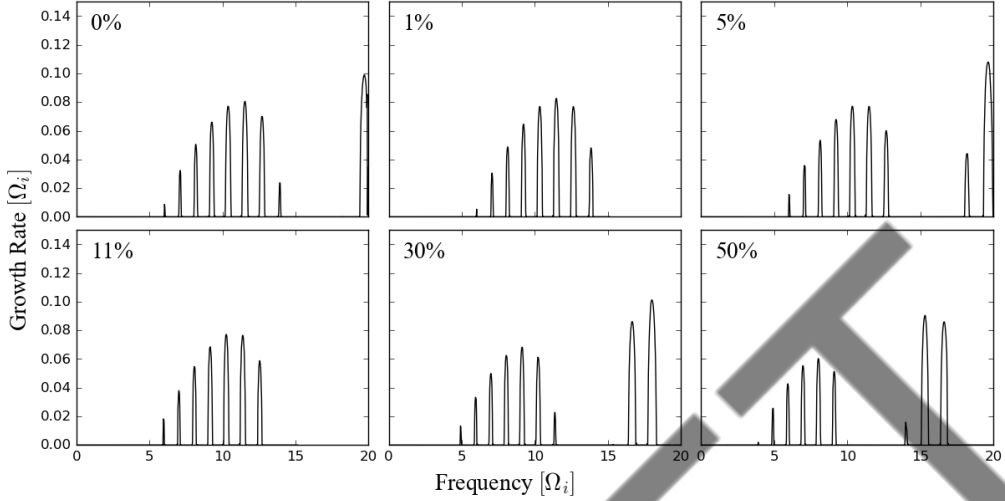


Figure 6.4: Linear MCI growth rates plotted versus frequency (both normalised to Ω_i) extracted along the magnetic field isoangle 89° in the (k_\perp, k_\parallel) plane for tritium concentrations which are labelled at top left, and are representative of those in the PIC study of Ref. [110].

The main qualitative differences between the zero tritium panels (a,c) and the 95% tritium panels (b,d) of Fig. 6.3 are the weaker growth rates at the lower harmonics for (a,c) and at the 10th, 11th and 12th harmonics for (b,d). In panel (c), the growth rates for frequencies $2 < \omega/\Omega_i < 6$ are approximately the same, whereas there is a steady increase in growth rates in the same range in panel (d). Doublet splitting is present across most frequencies in both panels (c) and (d), but is especially prevalent for $\omega/\Omega_i > 10$ in a 95% tritium bulk plasma.

Figure 6.4 shows growth rates for a propagation angle of 89° with respect to the magnetic field at tritium concentrations equal to those explored in recent PIC simulations of three ion component DT- α plasmas, see Table 2 of Ref. [110]. This utilises the growth rate extraction method presented in Appendix D, which differs from that used to produce panels (a) and (b) of Fig. 6.3, in that the algorithm treats $\Delta\theta$ as zero, and instead interpolates values between discretised line coordinates in (k_\perp, k_\parallel) space, so as construct the matrix of growth rates, in the same space, $\gamma(k_\perp, k_\parallel)$.

The top left panel of Fig. 6.4 represents the same dataset as panel (a) of Fig. 6.3, extended to a higher upper frequency limit of $20\Omega_i$. The remaining panels reveal the gradual lowering of growth rates between frequencies $5 < \omega/\Omega_i < 11$ as a consequence of increasing tritium concentration, together with the emergence of additional growth rates at frequencies $\omega/\Omega_i \geq 15$ for the 25% and 50% tritium concentrations.

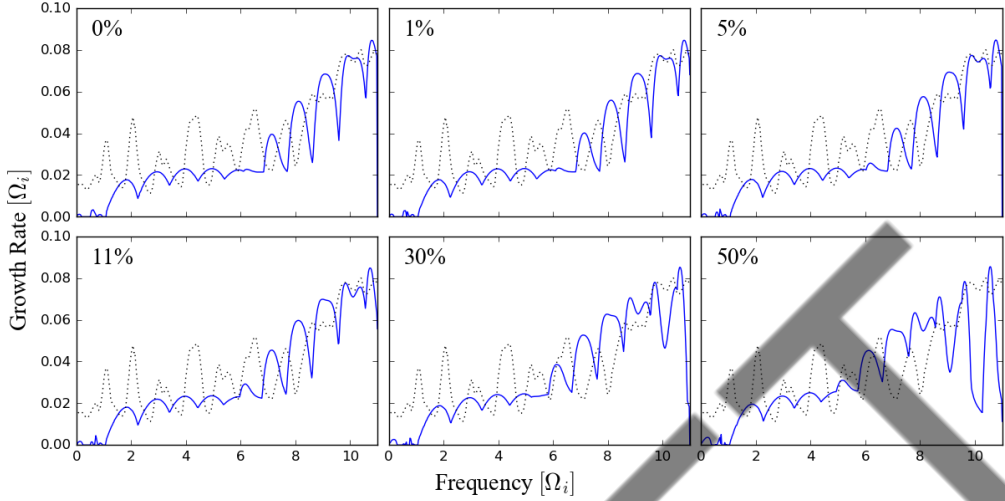


Figure 6.5: Maximum linear growth rates for all parallel wavenumbers (blue) compared against the re-scaled ICE signal from JET plasma 26148 (black dotted) digitised from Fig. 2 of Ref. [58], as a function of frequency normalised by Ω_i for a selection of tritium concentrations featured in PIC simulation results presented in Ref. [110], labelled top left.

For the same tritium concentrations, we present the total growth rate spectra across all k_{\parallel} values in Fig. 6.5, with an additional black trace representative of the JET ICE intensity signal from Fig. 2 of Ref. [58]. These are plotted on a modified logarithmic scale to match the range of the linear MCI growth rates. It is clear that, irrespective of tritium concentration, the most strongly driven linearly unstable modes occur for harmonics seven and above. This tends to confirm that the lower harmonics (six and below) observed in the ICE spectrum must be nonlinearly driven.

Figure 6.5 shows doublet splitting structure of the 10th and 11th cyclotron harmonic that arguably correlates to that seen in JET spectra. As the ICE amplitudes of the JET data presents the fully nonlinear structure of the MCI, whereas our LMV results present only linear growth rates, it is difficult to determine from Fig. 6.5 which tritium concentration best represents the ICE power spectra from JET plasma 26148. It is helpful, therefore, to complement LMV output with PIC simulations that can carry the MCI into its fully nonlinear regime, as in Ref. [110].

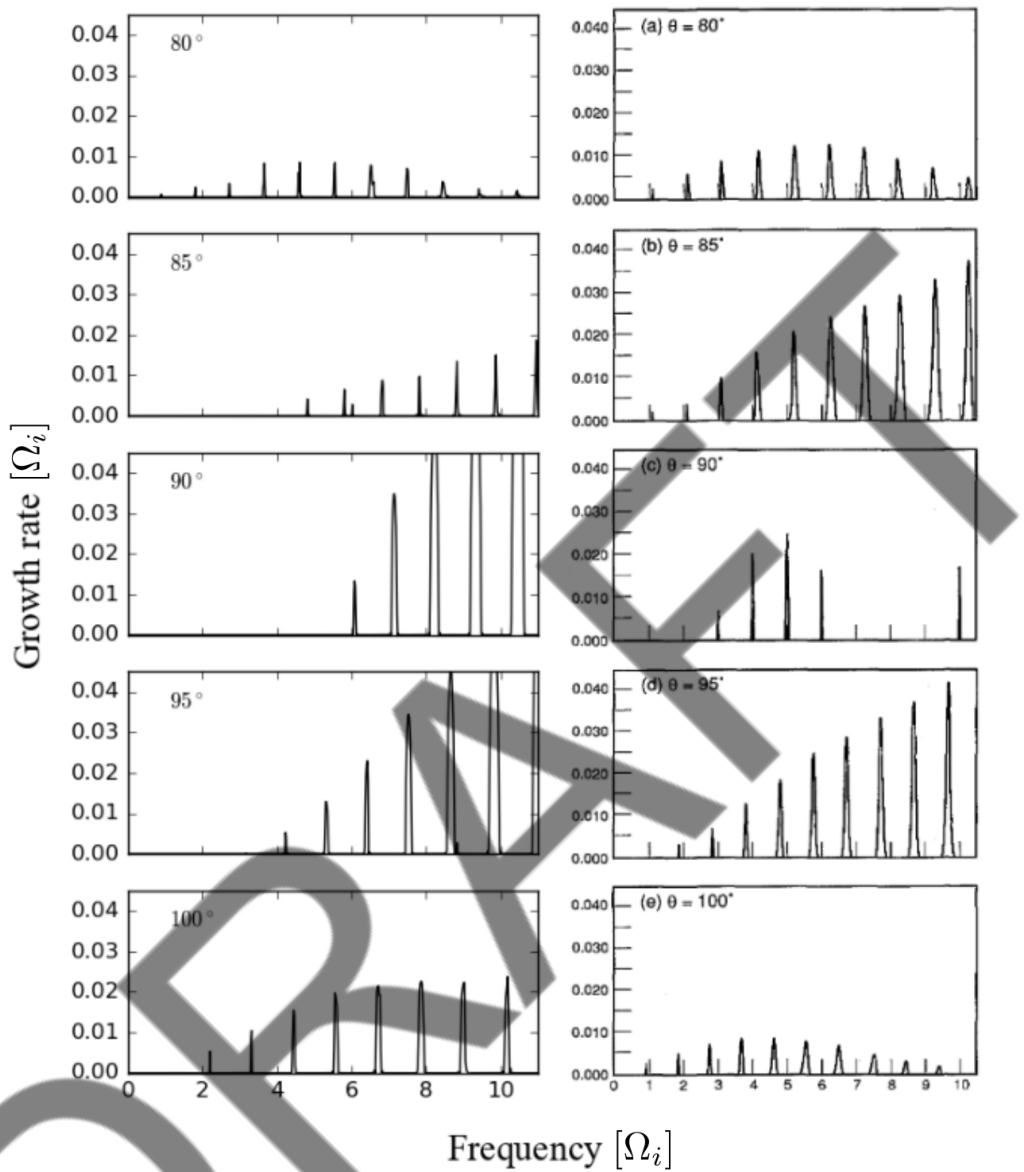


Figure 6.6: *Left:* growth rates found using the LMV code extracted along magnetic field isoangle lines in $(k_{\perp}, k_{\parallel})$ space for a pure deuterium plasma. Isoangles are positive valued clockwise from the vertical k_{\parallel} line, a description of the extraction process can be found in Appendix D, Fig. D.2. *Right:* theoretical growth rates of the MCI as adapted from Fig. 3 of Ref. [39].

6.3 LMV output as a representation of MCI linear theory

The left-hand column of Fig. 6.6 presents MCI growth rates for a pure deuterium plasma, obtained from the LMV code, along lines in $(k_{\perp}, k_{\parallel})$ space which correspond to magnetic field orientations between $\theta = 80^\circ$ and 100° , in 5° increments. Appendix D provides details of how these plots are obtained. The right-hand column of Fig. 6.6 reproduces the results of Fig. 3 of Ref. [39]: these are the original linear MCI growth rates obtained analytically for an equivalent plasma with the same magnetic field strength and wavevector orientations (see the top left of each panel). Overall there is excellent agreement across the two columns. Non-zero parallel drift velocities introduce a Doppler shift, which leads to asymmetries between features above and below the $k_{\parallel} = 0$ line, and is consistent with Ref. [39], where the bulk parallel velocity $v_{\parallel} = 0.25u_0$ is of opposite sign.

The primary differences between the left and right-hand columns of Fig. 6.6 are a result of the difference in approaches to their calculation. Whereas Ref. [39] extracts solutions to $\underline{\epsilon} = 0$ through a linearisation process, Ref. [37] uses the full hot dielectric tensor description and extracts solutions in the complex frequency plane. The linearisation process only uses Eq. (2.19) to calculate real frequencies at a given $(k_{\perp}, k_{\parallel})$, whereas the LMV code uses these values as initial steps for further iterations. At higher frequencies, the divergence between these two approaches to representing the FAW dispersion relation becomes apparent, leading to slight differences in the location of instability bands in frequency space, see Fig. 5 of Ref. [37].

There are slight differences between the parameters used here to extract linear growth rates using the LMV code, as compared to the analytical linear theory calculations of Refs. [117] and [39]. We use a smaller parallel thermal spread ($0.01u$ rather than $0.05u$) and a 1.5 times higher concentration of alpha-particles. Another difference between our work and the growth rates presented three decades ago in Ref. [39] is the implementation of a Maxwellian perpendicular velocity distribution, including a non-zero thermal velocity spread. Along with the improvement in the method used to extract these growth rate solutions, the frequency and strength of these excitations now better represent first-principles MCI theory.

6.4 Treatment of linear trends in peak growth rates

Trends in the frequency location of MCI spectral features derived from the LMV code were initially considered in Ref. [110], and can be seen in the linear growth rates plotted here in Fig. 6.3. We focus here on the changes in these growth rates with respect to frequency as the concentration of tritium is varied for all values of k_{\parallel} , representing all magnetic field orientations, which otherwise miss the asymmetric multi-parallel-wavenumber-variable doublet splitting. Figure 6.7 plots growth rates with respect to frequency across all k_{\parallel} values (employing the method described in Appendix D) for tritium concentrations between zero and 90%, as labelled at top left.

There is a prominent doublet split feature visible across all concentrations in Fig. 6.7, which can be seen for a pure deuterium plasma (top left panel) at the 11th alpha-particle cyclotron harmonic. This Figure presents other interesting features, including the strong dependence of growth rates at frequencies $> 10\Omega_i$ on the tritium concentration. This is a consequence of the corresponding change in the value of v_A , together with the fact that $u_{\perp} \simeq v_A$ for the strongest MCI growth.

Figure 6.8 presents zoomed in plots of the (initially pure deuterium plasma's) evolving 11th cyclotron harmonic doublet splitting feature identified in Fig. 6.7 and highlighted by curved red lines. Following a 10% increase in tritium concentration this feature evolves down in frequency space by half of a harmonic. Following an increase in the tritium concentration between zero and $\xi_T = 0.9$, there is an approximately linear frequency shift on the doublet split features by $\Delta\omega \simeq -5\Omega_i$. In other terms, features are translated downwards in frequency space by one whole deuterium cyclotron harmonic in consequence of a 20% increase in the concentration of tritium ions with respect to electron number density. Previous PIC results for three ion DT- α fusion plasmas modelled after the JET plasma 26148 [110] arrived at a similar trend in power spectral features of $\Delta\omega/\Delta\xi_T = -4.74\Omega_i$.

6.5 Peak frequency and growth rate dependence on tritium concentration

Trends in the frequency location of MCI spectral features derived from the LMV code were initially considered in Ref. [110], and can be seen in the linear growth rates plotted here in Fig. 6.3. We now draw focus to the changes in these growth rates with respect to frequency as the concentration of tritium is varied

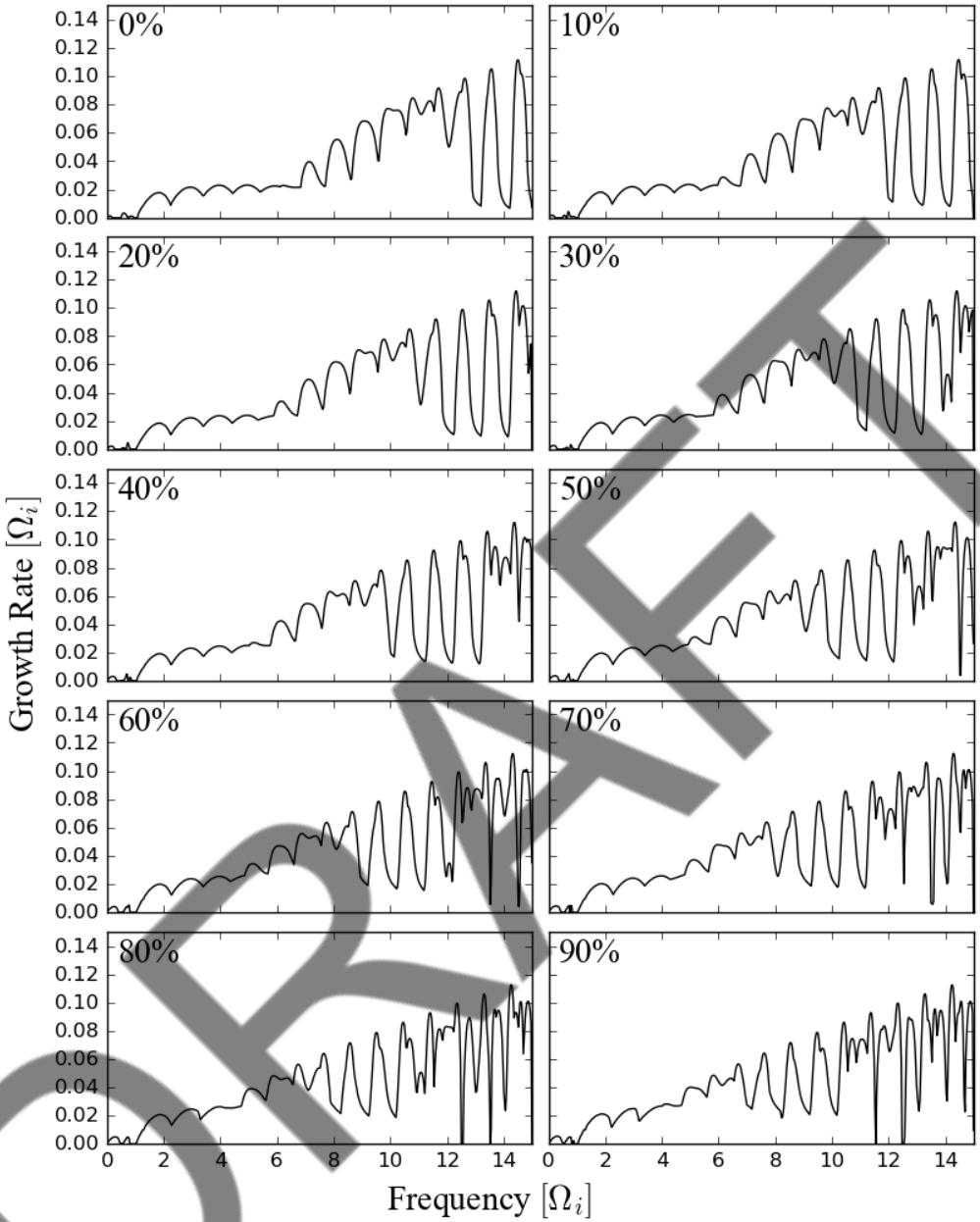


Figure 6.7: Growth rates derived from data given in (k_\perp, k_\parallel) space such as Fig. 6.3, as a function of frequency normalised by Ω_i for all parallel wavenumbers, and for tritium concentrations between $0 \leq \xi_T \leq 0.9$ in increments of 10%, as given in the top left of each panel.

for all values of k_\parallel . In this representation, we are able to cover all magnetic field orientations, as doing otherwise would miss the asymmetric multi-parallel-wavenumber-variable doublet splitting.

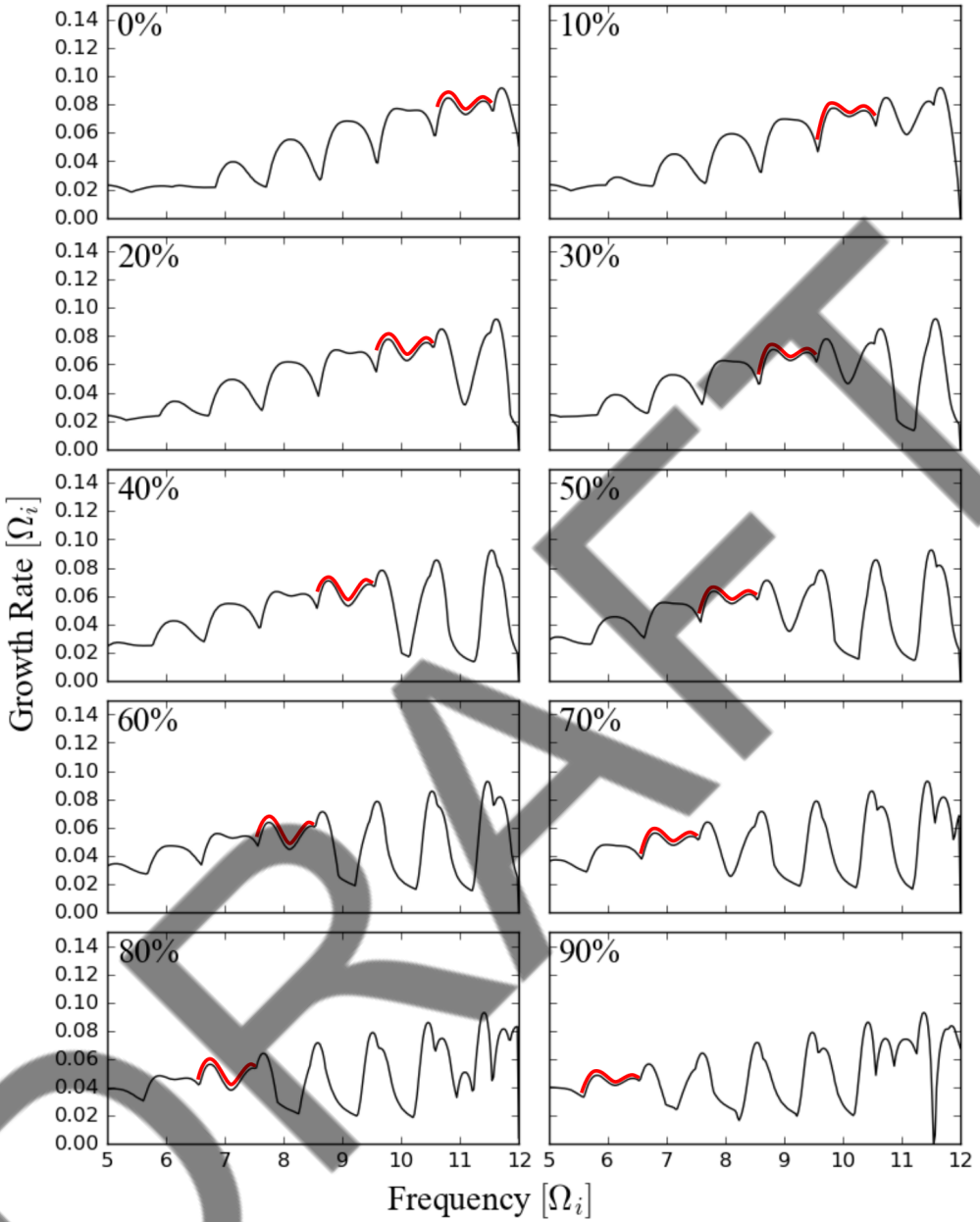


Figure 6.8: Zoom in plot of the data presented in Fig. 6.7 for frequencies greater than $5\Omega_i$, focused specifically on the frequency location of the 11th ion cyclotron harmonic's (highlighted with a red line) doublet split feature's dependency on tritium concentrations between zero and 90%, as labelled top left.

Figure 6.9 presents linear MCI growth rates calculated using the LMV code and plotted as a function of frequency for each tritium concentration. It is derived from growth rate data such as those shown in Fig. 6.3, and the linear

scale colour-bar represents the normalised growth rate to Ω_i . The strongest growth rates $\gamma(\omega)$, extracted across a binned frequency axis, are used to build the upper panel of Fig. 6.9. The most prominent peaks are then identified by means of a standard peak-finding algorithm, and plotted in the lower panel of Fig. 6.9. This bottom panel enables identification of two significant dependencies on tritium concentration, for frequencies greater than $5\Omega_i$, that are unresolved in the upper panel.

These dependencies, labelled (A) and (B) in Figs. 6.9 and 6.10, relate to the onset of spectral peak splitting (A) and spectral peak frequency (B). They are respectively steep and shallow when expressed in terms of $\Delta\omega/\Delta\xi_T$. That is, the change of location in frequency space is sensitive (A) and insensitive (B) to changes in tritium concentration. Both relationships can be quantified as a linear response in frequency to a change in tritium concentration; written as $\Delta\omega \propto A\xi_T$ and $\Delta\omega \propto B\xi_T$, we infer that the constants are $A \simeq -5.0\Omega_i$ and $B \simeq -0.5\Omega_i$ from the respective white dashed lines in Figs. 6.9 and 6.10. Both of these relationships appear to correlate with the decrease in Alfvén speed v_A consequent on the increase in plasma density with ξ_T . This alters the resonance conditions of the MCI (in the lower frequency regime $\omega \simeq l\Omega_i \simeq kv_A$) and shifts resonant phenomena to lower frequencies.

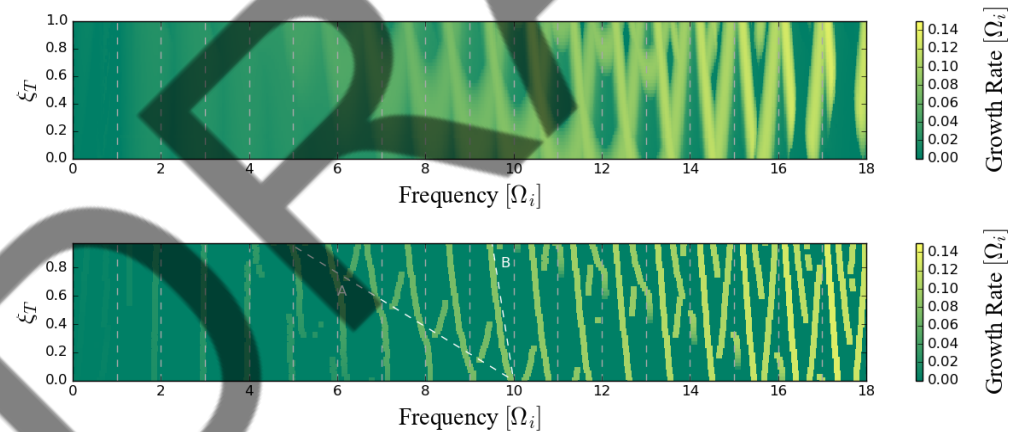


Figure 6.9: Peak growth rates through frequency and ξ_T space obtained from spectra such as those presented in Fig. 6.3, with growth rates normalised to the alpha-particle cyclotron frequency given as a linear colour scale. *Top panel:* maximal growth rates in frequency bins of size $0.0225\Omega_i$. *Lower panel:* distinct peaks of the spectra shown in the top panel extracted by a peak-finding algorithm, demonstrating trends in frequency peak excitation, indicated by the dashed white lines labelled (A) and (B).

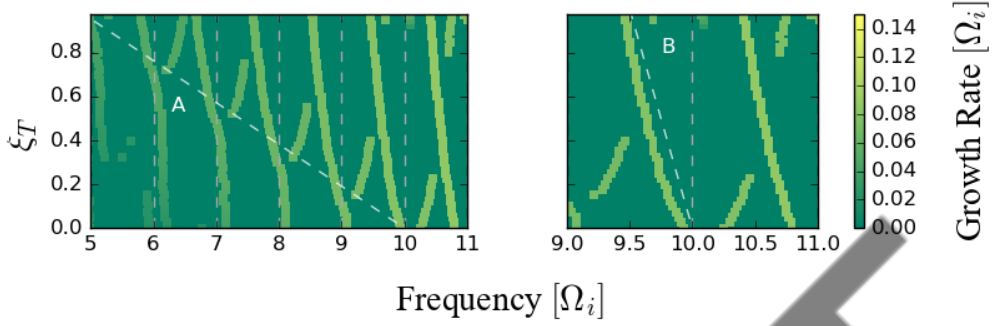


Figure 6.10: Zoom in plot of the data presented in Fig. 6.9 of peak growth rates through concentration space highlighting the trends labelled A (left) and B (right) as dashed white lines.

Trend (A) was identified in Fig. 6.3 and in previous nonlinear PIC simulations of DT- α plasmas [110] in terms of a similar linear relationship. In both this paper and in Ref. [110], the same coefficient is found. That is, the relation $\Delta\omega/\Omega_i \propto -5.0\xi_T$ links the lowest frequency at which doublet splitting occurs for a given harmonic to the tritium concentration. Neither linear relationship (A) and (B) is observed in the low frequency regime, $\omega/\Omega_i \leq 6$, but both are clearly visible at frequencies between $5\Omega_i$ and $11\Omega_i$, and in a second tranche between $11\Omega_i$ and $18\Omega_i$.

The change in frequency of trend (B) following an increase in tritium concentration is shallow and is exhibited by each harmonic peak above $5\Omega_i$, reducing the frequency at which peak linear MCI growth is found for each harmonic as ξ_T increases. It scales approximately linearly with respect to tritium concentration, and arises for each harmonic only after its first doublet split, the location of which is dependent on trend (A). As an example, for the case of the eighth cyclotron harmonic shown in the left hand panel of Fig. 6.10, we see that trend (B) acts to shift the frequency of the dominant harmonic only after the tritium concentration has risen to $\sim 30\%$. The change in frequency of trend (A) per incremental increase in tritium concentration on the other hand is steeper, and is present in the features of peak growth rates, demonstrating a shifting to lower frequencies of a doublet split. This is seen over a range of frequencies, but most prominently between $5 < \omega/\Omega_i < 11$.

6.6 Equivalent Alfvén speed in D and DT plasmas

A key parameter of strong linear drive of the MCI is the ratio between the perpendicular birth velocity and the Alfvén speed v_A . Consider now two different

plasmas, one of pure deuterium and another of some DT admixture, but with equal mass densities and hence equal Alfvén speeds. Through the use of the LMV code, we can compare the strength of the linear growth rates of the MCI, observing its dependencies purely on tritium concentration and independent of v_A and pitch-angle.

For a pure deuterium plasma to have an equal Alfvén speed to its DT plasma counterpart, it needs to have an equivalent mass density. Whilst maintaining quasi-neutrality, this requires an alteration to the number density of electrons and deuterons. By equating their Alfvén speeds $v_A^{[DT]}(\xi_T) = v_A^{[D]}$, we rearrange for the electron density required by the pure D plasma, n'_e , to provide the higher mass density for v_A matching. This is written as

$$n'_e = n_{e0} \left[1 + \xi_T \left(\frac{m_T - \frac{Z_T}{Z_D} m_D}{\frac{m_D}{Z_D} + (m_\alpha - \frac{Z_\alpha}{Z_D} m_D) \xi_\alpha} \right) \right], \quad (6.1)$$

where Z_σ are the charge numbers of each ion and n_{e0} is the electron density of the pure D plasma, and corresponds to that used in the DT plasmas, see Table 6.1.

Equation (6.1) shows that the electron number density of the pure deuterium plasma is linearly proportional to the tritium concentration. Running the LMV code for multiple ξ_T equivalent pure deuterium plasmas, we construct a collection of DT and D JET-like plasmas with equal v_A , and compare location and strength of the linear growth rates of the MCI in two dimensional wavenumber space.

Figure 6.11 presents the subtraction between growth rate solutions of LMV runs with DT bulk thermal ions and pure bulk deuterium with equivalent Alfvén speeds. The red (blue) colouring shows where DT growth rates are stronger (weaker) than those of a pure deuterium plasma. Figure 6.11 reveals that, even at low tritium concentrations, there are significant differences in the growth rates between a DT- α and D- α plasma. This reveals that MCI growth is not purely dependent on the ratio between perpendicular velocity and Alfvén speed v_\perp/v_A , but on the plasma's constituent ions. Differences between linear growth rate maps are amplified for high tritium concentrations. We see from Fig. 6.11 that the growth rates of the DT plasma conform less rigidly to isofrequency harmonic lines as opposed to its pure deuterium plasma counterpart. This effect is stronger for higher tritium concentrations. Unlike doublet splitting observed in the growth rates in Ref. [37] and panel (c) of Fig. 6.3, doublet splitting is not observed in pure deuterium plasmas for perpendicular wavenumbers $k_\perp v_A/\Omega_i \geq 10$ and $|k_\parallel| \leq 0.5$.

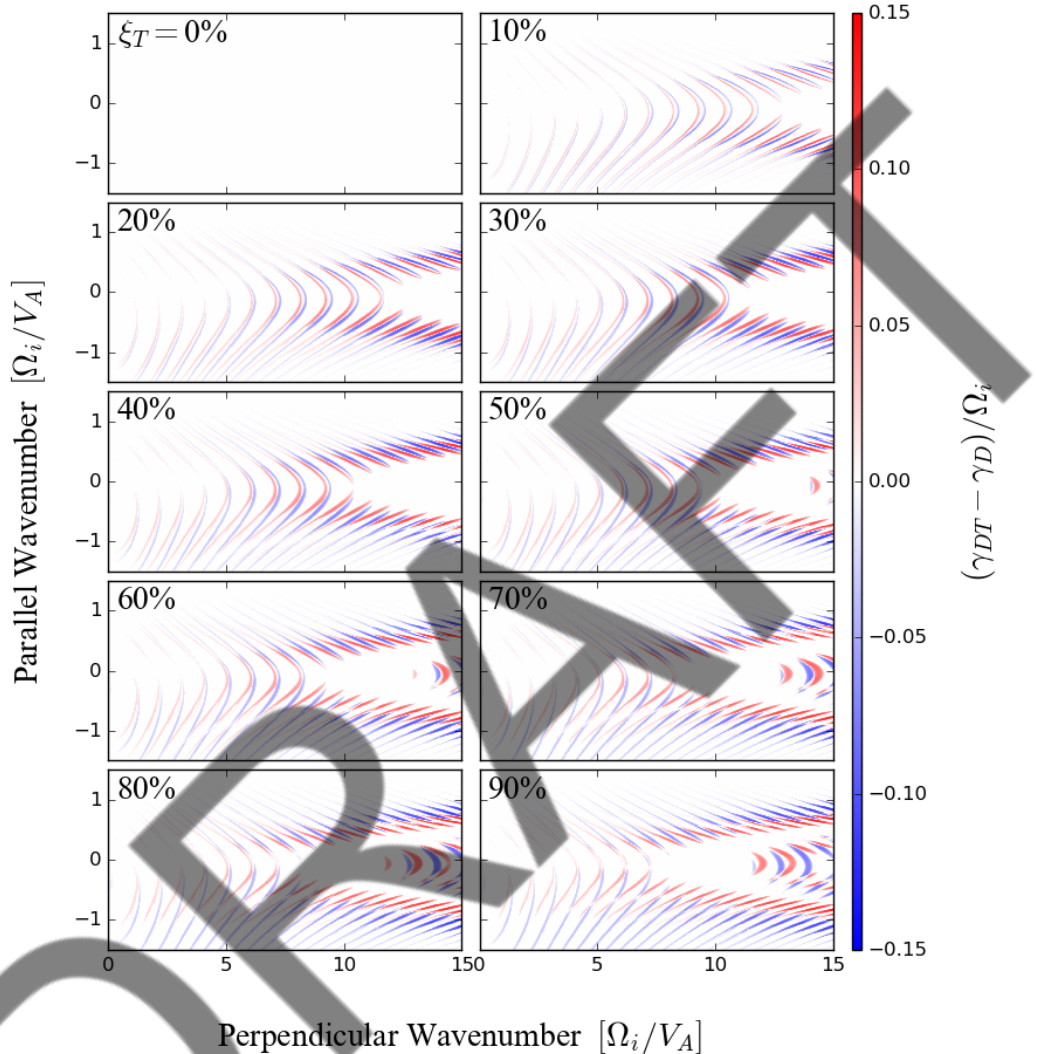


Figure 6.11: Subtraction of growth rates between LMV runs with bulk DT plasmas and deuteron bulk plasmas with equivalent v_A through alterations to the pure deuterium plasmas electron number density, Eq. (6.1). Tritium concentration (also representative of the equivalent electron number density) is annotated in the top left of each panel. Difference between linear MCI growth rate maps $\gamma_{DT}(k_\perp, k_\parallel) - \gamma_D(k_\perp, k_\parallel)$, normalised by the alpha-particle cyclotron frequency Ω_i , given by the linear scale colour bar.

6.7 Summary and conclusions

In the present paper, we have used the newly developed LMV code which provides computationally enabled analytical calculations of MCI linear growth rates γ_{MCI} , spanning the whole of (k_\perp, k_\parallel) space, for any given set of plasma parameters and for any velocity-space distribution function for the energetic ions. We have focused on parameters appropriate to the region of JET DT plasma 26148 from which widely studied ICE spectra, driven by marginally trapped 3.5 MeV fusion-born alpha-particles, were obtained, exploring the dependence of γ_{MCI} on tritium concentration ξ_T across (k_\perp, k_\parallel) space. This work complements a recent kinetic study of tritium dependence of the MCI for similar plasmas, using the EPOCH PIC code, which extends into the nonlinear regime but was necessarily restricted in the choice of singular magnetic field orientations. One key advantage of the LMV code is its speed compared to the PIC approach, even with the inclusion of a tertiary ion, and hence when used in conjunction with fully nonlinear PIC simulations is a powerful complementary tool for ICE signal analysis.

As a result of non-zero ξ_T , at all real concentrations, the LMV code, which encapsulates both the previous linear theory of the MCI for oblique magnetic field angles as well as the full two dimensional wavenumber, reveals several key features of the dependence on ξ_T of γ_{MCI} , which is intrinsically highly structured across wavenumber space. Provided that the Alfvén speed is kept constant for equivalent DT and pure D plasma, we were able to show that the intensity of the linear MCI growth rate was significantly dependent upon the plasmas admixture of ions, and their charge-to-mass ratios. Location of the features of the growth rates spectra in (k_\perp, k_\parallel) space revealed strong dependency on tritium concentration, too, including doublet splitting.

Given that the observed spectral peaks of ICE often correspond, as one might expect, to the most strongly linearly unstable frequencies, these results have immediate value for future DT plasma scenarios. Continuous plots of the variation of γ_{MCI} with ξ_T , displayed versus frequency, provide multiple insights into the physical phenomenology behind doublet split features, including: the dependency on ξ_T on their location of origin in frequency space; subsequent trends as ξ_T increases further; frequency cut-offs for doublet splitting; and previously observed nonlinear ghost features. For future DT fusion plasmas, one could therefore use the relations derived here and correlate them to the location of observed doublet split ICE features to determine the bulk ion concentration ratio. Further investigation into the dependency on the location of these doublet splits on parameters of the energetic minority would be highly advantageous.

Chapter 7

PIC simulations of aneutronic D– ^3He fusion plasmas and the generation of ICE

This chapter explores the development of the MCI in aneutronic D– ^3He plasmas through the measurement of the ICE diagnostic resulting from a drifting ring-beam population of 14.68 MeV energetic protons. PIC simulations are carried out using EPOCH for multiple concentrations of helium-3, similar to Chapter 5, but maintain a constant proton perpendicular birth velocity with respect to Alfvén speed. Whilst the D– ^3He plasma presents a unique charge-to-mass ratio bulk with which to study, the addition of choosing to study the energetic protons with a fixed perpendicular velocity ratio, exhibits novel consequences on the resonant criteria and location of ICE in frequency space, from their large parallel drift velocities. We investigate this parallel velocity Doppler shift effect on spatiotemporal Fourier transforms and power spectra, and discuss the gyro-resonant criteria, previously defined in Eq. (4.6), from the ions’ energy densities, and highlight the importance of ICE for its use as a diagnostic tool for future aneutronic fusion plasmas.

7.1 Cylindrical approach and approximating the location of perpendicular birth velocity resonance with the FAW

As stated in §1.1, aneutronic fusion reactions are an attractive alternative to current neutron producing fuels due to their lack of plasma poisoning, which lowers the costs incurred through irradiated waste management. Neutron reliance in

current tokamaks is already high as they are expected to breed a sufficient source of tritium from lithium blankets; be the primary source of energy extraction; and act as sources for multiple diagnostics, including fusion reactivity. It is, therefore, in the best interest of fusion plasma research that the ICE diagnostic, one which does not rely on neutrons and whose intensity scales linearly with fusion reactivity, is investigated in these aneutronic and high energy product fusion plasmas, such as the 14.68 MeV protons.

The condition for the development of the MCI is a population distribution inversion in velocity space to a strongly non-Maxwellian form, such as a drifting ring-beam. The ratio between the energetic fusion product's perpendicular velocity v_{\perp} to the local Alfvén speed v_A dictates the strength of the resonance between the energetic species cyclotron frequency and the FAW, and hence, the magnitude of the growth of the MCI and the intensity of ICE. It would be sensible, before running computationally and monetarily expensive PIC simulations, to estimate the v_{\perp}/v_A ratio through the cross-section of a tokamak (i.e. as a function of radial distance). This model allows for a determination of the spatial resonance location in the cross-sectional plane of the tokamak of the D- 3 He energetic fusion products.

Utilising the slab geometry model consistent with MCI linear theory, we cal-

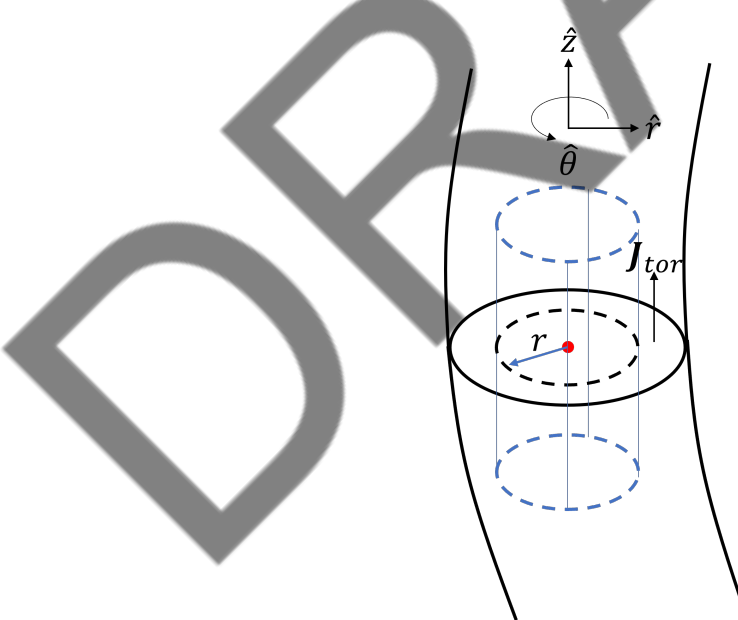


Figure 7.1: A schematic of the cylindrical approximation used in a simple model to derive the location of $v_{\perp} \sim v_A$ in a tokamak (see Fig. 1.4 for the schematic of a tokamak)

culate the Alfvén speed as a function of horizontal radius, $v_A(r)$, using analytical forms of the magnetic field and plasma density. Using the cylindrical coordinate system shown in Fig. 7.1, one can derive the poloidal magnetic field from the toroidal current equation [204, 205]

$$\mathbf{J}_\phi = j_0 \left[1 - \left(\frac{r}{a} \right)^2 \right] \hat{z}, \quad (7.1)$$

where $r = R - R_0$. Using Ampère's circuital law in integral form,

$$\oint_l \mathbf{B}_\theta \cdot d\mathbf{l} = \mu_0 \int_S \mathbf{J}_\phi \cdot d\mathbf{S}, \quad (7.2)$$

and substituting the cylindrical basis vectors with $d\hat{\mathbf{l}} = r d\theta \hat{\theta}$ and $d\hat{\mathbf{S}} = r dr d\theta \hat{z}$, gives the poloidal field as a function of radial distance

$$B_\theta(r) = \frac{\mu_0 j_0}{r} \left[\frac{r^2}{2} - \left(\frac{r^2}{2a} \right)^2 \right]. \quad (7.3)$$

Here, the initial current density j_0 defined in our simple current density model is determined from the integral of current density over the surface, giving the total current through the plasma. This current is known to the experimentalist as it is the same plasma current I_p that is used to generate the poloidal field. Taking the integral of \mathbf{J}_ϕ over the surface and rearranging for j_0 we get

$$j_0 = \frac{2I_p}{\pi a^2}. \quad (7.4)$$

Thankfully, the toroidal magnetic field can be described more easily as

$$B_\phi(r) \approx \frac{B_0}{R}. \quad (7.5)$$

Under the same cylindrical coordinate system, the plasma number density can be modelled as in Refs. [135, 206, 207],

$$n(r) = n_0 \left[1 - \left(\frac{r}{a} \right)^2 \right]^\alpha, \quad (7.6)$$

where $\alpha \simeq 1.04$ [206]. Combining Eqs. (7.3) – (7.6) one can write the Alfvén speed as a function of radial distance to be

$$v_A(r) = \frac{[(\mu_0 j_0/r)(r^2/2 - r^4/4a^2)]^2 + [B_0/(r + R_0)]^2}{\mu_0 \rho_0 (1 - r^2/a^2)^\alpha}. \quad (7.7)$$

Which, taking $\alpha \simeq 1$, can be rearranged into a quartic in r , giving solutions, per energetic ion, of the spatial location at which $v(A) \simeq v_{ion}$. This is possible if one assumes that: the birth velocity of the energetic ion is purely kinetic (no

collisions or cyclotron losses); energetic ion propagation is purely perpendicular (slab model) such that in velocity space $f(\mathbf{v}) = \delta(v_{\parallel})\delta(v_{\perp} - u_0)$; and ions have sufficient energy to traverse throughout the tokamak.

Figure 7.2 presents the normalised magnetic field, plasma density (assuming a bulk ion species of deuterons) and Alfvén speed throughout the tokamak cross-section in units of r/a for both the 3.67 MeV alpha-particle and 14.68 MeV proton (as labelled), of the aneutronic D– ^3He reaction. A plasma current (I_p) of 2 MA was applied in the calculation of Eq. (7.4) and remaining plasma parameters are given in Table 7.1. The embedded figure represents the ratio between each ion’s velocity to the Alfvén speed across the same r/a axis. One can see that the location of potential resonance is within the edge regions of the tokamak wall for both energetic ions, with $|r/a| > 0.6$ for the alpha-particles and $|r/a| > 0.9$ for the protons, confirming that the MCI condition for strongest growth will occur at the spatial locations previously seen to emit ICE [58]. With more physically motivated velocity distributions, the spatial regions of $v_A(r) \simeq v_{ion}$ are pulled in from the outer edges, melding our ICE signal origins from purely edge, to partially core.

Using this simple model, we are now motivated to study further the MCI in D– ^3He aneutronic fusion plasmas as a result of the highly energetic minority proton species, satisfied that it can, realistically, conform to the conditions necessary for ICE observations typical of the past DT fusion plasmas.

Parameter	Value
R_0	3.0 m
a	1.25 m
B_0 [21]	3.7 T
n_e	10^{19} m^{-3}
v_p^2	$14.68[\text{MeV}] / (m_p/2)$
α [206]	1.04
I_p	2 MA

Table 7.1: Simplified cylindrical model parameters for the D– ^3He fusion plasma and its 14.68 MeV energetic proton particle.

7.2 Simulating Aneutronic Experiments

We showed in §7.1 that the birth velocity of the protons, assuming it is born and remains as a Dirac delta distribution, Eq. (1.46), is comparable to the Alfvén

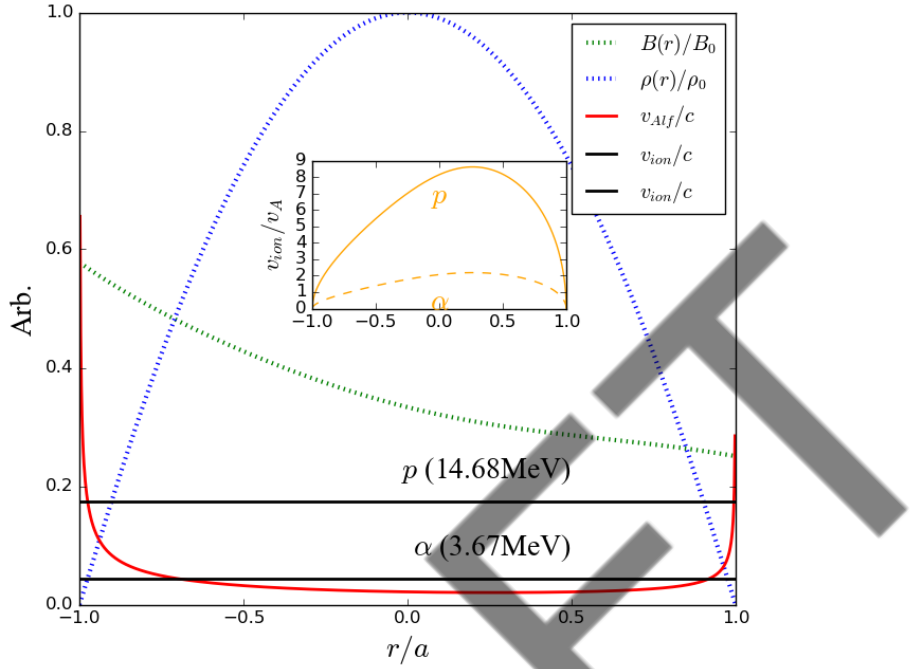


Figure 7.2: Velocity, magnetic field and ion density through the cross-section of a tokamak as a function of radius normalised by the minor radius. Inlay figure is the ratio between an energetic products velocity and Alfvén speed, presenting as sub-Alfvénic at the edge regions, where plasma density falls, and super-Alfvénic elsewhere.

speed in the tokamak edge region. This was an upper boundary calculation, as the introduction of non-zero thermal spreads and parallel velocity components will reduce the proton velocity at the edges. This hence justifies the use of PIC simulations for these future aneutronic scenarios, of which exist within multiple parameter spaces to explore.

The 14.68 MeV protons are distinctive, in terms of their much higher energy, compared to the alpha-particles born in contemporary DT plasmas at 3.5 MeV, and those born as the other main fusion product species at 3.67 MeV in the D– ^3He reaction. For this reason, we focus here on the correspondingly distinctive features of these protons’ possible ICE spectra. This in turn requires us to choose specific scenarios for the velocity-space distribution function of the relevant sub-population of 14.68 MeV protons, and for the parameters of the majority thermal D– ^3He plasma in which these protons are embedded.

Our choice of velocity-space distribution for the 14.68 MeV proton population is motivated by recent observations of ICE which was found to be driven by unexpected sub-populations of confined 3.0 MeV fusion-born protons in deuterium

plasmas, both in the KSTAR tokamak [112, 113] and in the LHD heliotron-stellarator [79]. In both scenarios, the ICE observations [79, 112, 113] led to the identification of the location in velocity-space of small sub-populations of confined ICE-driving fusion-born protons, whose presence was unanticipated prior to the ICE observations. For interpreting these ICE spectra using the first-principles kinetic approach, the approximation of a drifting ring-beam model for the velocity-space distribution of these sub-populations of fusion-born protons proved successful [79, 112, 113].

Confining the great majority of 14.68 MeV protons would not at present be possible in any contemporary toroidal MCF facility if it contained a D– ^3He plasma. Therefore, we simulate ICE from a conjectural confined sub-population of these protons, which might exist analogous to those identified in KSTAR and LHD. We adopt the hypothesis of a $v_{\parallel} \gg v_{\perp}$ regime (as in KSTAR) where also $v_{\perp} \sim v_A$ (as in LHD); where the balance of the birth energy then determines v_{\parallel} , which will also allow for strongly driven MCI.

We therefore initialise the velocity-space distribution of the minority 14.68 MeV proton population in our simulations as a drifting ring-beam, Eq. (1.48), with parameters determined by the foregoing assumptions. This approach also provides continuity by enabling comparison of the outputs of the present simulations with those from previous drifting ring-beam kinetic treatments that were used to simulate ICE observations from other plasmas, notably JET [62, 100, 101, 105, 110] and ASDEX-Upgrade [103, 111] in addition to KSTAR [112–114] and LHD [79, 104, 115, 116].

Our parameters, listed in Table 7.2, are broadly characteristic of contemporary medium-to-large MCF plasmas, assisting comparison of the ICE physics identified here with that found in previous simulations. We investigate the variation of the simulated ICE spectra with respect to ^3He concentration, which we are able to address using techniques recently developed to study the dependence of simulated ICE spectra on the thermal tritium concentration in DT plasmas, see Chapters 4 and 5. We also investigate the partitioning of energy between the excited electric and magnetic fields and the thermal D and ^3He ion populations.

Taken all together, our model thus corresponds to a not-inconceivable future scenario whereby D– ^3He plasmas in a JET-scale MCF facility contain a KSTAR-type confined sub-population (referring again to Fig. 2 of Ref. [112]) of 14.68 MeV fusion-born protons. This will provide distinctive and physically interesting new features in the simulated ICE spectrum, arising from the extension of MCI physics to this new regime. These features would in turn assist the exploitation of ICE as a diagnostic for fusion reactivity in this aneutronic context.

7.3 Particle-in-cell approach

Our simulations are carried out using the particle-in-cell (PIC) code EPOCH [145], distributing tens of millions of computational particles across a 1D3V grid, which comprises N_x cells each of length Δx . This is the same slab geometry implicit in linear MCI theory [39, 62, 100, 101, 105, 112]. Particles and electric and magnetic fields then evolve self-consistently under the Maxwell-Lorentz system of equations. For a summary of this approach in the context of ICE simulations, see for example Appendix C of Ref. [113]. These equations are self-consistently solved, with particle momenta and electromagnetic fields updated on temporal and spatial scales which well resolve the gyro-orbit motion of each ion and of the neutralising electrons. The background magnetic field, B_z , is chosen to be orientated at an angle of 89° to the simulation domain, \hat{x} , because the MCI is known to grow most strongly for quasi-perpendicular angles of propagation [37, 39, 58, 121].

The energetic minority proton population is initially represented by a drifting ring-beam distribution in velocity space, Eq. (1.48), and therefore the perpendicular and parallel distributions of energetic proton velocity are represented by two Gaussians, centred on the birth velocities $u_{\parallel 0}$ and $u_{\perp 0}$, with characteristic spreads $u_{\parallel r}$ and $u_{\perp r}$. This model is commonly used throughout MCI theory [39, 58, 59, 97–99, 120, 208] and ICE simulation [62, 78, 79, 100, 101, 103–105, 112–114, 116, 209, 210].

Table 7.2 lists the key simulation parameters, including domain length L , cell length Δx , electron number density n_e and background magnetic field strength B_0 . The thermal ion and electron temperatures are reduced by a factor of one hundred, as compared to the actual temperatures required for fusion in the core of D– 3 He plasmas, to 2 keV. This might correspond to edge plasma conditions, and is in any case necessary here in order to reduce the thermal background noise in our simulations, which are already computationally expensive. This choice does not significantly affect the underlying physical processes which lead to our simulated ICE, but does enable better defined computational outputs.

Characteristic Larmor radii of the thermal ions and energetic protons are displayed in Table 7.3. Normalisations with respect to cell width Δx and spatial domain length L are also given, demonstrating the high spatial resolution of our PIC simulations which, importantly, fully resolve the ion gyro-motion.

Parameters specific to each simulation, such as ion concentrations and proton pitch-angles, are detailed in Table 7.4, which also includes the perpendicular birth velocity of the energetic protons. This is set at 90% of the Alfvén speed for each value of the 3 He concentration, which corresponds to the regime for which

the MCI is characteristically strongly driven [100, 101, 104, 105].

Quantity	Value
L	1.5 m
Δx	$0.95 \lambda_{De}$
λ_{De}	$47.0 \mu\text{m}$
t_{end}	$10\tau_{cp}$
Δt	$8.33 \times 10^{-3}\tau_{cp}$
τ_{cp}	$17.7 \mu\text{s}$
$T_{D,He3,e}$	2 keV
n_e	$5 \times 10^{19} \text{ m}^{-3}$
B_0	3.7 T

Table 7.2: Plasma and simulation domain parameters in our simulations. From top: the domain length, L ; computational grid spacing, Δx ; electron Debye length, λ_{De} ; simulation duration, t_{end} and time step Δt in units of proton cyclotron period τ_{cp} ; deuterium, helium-3 and electron temperatures, $T_{D,He3}, T_e$; electron number density, n_e ; and equilibrium magnetic field strength, B_0 .

7.3.1 Plasma density as a function of ^3He concentration

The parallel and perpendicular birth velocity ($u_{\parallel 0}$ and $u_{\perp 0}$ respectively, as in Eq. (1.48)) of the fusion-born protons, can be expressed as a function of their initial kinetic energy,

$$\left(\frac{u_{\parallel}}{v_A}\right)^2 = \left[\frac{2\mu_0\rho}{B_0^2}\right] \left(\frac{E_p}{m_p}\right) - \left(\frac{u_{\perp}}{v_A}\right)^2. \quad (7.8)$$

Here E_p is the 14.68 MeV birth energy, m_p is the proton mass and other variables are previously defined. As mentioned, we keep the value of $u_{\perp 0}/v_A = 0.9$ con-

Quantity	D	^3He	p
$r_L [10^{-3}\text{m}]$	9.14	5.59	0.22
$r_L/\Delta x$	204.50	125.16	490.20
L/r_L	164.15	268.29	68.41

Table 7.3: Characteristic Larmor radii $r_L = \sqrt{2Em}/qB$, assuming all kinetic energy E is perpendicular; $E = mv_{\perp}^2/2$, with normalisation to cell width Δx and domain length L , for each population of thermal deuterons, helium-3 ions and energetic protons.

Quantity	${}^3\text{He}$ concentration [%]								
	0	5	10	15	22	25	34	38	45
ξ_{He3}	0.0	0.05	0.10	0.15	0.22	0.25	0.34	0.38	0.45
ξ_D	0.999	0.899	0.799	0.699	0.559	0.499	0.319	0.239	0.099
ξ_p	0.001	0.001	0.001	0.001	0.001	0.001	0.001	0.001	0.001
(ξ_{He3}/ξ_D)	0.00	0.0556	0.125	0.215	0.394	0.501	1.07	1.59	4.55
$v_A/c [10^{-3}]$	26.9	27.3	27.6	28.0	28.6	28.8	29.6	30.0	30.6
$u_{\perp 0}/v_A$	0.900	0.900	0.900	0.900	0.900	0.900	0.900	0.900	0.900
$u_{\parallel 0}/v_A$	6.51	6.42	6.34	6.25	6.13	6.08	5.91	5.84	5.71
$\arctan(u_{\perp 0}/u_{\parallel 0}) [^\circ]$	7.88	7.98	8.08	8.19	8.35	8.43	8.66	8.76	8.96

Table 7.4: Summary of particle species parameters in each simulation for different relative ${}^3\text{He}$ concentrations, ξ_{He3} , with respect to electron number density. The Alfvén speed, normalised to that of light, and the proton birth velocity components, normalised to v_A , are given. These vary with ${}^3\text{He}$ concentration as a result of the conservation of energy given fixed perpendicular velocity $u_{\perp 0}/v_A$, as discussed following Eq. (7.10). Pitch-angle $\phi = \arctan(u_{\perp 0}/u_{\parallel 0})$ is given in the final row of the Table, which increases with increasing ${}^3\text{He}$ concentration.

stant in Eq. (1.48) across all simulations, irrespective of the ${}^3\text{He}$ concentration, which ranges from zero to 45%. In consequence, in these simulations, the mass density ρ decreases with increasing ${}^3\text{He}$ concentration, resulting in the variation of v_A displayed in Table 7.4.

This may appear counterintuitive, insofar as lighter deuterium nuclei are replaced by heavier ${}^3\text{He}$ ones, but it follows from the fact that the substitution is charge-weighted. Specifically, charge neutrality imposes $n_e \approx Z_D n_D + Z_{He3} n_{He3}$ and, since the mass density ρ scales as $\rho \approx n_D m_D + n_{He3} m_{He3}$, it follows that

$$\rho \approx n_e \left[\xi_{He3} \left(m_{He3} - \frac{Z_{He3}}{Z_D} m_D \right) + \frac{m_D}{Z_D} \right], \quad (7.9)$$

which, substituting for $m_D \simeq (2/3)m_{He3}$, $Z_{He3} = 2$ and $Z_D = 1$, gives

$$\rho \approx n_e \left[m_D \left(1 - \frac{\xi_{He3}}{2} \right) \right]. \quad (7.10)$$

Thus, as ${}^3\text{He}$ concentration increases, mass density decreases, leading to a rise in Alfvén velocity. Hence the value of $u_{\parallel 0}/v_A$ declines correspondingly, as seen in the penultimate row of Table 7.4.

The corresponding pitch-angle, shown in the final row of Table 7.4, therefore slightly increases with ${}^3\text{He}$ concentration, given that $u_{\perp 0}/v_A$ is chosen to

remain fixed. This increase is on the order of one degree over the 45% increase in ^3He concentration. Pitch-angle values, in the range 8° to 9° are also characteristic of the fusion-born proton population observed to drive ICE in deuterium plasmas in the KSTAR tokamak [112, 113].

7.3.2 Number of particles per cell

Particle-in-cell simulations which incorporate more than one majority thermal ion species, here deuterium and helium-3, must maintain constant number-density-weighting (NDW) between all particle species, including electrons, as detailed in §4.1.2. Repeated here, the NDW condition requires that, for each species σ , there is a fixed ratio n_σ/N_σ between its physical number density n_σ and the number N_σ of computational macroparticles which represent the species in the simulation. We note that N_σ scales linearly with grid size L and inversely with cell size Δx , since $N_\sigma = (L/\Delta x)C_\sigma$, where C_σ is the number of computational PPCPS - §4.2.1. The quasi-neutrality condition §1.2.1 requires that the deuteron and ^3He ion populations are simulated using $C_\sigma = (\xi_\sigma/\xi_p)C_p$ particles per cell, which is inversely proportional to the energetic minority proton concentration. The computational limits imposed by the constraint of constant NDW requires that the number of computational particles per cell in our simulations is set to five for the energetic protons and 5000 for the electrons, in the context of overall charge neutrality.

Partly due to the increased computational cost of simulating multiple ion species, which follows from the NDW constraint, our simulations have a duration of ten proton gyro-periods, $10\tau_{cp}$, and the concentration of minority proton ions is $\xi_p = 10^{-3}$ (see Table 7.4). These values are sufficient to follow the full evolution of the MCI through its initial linear phase and into its nonlinear, saturated regime, as shown in Fig. 7.3.

7.3.3 Spatial resolution considerations

The cell length Δx in PIC codes such as EPOCH is required to be shorter than the Debye length λ_{De} , beyond which charges are shielded. Resolution of the Debye length is essential for capturing the self-consistent dynamics of particles and fields; if this condition is not met, PIC simulated plasmas numerically self-heat. The resolution of each PIC simulation presented here is high enough to capture the full spatial gyro-motion of each ion species, including the energetic protons, whose gyro-orbits typically traverse over 490 grid cells (see Table 7.3). The simulations do not resolve the electron gyro-radius r_{Le} , in consequence of the computational cost. Our results show that this leads to a very low level

of numerical electron heating on the relevant timescale of $10\tau_{cp}$, which can be disregarded.

7.4 Results

7.4.1 Time evolution of field and particle energy densities

Figure 7.3 shows the time evolution of the energy densities of particles and fields for a plasma consisting initially of thermal Maxwellian deuteron and helium-3 populations and a minority energetic 14.68 MeV proton population distributed as a drifting ring-beam, Eq. (1.48). The different panels of Fig. 7.3 relate to ^3He concentrations between five and 45% with respect to the electron number density. The free energy of the protons is transferred both to the excited electromagnetic (ΔB_z) and electrostatic (E_x) components of the fields, as well as to the thermal deuterons and helium-3 ions whose oscillation helps to support the excited waves. The initial exponential growth of the MCI, followed by a nonlinear phase leading to saturation, is evident across all traces, at each ^3He concentration. The traces shown in Fig. 7.3 are similar to those obtained in previous simulations of the relaxation of a drifting ring-beam of minority energetic ions under the MCI in ICE studies; see, for example, Figs. 2 of Refs. [101, 111] and Fig. 12 of Ref. [79]. Comparisons of the eight panels in Fig. 7.3 show that the total energy transferred, at the time of saturation, from the protons to the thermal ions and excited field components increases slightly with ^3He concentration.

The ratio between the change in the electric and magnetic field energy densities, inferred from the corresponding traces in Fig. 7.3, are shown in Fig. 7.4. This ratio tends to unity for times well into the nonlinear saturated regime of the MCI, and is minimised in simulations with ^3He concentrations between 22% and 34%. Previous analyses of ICE driven by neutral beam injected (NBI) ions [96, 104, 114, 116, 137] suggest stronger electrostatic components of the MCI, however, in all these cases, the NBI ions were sub-Alfvénic. We infer future observations of ICE from the 14.68 MeV protons born in D– ^3He plasmas may be possible using either an antenna (electromagnetic) or probes (electrostatic), or both.

7.4.2 Energy partitioning via gyro-resonance

The partitioning of the kinetic energy transferred to thermal ions, between the deuterium and ^3He populations, is of interest in relation to the fundamental plasma physics of ICE excitation and the MCI. For all eight panels of Fig. 7.3,

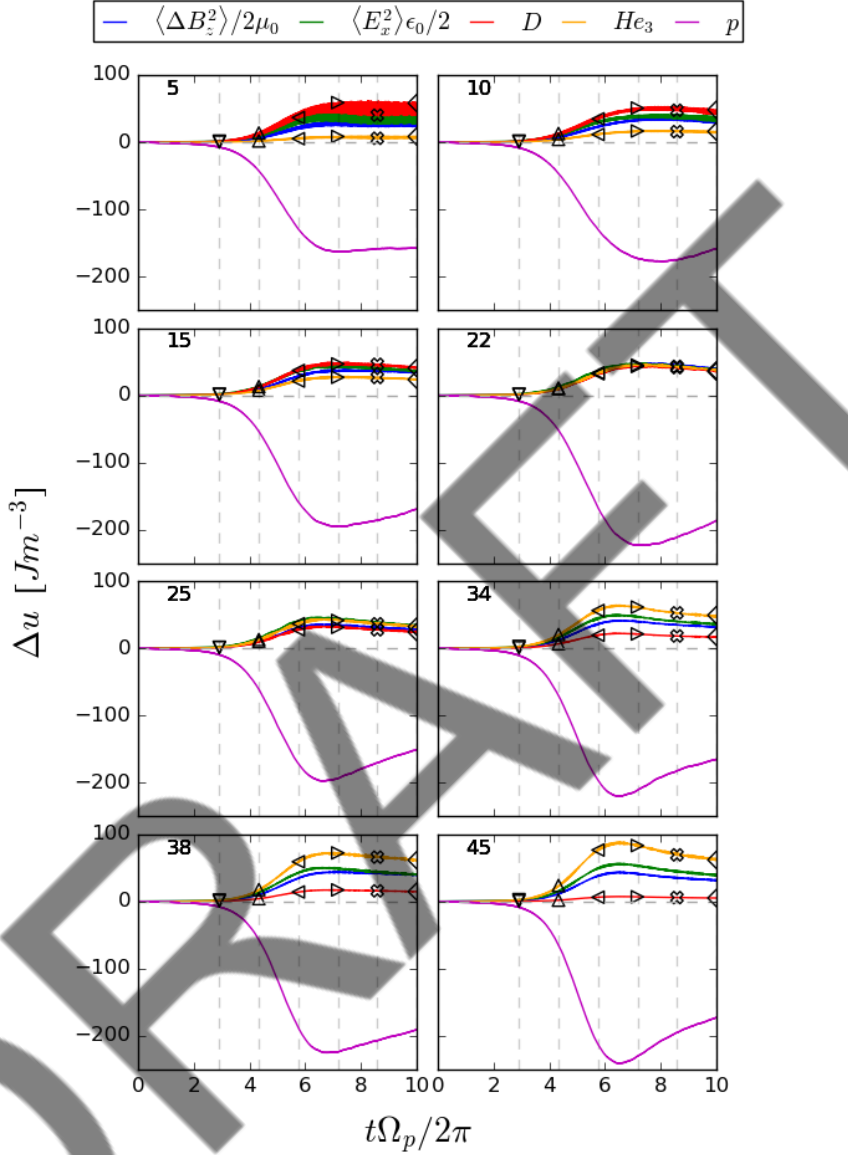


Figure 7.3: Time evolution, normalised to the proton cyclotron period, $2\pi/\Omega_p$, of the change in E_x and ΔB_z field energy densities, and deuteron (D), helium-3 (${}^3\text{He}$) and proton (p) kinetic energy densities, as labelled, in units of $[Jm^{-3}]$. These panels are for multiple ${}^3\text{He}$ concentrations, displayed at top left as a percentage of electron number density, with a minority energetic 14.68 MeV proton particle population initially distributed in velocity space as a drifting ring-beam, see Eq. (1.48). Markers and vertical lines correspond to equally spaced times used to calculate the relative transfer of kinetic energy to deuterons and helium-3, see Fig. 7.5. For parameters, see Tables 7.2 and 7.4.

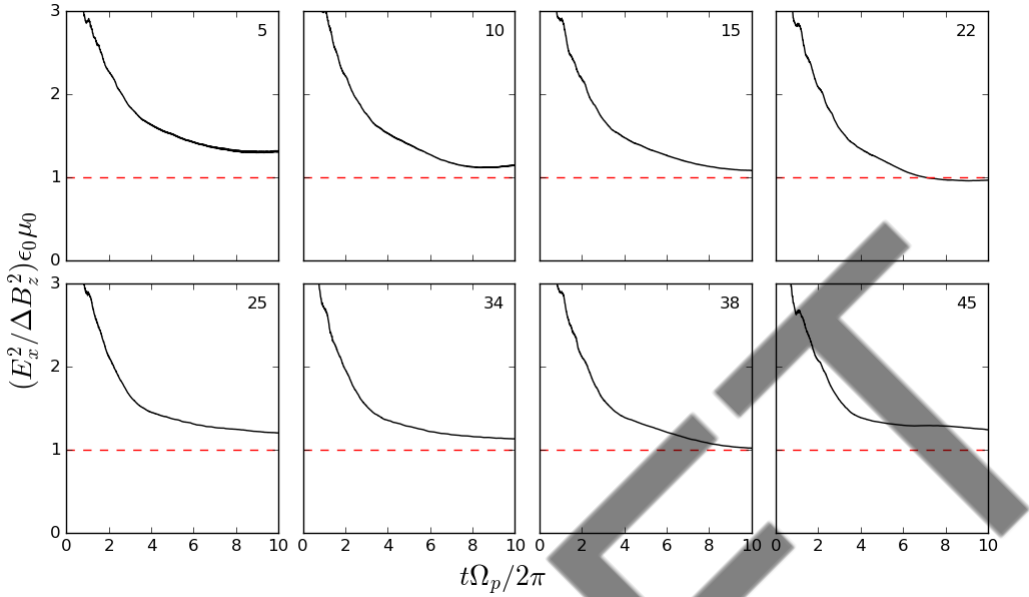


Figure 7.4: Time evolution, normalised to the proton cyclotron period, $2\pi/\Omega_p$, of the moving average of the ratio of electrostatic (green trace in Fig. 7.3) to electromagnetic (blue trace in Fig. 7.3) field energy oscillations excited by the MCI in our PIC simulations. Each trace corresponds to a ${}^3\text{He}$ concentration given top right as a percentage of electron number density.

we find that the ratio of the mean change in kinetic energy per ion for the two species, denoted $\Delta E_D(t)/\Delta E_{He3}(t)$, converges at saturation to the value 0.374 which equates to that of $(m_{He3}/m_D)(q_D/q_{He3})^2$, as discussed further below. This convergence is demonstrated in Fig. 7.5, where each vertical grouping of symbols provides a series of snapshots, for each value of ${}^3\text{He}$ concentration, of the value of $\Delta E_D(t)/\Delta E_{He3}(t)$ derived from the red (deuterium) and yellow (${}^3\text{He}$) traces in Fig. 7.3.

The earliest data points in Fig. 7.5 (those with the ∇ shape) correspond to times within the linear MCI growth phase (see Fig. 7.3) of the simulations such that the nonlinear saturated regime has not yet been reached. In contrast, the other data points in Fig. 7.5 correspond to later times and are narrowly clustered at the 0.374 line. This is the second PIC code study of MCI physics in a scenario involving three ion species, of which two are thermal majorities and one is an energetic minority. The previous study [110] was for thermal deuterons and tritons at 1 keV with energetic 3.5 MeV alpha-particles. There, the energy transfer ratio at saturation was found empirically to correspond to a simple physical condition which represented a previously unexplored feature of

wave-particle cyclotron resonance instability in the nonlinear regime. Namely, the two thermal ion species that acquire energy under the MCI evolved to a saturated state such that the changes in their mean squared Larmor radii were equal, see Eq. (2) of Ref. [110]. Applying this criterion, as laid out in §5.2.3, to our thermal deuterons and ^3He ions, implies that the ratio of the spatially averaged change in kinetic energy is

$$\left\langle \frac{\Delta E_D}{\Delta E_{He3}} \right\rangle = \left(\frac{m_{He3}}{m_D} \right) \left(\frac{q_D}{q_{He3}} \right)^2 \simeq 0.374 , \quad (7.11)$$

where the brackets $\langle \cdot \rangle$ denote spatial averaging. This value is identical to that found empirically in Fig. 7.5, as noted above.

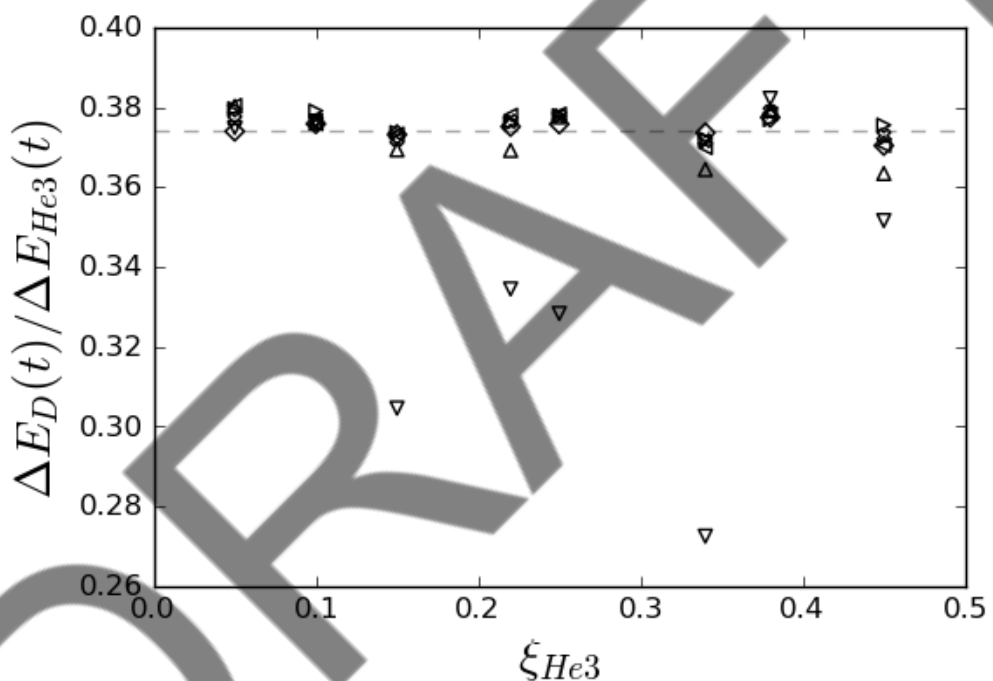


Figure 7.5: The ratio between the change in the mean ion kinetic energy per ion of the thermal deuteron and helium-3 populations plotted versus ^3He concentration. Marker shapes correspond to those found in Fig. 7.3, representing different times, and the horizontal dashed grey line corresponds to the invariant $(m_{He3}/m_D)(q_D/q_{He3})^2$ ratio equal to 0.374, see Eq. (7.11).

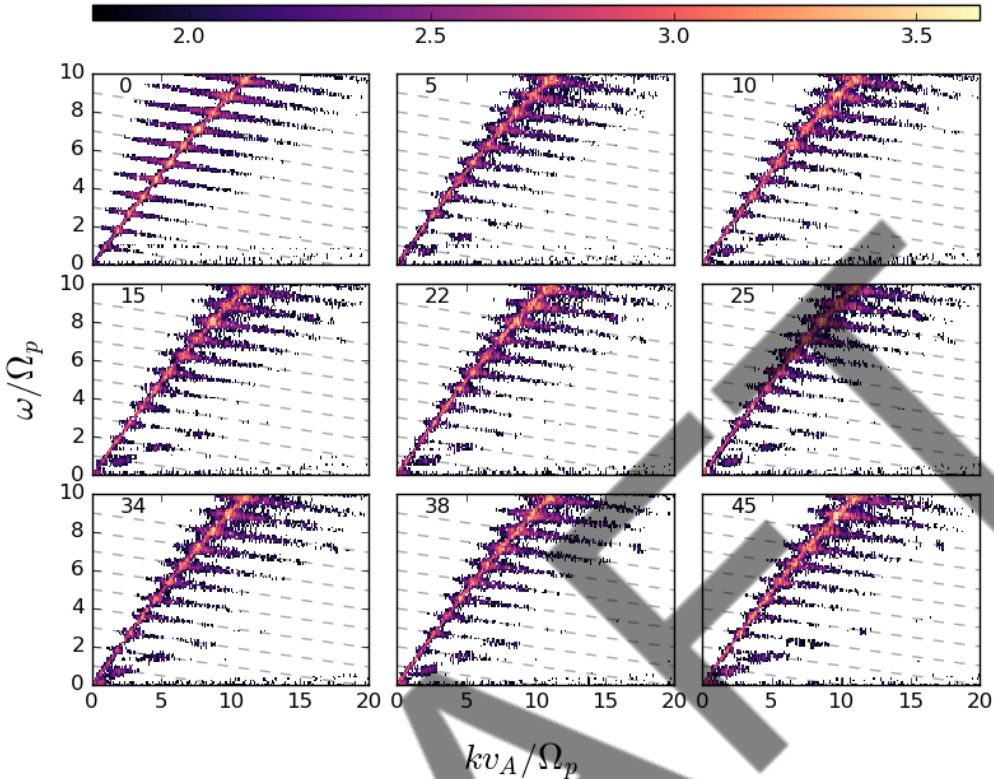


Figure 7.6: Distribution of energy in the oscillatory B_z magnetic field component in dimensionless wavenumber-frequency space, for ^3He concentrations from zero to 45%, as labelled at top left of each panel. Shading (see top colour bar) is logarithmic base 10 and denotes the FFT magnitude above a threshold. The dominant features occur near successive integer harmonics of Ω_p , and exhibit a systematic downward linear trend in (ω, k) space from left to right. This is highlighted by the evenly spaced dashed dark-grey diagonal lines, and is caused by Doppler effects arising from high parallel velocities, see Eq. (7.13). Frequency is normalised to the proton cyclotron frequency Ω_p and wavenumber is normalised using the Alfvén speed v_A .

7.4.3 Doppler shifted ICE spectra and the spatiotemporal distribution of excited field energy

Figure 7.6 presents spatiotemporal Fourier transforms of the energy in the B_z component of the excited fields. These are obtained using FFT techniques, integrating over the full temporal duration of each simulation and the entire 1D spatial domain. Each of the nine panels corresponds to simulations with different values of the ^3He concentration as labelled in the top-left corner.

It is evident from Fig. 7.6 that the energy of the excited fields is concentrated in successive tilted bands in (ω, k) space, each of which is separated from its nearest neighbours by a frequency interval Ω_p . Similarly to Fig. 15 of Ref. [79], these bands slope downwards with increasing wavenumber k . Their strongest excitation is localised to the intersection between these bands and the upward diagonal feature, which corresponds to the FAW. In almost all previous EPOCH simulations of ICE scenarios, the plots corresponding to Fig. 7.6 typically display strictly horizontal bands. For example, we refer to Figs. 3, 5, 3 and 8 of Refs. [100, 104, 106] and [116], respectively. The downward slope found in the present work arises from Doppler effects in consequence of the high parallel velocities of the driving protons. This effect was first noted in Fig. 15 of Ref. [79], for simulations supporting interpretation of ICE observations driven by 3 MeV fusion-born protons in deuterium plasmas in LHD, for which $u_{\perp} \simeq v_A$ and $u_{\parallel} \simeq 2v_A$.

7.4.4 Simulated ICE power spectra

The measured power spectrum with respect to frequency is the most easily accessible experimental feature of ICE. For comparison with such measurements, simulated ICE power spectra are typically obtained by integrating the spatiotemporal FFT over wavenumber; that is, over successive horizontal bands, thus yielding total power as a function of frequency. Applied to the present datasets, this standard approach leads to the power spectra shown in Fig. 7.7. We note that the intensity of these spectra is at least an order of magnitude greater than the noise floor everywhere, which we compute by running a simulation containing no energetic ions, further confirming that the phenomenology studied here is a collective energetic particle effect. We also note that at higher frequencies, $\omega/\Omega_p > 10$, in this power spectra representation, peaks undergo an upward frequency shift following an increase in ${}^3\text{He}$ concentration. In order to accommodate the tilting shown in Fig. 7.6, it may be helpful to adjust the standard technique as follows, leading to the simulated ICE spectra shown in Fig. 7.8. This requires consideration of the Doppler shift, which relates the observed frequency ω' to the frequency ω in the rest frame of the emitting particles through the scalar product of the wave-vector \mathbf{k} and the particle velocity \mathbf{u} ,

$$\omega' = \omega - \mathbf{k} \cdot \mathbf{u} . \quad (7.12)$$

Our 1D3V PIC simulations have a one-dimensional spatial domain whose orientation with respect to the magnetic field defines the direction of all possible \mathbf{k} vectors. The particle's parallel velocity component is determined by its pitch-

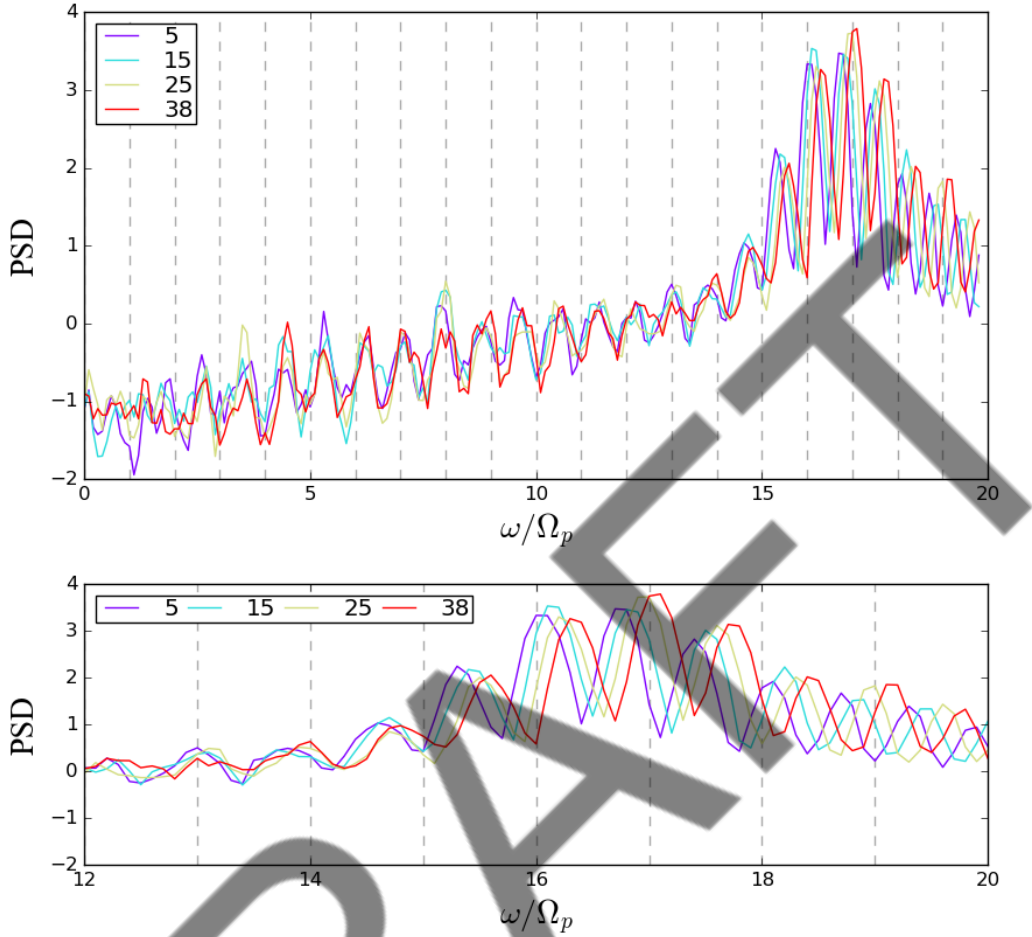


Figure 7.7: (Upper) Logarithmic (base 10) power spectral densities (PSD) of simulated ICE in frequency range $0 < \omega < 20\Omega_p$, for ${}^3\text{He}$ concentrations between five and 45%, see legend. Vertical dashed lines indicate successive integer harmonics of the proton cyclotron frequency Ω_p . (Lower) Expanded version of the upper panel for the range $12\Omega_p < \omega < 20\Omega_p$, showing increasingly strong dependence of the frequency location of ICE spectral peaks on ${}^3\text{He}$ concentration.

angle on initialisation, which is related to its corresponding value of $u_{\perp 0}/v_A$, which also depends upon the concentration of the ${}^3\text{He}$ ions, as discussed in §7.3.1, leading to Table 7.4. Let us write the parallel component of the wavevector as $k_{\parallel} = |\mathbf{k}| \cos \theta$, where θ is the angle between the magnetic field direction and the 1D simulation domain. The parallel velocity component is $u_{\parallel} = |\mathbf{u}| \cos \phi$, where ϕ is the particle's pitch-angle defined by $\phi = \arctan(u_{\perp}/u_{\parallel})$. In the present context, $|\mathbf{u}| = u_p$ is the birth velocity of the protons, defined in terms of their birth energy, E_p , by $u_p = \sqrt{2E_p/m_p}$, and our spatially one-dimensional PIC

simulations have wavevector magnitudes $|\mathbf{k}|$, denoted by k .

In general, the spectral peaks of ICE are excited around frequencies corresponding to integer multiples of the cyclotron frequency of the minority energetic protons $l\Omega_p$ in their rest frame. The corresponding Doppler shifted l^{th} cyclotron harmonic for a given proton, as observed in the rest frame of the bulk plasma, is therefore

$$\begin{aligned}\omega' &= \omega - ku_{\parallel 0} \cos \theta , \\ \omega'_l &= l\Omega_p - ku_p \cos \theta \cos \phi ,\end{aligned}\tag{7.13}$$

where all symbols are as previously defined.

Since our proton species is initially distributed as Eq. (1.48), the predominant values of $u_p \cos \phi$ in Eq. (7.13) lie close to $u_{\parallel 0}$. The value of θ in Eq. (7.13) is fixed by the choice of the spatial domain orientation with respect to the magnetic field. It follows from Eq. (7.13) that the spectral features in Fig. 7.6, corresponding to strong MCI drive by these protons, will slope downwards across (ω, k) space, with their gradient conditioned by the value of $u_{\parallel 0}$, centred on lines that intersect integer values of $l\Omega_p$ at $k = 0$.

The power spectra shown in Fig. 7.8, which connects for this effect, are obtained by integrating the spatiotemporal FFTs of Fig. 7.6 along Doppler-shifted isofrequency lines, yielding simulated ICE power spectra plotted with respect to the frequency ω' defined by Eq. (7.13). The method is described in Appendix D, and the resulting power spectra using theoretical Doppler velocity inferred from the white dashed diagonal lines in Fig. 7.6, is presented in Fig. 7.8.

Since the Doppler shifted frequency ω' is dependent on the wavevector \mathbf{k} , it can be expressed as a velocity $v_{dop} = d\omega/dk$, which can then be normalised to the Alfvén speed, v_{dop}/v_A . Regardless of the plasma density which influences v_A , one can equally define the gradient by some angle Θ . This is orientated clockwise from the frequency axis in wavenumber-frequency space and which, when properly normalised to grid, is independent of Alfvén velocity. For our Doppler shift theory calculation in Eq. (7.13), this is given by $\Theta_{dop} = \arctan(\Delta\omega/(v_{dop}\Delta k))$. Both the velocity and angular description of the extent of ICE Doppler shifting is found as a function of ^3He concentration an presented in Table 7.5 under the first and second columns respectively.

If information regarding the magnetic field angle θ , pitch-angle ϕ or minority particle's velocity at birth u_p is unknown in Eq. (7.13), then we propose the computational method of gradient detection in images using the kernel gradient algorithm. Detailed in Appendix C, this method calculates convolutions

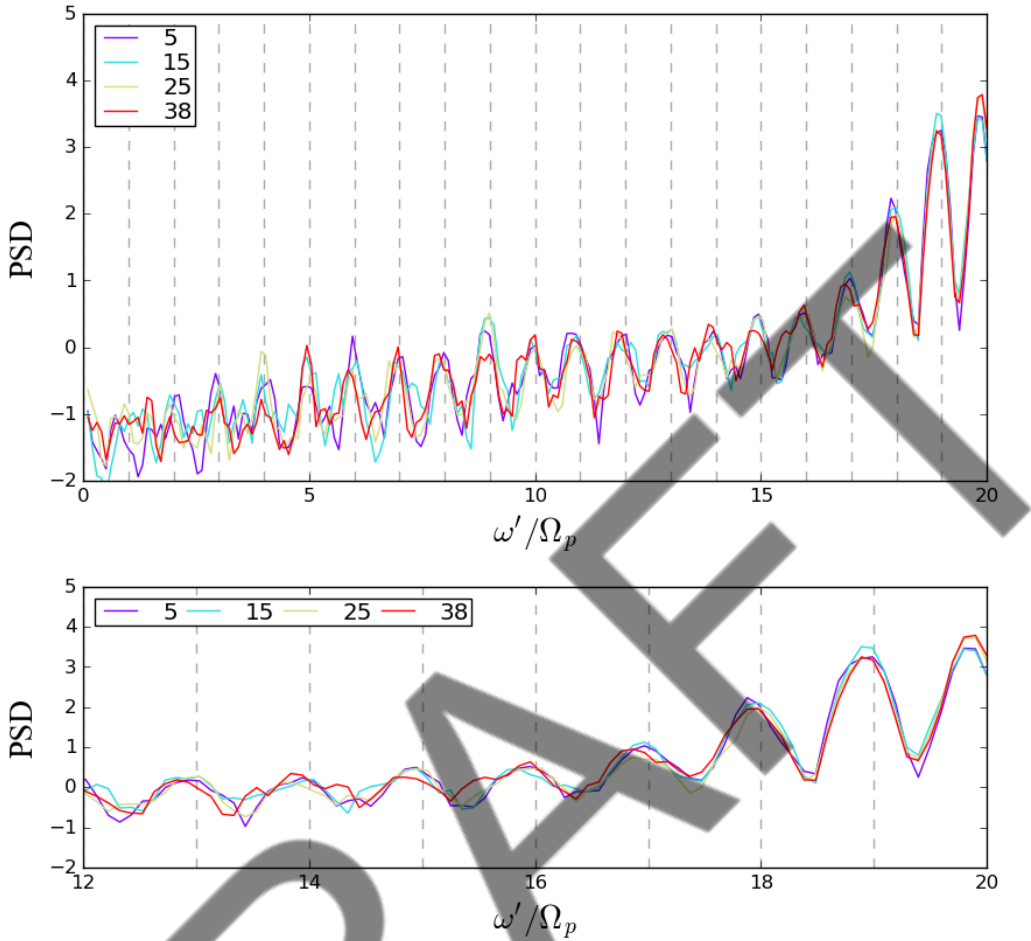


Figure 7.8: Simulated ICE power spectra plotted with respect to Doppler-shifted frequency ω' normalised to Ω_p . Like Fig. 7.7, these spectra are derived from the data displayed in Fig. 7.6. Here, however, the integration of the spatiotemporal FFT with respect to wavenumber is performed along Doppler shifted isofrequency lines, shown as dark-grey dashes in Fig. 7.6, following Eq. (7.13). See also Appendix D for a description of the method used.

of the pixel image grid to directional matrices which yield gradient maps as a function of pixel coordinate (i, j) , corresponding to real frequency coordinates of (ω_i, k_j) . These gradient maps yield useful information regarding features in images, and has wide applications in fields other than physics. By binning both axes, one computes the histogram of gradients across the user defined frequency-wavenumber area of interest. These histograms then reveal most likely gradients in terms of the angle Θ_{kernel} , which can be pre-processed into an equivalent velocity v_{kernel}/v_A . These are both given in the third and fourth columns of Table

ξ_{He3} [%]	Θ_{dop} [°]	$ v_{dop}/v_A $	Θ_{kernel} [°]	$ v_{kernel}/v_A $
0	6.18	0.114	7.45	0.137
5	6.18	0.112	8.52	0.134
10	6.18	0.111	8.52	0.134
15	6.18	0.109	8.58	0.132
22	6.18	0.107	8.57	0.129
25	6.18	0.106	8.53	0.128
34	6.17	0.103	8.58	0.124
38	6.17	0.102	8.51	0.122
45	6.17	0.100	8.54	0.121

Table 7.5: Extent of Doppler shifting on ICE signals in terms of angles and velocity gradient equivalents on the 2D FFT wavenumber-frequency plane as predicted by theory Eq. (7.13). Angles are defined as positive clockwise from the frequency axis.

7.5, respectively. This method reveals that we are able to predict the particle's birth velocity or magnetic field angle, if they are unknown, to within 3% of its actual value.

Figure 7.8 shows that by calculating the power spectrum along the Doppler shifted isofrequency lines, Eq. (7.13), the frequency shifting of ICE spectral features that are present in Fig. 7.7 can be removed entirely. This re-establishes the mapping of simulated ICE spectral peaks onto the minority proton cyclotron harmonics for all ${}^3\text{He}$ concentrations, and suggests that inadequate post-processing techniques will miss ICE excitations from the 14.68 MeV energetic protons or for other low pitch-angled fusion-born products.

7.4.5 Exploring energy of minority species

We showed in §7.4.4 and Eq. (7.13) that the extent of Doppler shifting is dependent on the velocity u_p , and hence kinetic energy, $u_p = \sqrt{2E_p/m}$, of the minority proton. We explore the same simulation scenarios presented in the sixth column of Table 7.4 for $\xi_{He3} = 0.25$, but for different initial proton energies. The spatiotemporal Fourier transforms of four simulations with proton energies of 5, 12, 15 and 20 MeV, are given in Fig. 7.9 (see panel titles). Here, the normalised velocity equivalent Doppler shift gradients - for example see Table 7.5 - in frequency-wavenumber space, v_{dop}/v_A , are (from low to high energy) 0.062, 0.096, 0.107 and 0.124, shown by the dashed-white lines in each panel. These are each unique for a constant mass density plasma, and hence a constant

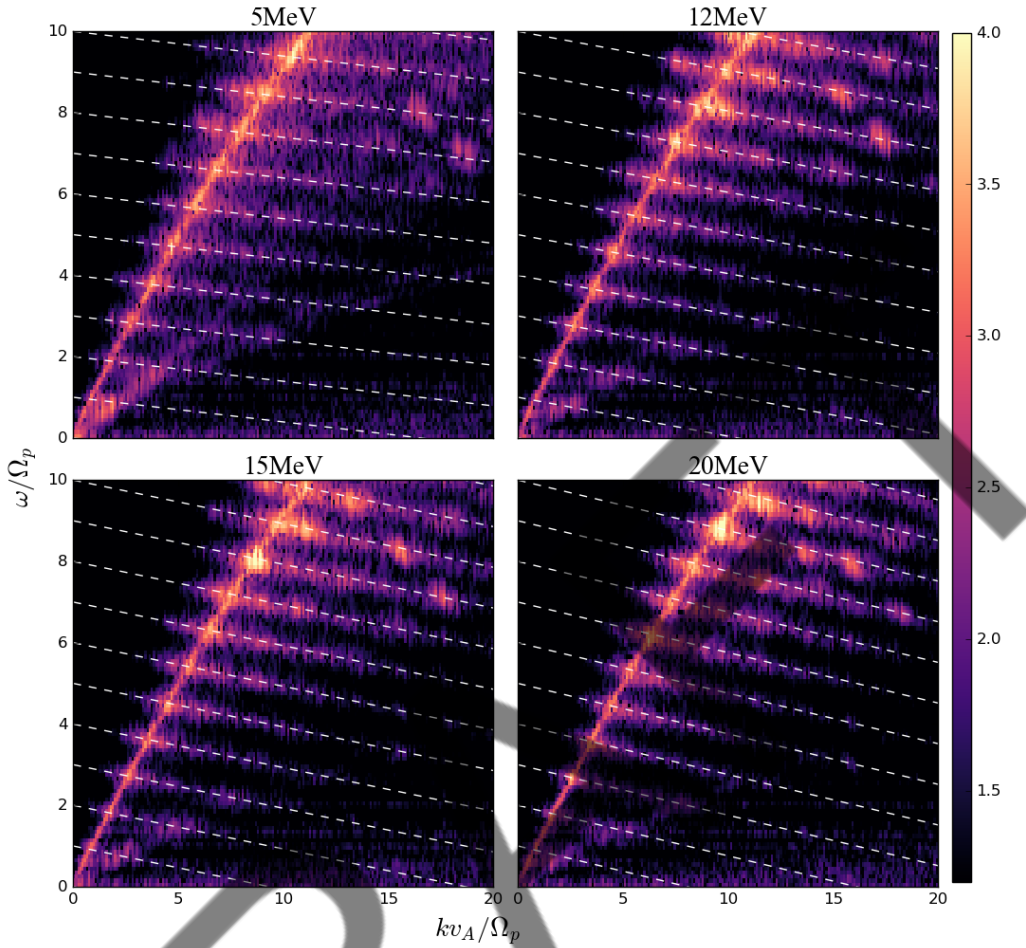


Figure 7.9: Spatiotemporal Fourier transforms of the oscillating ΔB_z component for a thermal D- ${}^3\text{He}$ plasma at a ${}^3\text{He}$ concentration of $\xi_{\text{He}3} = 0.25$. A drifting ring-beam of protons are initialised with increasing energy, see each panel's title. Logarithmic base 10 scale of the oscillatory magnetic field ΔB_z^2 given as colour bar right. Theoretical Doppler shift given by Eq. (7.13) for multiples l of the proton cyclotron harmonic Ω_p overlaid as diagonal dashed white lines, increasing in gradient descent magnitude with proton energy.

Alfvén speed v_A normalisation.

Figure 7.9 confirms that, for constant pitch-angle, the Doppler shift of the ICE harmonics are dependent on the energy of the minority species. We have not investigated magnetic field orientations away from quasi-perpendicular, but the Doppler shift is still significantly dominant

7.5 Summary and conclusions

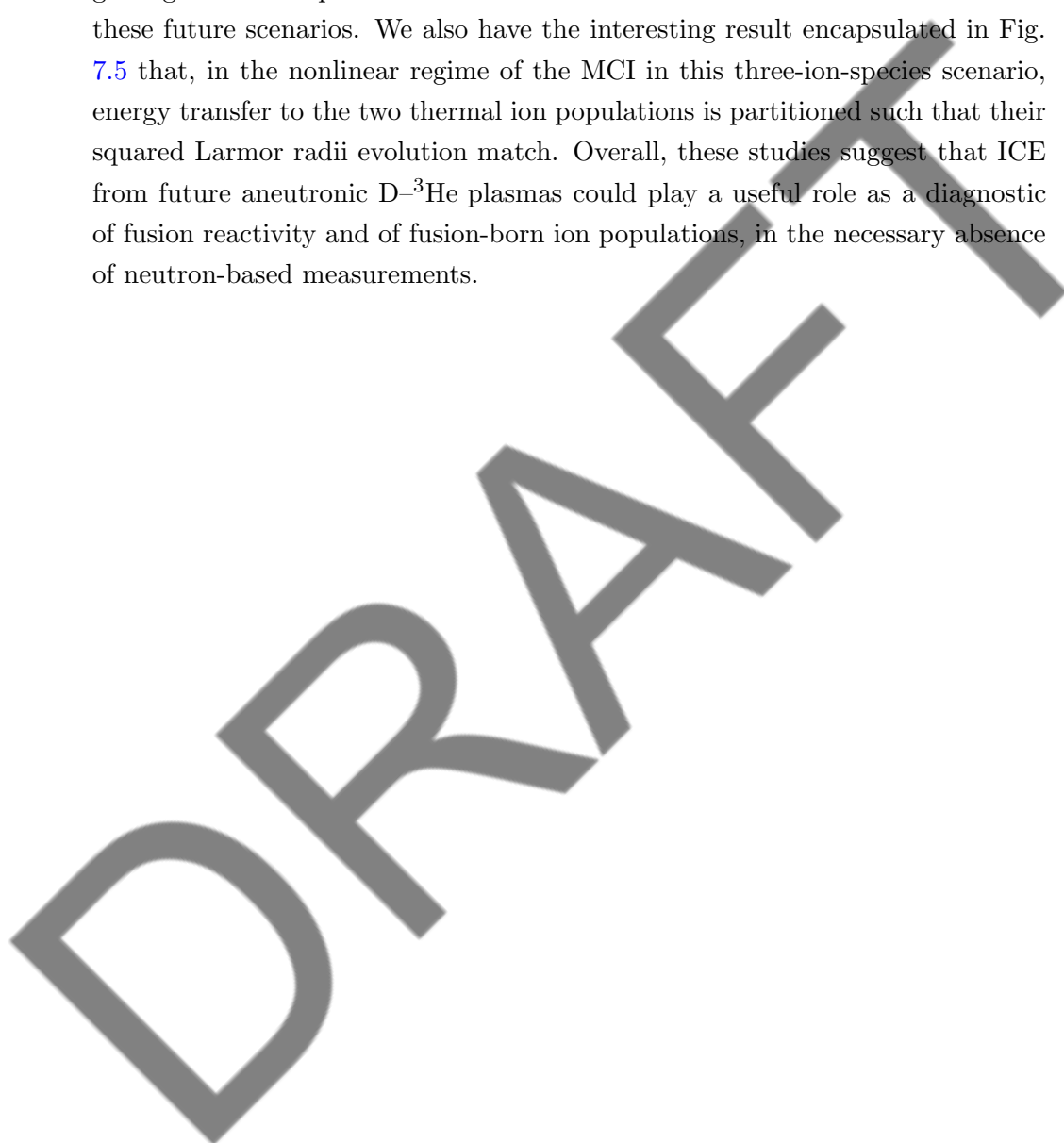
We have addressed two key questions regarding the potential characteristics of ICE signals that might be measured from future aneutronic MCF plasmas whose thermal ion populations comprise deuterium and helium-3. First, what are the predicted ICE power spectra and, second, how would the ICE spectral properties vary with the mix of deuterium and helium-3? The ICE-generative properties of the 3.67 MeV alpha-particles born in these plasmas would presumably resemble those of their 3.5 MeV counterparts born in DT plasmas, which have already been widely studied in the ICE literature; therefore we focus here on the 14.68 MeV protons, which present novel features because they are substantially faster.

In constructing scenarios for our kinetic simulations of ICE using the EPOCH PIC code, we are motivated by: (1) recent observations of ICE from unexpected confined trace fusion-born proton populations in deuterium plasmas in the KSTAR tokamak and LHD heliotron-stellarator, which may represent plausible counterparts to future early instances of ICE from D– ^3He plasmas; and (2) continuity with respect to the existing observational and interpretive literature on ICE from contemporary large toroidal MCF plasmas. Together, (1) and (2) steer us towards scenarios in which plasma and magnetic field parameters are similar to those at the outer mid-plane of JET, and the velocity-space distribution of the 14.68 MeV protons is a drifting ring-beam for which $v_{\perp} \sim v_A$, with a much larger component of kinetic energy directed parallel to the magnetic field.

We find that, in these scenarios, the 14.68 MeV proton population relaxes collectively under the MCI (Fig. 7.3), which is widely regarded as the primary emission mechanism for ICE. In the present approach, the MCI emerges spontaneously from self-consistent particle and field dynamics, calculated at the level of Maxwell’s equations and the Lorentz force. The spatiotemporal Fourier transform of the oscillating magnetic field excited by the MCI exhibits strong distinctive tilting of the primary spectral features in (ω, k) space (Fig. 7.6), with respect to the horizontal wavenumber axis. This is a consequence of Doppler shifts arising from the large parallel velocities of the protons, and is found to be invariant against a change in the ^3He concentration across different simulations (Table 7.2), as one would expect. The set of simulated ICE power spectra obtained by horizontally integrating the spatiotemporal Fourier transform over all wavenumbers at each frequency, is shown in Fig. 7.7. Figure 7.8 shows that it is possible to correct for Doppler shifts by performing slanted integrations along Doppler-shifted isofrequency lines, yielding simulated ICE power spectra which have strong spectral peaks at Doppler-shifted proton cyclotron harmonics.

Our results show that future experimental studies of ICE from D– ^3He plasmas

would benefit from having good resolution in wavevector, in addition to frequency, to enable to reconstruction of Doppler-shifted spectra (Fig. 7.8) from the data. The excited fields have electrostatic and electromagnetic components that are broadly comparable in the scenarios considered here, see Fig. 7.3, suggesting that both probes and antennas could be effective detectors of ICE in these future scenarios. We also have the interesting result encapsulated in Fig. 7.5 that, in the nonlinear regime of the MCI in this three-ion-species scenario, energy transfer to the two thermal ion populations is partitioned such that their squared Larmor radii evolution match. Overall, these studies suggest that ICE from future aneutronic D– 3 He plasmas could play a useful role as a diagnostic of fusion reactivity and of fusion-born ion populations, in the necessary absence of neutron-based measurements.



Chapter 8

Summary & Conclusions

In this thesis we have run PIC simulations of deuterium-tritium (DT) and aneutronic deuterium-helium-3 ($D-^3He$) plasmas to investigate the effects of non-zero concentrations of tritium and helium-3, respectively, on the simulated power spectra of ICE, the ensemble exchange of energies between ion populations, and additional resonant particle behaviour. In Chapter 5, we simulated the well-studied JET DT plasma 26148, which comprised of an admixture of 11% tritium at its maximum power output within the bulk DT plasma. Comparative power spectral studies revealed correlations between features in our simulated spectra at the same concentration, confirming the importance of non-zero tertiary ion concentrations. Then, in Chapter 6, we utilised the modified linearised Maxwell-Vlasov (LMV) code [40] to present computationally extracted growth rates of the MCI with an imposed drifting ring-beam population of 3.5 MeV energetic alpha-particles. Our modification allowed for the inclusion, again, of tritium for concentrations (with respect to electron number density) between zero and 97.5%, resembling that of JET plasma 26148, complimenting our earlier simulations of the same plasma. These studies revealed dependencies on the doublet split on tritium concentrations that were originally understood to be the result of dips in growth rates along the band of instability as k_{\parallel} changes sign, and hence provided a powerful tool for determining relative ion concentrations and other plasma parameters. Finally, in Chapter 7, PIC simulations of aneutronic $D-^3He$ plasmas with a drifting ring-beam population of 14.68 MeV energetic protons were investigated for 3He concentrations between zero and 45%. Results were presented in terms of their energy exchange, Fourier transformations and power spectra. Here, it was revealed (and complimented by derived Doppler shift theory) that the parallel velocity components, $u_{\parallel 0}$, of energetic ions involved in the evolution of the MCI lead to Doppler shifts in wavenumber space of each ICE harmonic.

Here we repeat brief summaries of each of the results chapters, providing links, where possible, between each, and interpret the results in terms of the long-term goals of fusion energy cited at the start of this thesis.

8.1 ICE from simulated DT plasmas

For reasons of computational cost, previous simulations of the MCI and ICE [37, 100, 113] have not included the thermal triton population, so that their plasmas were populated by a single thermal ion species. This work explored, for the first time, the consequences for ICE simulation outcomes in relation to the observed ICE spectra from JET plasma 26148, by including a thermal triton population, in addition to the thermal deuterons. The experimental ICE spectra has been used to benchmark first principles computational simulations of the MCI [100, 115, 118] and to shed light on the relative contribution of linear and nonlinear MCI phases in building the observed ICE spectrum [100, 101, 105]. Validation of previous findings and further parameter studies hence prove valuable for ICE's diagnostic use. Through measuring the correlation emission frequencies of dominant ICE power spectral features between simulations and experiment, we were able to quantify the relation between frequency shifts and tritium concentration with respect to electron number density. These suggest that additional wave-particle resonance and degenerate harmonics play a role in downshifting (also termed reddening) the frequency of successive ICE peaks. This is realised such that following a 20% increase in the tritium concentration - which is also a $\lesssim 10\%$ increase in mass density - leads to power spectral features appearing at frequencies one whole deuteron cyclotron frequency less.

A key finding of this chapter was the gyro-resonant behaviour first observed in our change in energy through time plots. These revealed, in a 50:50 DT simulation, an energy exchange between the deuterons and tritons on the order of their mass ratios. Zero order approximate theory suggested that this was the result of a collective gyro-resonant behaviour, in which the change in the squared Larmor radii of both species is equivalent. This is supported by results presented in Chapters 4 and 7, in which ensemble perpendicular velocities of D-³He confirmed that the change in the squared Larmor radii of these particles evolve at the same rate, at all times.

Through two-dimensional maximal likelihood statistics, previously utilised in comparing the evolution of stellar clusters on colour-magnitude diagrams, we drew correlations between normalised peaks in ICE spectra with those of the JET 26148 experimental data, which happened to contain an 11% tritium ad-

mixture to deuterium at peak performance [58, 187, 211]. The power spectra of a simulation with 11% tritium concentration best matched those of the real experiment, reinforcing the importance of simulating non-zero tertiary ion concentration plasmas to accurately depict power spectral data from experiment.

This chapter served as *fundamentum opus* for the succeeding results chapters, as it highlighted the importance of the tertiary ion in PIC simulations in encapsulating the degenerate driving of harmonics, gyro-resonant behaviour and additional particle resonant phenomenology. It also demonstrated the need in linear growth rate MCI theory for the description of the additional bulk ion species, at non-equal concentrations.

8.2 Analytically sourcing growth rates of the MCI

In Chapter 6, we utilised the linearised Maxwell-Vlasov (LMV) code [40] to present computationally extracted linear growth rates of the MCI for a JET 26148 like plasma with an imposed drifting ring-beam population of 3.5 MeV energetic alpha-particles. As per the previous chapter, we modified the LMV code to summate the dielectric tensor integral, Eq. (1.32), over an additional population of thermal tritium ions, for concentrations between zero and 97.5%, with an energetic alpha-particle population held at a concentration of $\xi_\alpha = 1.5 \times 10^{-4}$.

Our modification allowed for the comparison to the PIC code results of the same plasma, presented in Chapter 5, and extended linear MCI theory into the multiple component plasma regime, of which it had not been utilised for. Key features of the growth rate spectra (a proxy for power spectra) of the MCI include the location in frequency space of the doublet splitting features. Doublet splitting is a unique phenomena that occurs asymmetrically around $k_{\parallel} = 0$, where Doppler shifts arise from the parallel birth velocity of the energetic ions u_{\parallel} - see Eq. (7.13). It was noted in Ref. [37] that the doublet splitting effect is larger for higher frequency harmonics until growth rates eventually diminish to zero for $k_{\parallel} = 0$. The cause of the splitting is still as of yet unknown, but it was postulated that the underlying mechanism of doublet splitting could be a form of grad-B or curvature drift, both of which involve Doppler shifting.

Because of the uniqueness of the doublet splitting, it was interesting to find from this chapter that its location in frequency is dependent on the plasma density as a parameter of tritium concentration. This was shown in Fig. 6.9, where peak growth rates are extracted at each tritium concentration LMV run. This revealed that the doublet splitting feature can be tracked to the concentration

of tritium ions via an approximately linear relationship, one which was also predicted in the preceding chapter. This visualisation has allowed for a mapping between frequency power spectra and plasma ion constitution. Considering the speed, availability and generalisation of the LMV code, this has potential application for research on multiple plasma instabilities, including investigations of solar wind.

8.3 ICE from simulated D– ${}^3\text{He}$ plasmas

Finally, Chapter 7 presented PIC simulations of aneutronic D– ${}^3\text{He}$ plasmas with a drifting ring-beam population of 14.68 MeV energetic protons for ${}^3\text{He}$ concentrations between zero and 45%. Results were again presented in terms of their energy exchange, Fourier transformations and power spectra. Motivation for this study was two fold. Firstly, aneutronic D– ${}^3\text{He}$ plasmas are vastly different in parameter space to the previously explored DT plasmas, specifically in their charge, mass, concentration ratios and the energy of the fusion-born ions. For this reason, we were justified in exploring, first, the well known case of JET plasma 26148 in Chapter 5 to establish a baseline of multicomponent plasma PIC simulations, revealing the importance of the NDW criteria and other computational restraints. Secondly, the use of aneutronic fuels in future fusion reactions are (current temperature limitations aside) the most advantageous for long-term sustainable fusion as a source of energy production.

It was revealed that, as a result of initial perpendicular speeds characteristic of strong linear MCI growth, $v_{\perp} \sim v_A$, leading to super-Alfvénic parallel velocities for our 14.68 MeV protons, the resonance between the FAW and multiple proton cyclotron harmonics is Doppler shifted in wavenumber space as per Eq. (7.13). This was striking, in that it had been undocumented until its recent sighting in Ref. [79], but was first explored in depth in this chapter, where Doppler shift theory was mapped to the simulated ICE spatiotemporal Fourier transforms. In this chapter, we also presented a method previously used in image manipulation and numismatics (the study of coins and tokens) to computationally extract the gradient in frequency-wavenumber space of the Doppler shifted ICE harmonics. This can be used when either the: pitch-angle, particle energy or magnetic field orientation is unknown, and returns the gradients of Doppler shifted ICE to within 3% of its analytical value. Likewise, this chapter proposes an improvement into the power spectral calculation to produce spectra that is in the parallel reference frame of the energetic ion. Traditional power spectra summates the square of a field’s spatiotemporal Fourier energy density

across horizontal frequency bands for a range of wavenumbers. Our alteration redefines the isofrequency to one that is angled Θ_{dop} clockwise to the frequency axis, allowing for summations over Doppler shifted isofrequencies instead of “lab-frame” frequencies. This chapter revealed that, whilst ICE is present in future aneutronic scenarios, there needs to be a greater importance placed on experimental spatial resolution to better utilise the ICE diagnostic for plasmas with super-Alfvénic products.

8.3.1 Future work

We present a few ideas for future work, both following the work of this thesis but also more generally in the field of fusion plasma research.

- (1) Explore the Buchsbaum resonant frequency, Eq. (1.13), using the PIC regime focused on low frequencies $\omega \simeq \Omega_i$.
- (2) Run multicomponent aneutronic fusion p–¹¹B simulations. Build up understanding of the MCI and ICE in more extreme plasma parameter scenarios, including magnetic field strengths and orientations, minority species energy and pitch-angles. This would also confirm ICE Doppler shift simulation results seen in Fig. 7.6.
- (3) The origin of the MCI most excited region (see intensities between $15 < \omega/\Omega_D < 22$ in Fig. 5.8) remains unresolved in fusion plasma PIC simulations. We found, for our DT and D–³He plasmas, close correlation between the FAW’s real and imaginary solutions at frequencies associated with this region, suggesting a form of FAW evanescent wave driving.
- (4) To explore gyro-resonant theory. Derive from first principles its origin and investigate the principle of least action for two different particle species under the influence of a background magnetic field. Investigation should also consider the conservation of a charged particle’s canonical momentum.
- (5) The LMV’s strength in quicker run times and lower computational cost makes it an obvious candidate for machine learning (ML) models to build relationships between observed power spectra and linear MCI growth rates. Once a model has been built, this would reveal unknown plasma parameters responsible for a specific set of experimentally observed power spectra, greatly improving ICE’s plasma diagnostic capability.

Appendix A

The shared area between curves

A.1 Shared area method

The shared area method was developed to compare the power spectra output from PIC simulations of multiple-ion plasmas, and to determine scaling relations between the location of ICE harmonics and the most strongly excited MCI region to the concentration of secondary bulk ions. It is similar to the cross-correlation algorithm, which for two signals f and g is written

$$f(t) * g(t) = \int_0^t f(\tau)g(t - \tau)d\tau' , \quad (\text{A.1})$$

where τ is a sliding offset applied to the signal g . The shared area method works for real-valued functions and adopts two boolean arrays, B_f and B_g , which are defined by the lower bounded function of f and g at position t , iterated over all offsets τ ,

$$SA(\tau) = \int_0^T \left[B_f(t, \tau)f(t) + B_g(t, \tau)g(t - \tau) \right] dt . \quad (\text{A.2})$$

For example, if $f(t) < g(t - \tau)$, then $B_f(t, \tau) = 1$ and $B_g(t, \tau) = 0$, so the integral collapses to just over the signal $f(t)$ at t . Whereas, if $f(t) > g(t - \tau)$, the inverse is true, so the integral collapses to over the shifted $g(t - \tau)$ signal. This returns an array, SA , which represents the area as a function of offset, τ , between both signals, hence the dependency of the boolean arrays on this offset. The area is maximised for the minimum offset between each signal, i.e. the distance between their “centres”. Since the boolean arrays are opposites of one another, they can also be re-written as $B_g(t, \tau) = 1 - B_f(t, \tau)$.

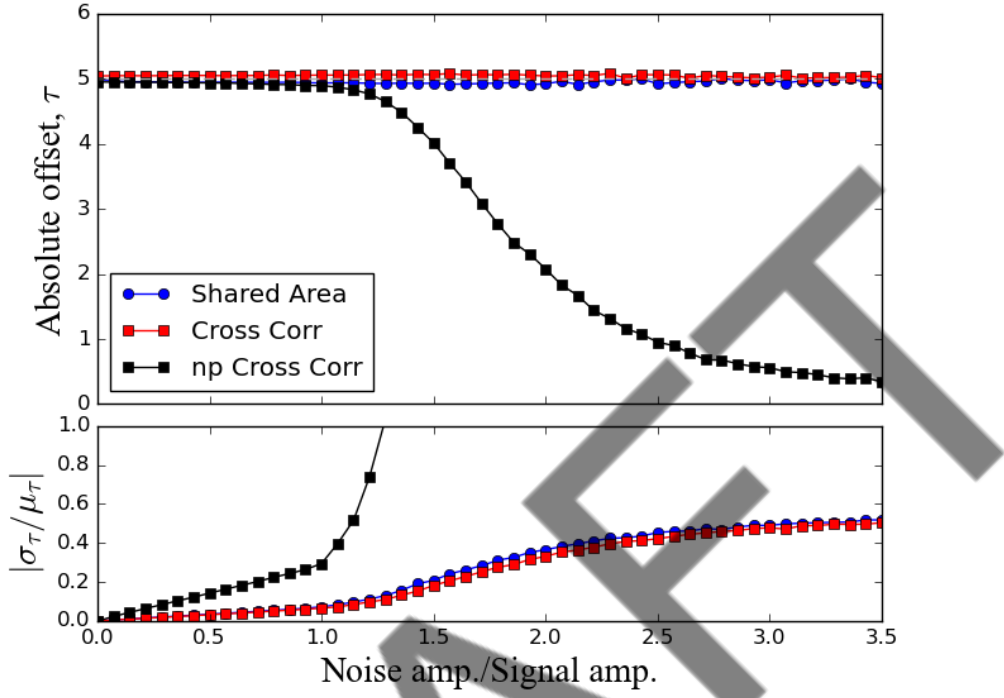


Figure A.1: Shared area method on noisy Gaussian signals separated by $\tau = 5$, using a Monte Carlo method for 10^4 randomly selected white noise distributions at each noise amplitude. *Top panel*: scatter points representing the mean offset calculated from the maxima of the shared area method (blue) and the maxima of the cross-correlation algorithm (red). *Bottom panel*: standard deviation of the calculated offset, σ_τ , normalised to the mean offset, μ_τ , for a given noise amplitude over 10^4 noise iterations.

Offsets derived from the shared area method are dependent on whether the observer is comparing peaks or troughs, as this determines whether the maximised or minimised shared area, respectively, is representative of the offset between the signal's curve. Also, if one of the two signals is much greater in amplitude, then the shared area plateaus, and so the offset is taken as the plateau's mid-point.

The shared area method works exceptionally well for signals with a noise component whose amplitude is comparable to, or greater than, the signal amplitude. To fully explore this regime, look to Fig. A.1, which draws comparisons between the cross-correlation and shared area methods, for two Gaussian curves with increasing levels of random noise up to three and a half times the signal amplitude., as per the example in §2.4.2. We see in Fig. A.1 the (*top panel*)

mean offset and (*bottom panel*) normalised standard deviation for 10^4 variations of random white noise applied to each Gaussian curve. By using this Monte Carlo method, we build a collection of randomised noise seeds so we can comment on both method’s ability, and compare them quantitatively. The ensemble mean of our noise samples show that the shared area method can predict the original offset between two signals to within 2% for noise amplitudes 3.5 times larger than the signal amplitude. Conversely, the NumPy python package implementation of the cross-correlation algorithm (labelled np Cross Corr), for the same number of noise samples, is unable to predict signal offsets even within 10% for noise amplitudes greater than 1.5 the signal amplitude.

The bottom panel of Fig. A.1 presents the error of each method normalised by the arithmetic mean offset between both signals. For the shared area method, this error plateaus for noise amplitudes greater than 2.5, whereas normalised errors in the cross-correlation algorithm greatly exceed 1 for noise amplitudes greater than the signal amplitude. Our implementation of the cross-correlation algorithm (labelled Cross Corr), which suffers from the same optimisation issues as our shared area method, Fig. A.2, does equally as well at extracting offsets. Whereas, the optimised NumPy implementation fares much worse. However, its tendency towards zero with increasing noise amplitudes (and hence its exponentially growing error bars) arises as a result of the algorithm’s zero-padding at the signal edges to provide equal array lengths for a full signal comparison. For signals with significant noise, one could subtract the signal’s root-mean-square to all points, assuming that there are no underlying trends in the data. This would guarantee that both signals oscillate around zero, and hence zero padding would not affect the result. Since the shared area method treats the boundaries of the domain as periodic, assumes dominant features are above noise floors and makes no assumption about trends in the data, it does not suffer from a tendency to zero for large noise amplitudes, and requires no pre-processing of this form.

It may be of importance to some to understand the computational cost of the shared area method in comparison to cross-correlation and NumPy’s equivalent function. Time differences between the shared area method, our implemented version of the cross-correlation algorithm and NumPy’s equivalent, can be found in Fig. A.2. Because of the calculation of the boolean matrix for the shared area method, it performs worse across all array sizes, rising approximately exponentially, alongside our implementation of the cross-correlation. The NumPy’s cross-correlation algorithm has been optimised in Python and is the best performing by at least one order of magnitude across all array lengths. However, the shared area function here has not be parallelised, which is easily possible in

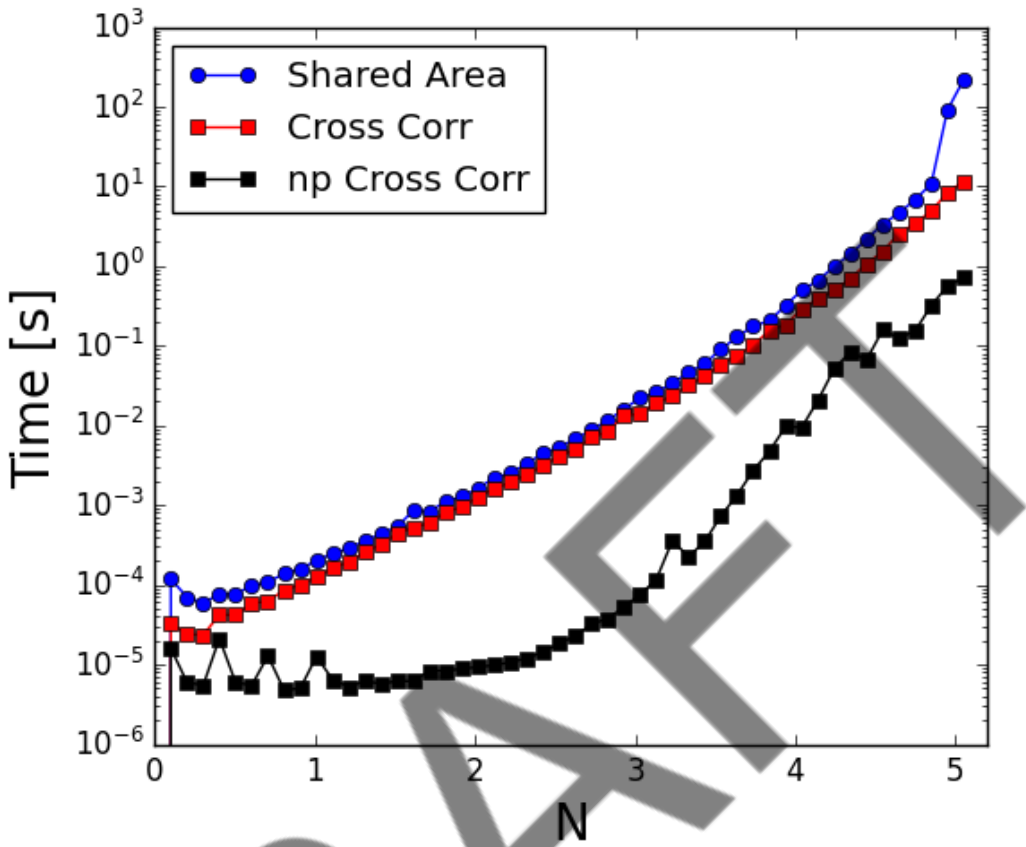


Figure A.2: Time comparison between the shared area and cross-correlation methods for two curves, $f(x)$ and $g(x)$, composed of random noise and 10^N data points. The NumPy implementation of the cross-correlation algorithm (*black*) is much faster, across all values of N , than the shared area method (*blue*) and our own implementation of the cross-correlation algorithm (*red*). The shared area method is marginally slower than cross-correlation (*red*) due to the calculation of the two boolean matrices B_f and B_g .

Python, and could therefore be made quicker if needed.

A.2 Alternative uses and multidimensionality

Other uses of the shared area method can include: calculation of the y -offset between signals, measuring the scale difference between signals (in both x and y directions) and its extension to multiple dimensions. In 2D, if we consider the spatial coordinates (x, y) and their offsets $(\Delta x, \Delta y)$ instead of time, Eq. (A.2) is extended in the y -domain such that the shared area is written as

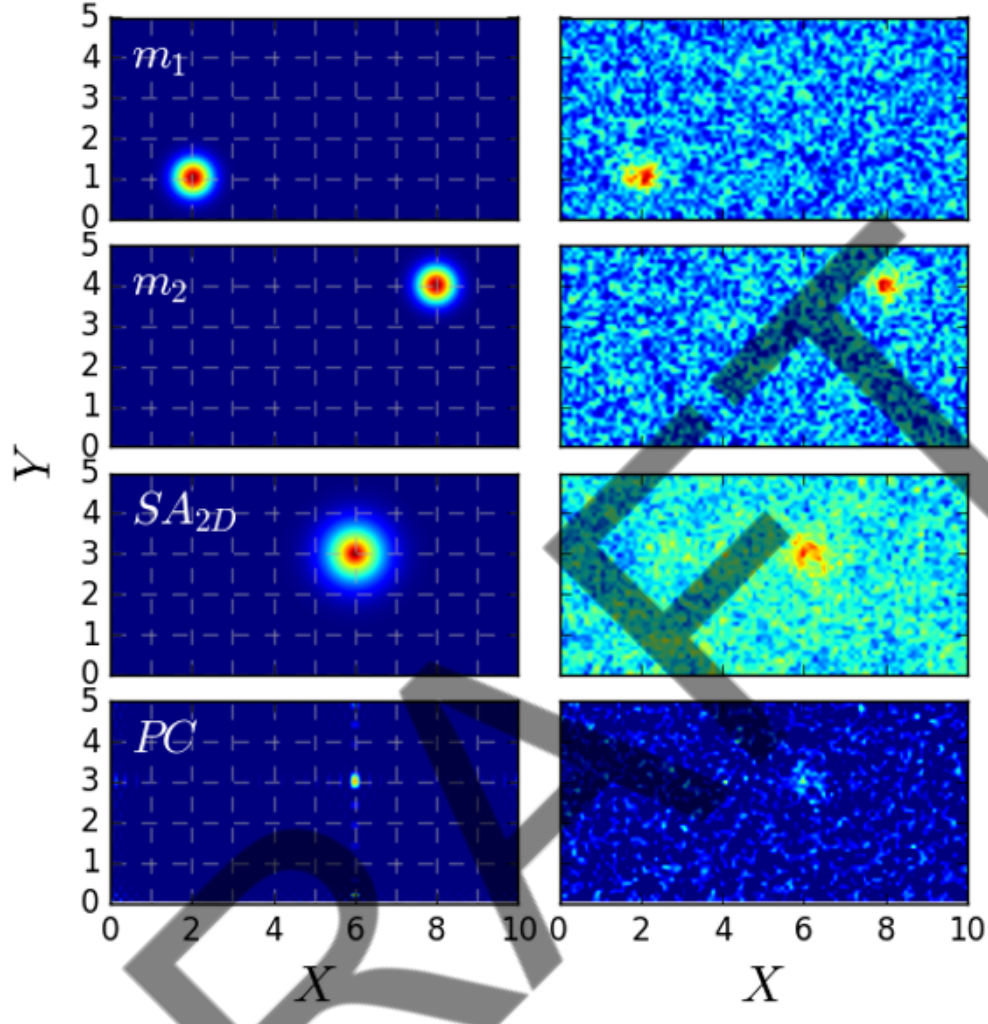


Figure A.3: Shared area method generalised for a two-dimensional plane (X, Y) of the two Gaussian signals $m_1(X, Y)$ and $m_2(X, Y)$ which are centred on coordinates (2,1) and (8,4) respectively. Left-hand column represents in each row: both of the source images m_1 and m_2 , the shared area 2d calculation and the equivalent phase-correlation coordinate offset. Right-hand column shows the same as the left, but with inconsistent noise floors added to each, of amplitudes ranging between 0 and 100% of the signal Gaussian amplitudes, in the source images. See that in the right-hand column the maximum phase-correlation is no longer able to accurately predict the coordinate offset, whereas maximum shared area can.

$$SA(\Delta x, \Delta y) = \int_X \int_Y dx dy \left[B_f(x, y, \Delta x, \Delta y) \cdot f(x, y) + B_g(x, y, \Delta x, \Delta y) \cdot g(x - \Delta x, y - \Delta y) \right]. \quad (\text{A.3})$$

For N number of dimensions, whether spatial or temporal, the shared area is generalised by the multi-dimensional vector \mathbf{r} and its offset vector Δ ,

$$SA(\Delta) = \int_{\mathbb{R}^N} d^N \mathbf{r} \left[B_f(\mathbf{r}, \Delta) \cdot f(\mathbf{r}) + B_g(\mathbf{r}, \Delta) \cdot g(\mathbf{r} - \Delta) \right]. \quad (\text{A.4})$$

Let us now run through a two dimensional shared area example. Consider two matrices $m_1(X, Y)$ and $m_2(X, Y)$ which are both Gaussian sources centred on (2,1) and (8,4) respectively. The matrices, shared area value, and phase-correlation (see §2.4.2) between both signals are presented in the rows (top to bottom) of Fig. A.3. Interestingly, the phase-correlation has historically found more applications in two dimensions as its use was originally intended for television pixel offsets. The left-hand column feature no noise, and the right-hand column introduces inconsistent random white noise between both signals m_1 and m_2 .

For zero noise (*left column*) both the shared area and phase-correlation methods (as labelled top-left of each panel) do well at extracting the offset between images. When the noise is no longer consistent (*right column*) the phase-correlation method returns a loosely accurate prediction of coordinate offset, but its values are not significant against its background, so some form of density score algorithm would be needed to determine where exactly the centre of peak offsets lie. Shared area on the other hand, whilst also noisy, is still able to extract the coordinate offset with no need for any further processing, as its value is significant against its background.

Appendix B

A two-dimensional maximal likelihood statistic

The τ^2 method [201–203] is a maximum likelihood statistical fitting method, originally used to compare two-dimensional isochrone models to colour-magnitude diagrams of evolved stellar clusters. Tau-squared is minimised for a better fitting data-set to the given model, and hence allows the user to differentiate simulated data by their goodness of fit on a 2D space. Tau-squared is defined for a normalised probability density plane, $\rho(x, y)$, as,

$$\tau^2 = -2(\ln(L) - C) = -2 \sum_{i=1}^N \ln [\rho(x_i, y_i)] , \quad (\text{B.1})$$

where C is a constant, L is the model likelihood and N is the number of points in the data set. For data points falling outside of the model probability, such that $\rho(x, y) = 0$, a floor value and weight are formulated such that the integrated model probability is still unity. This is defined in Ref. [203] as

$$\rho' = (1 - \mathfrak{F})\rho_f + \mathfrak{F}\rho , \quad (\text{B.2})$$

where \mathfrak{F} is the model weighting and ρ_f is the constant floor probability, defined across the fixed rectangular area on the plane which contains the full extent of the model. This alters Eq. (B.1), replacing ρ with ρ' . Model weighting is set as constant to 0.7, and the floor probability is calculated as $\rho_f = 1/A$, where A is the rectangular area of the x-y plane considered, $A = \int dx \int dy$.

An example of the τ^2 method for an arbitrary sinusoidal curve is presented in Fig. B.1. Here, the model curve (panel (a)) is sinusoidal in x with additive random Gaussian noise in y . The model probability plane is presented in panel (b) where we have used a calculating area with bounds equal to the minimum and

maximum of both the x and y sinusoid data. In this τ^2 example, the theoretical predictions or “simulation output” of sinusoidal curves with various phase offsets, $y = \sin(x + \phi)$, are plotted in panel (c). The colouring on these output curves are representative of negative (blue), positive (red) and zero (black) phase offset from the pure sinusoid. Finally, the τ^2 statistic as a function of phase offset (x_{off} equivalent) is shown in panel (d). Here we see that, through a minimisation of τ^2 , our theoretical sinusoid with zero offset best matches the reference model data, as expected. There is a skew in τ^2 to negative offsets which is likely a result of the spread in the model data.

A failure of this method in this minimal working example is that, if we were to calculate τ^2 for offsets between $-0.25 < x_{off} < 0$, it is likely that a sinusoid with non-zero phase offset will best match the model according to the minimisation of τ^2 . This fault shows that, for high levels of noise in the model data, there is an associated error in the τ^2 value which is not inherently obvious from its calculation. Further consideration, therefore, is required when utilising this method, and it is recommended not to take fits of the τ^2 curve in order to find a best fit to the model, but instead find the parameter which minimises it.

Throughout this thesis we have not used a minimal working example, but instead relied on a new metric called the peak-power ratio (PPR). This extracts locations of power spectral density peaks on the frequency-PSD intensity plane by utilising a gradient minimisation neighbour-comparison algorithm. Ratios between successive peaks are taken, ignoring the 0^{th} peak, transforming the space to one of frequency-PPR. With binned frequency axes giving bin widths of $\pm 0.5\Omega_i$, a normalised probability density is then mapped to the frequency-PPR plane for an observed model spectrum. The reference model spectra used throughout Chapter 5 was the alpha-particle driven ICE spectra of the JET DT plasma 26148 [58], but in theory any spectra from experimental results can be used.

The cumulative contribution of the natural log of the probability for a given simulations output PPR to fall in a bin on this model PPR probability plane equates to a simulations τ^2 statistic, which is minimised for a “most-likely” set of simulation PPRs. Relative to one another, this statistic reveals which simulation best maps to the model spectra, according to the position and shape of their own power spectra in frequency-PPR space. As such, no expected values of τ^2 can be given, rather just the minimisation of τ^2 over a range of parameters, i.e. bulk ion species concentration ratios. For a specific use case of the tau-squared method in this thesis on ICE spectra, which calculates τ^2 on the frequency (ω) and PPR plane, see §5.8.

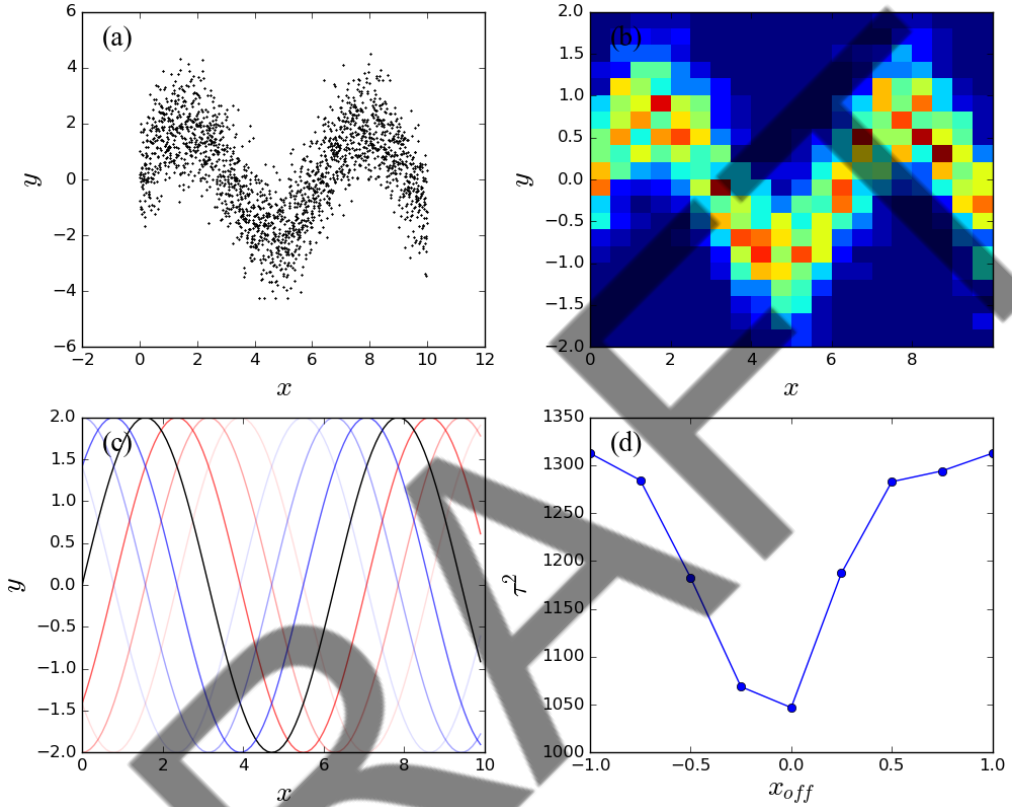


Figure B.1: Tau-squared example of a sinusoid with noise. Panels correspond to (a) the example sinusoid model data with zero phase shift and Gaussian sampled random noise in its amplitude, (b) kernel density estimation (KDE) of model data, (c) examples of potential fitted curves to the original data (sinusoid) for various phase shifts (coloured as blue for negative and red for positive) and where fainter traces represent greater phase shifting magnitudes, and (d) is the τ^2 result of the results (c) on the model KDE (b). See in panel (d) that τ^2 is minimised, and hence best fits the result, for the fitted sinusoid with zero phase shift.

Appendix C

Gradient detection in (k, ω) space using kernels

Principles of gradient detection [212] are well established in fields of image manipulation, image processing, edge detection and pattern recognition. It has found multiple applications in live-feed cameras as well as numismatics [213], and is well rooted in a real-life context. Here we define the process of gradient detection in images as related to ICE signals as seen in spatiotemporal Fourier transformations. These methods have not found previous application to ICE Doppler shifts as a result of simulations featuring low (relative to aneutronic energetic protons, see §1.1) birth energy products. For this reason, we are motivated to study the gradient detection approach and attempt to bring the method into the sphere of plasma physics, adding it to the roster of simulation analyses methods.

Any data D can be discretised into a set of images I that are centred on each pixel coordinate (x, y) and are surrounded by the closest adjacent pixels, see Fig. C.1 for a schematic. The vector gradient of the pixel at position (x, y) is determined by the partial derivatives of the image in both directions

$$\begin{aligned}\nabla I(x, y) &= \left[\frac{\partial I(x, y)}{\partial x}, \frac{\partial I(x, y)}{\partial y} \right] \\ &\equiv [G_x(x, y), G_y(x, y)] .\end{aligned}\tag{C.1}$$

The magnitude of this vector gradient can be written as

$$||\nabla I(x, y)|| = \sqrt{G_x(x, y)^2 + G_y(x, y)^2} ,\tag{C.2}$$

where the angle it makes with-respect-to the y-axis (North) of the (x, y) pixel is

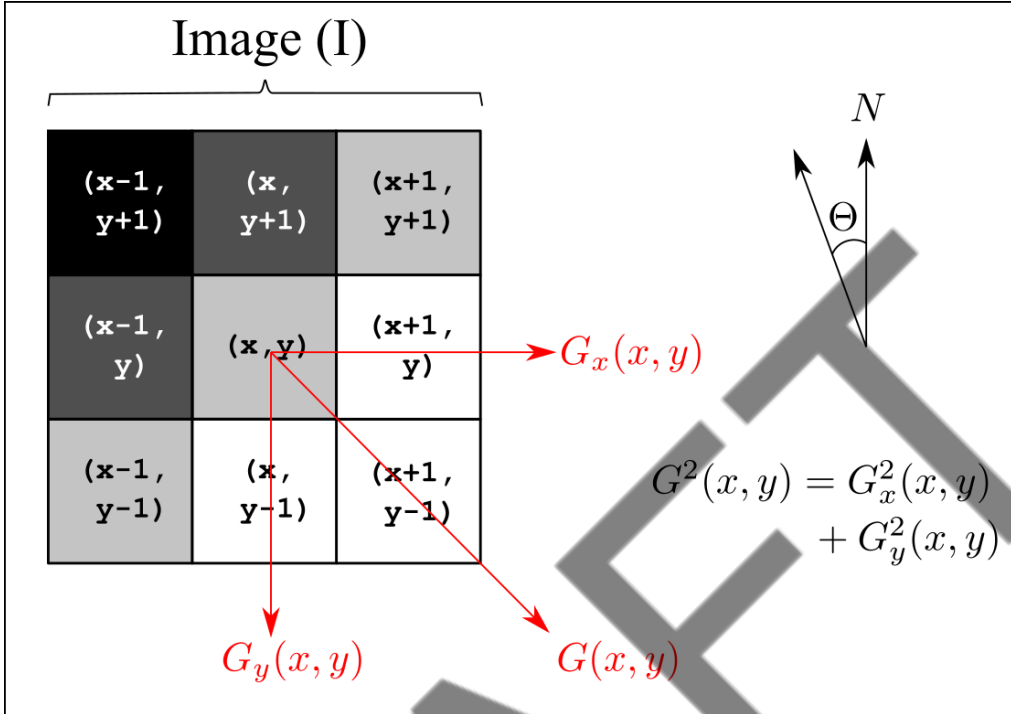


Figure C.1: Diagram of the kernel gradient estimation method, Eq. (C.1), using a 3×3 grid of the image I with positive angles anti-clockwise from North.

$$\Theta(x, y) = \arctan 2\left(\frac{G_y}{G_x}\right), \quad (\text{C.3})$$

the function `arctan2()` measures the angle between $\pm\pi$ as opposed to $\pm\pi/2$, so that the sign of our gradient also indicates the quadrant in which it points. Gradient angles for oscillating images, such as a 45° sinusoid, will be present at both Θ and the phase shifted ($\Theta - \pi$), as it signifies opposite direction, but will have equal magnitude image gradients.

To calculate the gradients for each pixel we take the convolution, denoted by the symbol $*$, of the image $I(x, y)$ with the kernel,

$$\begin{aligned} G_x(x, y) &= S_x * I(x, y), \\ G_y(x, y) &= S_y * I(x, y). \end{aligned} \quad (\text{C.4})$$

This is equivalent to taking the element-wise Hadamard product (\circ) and grand sum of the resulting 3×3 matrix at each $x + i$ and $y + j$ position. Here, the per-cell total gradient is then calculated as the Pythagorean sum between its x and y components,

$$G^2(x, y) = G_x^2(x, y) + G_y^2(x, y). \quad (\text{C.5})$$

Gradient angles are then calculated as Eq. (C.3), which are positive valued as defined by which kernel is being used. Typical choices include the kernels of Sobel Eq. (C.6) and Scharr Eq. (C.7) (see Ref. [214]). The Sobel kernel components are given as

$$S_x = \begin{bmatrix} 1 & 0 & -1 \\ 2 & 0 & -2 \\ 1 & 0 & -1 \end{bmatrix}, \quad S_y = \begin{bmatrix} 1 & 2 & 1 \\ 0 & 0 & 0 \\ -1 & -2 & -1 \end{bmatrix}. \quad (\text{C.6})$$

and the Scharr kernels as

$$S_x = \begin{bmatrix} 3 & 0 & -3 \\ 10 & 0 & -10 \\ 3 & 0 & -3 \end{bmatrix}, \quad S_y = \begin{bmatrix} 3 & 10 & 3 \\ 0 & 0 & 0 \\ -3 & -10 & -3 \end{bmatrix}. \quad (\text{C.7})$$

Generally, we can write the x and y kernels as matrices with components indexed (i, j) ranging from -1 to 1,

$$S_x = \begin{bmatrix} s_{-1,1}^{(x)} & s_{0,1}^{(x)} & s_{1,1}^{(x)} \\ s_{-1,0}^{(x)} & s_{0,0}^{(x)} & s_{1,0}^{(x)} \\ s_{-1,-1}^{(x)} & s_{0,-1}^{(x)} & s_{1,-1}^{(x)} \end{bmatrix}, \quad S_y = \begin{bmatrix} s_{-1,1}^{(y)} & s_{0,1}^{(y)} & s_{1,1}^{(y)} \\ s_{-1,0}^{(y)} & s_{0,0}^{(y)} & s_{1,0}^{(y)} \\ s_{-1,-1}^{(y)} & s_{0,-1}^{(y)} & s_{1,-1}^{(y)} \end{bmatrix}. \quad (\text{C.8})$$

Therefore, generally, each gradient component at the (x, y) cell position can be written as

$$\begin{aligned} G_x(x, y) &= s_{-1,1}^{(x)} I(x-1, y+1) + s_{0,1}^{(x)} I(x, y+1) + s_{1,1}^{(x)} I(x+1, y+1) \\ &\quad + s_{-1,0}^{(x)} I(x-1, y) + s_{0,0}^{(x)} I(x, y) + s_{1,0}^{(x)} I(x+1, y) \\ &\quad + s_{-1,-1}^{(x)} I(x-1, y-1) + s_{0,-1}^{(x)} I(x, y-1) + s_{1,-1}^{(x)} I(x+1, y-1) \\ G_y(x, y) &= s_{-1,1}^{(y)} I(x-1, y+1) + s_{0,1}^{(y)} I(x, y+1) + s_{1,1}^{(y)} I(x+1, y+1) \\ &\quad + s_{-1,0}^{(y)} I(x-1, y) + s_{0,0}^{(y)} I(x, y) + s_{1,0}^{(y)} I(x+1, y) \\ &\quad + s_{-1,-1}^{(y)} I(x-1, y-1) + s_{0,-1}^{(y)} I(x, y-1) + s_{1,-1}^{(y)} I(x+1, y-1). \end{aligned}$$

Dealing with image boundaries is a primary concern in edge detection algorithms. Boundaries are typically handled through a mimicked ghost boundary, which allows for smoother edge gradients. Other approaches include wrapping, mirroring, constant or crop. For the purpose of this work, we pad the image with a single pixel wide border of zeros, looping over the original image size,

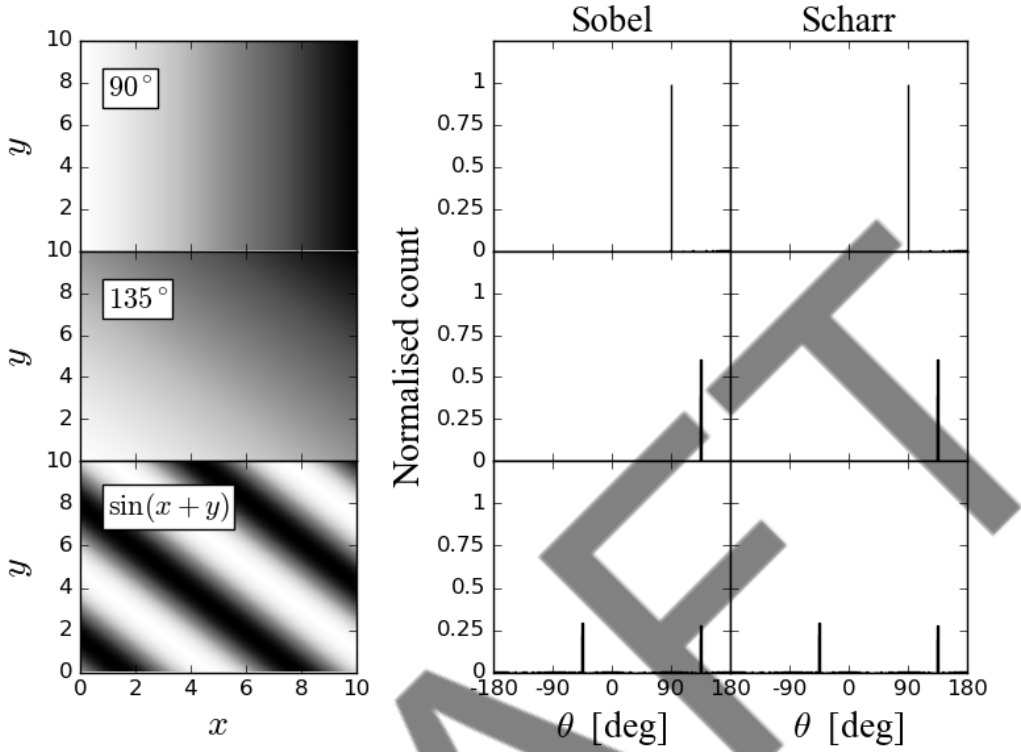


Figure C.2: Left hand side: example gradient maps of varying degrees (positive angles are anti-clockwise from North) along with a sinusoidal map, all as labelled. Right hand side: normalised histograms of each gradient map, for the Sobel and Scharr kernels as defined in Eq. (C.6) and Eq. (C.7).

then dropping the outer gradients. This works well as our region of interest is not at the edges, but in the image centre. If they were not dropped, these edge case excessively large gradients would also have been filtered out in our post-processing data cleaning and analysis.

To extract actionable data from our gradient maps, we utilise a form of the Histogram of Oriented Gradients method [213]. This involves the binning of gradient angles and magnitudes across the $x - y$ plane, bounded by appropriate gradient limits. From these we are able to extract modal gradients within images, and hence, for ICE, can determine it's gradient(s) in frequency space.

Examples of data maps and the use of kernel gradient detection is presented in Fig. C.2. Here, three example data maps are shown; two of equal magnitude but varying gradient, and one of equal magnitude but oscillating gradient in the form of a 45 degree sinusoid. Alongside these maps is the histogram of their gradients across the total $x - y$ domain, when both Sobel and Scharr kernels are used, in terms of their angle in degrees. For both the constant magnitude

and varying gradient, we see sharp peaks in the gradient histograms at 90° and 135° respectively. This is because the kernels used provide angles which are positively valued anti-clockwise from North, and since lighter pixel values are higher valued, the gradients will point to the left and bottom left corner, respectively. The sinusoidal map more closely resembles the Doppler shift power spectra which this method is being used for. In this example we see two peaks equal in magnitude in the gradient histogram at -45° and 135° . This is because as the kernel moves across the domain it points to the upper right corner (-45°) and lower left corner (135°).

Hence, for its use in analysing Doppler shifted power spectra, we should see two peaks at angles 180° apart, both positive and negative. Using these, we should be able to define the gradient, both in terms of its angle, but also by the resolution of the spatiotemporal Fourier transform grid, i.e. $d\omega/dk$, which, conveniently, has units of velocity.

DRAFT

Appendix D

Isoangle data extraction in (\mathbf{k}, ω) and (k_\perp, k_\parallel) space

D.1 Constructing Doppler shifted power spectra in (\mathbf{k}, ω) space

Calculation of the simulated ICE power spectra with respect to frequency involves summation of spatiotemporal FFTs, such as those obtained in Fig. 7.6, across horizontal bands in wavenumber space for a constant frequency. To calculate Doppler-shifted power spectrum, we rotate our effective isofrequency line by some angle Θ_{dop} , defined as positive clockwise from the frequency-axis, before integrating the FFT magnitude across wavenumber space to obtain the power spectrum with respect to the corresponding Doppler shifted frequency ω' . Values of the FFT magnitude used in the calculation of the power spectra are extracted from the line coordinates via a first order spline interpolation. Examples of four such isofrequency lines are shown in Fig. D.1. Line (b) aligns with the Doppler shift corresponding to the relevant value of $u_{\parallel 0}$, as per Eq. (7.8) and Table 7.4 in Chapter 7. The corresponding power spectrum displays clear successive peaks at integer harmonics, as compared to the horizontal (a) and other (c-d) lines.

We can see from Fig. D.1 that the average magnitude of the power spectra density gradually falls as the Doppler angle is increased beyond a right-angle, and for particularly steep angles the power falls rapidly. This is the result of summing fewer FFT data points and is not physical. It is noted however that the average power of isofrequency line corresponding to $u_{\parallel 0}$ will result in higher resolution ICE spectral peaks from the increased mean intensity.

Along with the empirical gradient detection method presented in Appendix C, maximising the definition and power of ICE spectral features over Doppler

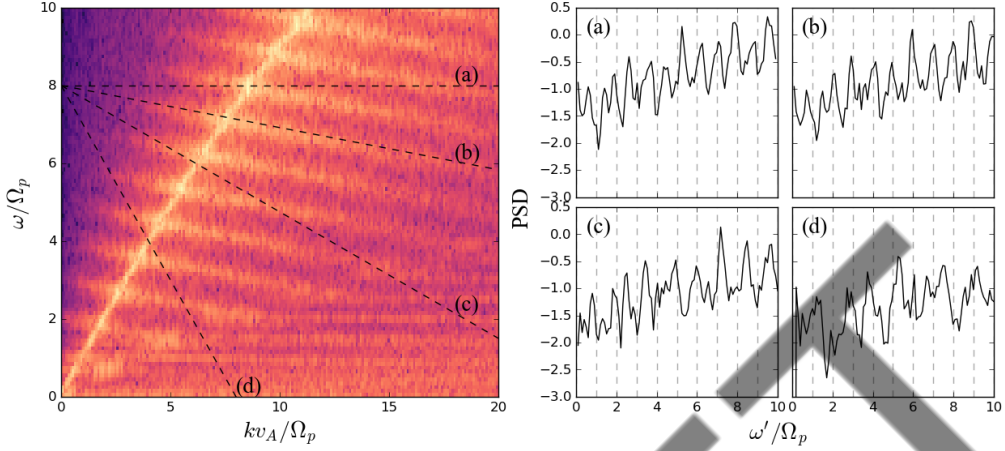


Figure D.1: Examples of power spectral density extraction which accommodate Doppler shifts. (Left) Spatiotemporal FFT magnitude of the five percent ^3He concentration simulation, where axes are normalised by the proton cyclotron frequency, Ω_p and Alfvén speed v_A . (Right) Logarithmic (base 10) power spectral densities (PSD) of the four diagonal lines shown in the left panel, labelled (a–d). These lines correspond to Doppler shifted lines of angle, clockwise from the frequency axis, 90° , 96.18° , 108° and 135° .

shifted isofrequency lines can be used as alternative empirical approach in determining the minority energetic particles pitch-angle. It follows that in experimental scenarios where a counterpart to Fig. D.1 has been obtained by a diagnostic, the value of $u_{\parallel 0}$ could be inferred from the dataset using post-processing of this kind.

D.2 Extracting growth rates for arbitrary magnetic field angles in (k_\perp, k_\parallel) space

Results presented in panels (a) and (b) of Fig. 6.3 utilise a wavenumber search across the (512×512) two dimensional wavenumber plane for wavenumber pairs (k_\perp, k_\parallel) that satisfy the condition $\theta + \Delta\theta = \arctan(k_\perp/k_\parallel)$. This method scales poorly with wavenumber grid size and requires some non-zero angular tolerance $\Delta\theta$, dependent on the resolution of the (k_\perp, k_\parallel) grid, which in this case is $\Delta\theta = 0.22^\circ$. Instead, a straight isoangle line, defined by the magnetic field angled positive clockwise from the vertical k_\parallel axis, is drawn across the two dimensional wavenumber grid and the pixel coordinates of the line are interpreted as the real (k_\perp, k_\parallel) values that they represent. This method is significantly quicker and can allow for $\Delta\theta \rightarrow 0$. We visualise this process in Fig. D.2, where black dashed lines

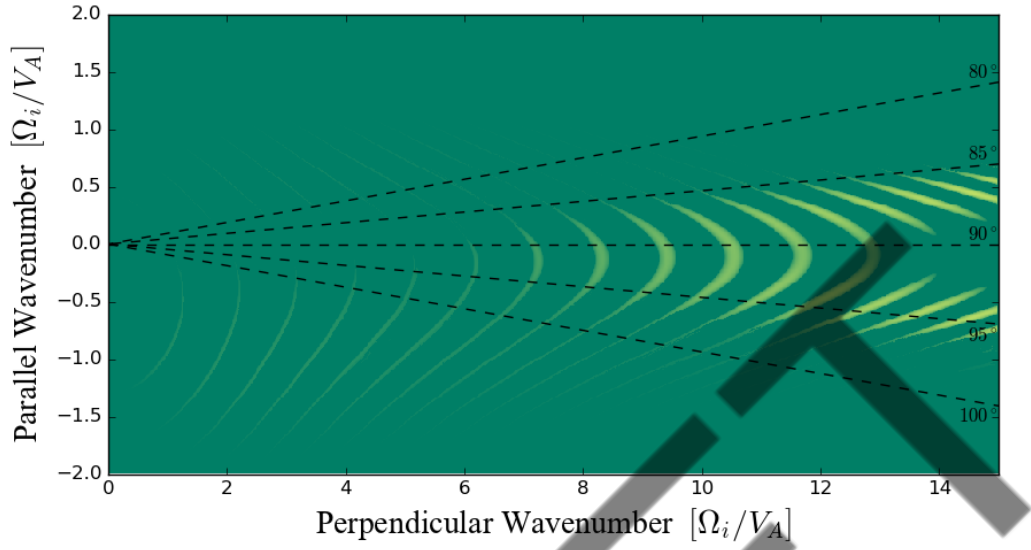


Figure D.2: Growth rate extraction in $(k_{\perp}, k_{\parallel})$ space along lines corresponding to angles positive valued clockwise from the vertical k_{\parallel} line, as labelled.

correspond to the magnetic field angles 80° to 100° in 5° increments, as used in Fig. 6.6. Since the grid is discretised, growth rates, $\gamma(k_{\perp}, k_{\parallel})$, are interpreted from the line to the pixel grid points by a first order spline.

To reproduce one dimensional growth rate spectra for a given magnetic field angle as a function of frequency, both components of the complex frequency $z_{\omega} = \omega_r + i\gamma$ are extracted along the black-dashed line from their position in wavenumber space, thereby giving the growth rate of the instability γ at each frequency ω_r .

Bibliography

- [1] DESNZ 2023 “Historical electricity data” (available at: <https://www.gov.uk/government/statistical-data-sets/historical-electricity-data>)
- [2] Weston T 2023 “The role of nuclear in the UK’s energy supply” Tech. rep. UK House of Lords Library URL <https://lordslibrary.parliament.uk/the-role-of-nuclear-in-the-uks-energy-supply/>
- [3] McCracken G and Stott P 2013 “Chapter 1 - What Is Nuclear Fusion?” *Fusion (Second Edition)* ed McCracken G and Stott P (Boston: Academic Press) pp 1–5 ISBN 978-0-12-384656-3
- [4] Neilson G 2016 *Magnetic Fusion Energy: From Experiments to Power Plants* pages: 613
- [5] Yushmanov E “The power gain factor Q of an ideal magneto-electrostatic fusion reactor” 1980 *Nuclear Fusion* **20** 3
- [6] Kramer D 2022 “National Ignition Facility surpasses long-awaited fusion milestone” (available at: <https://pubs.aip.org/physicstoday/online/41898/National-Ignition-Facility-surpasses-long-awaited>)
- [7] Crepaz L 2024 “Fusion research facility JET’s final tritium experiments yield new energy record” (available at: <https://ccfe.ukaea.uk/fusion-research-facility-jets-final-tritium-experiments-yield-new-energy-record/>)
- [8] Strachan J D, Adler H, Alling P, Ancher C, Anderson H, Anderson J L, Ashcroft D, Barnes C W, Barnes G, Batha S, Bell M G, Bell R, Bitter M, Blanchard W, Bretz N L, Budny R, Bush C E, Camp R, Caorlin M, Cauffman S, Chang Z, Cheng C Z, Collins J, Coward G, Darrow D S, DeLooper J, Duong H, Dudek L, Durst R, Efthimion P C, Ernst D, Fisher

R, Fonck R J, Fredrickson E, Fromm N, Fu G Y, Furth H P, Gentile C, Gorelenkov N, Grek B, Grisham L R, Hammett G, Hanson G R, Hawryluk R J, Heidbrink W, Herrmann H W, Hill K W, Hosea J, Hsuan H, Janos A, Jassby D L, Jobes F C, Johnson D W, Johnson L C, Kamperschroer J, Kugel H, Lam N T, LaMarche P H, Loughlin M J, LeBlanc B, Leonard M, Levinton F M, Machuzak J, Mansfield D K, Martin A, Mazzucato E, Majeski R, Marmor E, McChesney J, McCormack B, McCune D C, McGuire K M, McKee G, Meade D M, Medley S S, Mikkelsen D R, Mueller D, Murakami M, Nagy A, Nazikian R, Newman R, Nishitani T, Norris M, O'Connor T, Oldaker M, Osakabe M, Owens D K, Park H, Park W, Paul S F, Pearson G, Perry E, Petrov M, Phillips C K, Pitcher S, Ramsey A T, Rasmussen D A, Redi M H, Roberts D, Rogers J, Rossmassler R, Roquemore A L, Ruskov E, Sabbagh S A, Sasao M, Schilling G, Schivell J, Schmidt G L, Scott S D, Sissingh R, Skinner C H, Snipes J A, Stevens J, Stevenson T, Stratton B C, Synakowski E, Tang W, Taylor G, Terry J L, Thompson M E, Tuszewski M, Vannoy C, Von Halle A, Von Goeler S, Voorhees D, Walters R T, Wieland R, Wilgen J B, Williams M, Wilson J R, Wong K L, Wurden G A, Yamada M, Young K M, Zarnstorff M C and Zweber S J “Fusion power production from TFTR plasmas fueled with deuterium and tritium” 1994 *Physical Review Letters* **72** 3526–3529

- [9] Friedman I “Deuterium content of natural waters and other substances” 1953 *Geochimica et Cosmochimica Acta* **4** 89–103
- [10] Phillips J E and Easterly C E 1980 “Sources of tritium” Tech. Rep. ORNL/TM-6402 Oak Ridge National Lab., TN (USA) URL <https://www.osti.gov/biblio/6867774>
- [11] DESNZ U 2023 “Managing Radioactive Substances and Nuclear Decommissioning; UK policy framework” Tech. rep. UK Department for Energy Security and Net Zero
- [12] Talens Peiró L, Villalba Méndez G and Ayres R U “Lithium: Sources, Production, Uses, and Recovery Outlook” 2013 *JOM* **65** 986–996
- [13] Kavanagh L, Keohane J, Garcia Cabellos G, Lloyd A and Cleary J “Global Lithium Sources—Industrial Use and Future in the Electric Vehicle Industry: A Review” 2018 *Resources* **7** 57
- [14] Feldbacher R and Heindler M “Basic cross section data for aneutronic reactor” 1988 *Nuclear Instruments and Methods in Physics Research Section*

- [15] Stott P E “The feasibility of using D-3He and D-D fusion fuels” 2005 *Plasma Physics and Controlled Fusion* **47** 1305–1338
- [16] Baccou C, Depierreux S, Yahia V, Neuville C, Goyon C, De angelis R, Consoli F, Ducret J, Boutoux G, Rafelski J and Labaune C “New scheme to produce aneutronic fusion reactions by laser-accelerated ions” 2015 *Laser and Particle Beams* **33** 117
- [17] Ryzhkov S V “Helium-3 as a Perspective Fuel for Power Generation through Aneutronic Thermonuclear Fusion” 2020 *Physics of Atomic Nuclei* **83** 1434–1439
- [18] Mazzucato E “A D-3He fusion reactor for the mitigation of global warming” 2023 *Fundamental Plasma Physics* **6** 100022
- [19] Liu M s, Xie H s, Wang Y m, Dong J q, Feng K m, Gu X, Huang X l, Jiang X c, Li Y y, Li Z, Liu B, Liu W j, Luo D, Peng Y K M, Shi Y j, Song S d, Song X m, Sun T t, Tan M z, Wang X y, Yang Y m, Yin G and Zhao H y “ENN’s roadmap for proton-boron fusion based on spherical torus” 2024 *Physics of Plasmas* **31** 062507
- [20] Sharapov S, Hellsten T, Kiptily V, Craciunescu T, Eriksson J, Fitzgerald M, Girardo J B, Goloborod’ko V, Hellesen C, Hjalmarsson A, Johnson T, Kazakov Y, Koskela T, Mantsinen M, Monakhov I, Nabais F, Nocente M, Perez von Thun C, Rimini F, Santala M, Schneider M, Tardocchi M, Tsalas M, Yavorskij V, Zoita V and JET Contributors “Fusion product studies via fast ion D-D and D-³ He fusion on JET” 2016 *Nuclear Fusion* **56** 112021
- [21] Kiptily V G, Kazakov Y O, Nocente M, Ongena J, Belli F, Dreval M, Craciunescu T, Eriksson J, Fitzgerald M, Giacomelli L, Goloborodko V, Iliasova M V, Khilkevitch E M, Rigamonti D, Sahlberg A, Salewski M, Shevelev A E, Garcia J, Oliver H J C, Sharapov S E, Stancar Z and Weisen H “Excitation of Alfvén eigenmodes by fusion-born alpha-particles in D-³He plasmas on JET” 2022 *Plasma Physics and Controlled Fusion* **64** 064001
- [22] Kirtley D 2024 “APS -66th Annual Meeting of the APS Division of Plasma Physics - Event - Fundamental theory of the direct magnetic energy recov-

- ery in a thermonuclear field reversed configuration system” *Bulletin of the American Physical Society* (American Physical Society)
- [23] Magee R M, Ogawa K, Tajima T, Allfrey I, Gota H, McCarroll P, Ohdachi S, Isobe M, Kamio S, Klumper V, Nuga H, Shoji M, Ziae S, Binderbauer M W and Osakabe M “First measurements of p11B fusion in a magnetically confined plasma” 2023 *Nature Communications* **14** 955
- [24] Trkov A and Brown D A 2018 “ENDF-6 formats manual: data formats and procedures for the evaluated nuclear data files” Tech. rep. Brookhaven National Lab.(BNL), Upton, NY (United States)
- [25] Xianzu G, Liqing X, Jinping Q and Juan H “Realization of Te0 > 10 keV long pulse operation over 100 s on EAST” 2023 *Plasma Science and Technology* **25** 022001
- [26] Hora H, Korn G, Giuffrida L, Margarone D, Picciotto A, Krasha J, Jungwirth K, Ullschmied J, Lalousis P, Eliezer S and others “Fusion energy using avalanche increased boron reactions for block-ignition by ultrahigh power picosecond laser pulses” 2015 *Laser and particle Beams* **33** 607–619
- [27] Wesson J and Campbell D J 2011 *Tokamaks* vol 149 (Oxford university press)
- [28] Conrads H and Schmidt M “Plasma generation and plasma sources” 2000 *Plasma Sources Science and Technology* **9** 441
- [29] Erckmann V and Gasparino U “Electron cyclotron resonance heating and current drive in toroidal fusion plasmas” 1994 *Plasma Physics and Controlled Fusion* **36** 1869
- [30] Menzel K, Arp O and Piel A “Chain of coupled van der Pol oscillators as model system for density waves in dusty plasmas” 2011 *Physical Review E—Statistical, Nonlinear, and Soft Matter Physics* **84** 016405
- [31] Chen F F 1984 *Introduction to plasma physics* (New York: Plenum press,)
- [32] Stix T H 1992 *Waves in Plasmas* (Springer Science & Business Media) ISBN 978-0-88318-859-0
- [33] Buchsbaum S J “Resonance in a Plasma with Two Ion Species” 1960 *Physics of Fluids* **3** 418
- [34] Dendy R 1990 *Plasma Dynamics* Oxford science publications (Clarendon Press) ISBN 978-0-19-852041-2

- [35] Dendy R O 1995 *Plasma Physics: An Introductory Course* (Cambridge University Press) ISBN 978-0-521-48452-7
- [36] Krall N A and Trivelpiece A W 1973 *Principles of plasma physics*
- [37] Cook J W S “Doublet splitting of fusion alpha particle driven ion cyclotron emission” 2022 *Plasma Physics and Controlled Fusion* **64** 115002
- [38] Dendy R O, Lashmore-Davies C N and Kam K F “A possible excitation mechanism for observed superthermal ion cyclotron emission from tokamak plasmas” 1992 *Physics of Fluids B: Plasma Physics* **4** 3996–4006
- [39] Dendy R O, Lashmore-Davies C N, McClements K G and Cottrell G A “The excitation of obliquely propagating fast Alfvén waves at fusion ion cyclotron harmonics” 1994 *Physics of Plasmas* **1** 1918–1928
- [40] Cook J W S 2022 “LinearMaxwellVlasov.jl” (<https://doi.org/10.5281/zenodo.6529288>)
- [41] Birdsall C K and Langdon A B 1991 *Plasma Physics via Computer Simulation* (CRC Press) ISBN 0-7503-0117-1
- [42] Dendy R O and McClements K G “Ion cyclotron emission from fusion-born ions in large tokamak plasmas: a brief review from JET and TFTR to ITER” 2015 *Plasma Physics and Controlled Fusion* **57** 044002
- [43] Bernstein I B “Waves in a plasma in a magnetic field” 1958 *Physical Review* **109** 10
- [44] Bellan P M 2006 *Fundamentals of Plasma Physics* (Cambridge university press)
- [45] Meyer-Vernet N, Moncuquet M and Hoang S “Temperature inversion in the Io plasma torus” 1995 *Icarus* **116** 202–213
- [46] Ono M “Ion Bernstein wave heating research” 1993 *Physics of Fluids B: Plasma Physics* **5** 241–280
- [47] Noreen N, Riaz F, Malik S and Zaheer S “Ion Bernstein mode instability with ring velocity distribution function” 2019 *Progress of Theoretical and Experimental Physics* **2019** 053E01
- [48] TFR E “High-power neutral injection and ion power balance in TFR” 1978 *Nuclear Fusion* **18** 1271

- [49] Bhadra D K, Chiu S C, Buchenauer D and Hwang D “Electromagnetic emission from a neutral-beam-injected plasma” 1986 *Nuclear Fusion* **26** 201
- [50] Duong H H, Heidbrink W W, Strait E J, Petrie T W, Lee R, Moyer R A and Watkins J G “Loss of energetic beam ions during TAE instabilities” 1993 *Nuclear Fusion* **33** 749
- [51] Heidbrink W W, Austin M E, Fisher R K, García-Muñoz M, Matsunaga G, McKee G R, Moyer R A, Muscatello C M, Okabayashi M, Pace D C, Shinohara K, Solomon W M, Strait E J, Zeeland M A V and Zhu Y B “Characterization of off-axis fishbones” 2011 *Plasma Physics and Controlled Fusion* **53** 085028
- [52] Thome K E, Pace D C, Pinsker R I, Meneghini O, del Castillo C A and Zhu Y “Radio frequency measurements of energetic-particle-driven emission using the ion cyclotron emission diagnostic on the DIII-D tokamak” 2018 *Review of Scientific Instruments* **89** 10I102
- [53] Thome K E, Pace D C, Pinsker R I, Van Zeeland M A, Heidbrink W W and Austin M E “Central ion cyclotron emission in the DIII-D tokamak” 2019 *Nuclear Fusion* **59** 086011
- [54] DeGrandchamp G H, Thome K E, Heidbrink W W, Holmes I and Pinsker R I “Upgrades to the ion cyclotron emission diagnostic on the DIII-D tokamak” 2021 *Review of Scientific Instruments* **92** 033543
- [55] DeGrandchamp G H, Lestz J B, Zeeland M A V, Du X D, Heidbrink W W, Thome K E, Crocker N A and Pinsker R I “Mode structure measurements of ion cyclotron emission and sub-cyclotron modes on DIII-D” 2022 *Nuclear Fusion* **62** 106033
- [56] Cauffman S and Majeski R “Ion cyclotron emission on the Tokamak Fusion Test Reactor” 1995 *Review of Scientific Instruments* **66** 817–819
- [57] Cottrell G A and Dendy R O “Superthermal radiation from fusion products in JET” 1988 *Physical Review Letters* **60** 33–36
- [58] Cottrell G A, Bhatnagar V P, Costa O D, Dendy R O, Jacquinot J, McClements K G, McCune D C, Nave M F F, Smeulders P and Start D F H “Ion cyclotron emission measurements during JET deuterium-tritium experiments” 1993 *Nuclear Fusion* **33** 1365–1387

- [59] McClements K G, Hunt C, Dendy R O and Cottrell G A “Ion Cyclotron Emission from JET D-T Plasmas” 1999 *Physical Review Letters* **82** 2099–2102
- [60] Cottrell G A “Identification of Minority Ion-Cyclotron Emission during Radio Frequency Heating in the JET Tokamak” 2000 *Physical Review Letters* **84** 2397–2400
- [61] Jacquet P, Berger-By G, Bobkov V, Blackman T, Day I E, Durodié F, Graham M, Hellsten T, Laxåback M, Mayoral M L, Monakhov I, Nightingale M, Sharapov S E, Vrancken M, JET- EFDA contributors, Phillips C K and Wilson J R 2011 “Parasitic signals in the receiving band of the Sub-Harmonic Arc Detection system on JET ICRF Antennas” (Newport, (USA)) pp 17–20
- [62] McClements K, Brisset A, Chapman B, Chapman S, Dendy R, Jacquet P, Kiptily V, Mantsinen M, Reman B and JET Contributors “Observations and modelling of ion cyclotron emission observed in JET plasmas using a sub-harmonic arc detection system during ion cyclotron resonance heating” 2018 *Nuclear Fusion* **58** 096020
- [63] Shalashov A G, Suvorov E V, Lubyako L V, Maassberg H and Team t W A “NBI-driven ion cyclotron instabilities at the W7-AS stellarator” 2003 *Plasma Physics and Controlled Fusion* **45** 395
- [64] Askinazi L G, Abdullina G I, Belokurov A A, Blekhshstein M D, Zhur N A, Kornev V A, Krikunov S V, Lebedev S V, Razumenko D V, Smirnov A I and Tukachinsky A S “The Spectrum of Ion Cyclotron Emission from Neutral Beam Injection Heated Plasma on the TUMAN-3M Tokamak” 2018 *Technical Physics Letters* **44** 1020–1023
- [65] Askinazi L G, Belokurov A A, Gin D B, Kornev V A, Lebedev S V, Shevelev A E, Tukachinsky A S and Zhur N A “Ion cyclotron emission in NBI-heated plasmas in the TUMAN-3M tokamak” 2018 *Nuclear Fusion* **58** 082003
- [66] D’Inca R, Garcia-Munoz M, Tardini G and Noterdaeme J M 2011 “Characteristics of Ion Cyclotron Emission on ASDEX Upgrade”
- [67] Ochoukov R, Bilato R, Bobkov V, Chapman B, Chapman S C, Dendy R O, Dunne M, Faugel H, García-Muñoz M, Geiger B, Kallenbach A, Kappatou A, McClements K G, Moseev D, Nielsen S, Rasmussen J, Schneider P,

- Weiland M, Noterdaeme J M, Team A U and Team E M “Core plasma ion cyclotron emission driven by fusion-born ions” 2018 *Nuclear Fusion* **59** 014001
- [68] Ochoukov R, McClements K G, Bilato R, Bobkov V, Chapman B, Chapman S C, Dendy R O, Dreval M, Faugel H, Noterdaeme J M, Salewski M, Weiland M, Team A U and Team E M “Interpretation of core ion cyclotron emission driven by sub-Alfvénic beam-injected ions via magnetoacoustic cyclotron instability” 2019 *Nuclear Fusion* **59** 086032
- [69] Ochoukov R, Bilato R, Bobkov V, Chapman S C, Dendy R, Dreval M, Faugel H, Kappatou A, Kazakov Y O, Mantsinen M, McClements K G, Moseev D, Nielsen S K, Noterdaeme J M, Salewski M, Schneider P, Weiland M, team A U and team M “High frequency Alfvén eigenmodes detected with ion-cyclotron-emission diagnostics during NBI and ICRF heated plasmas on the ASDEX Upgrade tokamak” 2020 *Nuclear Fusion* **60** 126043
- [70] Kimura H, Kusama Y, Saigusa M, Kramer G J, Tobita K, Nemoto M, Kondoh T, Nishitani T, Costa O D, Ozeki T, Oikawa T, Moriyama S, Morioka A, Fu G Y, Cheng C Z and Afanas’ev V I “Alfvén eigenmode and energetic particle research in JT-60U” 1998 *Nuclear Fusion* **38** 1303
- [71] Ichimura M, Katano M, Yamaguchi Y, Sato S, Motegi Y, Muro H, Ouchi T, Moriyama S, Ishikawa M, Shinohara K, Sakamoto Y, Kojima A and Watanabe T 2008 *Study of Ion Cyclotron Emissions due to DD Fusion Product Ions on JT-60U*
- [72] Ichimura M, Higaki H, Kakimoto S, Yamaguchi Y, Nemoto K, Katano M, Ishikawa M, Moriyama S and Suzuki T “Observation of spontaneously excited waves in the ion cyclotron frequency range on JT-60U” 2008 *Nuclear Fusion* **48** 035012
- [73] Sato S, Ichimura M, Yamaguchi Y, Katano M, Imai Y, Murakami T, Miyake Y, Yokoyama T, Moriyama S, Kobayashi T, Kojima A, Shinohara K, Sakamoto Y, Watanabe T, Hojo H and Imai T “Observation of Ion Cyclotron Emission Owing to DD Fusion Product H Ions in JT-60U” 2010 *Plasma and Fusion Research* **5** S2067–S2067
- [74] Sumida S, Shinohara K, Ikezoe R, Ichimura M, Sakamoto M, Hirata M and Ide S “Characteristics of fast ^3He ion velocity distribution exciting ion cyclotron emission on JT-60U” 2019 *Plasma Physics and Controlled Fusion* **61** 025014

- [75] Saito K, Kasahara H, Seki T, Kumazawa R, Mutoh T, Watanabe T, Shimpo F, Nomura G, Osakabe M, Ichimura M, Higaki H and Komori A “Measurement of ion cyclotron emissions by use of ICRF heating antennas in LHD” 2009 *Fusion Engineering and Design* **84** 1676–1679
- [76] Saito K, Kumazawa R, Seki T, Kasahara H, Nomura G, Shimpo F, Igami H and Isobe M “Measurement of Ion Cyclotron Emissions by Using High-Frequency Magnetic Probes in the LHD” 2013 *Plasma Science and Technology* **15** 209
- [77] Saito K, Igami H, Toida M, Akiyama T, Kamio S, Seki R and LHD Experiment Group “RF Wave Detection with High-Frequency Magnetic Probes in LHD” 2018 *Plasma and Fusion Research* **13** 3402043–3402043
- [78] Toida M, Saito K, Igami H, Akiyama T, Kamio S and Seki R “Simulation Study of High-Frequency Magnetosonic Waves Excited by Energetic Ions in Association with Ion Cyclotron Emission” 2018 *Plasma and Fusion Research* **13** 3403015–3403015
- [79] Reman B C G, Dendy R O, Igami H, Akiyama T, Salewski M, Chapman S C, Cook J W S, Inagaki S, Saito K, Seki R, Toida M, Kim M H, Thatipamula S G and Yun G S “First observation and interpretation of spontaneous collective radiation from fusion-born ions in a stellarator plasma” 2022 *Plasma Physics and Controlled Fusion* **64** 085008
- [80] Gorelenkov N N and Cheng C Z “Excitation of Alfvén cyclotron instability by charged fusion products in tokamaks” 1995 *Physics of Plasmas* **2** 1961–1971
- [81] Sharapov S E, Lilley M K, Akers R, Ayed N B, Cecconello M, Cook J W S, Cunningham G, Verwichte E and MAST Team “Bi-directional Alfvén cyclotron instabilities in the mega-amp spherical tokamak” 2014 *Physics of Plasmas* **21** 082501
- [82] Fredrickson E D, Gorelenkov N N, Bell R E, Diallo A, LeBlanc B P and Podesta M “Emission in the ion cyclotron range of frequencies (ICE) on NSTX and NSTX-U” 2019 *Physics of Plasmas* **26** 032111
- [83] Fredrickson E D, Gorelenkov N N, Bell R E, Diallo A, LeBlanc B P, Lestz J, Podesta M and team t N “Chirping ion cyclotron emission (ICE) on NSTX-U” 2021 *Nuclear Fusion* **61** 086007

- [84] Tong R H, Fang K R, Yu X, Liu L Z, Shi Z B, Yang Z C, Zhong W L, Zhou Y, Jiang M, Shi P W, Wen J, Deng W C, Xu M and team t H A “Development of the ion cyclotron emission diagnostic on the HL-2A tokamak” 2022 *Journal of Instrumentation* **17** C01063
- [85] Liu L N, Zhang X J, Zhu Y B, Qin C M, Zhao Y P, Yuan S, Mao Y Z, Li M H, Chen Y, Cheng J, Ping L L, Li H and Ai L “Ion cyclotron emission diagnostic system on the experimental advanced superconducting tokamak and first detection of energetic-particle-driven radiation” 2019 *Review of Scientific Instruments* **90** 063504
- [86] Liu L, Zhang X, Zhu Y, Qin C, Zhao Y, Yuan S, Mao Y, Li M, Chen J, Li H and Ai L “Detection of edge ion cyclotron emission driven by energetic deuterium ions in the EAST” 2020 *AIP Conference Proceedings* **2254** 040001
- [87] Liu L, Zhang X, Zhu Y, Qin C, Zhao Y, Yuan S, Mao Y, Li M, Zhang K, Cheng J, Ai L and Cheng Y “Ion cyclotron emission driven by deuterium neutral beam injection and core fusion reaction ions in EAST” 2020 *Nuclear Fusion* **60** 044002
- [88] Kim M H, Thatipamula S G, Lee J E, Choi M J, Park H K, Akiyama T and Yun G S “Distinct stages of radio frequency emission at the onset of pedestal collapse in KSTAR H-mode plasmas” 2018 *Nuclear Fusion* **58** 096034
- [89] Thatipamula S G, Yun G S, Leem J, Park H K, Kim K W, Akiyama T and Lee S G “Dynamic spectra of radio frequency bursts associated with edge-localized modes” 2016 *Plasma Physics and Controlled Fusion* **58** 065003
- [90] Moseev D, Ochoukov R, Bobkov V, Dendy R O, Faugel H, Hartmann D, Kallmeyer J P, Lansky J, Laqua H P, Marsen S, McClements K G, Nielsen S K, Reintrog A, Salewski M, Schmidt B S, Schulz T, Stange T and W7-X Team “Development of the ion cyclotron emission diagnostic for the W7-X stellarator” 2021 *Review of Scientific Instruments* **92** 033546
- [91] Sabot R, Clairet F, Giacalone J C, Hennequin P, Heuraux S, Honoré C, Leclert G, Molina D, Sirinelli A, Vermare L and Truc A “Reflectometry: A Reliable And Sensitive Plasma Diagnostic For Density Profile And Turbulence Measurements On Tore-Supra” 2006 *AIP Conference Proceedings* **812** 112–119

- [92] ITER Physics Expert Group on Diagnostics and ITER Physics Basis Editors “Chapter 7: Measurement of plasma parameters” 1999 *Nuclear Fusion* **39** 2541–2575
- [93] Belikov V S and Kolesnichenko Y I “Magnetoacoustic cyclotron instability in a thermonuclear plasma” 1975 *Sov. Phys. - Tech. Phys. (Engl. Transl.)*; (*United States*) **20:9** 1146
- [94] Dendy R O, Lashmore-Davies C N and Kam K F “The magnetoacoustic cyclotron instability of an extended shell distribution of energetic ions” 1993 *Physics of Fluids B: Plasma Physics* **5** 1937–1944
- [95] Belikov V S and Kolesnichenko Y I “Edge-Localized Thermonuclear Magnetoacoustic-Cyclotron Instability in Tokamaks” 1994 *Fusion Technology* **25** 258–265
- [96] Dendy R O, McClements K G, Lashmore-Davies C N, Majeski R and Cauffman S “A mechanism for beam-driven excitation of ion cyclotron harmonic waves in the Tokamak Fusion Test Reactor” 1994 *Physics of Plasmas* **1** 3407–3413
- [97] McClements K G, Dendy R O, Lashmore-Davies C N, Cottrell G A, Cauffman S and Majeski R “Interpretation of ion cyclotron emission from sub-Alfvénic fusion products in the Tokamak Fusion Test Reactor” 1996 *Physics of Plasmas* **3** 543–553
- [98] Fülöp T, Kolesnichenko Y I, Lisak M and Anderson D “Origin of superthermal ion cyclotron emission in tokamaks” 1997 *Nuclear Fusion* **37** 1281
- [99] Fülöp T and Lisak M “Ion cyclotron emission from fusion products and beam ions in the Tokamak Fusion Test Reactor” 1998 *Nuclear Fusion* **38** 761
- [100] Cook J W S, Dendy R O and Chapman S C “Particle-in-cell simulations of the magnetoacoustic cyclotron instability of fusion-born alpha-particles in tokamak plasmas” 2013 *Plasma Physics and Controlled Fusion* **55** 065003
- [101] Carbajal L, Dendy R O, Chapman S C and Cook J “Linear and nonlinear physics of the magnetoacoustic cyclotron instability of fusion-born ions in relation to ion cyclotron emission” 2014 *Physics of Plasmas* **21** 012106
- [102] Gorelenkov N N “Ion cyclotron emission studies: Retrospects and prospects” 2016 *Plasma Physics Reports* **42** 430–439

- [103] Liu L, Ochoukov R, McClements K, Dendy R, Bobkov V, Weiland M, Bilato R, Faugel H, Moseev D, Salewski M, Zhang W, Zhang X, Zhu Y, Chapman B and Zalzali A “Explanation of core ion cyclotron emission from beam-ion heated plasmas in ASDEX Upgrade by the magnetoacoustic cyclotron instability” 2021 *Nuclear Fusion* **61** 026004
- [104] Reman B C G, Dendy R O, Akiyama T, Chapman S C, Cook J W S, Igami H, Inagaki S, Saito K and Yun G S “Interpreting observations of ion cyclotron emission from large helical device plasmas with beam-injected ion populations” 2019 *Nuclear Fusion* **59** 096013
- [105] Carbajal L, Dendy R, Chapman S and Cook J “Quantifying Fusion Born Ion Populations in Magnetically Confined Plasmas using Ion Cyclotron Emission” 2017 *Physical Review Letters* **118** 105001
- [106] Chapman B, Dendy R O, Chapman S C, Holland L A, Irvine S W A and Reman B C G “Comparing theory and simulation of ion cyclotron emission from energetic ion populations with spherical shell and ring-beam distributions in velocity-space” 2020 *Plasma Physics and Controlled Fusion* **62** 055003
- [107] Liu L, Zhang X, Ochoukov R, Zhang W, McClements K G, Dendy R O, Salewski M, Zhu Y, Qin C, Moseev D, Bobkov V, Chapman-Olopoio B and Zalzali A “Interpretation of ion cyclotron emission from sub-Alfvénic beam-injected ions heated plasmas soon after L-H mode transition in EAST” 2023 *Plasma Physics and Controlled Fusion* **66** 015007
- [108] Lee J K and Birdsall C “Velocity space ring-plasma instability, magnetized, Part I: Theory” 1979 *The Physics of Fluids* **22** 1306–1314
- [109] Lee J K and Birdsall C “Velocity space ring-plasma instability, magnetized, Part II: Simulation” 1979 *The Physics of Fluids* **22** 1315–1322
- [110] Slade-Harajda T W, Chapman S C and Dendy R O “The consequences of tritium mix for simulated ion cyclotron emission spectra from deuterium-tritium plasmas” 2024 *Nuclear Fusion* **64** 126051
- [111] Chapman B, O Dendy R, C Chapman S, G McClements K and Ochoukov R “Origin of ion cyclotron emission at the proton cyclotron frequency from the core of deuterium plasmas in the ASDEX-Upgrade tokamak” 2020 *Plasma Physics and Controlled Fusion* **62** 095022

- [112] Chapman B, Dendy R O, McClements K G, Chapman S C, Yun G S, Thatipamula S G and Kim M H “Sub-microsecond temporal evolution of edge density during edge localized modes in KSTAR tokamak plasmas inferred from ion cyclotron emission” 2017 *Nuclear Fusion* **57** 124004
- [113] Chapman B, Dendy R O, Chapman S C, McClements K G, Yun G S, Thatipamula S G and Kim M H “Nonlinear wave interactions generate high-harmonic cyclotron emission from fusion-born protons during a KSTAR ELM crash” 2018 *Nuclear Fusion* **58** 096027
- [114] Chapman B, Dendy R O, Chapman S C, McClements K G, Yun G S, Thatipamula S G and Kim M H “Interpretation of suprathermal emission at deuteron cyclotron harmonics from deuterium plasmas heated by neutral beam injection in the KSTAR tokamak” 2019 *Nuclear Fusion* **59** 106021
- [115] Reman B C G 2018 *Interpreting observations of Ion Cyclotron Emission from energetic ion populations in large helical device plasmas* Ph.D. thesis (available at: <http://wrap.warwick.ac.uk/133789/>)
- [116] Reman B, Dendy R, Akiyama T, Chapman S, Cook J, Igami H, Inagaki S, Saito K, Seki R, Kim M, Thatipamula S and Yun G “Density dependence of ion cyclotron emission from deuterium plasmas in the large helical device” 2021 *Nuclear Fusion* **61** 066023
- [117] McClements K G and Dendy R O “Ion cyclotron harmonic wave generation by ring protons in space plasmas” 1993 *Journal of Geophysical Research* **98** 11689
- [118] Chapman B 2019 *Ion cyclotron emission from energetic ion populations in fusion plasmas* Ph.D. thesis (available at: <http://wrap.warwick.ac.uk/134556/>)
- [119] Dendy R O and McClements K G “Ion cyclotron wave emission at the quasi-perpendicular bow shock” 1993 *Journal of Geophysical Research* **98** 15531
- [120] Cauffman S, Majeski R, McClements K and Dendy R “Alfvenic behaviour of alpha particle driven ion cyclotron emission in TFTR” 1995 *Nuclear Fusion* **35** 1597–1602
- [121] Dendy R O, McClements K G, Lashmore-Davies C N, Cottrell G A, Majeski R and Cauffman S “Ion cyclotron emission due to collective instability

- of fusion products and beam ions in TFTR and JET” 1995 *Nuclear Fusion* **35** 1733–1742
- [122] Kong H, Xie H and Sun J “A linear parameters study of ion cyclotron emission using drift ring beam distribution” 2023 *Nuclear Fusion* **63** 126034
- [123] Cook J, Dendy R and Chapman S “Stimulated Emission of Fast Alfvén Waves within Magnetically Confined Fusion Plasmas” 2017 *Physical Review Letters* **118** 185001
- [124] Moseev D and Salewski M “Bi-Maxwellian, slowing-down, and ring velocity distributions of fast ions in magnetized plasmas” 2019 *Physics of Plasmas* **26** 020901
- [125] Schild P, Cottrell G and Dendy R “Sawtooth oscillations in ion cyclotron emission from JET” 1989 *Nuclear Fusion* **29** 834–839
- [126] Kikuchi M, Nagashima K, Aoyagi T, Kurita G, Ushigusa K, Neyatani Y, Kubo T, Tobita K, Masaki K, Kaminaga A, Hosogane N, Nagashima A, Miya N, Toyoshima N, Oguri S, Kitai T, Mori K, Nakagawa S, Kuriyama M, Yamamoto T, Takahashi Y, Hayashi T, Nagami M, Yoshida T, Otsuka M, Nakashima K, Nakagawa S and Suzuki T 1995 “Conceptual design of JT-60SU” *Proceedings of 16th International Symposium on Fusion Engineering* vol 1 pp 650–653 vol.1
- [127] Matsumoto Y, Nagaura T, Oikawa S i and Watanabe T “Particle Orbit Analysis under the Ion Cyclotron Range of Frequency Heating in the Large Helical Device” 2004 *Japanese Journal of Applied Physics* **43** 332
- [128] Seki R, Matsumoto Y, Suzuki Y, Watanabe K and Itagaki M “Particle Orbit Analysis in the Finite Beta Plasma of the Large Helical Device using Real Coordinates” 2008 *Plasma and Fusion Research* **3** 016–016
- [129] Ochoukov R, Bobkov V, Chapman B, Dendy R, Dunne M, Faugel H, García-Muñoz M, Geiger B, Hennequin P, McClements K G, Moseev D, Nielsen S, Rasmussen J, Schneider P, Weiland M and Noterdaeme J M “Observations of core ion cyclotron emission on ASDEX Upgrade tokamak” 2018 *Review of Scientific Instruments* **89** 10J101
- [130] Thatipamula S G, Kim M H, Kim J, Kim J H and Yun G S “Radio frequency emissions driven by energetic ions from neutral beam in KSTAR low confinement mode plasma” 2020 *Plasma Physics and Controlled Fusion* **62** 035004

- [131] Zalzali A I, Thome K E, Dendy R O, Chapman B, Chapman S C and Cook J W S 2021 “Simulations of ion cyclotron emission from DIII-D tokamak plasmas” *47th EPS Conference on Plasma Physics*
- [132] Crocker N, Tang S, Thome K, Lestz J, Belova E, Zalzali A, Dendy R, Peebles W, Barada K, Hong R, Rhodes T, Wang G, Zeng L, Carter T, DeGrandchamp G, Heidbrink W and Pinsker R “Novel internal measurements of ion cyclotron frequency range fast-ion driven modes” 2022 *Nuclear Fusion* **62** 026023
- [133] Zhang J, Zhao J, Liu L, Tong R, Zhong W and Luo Y “Experimental identification of ion cyclotron emission on HL-2A using YOLO neural network algorithm” 2024 *Nuclear Fusion* **64** 126070
- [134] Sumida S, Shinohara K, Ikezoe R, Ichimura M, Sakamoto M, Hirata M and Ide S “Comparison of Dispersion Model of Magneto-Acoustic Cyclotron Instability with Experimental Observation of ^3He Ion Cyclotron Emission on JT-60U” 2017 *Journal of the Physical Society of Japan* **86** 124501
- [135] McClements K G, D’Inca R, Dendy R O, Carbajal L, Chapman S C, Cook J W S, Harvey R W, Heidbrink W W and Pinches S D “Fast particle-driven ion cyclotron emission (ICE) in tokamak plasmas and the case for an ICE diagnostic in ITER” 2015 *Nuclear Fusion* **55** 043013
- [136] Marinoni A, Moeller C P, Rost J C, Porkolab M and Edlund E M “A Pockels cell enabled heterodyne phase contrast imaging diagnostic for detection of ion cyclotron emission” 2022 *Review of Scientific Instruments* **93** 083502
- [137] Samant O, Dendy R O, Chapman S C, Moseev D and Ochoukov R “Predicting ion cyclotron emission from neutral beam heated plasmas in Wendelstein7-X stellarator” 2024 *Nuclear Fusion* **64** 056022
- [138] Schmidt B S, Salewski M, Reman B, Dendy R O, Moseev D, Ochoukov R, Fasoli A, Baquero-Ruiz M and Järleblad H “Determining 1D fast-ion velocity distribution functions from ion cyclotron emission data using deep neural networks” 2021 *Review of Scientific Instruments* **92** 053528
- [139] Mohamed Z L, Kim Y, Knauer J P and Rubery M S “gamma-to-neutron branching ratio for deuterium-tritium fusion determined using high-energy-density plasmas and a fused silica Cherenkov detector” 2023 *Physical Review C* **107** 014606

- [140] Kim Y and Herrmann H W “Gamma-ray measurements for inertial confinement fusion applications” 2023 *Review of Scientific Instruments* **94** 041101
- [141] Kiptily V G, Cecil F E and Medley S S “Gamma ray diagnostics of high temperature magnetically confined fusion plasmas” 2006 *Plasma Physics and Controlled Fusion* **48** R59
- [142] Schmidt B S, Salewski M, Reman B C G, Dendy R O, Dong Y, Järleblad H, Moseev D, Ochoukov R, Rud M and Valentini A “Velocity-space sensitivity and inversions of synthetic ion cyclotron emission” 2023 *Physics of Plasmas* **30** 092109
- [143] Buneman O “The advance from 2D electrostatic to 3D electromagnetic particle simulation” 1976 *Computer Physics Communications* **12** 21–31
- [144] Pillepich A, Nelson D, Hernquist L, Springel V, Pakmor R, Torrey P, Weinberger R, Genel S, Naiman J P, Marinacci F and Vogelsberger M “First results from the IllustrisTNG simulations: the stellar mass content of groups and clusters of galaxies” 2018 *Monthly Notices of the Royal Astronomical Society* **475** 648–675
- [145] Arber T D, Bennett K, Brady C S, Lawrence-Douglas A, Ramsay M G, Sircombe N J, Gillies P, Evans R G, Schmitz H, Bell A R and Ridgers C P “Contemporary particle-in-cell approach to laser-plasma modelling” 2015 *Plasma Physics and Controlled Fusion* **57** 113001
- [146] Gorelenkov N N and Cheng C Z “Alfven cyclotron instability and ion cyclotron emission” 1995 *Nuclear Fusion* **35** 1743
- [147] Gorelenkov N N “Energetic particle-driven compressional Alfvén eigenmodes and prospects for ion cyclotron emission studies in fusion plasmas*” 2016 *New Journal of Physics* **18** 105010
- [148] Carbajal L and Calderón F A “On the 2D dynamics of the magnetoacoustic cyclotron instability driven by fusion-born ions” 2021 *Physics of Plasmas* **28** 014505
- [149] Yee K “Numerical solution of imital boundary value problems involving maxwell’s equations in isotropic media” 1966 *IEEE Transactions on Antennas and Propagation* **14** 302–307

- [150] Boris J P and Shanny R A 1971 “Proceedings of the Conference on the Numerical Simulation of Plasmas (4th) Held at the Naval Research Laboratory, Washington, D.C. on 2, 3 November 1970;” Tech. rep. Defense Technical Information Center Fort Belvoir, VA URL <http://www.dtic.mil/docs/citations/ADA023511>
- [151] Villasenor J and Buneman O “Rigorous charge conservation for local electromagnetic field solvers” 1992 *Computer Physics Communications* **69** 306–316
- [152] McMillan B F “Is it necessary to resolve the Debye length in standard or δf PIC codes?” 2020 *Physics of Plasmas* **27** 052106
- [153] Horký M, Miloch W J and Delong V A “Numerical heating of electrons in particle-in-cell simulations of fully magnetized plasmas” 2017 *Physical Review E* **95** 043302
- [154] Lee M U, Zalzali A, Dendy R O and Yun G S 2018 “Report of Visiting Research: EPOCH” Tech. rep.
- [155] Cook J W S 2011 *Fusion product driven lower hybrid electron current in tokamaks* PhD Thesis University of Warwick (United Kingdom) (available at: <https://wrap.warwick.ac.uk/49402/>)
- [156] Nelder J A and Mead R “A simplex method for function minimization” 1965 *Computer Journal* **7** 308–313
- [157] Kronrod A S “Nodes and weights of quadrature formulas. Sixteen-place tables” 1965 New York: Consultants Bureau (Authorized translation from the Russian)
- [158] Johnson S G 2013 “QuadGK.jl: Gauss–Kronrod integration in Julia” (available at: <https://github.com/JuliaMath/QuadGK.jl/>)
- [159] Foroosh H, Zerubia J and Berthod M “Extension of phase correlation to subpixel registration” 2002 *IEEE Transactions on Image Processing* **11** 188–200
- [160] Alba A, Aguilar-Ponce R M, Vigueras-Gómez J F and Arce-Santana E 2013 “Phase Correlation Based Image Alignment with Subpixel Accuracy” *Mexican international conference on artificial intelligence* (Springer Berlin Heidelberg) pp 171–182

- [161] Alba A, Arce-Santana E, Aguilar-Ponce R M and Campos-Delgado D U “Phase-correlation guided area matching for realtime vision and video encoding” 2014 *Journal of Real-Time Image Processing* **9** 621–633
- [162] Wu M C “Phase distribution and phase correlation of financial time series” 2006 *Physical Review E* **73**
- [163] Muquit M A, Shibahara T and Aoki T “A High-Accuracy Passive 3D Measurement System Using Phase-Based Image Matching” 2006 *IEICE TRANSACTIONS on Fundamentals of Electronics, Communications and Computer Sciences* **E89-A** 686–697
- [164] Takita K, Muquit M A, Aoki T and Higuchi T “A Sub-Pixel Correspondence Search Technique for Computer Vision Applications” 2004 *IEICE TRANSACTIONS on Fundamentals of Electronics, Communications and Computer Sciences* **E87-A** 1913–1923
- [165] Chien L H and Aoki T 2004 “Robust motion estimation for video sequences based on phase-only correlation” *6th IASTED International Conference on Signal and Image Processing* pp 441–446
- [166] Kim Y C and Powers E J “Digital Bispectral Analysis and Its Applications to Nonlinear Wave Interactions” 1979 *IEEE Transactions on Plasma Science* **7** 120–131
- [167] Moyer R A, Tynan G R, Holland C and Burin M J “Increased Nonlinear Coupling between Turbulence and Low-Frequency Fluctuations at the L-H Transition” 2001 *Physical Review Letters* **87** 135001
- [168] Holland C, Tynan G R, Diamond P H, Moyer R A and Burin M J “Evidence for Reynolds-stress driven shear flows using bispectral analysis: theory and experiment” 2002 *Plasma Physics and Controlled Fusion* **44** A453
- [169] Yamada T, Itoh S I, Maruta T, Kasuya N, Nagashima Y, Shinohara S, Terasaka K, Yagi M, Inagaki S, Kawai Y, Fujisawa A and Itoh K “Anatomy of plasma turbulence” 2008 *Nature Physics* **4** 721–725
- [170] Lee J, Yun G S, Choi M J, Kwon J M, Jeon Y M, Lee W, Luhmann N C and Park H K “Nonlinear Interaction of Edge-Localized Modes and Turbulent Eddies in Toroidal Plasma under $n = 1$ Magnetic Perturbation” 2016 *Physical Review Letters* **117** 075001

- [171] Irvine S W A 2018 *Collective Instability and Physics of the Anomalous Doppler Resonance in Fusion Plasmas* Ph.D. thesis (available at: <https://wrap.warwick.ac.uk/130719/>)
- [172] Kasaba Y, Matsumoto H and Omura Y “One and two dimensional simulations of electron beam instability: Generation of electrostatic and electromagnetic 2f p waves” 2001 *Journal of Geophysical Research* **106** 18693–18711
- [173] Thurgood J and Tsiklauri D “Self-consistent particle-in-cell simulations of fundamental and harmonic plasma radio emission mechanisms” 2015 *Astronomy and Astrophysics* **584** 11
- [174] Langdon A B “Kinetic theory for fluctuations and noise in computer simulation of plasma” 1979 *Physics of Fluids* **22** 163
- [175] Miller R H and Combi M R “A Coulomb collision algorithm for weighted particle simulations” 1994 *Geophysical Research Letters* **21** 1735–1738
- [176] Sherlock M and Rose S J “The persistence of Maxwellian D and T distributions during burn in inertial confinement fusion” 2009 *High Energy Density Physics* **5** 27–30
- [177] Derouillat J, Beck A, Pérez F, Vinci T, Chiaramello M, Grassi A, Flé M, Bouchard G, Plotnikov I, Aunai N, Dargent J, Riconda C and Grech M “Smilei : A collaborative, open-source, multi-purpose particle-in-cell code for plasma simulation” 2018 *Computer Physics Communications* **222** 351–373
- [178] McGuire K M 1997 “Fusion Energy 1996 Proceedings of an International Conference in Montreal, Canada, 7-11 October 1996” In *Fusion Energy 1996 (Proc. 16th Int. Conf. Montreal, Canada, 1996)* vol 1 (Montreal Canada: International Atomic Energy Agency) p 19
- [179] Keilhacker M “JET deuterium: tritium results and their implications” 1999 *Philosophical Transactions of the Royal Society of London. Series A: Mathematical, Physical and Engineering Sciences* **357** 415–442
- [180] Thomas P, Andrew P, Balet B, Bartlett D, Bull J, De Esch B, Gibson A, Gowers C, Guo H, Huysmans G and others “Observation of alpha heating in JET DT plasmas” 1998 *Physical review letters* **80** 5548
- [181] Team J E T and others “Alpha particle studies during JET DT experiments” 1999 *Nuclear Fusion* **39** 1619

- [182] Maslov M, Lerche E, Auriemma F, Belli E, Bourdelle C, Challis C, Chomiczewska A, Dal Molin A, Eriksson J, Garcia J, Hobirk J, Ivanova-Stanik I, Jacquet P, Kappatou A, Kazakov Y, Keeling D, King D, Kiptily V, Kirov K, Kos D, Lorenzini R, De La Luna E, Maggi C, Mailloux J, Mantica P, Marin M, Matthews G, Monakhov I, Nocente M, Pucella G, Riga-monti D, Rimini F, Saarelma S, Salewski M, Solano E, Štancar Stankunas G, Sun H, Tardocchi M, Van Eester D and Contributors J E T “JET D-T scenario with optimized non-thermal fusion” 2023 *Nuclear Fusion* **63** 112002
- [183] Garcia J, Kazakov Y, Coelho R, Dreval M, de la Luna E, Solano E R, Štancar Varela J, Baruzzo M, Belli E, Bonofgio P J, Candy J, Maggi C F, Mailloux J, Mazzi S, Ongena J, Ruiz J R, Poradzinski M, Sharapov S and Zarzoso D “Stable Deuterium-Tritium plasmas with improved confinement in the presence of energetic-ion instabilities” 2024 *Nature Communications* **15** 7846
- [184] Stringer T E “Radial profile of alpha -particle heating in a Tokamak” 1974 *Plasma Physics* **16** 651
- [185] Moseev D, Salewski M, Garcia-Muñoz M, Geiger B and Nocente M “Recent progress in fast-ion diagnostics for magnetically confined plasmas” 2018 *Reviews of Modern Plasma Physics* **2** 7
- [186] Salewski M, Nocente M, Madsen B, Abramovic I, Gorini G, Jacobsen A S, Kiptily V G, Korsholm S B, Moseev D, Nielsen S K, Poulsen A F L, Rasmussen J, Tardocchi M, Geiger B, Eriksson J, Contributors t J, Team t A U and Team t E M “Diagnostic of fast-ion energy spectra and densities in magnetized plasmas” 2019 *Journal of Instrumentation* **14** C05019
- [187] Team J “Fusion energy production from a deuterium-tritium plasma in the JET tokamak” 1992 *Nuclear Fusion* **32** 187
- [188] Tomabechi K, Gilleland J, Sokolov Y, Toschi R and ITER Team “ITER conceptual design” 1991 *Nuclear Fusion* **31** 1135–1224
- [189] ITER Physics Basis Editors, ITER Physics Expert Group Chairs, ITER Joint Central Team and Physics Integration Unit “Chapter 1: Overview and summary” 1999 *Nuclear Fusion* **39** 2137–2174
- [190] Dendy R, Chapman-Olopouli B, Reman B and Cook J “Mechanism for Collective Energy Transfer from Neutral Beam-Injected Ions to Fusion-

- Born Alpha Particles on Cyclotron Timescales in a Plasma” 2023 *Physical Review Letters* **130** 105102
- [191] Kaup D J, Reiman A and Bers A “Space-time evolution of nonlinear three-wave interactions. I. Interaction in a homogeneous medium” 1979 *Reviews of Modern Physics* **51** 275–309
- [192] Kravtchenko-Berejnoi V, Lefeuvre F, Krasnossel’skikh V and Lagoutte D “On the use of tricoherent analysis to detect non-linear wave-wave interactions” 1995 *Signal Processing* **42** 291–309
- [193] de Wit T D 2003 “Numerical Schemes for the Analysis of Turbulence — A Tutorial” *Space Plasma Simulation* ed Büchner J, Scholer M and Dum C T (Berlin, Heidelberg: Springer Berlin Heidelberg) pp 315–342 ISBN 978-3-540-36530-3
- [194] Itoh S I, Itoh K, Nagashima Y and Kosuga Y “On the Application of Cross Bispectrum and Cross Bicoherence” 2017 *Plasma and Fusion Research* **12** 1101003–1101003
- [195] Kotani T, Toida M, Moritaka T and Taguchi S “Simulation study of the harmonic structure of lower hybrid waves driven by energetic ions” 2023 *Physical Review E* **108** 035208
- [196] Toida M, Igami H, Saito K, Akiyama T, Kamio S and Seki R “Simulation Study of Energetic Ion Driven Instabilities near the Lower Hybrid Resonance Frequency in a Plasma with Increasing Density” 2019 *Plasma and Fusion Research* **14** 3401112–3401112
- [197] Ramchand L and Susmel R “Volatility and cross correlation across major stock markets” 1998 *Journal of Empirical Finance* **5** 397–416
- [198] Ochiai H and Imai H “On the distribution of the peak-to-average power ratio in OFDM signals” 2001 *IEEE Transactions on Communications* **49** 282–289
- [199] Baxley R and Zhou G “Power savings analysis of peak-to-average power ratio in OFDM” 2004 *IEEE Transactions on Consumer Electronics* **50** 792–798
- [200] Sandoval F, Poitau G and Gagnon F “Hybrid Peak-to-Average Power Ratio Reduction Techniques: Review and Performance Comparison” 2017 *IEEE Access* **5** 27145–27161

- [201] Naylor T and Jeffries R D “A maximum-likelihood method for fitting colour-magnitude diagrams” 2006 *Monthly Notices of the Royal Astronomical Society* **373** 1251–1263
- [202] Walmswell J J, Eldridge J J, Brewer B J and Tout C A “A transdimensional Bayesian method to infer the star formation history of resolved stellar populations” 2013 *Mon. Not. R. Astron. Soc.* **435** 2171–2186
- [203] Breimann A A, Matt S P and Naylor T “Statistical Fitting of Evolutionary Models to Rotation Rates of Sun-like Stars” 2021 *The Astrophysical Journal* **913** 75
- [204] Soltwisch H “Current density measurements in Tokamak devices” 1992 *Plasma Physics and Controlled Fusion* **34** 1669
- [205] Ludwig G, Rodrigues P and Bizarro J P “Tokamak equilibria with strong toroidal current density reversal” 2013 *Nuclear Fusion* **53** 053001
- [206] Chenna Reddy D and Edlington T “Plasma density measurements on COMPASS-C tokamak from electron cyclotron emission cutoffs” 1996 *Review of Scientific Instruments* **67** 462–468
- [207] Gorelenkov N N, Cheng C Z, Fredrickson E, Belova E, Gates D, Kaye S, Kramer G J, Nazikian R and White R “Compressional Alfvén eigenmode instability in NSTX” 2002 *Nuclear Fusion* **42** 977
- [208] Dendy R O, Lashmore-Davies C N, Cottrell G A, McClements K G and Kam K F “Ion Cyclotron Emission — a Natural Diagnostic for Fusion Alpha Particles” 1994 *Fusion Technology* **25** 334–340
- [209] Ali M, Zaheer S and Murtaza G “Propagation of Ordinary and Extraordinary Modes in Ultra-Relativistic Maxwellian Electron Plasma” 2010 *Progress of Theoretical Physics* **124** 1083–1095
- [210] Dendy R, Reman B, Akiyama T, Chapman S, Cook J, Igami H, Inagaki S, Saito K and Yun G 2017 “Modelling ion cyclotron emission from beam-injected ions in magnetic confinement fusion plasmas” *44th European Physical Society Conference on Plasma Physics, EPS 2017* (European Physical Society (EPS)) pp P5–145
- [211] Rebut P H “The JET preliminary tritium experiment” 1992 *Plasma Physics and Controlled Fusion* **34** 1749

- [212] Gao W, Zhang X, Yang L and Liu H 2010 “An improved Sobel edge detection” *2010 3rd International Conference on Computer Science and Information Technology* vol 5 pp 67–71
- [213] Hmood A K, Suen C Y and Lam L “An Enhanced Histogram of Oriented Gradient Descriptor for Numismatic Applications” *2018 Pattern Recognition and Image Analysis* **28** 569–587
- [214] Scharr H 2000 *Optimal operators in digital image processing* PhD Thesis (available at: <https://archiv.ub.uni-heidelberg.de/volltextserver/962/>)

DRAFT